Taming ultracold RbSr and Sr2

Ciamei, A.

Publication date
2018
Document Version
Final published version
License
Other

Taming ultracold RbSr and Sr_2

Alessio Ciamei

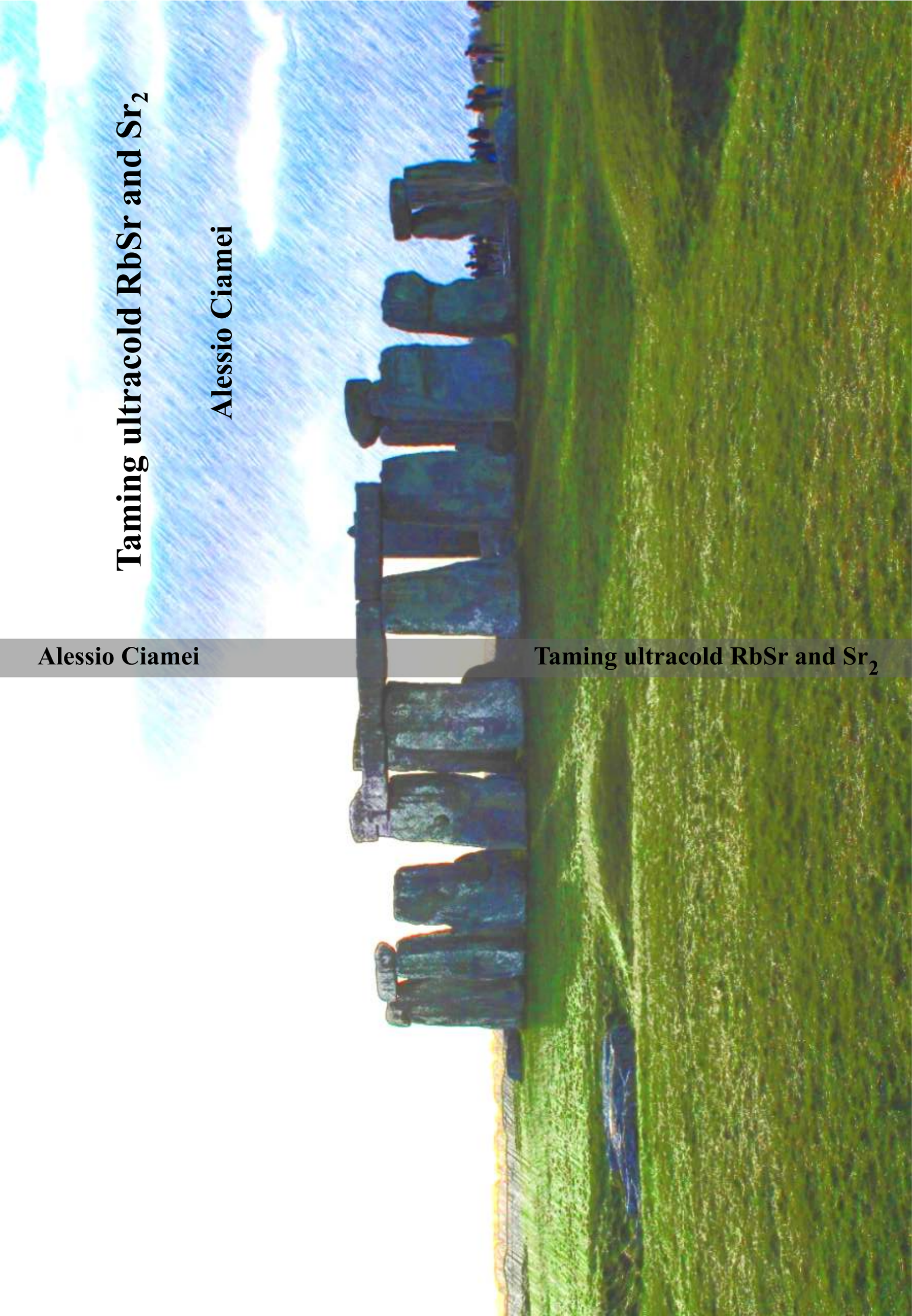

Taming ultracold RbSr and Sr_2

ACADEMISCH PROEFSCHRIFT
ter verkrijging van de graad van doctor
aan de Universiteit van Amsterdam
op gezag van de Rector Magnificus
prof. dr. ir. K.I.J. Maex
ten overstaan van een door het College voor Promoties ingestelde commissie,
in het openbaar te verdedigen in de Agnietenkapel
op donderdag 6 september 2018, te 14.00 uur
door Alessio Ciamei
geboren te Rome, Italy

Promotor:	prof. dr. F.E. Schreck	Universiteit van Amsterdam
Copromotor:	dr. B. Pasquiou	Universiteit van Amsterdam
Overige leden:	dr.ir. S.J.J.M.F. Kokkelmans	T.U. Eindhoven
	prof. dr. H.B. van Linden van den Heuvell	Universiteit van Amsterdam
	prof. dr. W.J. Buma	Universiteit van Amsterdam
	prof.dr. O. Dulieu	Universite Paris Sud, CNRS
	dr. A. de Visser	Universiteit van Amsterdam

Faculteit der Natuurwetenschappen, Wiskunde en Informatica

The research reported in this thesis was carried out at the Van der Waals-Zeeman Institute, Institute of Physics, University of Amsterdam. The work was financially supported by European Research Council (ERC) under Project No. 615117 QuantStro, and the NWO through the Veni grant No. 680-47-438.

"*Omnis ars naturae imitatio est*"

Lucius Annaeus Seneca, Epistulae Morales ad Lucilium
Liber VII, Ep. LXV

Contents

To B.C. . . .

Chapter 1

Introduction

1.1 Motivation

The interplay between quantum mechanics and interactions has had an unprecedented impact on the SI system of units and in fundamental science. Metrology will soon witness a revolution[1] based on the redefinition of fundamental constants in terms of universal physical quantities. The kg mass artifact, the temperature of the triple point of water, the mass of carbon-12 and the vacuum permeability will be dropped in favor of the Planck constant, the Boltzmann constant, the Avogadro number and the electric charge of the electron. In fundamental physics we have gained the interpretation of previously unexplained phenomena, e.g. black-body radiation, natural radioactivity and superconductivity, and discovered new ones, e.g. blue-light emitting diodes, a self-sustained nuclear chain reaction, and the Josephson effect. Both metrology and fundamental physics benefit from the understanding of quantum-mechanical interactions. In many cases great effort is necessary to understand a composite system based on its constituents and the rules governing them. This happens because a system of many interacting particles can exhibit properties that are hard or even impossible to foresee by looking at its building blocks [1]. The result of such foundational work can ultimately enable important new applications, and it can do so in unexpected ways. Scale and complexity make strongly interacting quantum systems computationally intractable and motivate new theoretical and experimental methods.

The complexity within atoms and molecules, the building blocks of chemistry and biology, is at present at the limit of our capabilities for accurate calculations from first principles. Experimental investigation of these systems has provided excellent understanding of their properties. Thus atoms and molecules represent our home base

[1] "The biggest revolution in metrology since the French Revolution", according to Prof. Klaus von Klitzing. See https://www.bipm.org/en/measurement-units/rev-si .

for applications such as metrology and precision measurements, and for exploration of emergent physics arising from the interaction *between* them. The importance of atoms and molecules to applications is evident since decades, as exemplified by the definition of the second via the ^{133}Cs hyperfine splitting, and by the precision measurement of the fine structure constant and the proton-to-electron mass ratio, and this progress seems far from saturation [2, 3, 4]. The role of atoms and molecules in the field of fundamental science is strengthened by recent experimental advancements. Experiments show that, by achieving full quantum control over these building blocks, open questions in both chemistry and physics can be addressed. In the former case, investigation of chemical reactions at their most fundamental quantum level is possible [5, 6, 7]. In the latter, quantum simulation experiments could allow exploration of phenomena such as high-temperature superconductivity, topological order and quantum magnetism [8, 7, 9, 10]. The reason for our interest in quantum simulation is two-fold. Firstly, the same physics is harder to study directly in other systems, e.g. condensed matter systems, on which the experimenter has not complete control and cannot tune the effects of interactions at will. Secondly, the same physics might not be observable in other systems in Nature.

In conclusion, it is desirable to exploit the physics *within* atoms and molecules for precision measurements (PM) and *between* them for investigation of few-body physics (FBP) and many-body physics (MBP).

1.2 Atoms vs molecules

Over the last four decades the advent of laser technology allowed the development of laser cooling and trapping techniques for neutral atoms. This technological advancement unlocked the possibility to cool atoms down to ultracold temperatures on the order of a millionth of degree Kelvin above the absolute zero. Over twenty years ago control of the atomic motion at the quantum level was achieved, marked by the realization of Bose-Einstein condensates (BEC), giving rise to the field of quantum gases. Ultracold and quantum gases of atoms contributed strongly to the research areas of our interest, of which we only give a few examples. In metrology we witnessed the advent of optical lattice clocks, in few-body physics the investigation of Efimov spectra, and in many-body physics the observation of the BEC to Bardeen-Cooper-Schrieffer crossover. However, for the temperatures achievable with today's technology, the energy scale of long-ranged interactions is not sufficiently high compared to the energy scale of thermal excitations to address urgent open fundamental questions, e.g. superconductivity, quantum magnetism, and topological order. Many research groups

have therefore turned their attention to systems with stronger, long-ranged interactions, most notably strongly-magnetic atoms, highly-excited Rydberg atoms and polar molecules. Each of these systems has advantages and disadvantages. While the creation of quantum-degenerate gases of strongly magnetic atoms is well established, the long-ranged interactions are weaker than for the other systems. Highly-excited Rydberg atoms provide the strongest interaction within this subset, but their lifetime is not long enough to allow for investigation of our target research areas. In this sense polar molecules represent a trade-off, which we believe to offer very good prospects.

Dimers, the simplest molecules, posses two main features that are expected to bring significant contributions to our three main research areas. The first, common to both homonuclear and heteronuclear dimers, is the richer internal structure compared to atoms, with the additional degrees of freedom of vibration and rotation. This corresponds to the presence of several coexisting energy-scales in a dimer, i.e. electronic, vibrational, rotational, fine and hyperfine, which are all addressable with current technology. The second, present only in heteronuclear dimers, is the existence of a permanent electric dipole moment in ground-state molecular levels. In the presence of a guiding electric field or between rotationally excited states, this electric dipole moment results in strong long-ranged anisotropic interactions between molecule pairs. Interesting physics arises from the competition of energy (or length) scales for particles with dipole moment d. For quantum effects to be observable the dipolar interaction energy E_{dd} should be high compared to the thermal energy $k_{\mathrm{B}}T$. Moreover the characteristic dipolar interaction length a_{dd} should be comparable to the s-wave scattering length a_s for identical bosons (typically $a_s \sim 10^2 a_0$) or the inverse of the Fermi wave-vector $1/k_F$ for identical fermions (typically $1/k_F \sim 10^2 a_0$) [2]. For point-like dipoles pinned to lattice sites, the interaction energy shift V_{dd} between nearest-neighbors should be compared to the tunneling rate. The figures of merit for the dipolar nature of the system, are then d, a_{dd} and V_{dd}, which can be compared across different species [11]. For an overview of such quantities for weakly-magnetic atoms, strongly-magnetic atoms, and polar molecules see table 1.1.

The three topic areas would strongly benefit from the use of ultracold dimers in the following terms [12]:

- **PM**: Novel time standards could be realized, for instance a clock in the tens-of-THz range, using vibrational transitions as reference [13], or an optical clock using ultra-narrow transitions [14]. These realizations have been proposed for dimers composed of bosonic alkaline-earth atoms, already widely employed for

[2] a_{dd} is defined in a way such that the ratio a_{dd}/a_s in BEC and the product $a_{dd}k_F$ in a Fermi gas are proportional to the ratio between dipolar interaction energy and mean-field energy or Fermi energy, respectively.

Particle	d_{E}	d_{M}	a_{dd} (a_0)	V_{dd}/h (Hz)
^{87}Rb	0	0.5 μ_B	0.18	0.02
^{52}Cr	0	6.0 μ_B	15	3.1
^{164}Dy	0	9.9 μ_B	130	8.4
^{168}Er	0	7.0 μ_B	67	4.2
^{168}Er$_2$	0	14.0 μ_B	533	16.9
KRb	0.57 D	0	3.9×10^3	0.32×10^3
RbCs	1.2 D	0	3.0×10^4	1.4×10^3
NaK	2.7 D	0	4.4×10^4	7.3×10^3
NaRb	3.3 D	0	1.1×10^5	1.1×10^4
KCs	1.9 D	0	6.0×10^4	3.7×10^3
LiK	3.5 D	0	5.3×10^4	1.2×10^4
LiRb	4.1 D	0	2.0×10^5	1.7×10^4
LiCs	5.5 D	0	4.0×10^5	3.0×10^4
RbSr	1.5 D	0.5 μ_B	3.9×10^4	2.4×10^3
RbYb	0.21 D	0.5 μ_B	1.1×10^3	44
LiYb	$\leq$ 0.1 D	0.33 μ_B	≤ 200	≤ 10

TABLE 1.1: Quantities relevant for observation of long-ranged dipolar interactions for several dipolar atomic and molecular systems, adapted from [11]. The magnetic (electric) dipole moment d_{M} (d_{E}) in units of μ_B (Debye) is shown together with dipolar length a_{dd} and energy shift V_{dd} for point-like dipoles at a distance of 532 nm. $d_{\mathrm{M,E}}$ are the values for the ground state of the particles (the singlet ground state in case of alkali dimers). a_{dd} and V_{dd} correspond to the magnetic or electric dipole in case of atoms or molecules.

atomic clocks, to which they could be compared. From a different perspective such systems could be used for precision spectroscopy measurements of the time variation of fundamental constants, i.e. the electron-to-proton mass ratio and fine-structure constant, for the search of possible deviations from Newtonian gravity, and the exploration of particle physics beyond the standard model[15].

- **FBP**: Time-resolved investigation of chemical reactions at the quantum level can be achieved [7, 6]. This problem is usually not addressed in chemistry, because most chemical reactions are investigated at temperatures above a few Kelvin, and thermal averaging prevents an analysis at the quantum-mechanical level. However, ultracold molecules at sub-microkelvin temperatures can be initialized in pure quantum-mechanical internal states and their collision kinematics, i.e. velocities and angular momenta, precisely controlled down to the level of a single partial wave. The resulting temporal evolution of the system through

transition states could be probed using, e.g., frequency comb spectroscopy or the resonance-enhanced multiphoton ionization technique [16]. Finally, the end reaction products can be determined together with the scattering cross-sections describing the conversion of reactants into products. Given the very low entropy of the initial collision states, electric and magnetic resonances between coupled states can be exploited to control the reaction paths.

- **MBP**: Quantum simulation experiments, observation of emergent phenomena and studies of many-body quantum states can be performed [9, 7]. This vast area of research is allowed by the existence of a strong electric-dipole moment in some ground-state heteronuclear dimers. Because of this, molecules feature long-range anisotropic interactions strong enough to result in significant effects. Furthermore, because of the anisotropic nature of the interaction, use of different trapping geometries and guiding electric fields will allow for investigation of dimensionality effects in such systems. As an example, sufficiently cold polar molecules in a two-dimensional trap can be stabilized by application of a strong perpendicular electric field. Dressing of this system via microwave fields could result in the formation of a topological superfluid, which might harbor Majorana fermions, that have applications for error-resilient quantum computation [17, 18, 19]. As a different example, molecules pinned down to sites of a three-dimensional optical lattice would realize a lattice-spin model of magnetism and represent a strongly frustrated system, intractable by theoretical tools due to the high degree of entanglement. Experimental investigation of phase diagrams could be possible.

1.3 State of the art

The techniques optimized throughout the years to cool and trap atoms can unfortunately not be directly applied to molecules. This is intrinsically connected to the richer internal structure of molecules, where the necessary cycling optical transitions exploited to cool atoms with light are typically absent. Two main approaches for the production of ultracold and quantum gases of molecules are being currently investigated. One seeks to extend cooling and trapping techniques to address specific molecular species using tools like buffer gas, Stark and Zeeman decelerators and even laser cooling [7, 12, 20]. The other consists in a two-step approach, first cooling and trapping atoms with the standard experimental toolbox, then associating pairs of atoms into molecules in a coherent manner therefore retaining the low entropy achieved by cooling the atoms. Although both approaches have seen impressive results, only the

second one has been able to produce a molecular gas with a phase-space-density close to quantum degeneracy.

The two-step approach resulting in a near-degenerate molecular gas was demonstrated ten years ago by Jin and Ye's group [21]. The second association step was an extraordinary example of quantum-engineering. ^{40}K and ^{87}Rb atoms in a quantum-degenerate mixture were first associated into weakly-bound molecules by exploiting a magnetically tunable Fano-Feshbach resonance, and then these highly-excited molecules were transferred to the rovibrational ground state via optical implementation of Stimulated Raman Adiabatic Passage (STIRAP). Since the association step only involves coherent population transfer, the entropy of the final molecular gas increases slightly due to imperfections. The overall efficiency was high enough to yield the desired high phase-space-density. Moreover, the dipolar molecular gas could be stabilized via application of suitable electric field and tight confinement in optical lattices. This represents an exemplary *production* scheme for ultracold molecular gases useful to target our main research areas. This strategy was subsequently applied to several other alkali dimers [22, 23, 24, 25].

Unfortunately, even this approach cannot be easily generalized to any ultracold atomic mixture. The weak link of the production chain is the magnetically-tunable resonance used to form the molecules in the first place. The underlying requirement on the two-body system in the electronic ground state is the existence of an atom-pair state and a molecular level with different magnetic moments and strong enough coupling between them to allow for an avoided crossing with sufficiently large energy gap. In this condition the magnetic field can be adiabatically swept across the resonance and induce efficient population transfer. The simultaneous requirement of magnetic moments and sufficient coupling strength makes this scheme particularly suitable for bi-alkali systems, which feature a rich hyperfine spectrum and strong spin-exchange interaction. However, its application to the molecules of our interest, i.e. AE-AE and A-AE dimers, is hard or even impossible.

Recent work by our group [26] and Zelevinsky's group [27] has demonstrated photoassociation of Sr_2, however these experiments did not result in long-lived quantum gases. Furthermore, application of this method to other species has not been studied yet.

1.4 Which type of molecule?

It is crucial to identify molecular species that best serve our purposes, both for applications, i.e. PM, and fundamental science, i.e. FBP and MBP. Firstly the feasibility of production of ultracold dimers, which can strongly depend on the molecular species,

should be assessed. Secondly, PM applications strongly rely on the properties of molecules determined by the physics *within* the molecules themselves. Thirdly, FBP and MBP can significantly benefit from the choice of one molecule instead of the other because the molecular properties strongly affect the physics arising from the interaction *between* them.

In the field of PM bosonic homonuclear alkaline-earth dimers (AE_2) are desirable and several experiments have been proposed in the last decade [13, 14]. This is due to the relative simplicity of these molecules or in other words the right amount of complexity beyond what atoms provide. Indeed, these systems are composed of two identical closed-shell $^1S_0$ atoms with zero nuclear moment in their ground state. This implies three facts. Firstly, the absence of an electric dipole moment in the ground state, therefore their insensitivity to external electric fields. Secondly, the absence of spin-exchange interaction and the presence of an isolated non-magnetic ground state, which is insensitive to external magnetic fields. Thirdly, the absence of hyperfine structure, which simplifies some experimental schemes. Recent work by our group [26] and Zelevinsky's group [27] has demonstrated photoassociation of $^{84}Sr_2$ and $^{88}Sr_2$, respectively. Although these experiments did not result in long-lived quantum gases, they represent an extremely good starting point for any further investigation.

In the field of FBP and MBP, alkali – alkaline-earth (A-AE) dimers are desirable. Thanks to the unpaired valence electron originating from the alkali element, A-AE ground-state molecules are open-shell molecules and posses a magnetic dipole moment in addition to the electric dipole moment. Because of this A-AE ground-state dimers are substantially different from alkali ground-state dimers, which are closed-shell molecules with zero electronic spin and no magnetic dipole moment. This is of great interest for investigation of FBP for two reasons. Firstly, so far only controlled reactions of ground-state alkali dimers have been experimentally studied, and separate investigation of A-AE dimers is necessary to understand the effect of the different internal structure. Secondly, the presence of the magnetic dipole moment in A-AE dimers makes it easier to tune the ratio between reactive-inelastic to elastic cross-sections of dimer-dimer scattering events [3]. Some of the methods proposed to this end rely on repulsive van der Waals interactions induced by the application of strong electric fields on molecules prepared in excited rotational states [28, 29, 30]. The requirements on the field strength is strongly reduced in the case of A-AE dimers thanks to higher number of spin states and possibility to shift the molecular levels thanks to the unpaired electron's spin. In particular RbSr is an excellent choice owing to a large electric dipole moment of 1.5 Debye [31], see table 1.1, and a high reduced mass leading to smaller rotational-level splittings. According to our collaborators J.

[3] An example of reactive scattering event is $RbSr+RbSr \rightarrow Rb_2+Sr_2$, which is energetically allowed and would make the molecular sample unstable.

Bohn and G. Quemenér, in RbSr a ratio between reactive-inelastic and elastic scattering cross-sections of order 1:100 can be reached by application of suitable magnetic field and electric field, the latter of order 100 V/cm. In alkali dimers like RbCs or KRb the same level of suppression of undesired processes would require more than a ten-fold increase in the electric field strength compared to RbSr, which is technically more challenging.

This effect, despite its own interest as FBP, is strongly beneficial for the prospects of MBP studies. Many of the proposals regarding MBP require a quantum-gas of polar molecules as starting point. This has never been experimentally realized, ultimately because of reactive-inelastic lossy collisions. Indeed, imperfections in the association step, from atom-pairs to dimers, lead to an increase of entropy in the system. This can be compensated by an additional evaporative cooling stage, which however is only successful in case the elastic collisional cross-section overwhelms the reactive-inelastic ones. As explained above RbSr molecules have very good prospects in this respect. Realization of such a dipolar quantum gas is one of the main drives in our field and would allow for the realization of a molecular BEC and possibly a Wigner crystal at low and high densities. Adiabatic loading of such a molecular BEC into optical lattice potentials would enable further investigation of MBP. RbSr molecules pinned to sites of a three-dimensional optical lattice could simulate a quantum magnetism model, where the pseudo-spin could be encoded in rotational states or directly in the electronic spin of the molecule [32]. RbSr molecules in a stack of two-dimensional traps and in the presence of a guiding electric field and microwave radiation would allow realization of topological superfluid phases.

A double BEC of Rb and Sr was realized in our group in 2013 [33]. Thanks to the different polarizability of ground-state Rb and Sr and shaping of the BECs with with help of a bi-chromatic dipole trap, an optical lattice with roughly 20×10^3 sites occupied by exactly one atom of each species was realized [34]. This represents an extremely good starting point for the first association step into weakly-bound molecules by either magneto- or photo-association. The subsequent step(s) necessary for the transfer to the rovibrational ground state has already been theoretically investigated and offers good feasibility prospects [35, 36, 37].

1.5 Objective of this thesis

The goal of this thesis is the investigation of efficient production schemes of ultracold molecules of our interest, AE-AE and A-AE dimers. We will focus our attention on two molecular species. We choose $^{84}Sr_2$ as example of AE-AE dimer and RbSr as example of A-AE dimer. This choice is motivated in the previous sections.

In both cases we will aim at identifying efficient production schemes, based either on photo- or magneto-association. By this, we mean experimental sequences that can provide dense and cold enough ground-state molecules to perform experiments in the main areas of PM, FBP, and MBP.

1.6 Overview of this thesis

Our research will be described in the following six chapters, most of which correspond to articles that have been published (chapters 3, 4 and 7) or are in preparation (chapters 5 and 6). In chapter 2, we will provide a brief overview over similar research in the world, we will present the main experimental methods and the experimental set-up. In chapter 3, we will investigate STIRAP applied to a Mott-insulator of Sr atoms, analyze its limitations experimentally and analytically and overcome them reaching molecule production with efficiency in excess of 80%. In chapter 4, we will report on our STIRAP attempts in a Sr BEC and demonstrate the first direct observation of photoassociation products together with the measurement of molecular inelastic collision rate constants. In chapter 5, we will describe one-color spectroscopy of RbSr close to the Sr intercombination line and analyze magnetic and optical properties of the observed transitions in view of unsuccessful STIRAP attempts on RbSr and the successful ones on Sr_2. In chapter 6 we will provide our main insight into the molecular physics of RbSr. In particular we show a joint work of our group and the group of Prof. Wlodzimierz Jastrzebski from Warsaw [4], combining two-color spectroscopy with thermal fluorescence and laser induced spectroscopy experiments, together with a novel joint data analysis and the resulting fitted potential energy curve for the open-shell, polar ground state of RbSr. Finally, in chapter 7, we will show the first experimental observation of Fano-Feshbach resonances in an A-AE system, i.e. RbSr, and the identification of predicted isotropic coupling mechanisms and novel anisotropic mechanisms. In chapter 8 we will give an outlook.

[4] Link to the group's website: http://info.ifpan.edu.pl/sdvs/pl/on2.5.html

Chapter 2

Overview of the research

2.1 Context

Research groups working on ultracold molecules have multiplied in the recent years. However, most of them work on alkali dimers, for which a molecule production scheme was experimentally demonstrated, as explained in the previous chapter. Our target systems are instead Sr_2 and RbSr dimers, which have a different structure and do not allow for a direct implementation of the molecule production methods developed for alkali dimers. Furthermore, these systems involve cooling and trapping of at least one AE element, and their investigation represents a recent effort in the ultracold molecule community. As for AE-AE dimers, our group and Zelevinsky's group produced $^{84}Sr_2$ and $^{88}Sr_2$ molecules in 2012, see previous chapter. As for A-AE dimers, there are seven experimental groups currently working on this topic around the world: Görlitz's and Porto's groups (RbYb) [38, 39], Takahashi's and Gupta's groups (LiYb) [40, 41], Cornish's group (CsYb) [42], Kleinert's group (RbCa) [43], and our group (RbSr). None of these groups has demonstrated coherent production of ultracold molecular samples so far. We propose to investigate molecule production schemes for both our target systems using the following experimental methods and setup.

2.2 Experimental methods

The research presented in this thesis requires several experimental methods for the preparation of the atomic sample and the investigation of molecule production schemes on Sr and Rb-Sr systems. We prepare ultracold thermal gases and quantum gases [44, 45, 34], on which we perform spectroscopy and study molecule production, respectively. In this section we outline our experimental techniques. Firstly, in section 2.2.1 we will give an overview of the relevant laser cooling and trapping techniques,

and we will outline the experimental sequence for preparation of Sr and Rb-Sr ultracold gases. Secondly, in section 2.2.2 we will describe the obtainment of quantum degeneracy, in particular of Bose-Einstein condensation (BEC), and the realization of atomic Mott insulators (MIs). In section 2.2.3 we will concentrate on the methods necessary for molecule production. Finally, in section 2.2.4 we will describe our atom detection methods.

2.2.1 Preparation of ultracold atomic samples

In order to perform high-precision molecular spectroscopy we prepare ultracold atomic samples. These samples are prepared using laser cooling and trapping techniques, which have been developed over the last four decades and have become standard tools in the atomic physics community [46, 47]. Most of those techniques rely on the scattering of laser light propagating opposite to the atoms, and the resulting net reduction of the atomic kinetic energy. In their simplest design, they exploit the Doppler effect, hence the expression Doppler cooling, and their lower temperature limit, known as Doppler temperature, is set by the linewidth of the employed atomic transition [48, 49]. More sophisticated schemes, which exploit the multi-level structure of the atoms, their (a)diabatic response to polarized laser radiation and the presence of "dark" states, are able to cool below the Doppler limit, and are hence called sub-Doppler techniques [50, 51, 52, 53, 54].

Cooling, trapping, manipulation and probing of the atoms require good vacuum conditions. The vacuum system, see Fig. 2.1, is essentially identical to the one of the FeLiKx machine [55] and is composed of two main parts, which are the oven chamber and, separated by a gate valve, the ultra-high vacuum (UHV) chamber. The gate valve allows us to refill the Rb and Sr reservoirs without disturbing the UHV chamber. Two differential pumping stages maintain a pressure difference of roughly two orders of magnitude between the two chambers. The glass cell, which guarantees good optical access for the lasers, is connected with bellows to the Zeeman slower (ZS) section and to the end section to which the ZS window is connected.

In our ultracold atom machine, the atoms, exiting an oven as an effusive beam, enter the UHV chamber and are firstly decelerated by Zeeman slowing [56]. This one-dimensional slowing technique provides deceleration by maximizing the scattering of a single laser beam propagating opposite to them, see ZS beams in Fig. 2.1. This requires laser light to be resonant with the atomic transition despite the deceleration of the atoms and it is realized by the application of a magnetic field suitable for compensating the velocity-dependent Doppler shift via the induced Zeeman shift, see ZS coils in Fig. 2.1. After this first stage, the atoms are slow enough to be captured in a three-dimensional magneto-optical trap (3D MOT), which results in both

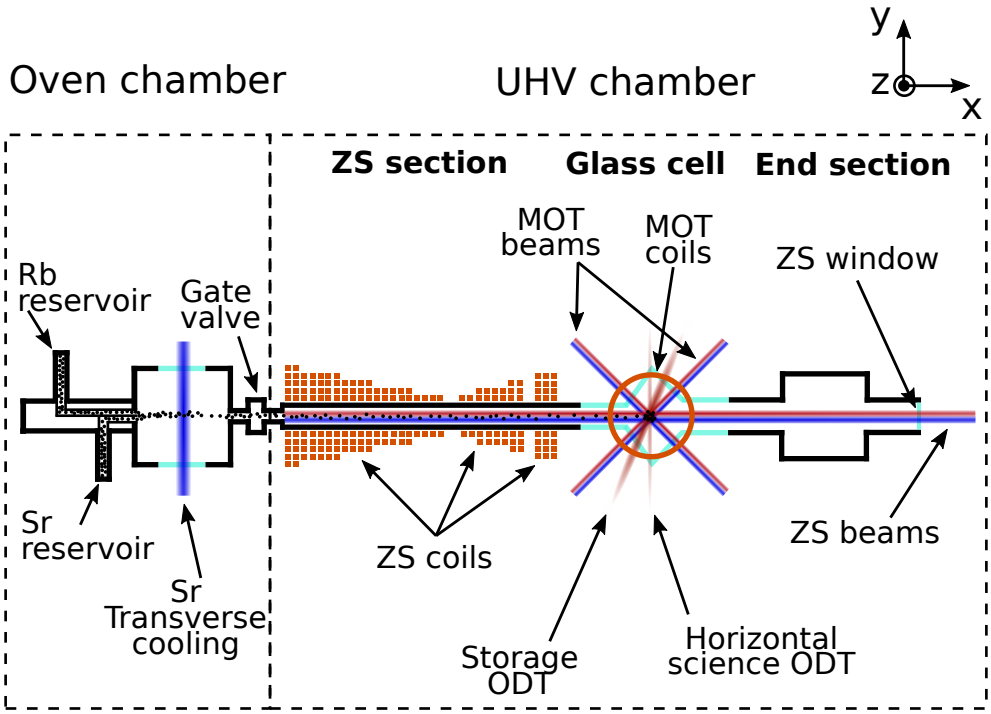

FIGURE 2.1: Sketch of the vacuum system. ZS, MOT and ODT are defined in the main text. Only laser beams used for cooling of Rb on the D_2 transition and cooling of Sr on the blue transition are shown for simplicity. Important vacuum components, e.g. ion and titanium-sublimation pumps, are not shown. Elements not on scale.

cooling and trapping in three dimensions [57, 58]. This technique, which exploits the radiative force of polarized light and spin-polarization of the atoms [59, 60], requires three orthogonal pairs of counter-propagating laser beams, red-detuned to the atomic transition, see MOT beams in Fig.2.1, and a quadrupole magnetic field at the desired location of the atomic cloud, see MOT coils in Fig. 2.1. Sub-Doppler cooling techniques, such as polarization gradient cooling in optical molasses, gray molasses, and Raman-sideband cooling [61, 62, 63, 64], can be applied to decrease the temperature even further. If the temperature is sufficiently low, the atomic cloud can be loaded into an optical dipole trap (ODT) [65], see storage ODT and horizontal science ODT in Fig. 2.1. This trapping technique exploits the electric dipole moment induced on the atoms by the electric field of an intense laser beam with frequency far away from any atomic excitation. The interaction between the electric dipole and the electric field results in a conservative trapping potential for the atoms. In such a conservative trapping potential controlled experiments on ultracold atoms can be performed.

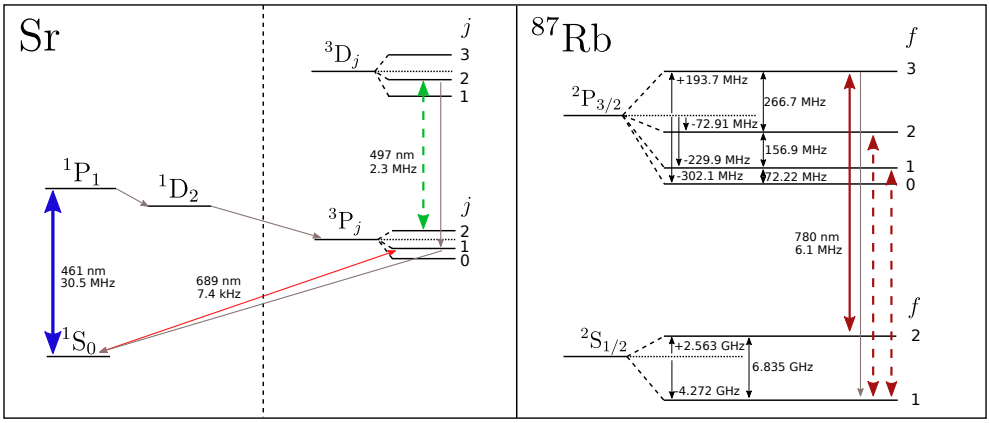

FIGURE 2.2: Subset of energy levels of bosonic ^{84,86,88}Sr and ^{87}Rb. Lines with double arrows represent optical transitions addressed by lasers with a color representative of the corresponding wavelength. Solid lines are cooling transitions, while dashed lines are optical-pumping transitions. Grey lines with single arrow represent spontaneous emission processes of relevance. Energy splittings not on scale.

In our experiment we exploit the exceptional Doppler-cooling properties of Sr for efficient production of ultracold Sr and Rb-Sr samples. Rb is an alkali atom with

a single valence electron and as a consequence its ground state is coupled to low-lying excited states by strong electric dipole transitions, see Fig. 2.2. In particular, the linewidth of the $^2S_{1/2}\rightarrow{}^2P_{3/2}$ cooling transition, known as the D_2 transition, is $\sim 6.1\,\mathrm{MHz}$, corresponding to a Doppler temperature of $\sim 150\,\mu\mathrm{K}$ [66]. Sub-Doppler cooling can reduce the temperature to $5-15\,\mu\mathrm{K}$ [67]. Sr, instead, has two valence electrons, hence its low-lying excited states have two possible electron spin quantum numbers, see Fig. 2.2. This results in the presence of both strong electric dipole transitions, if the spin is conserved, and weak electric-dipole-forbidden transitions, if a spin-flip is involved. Two transitions are used for laser cooling of Sr, one blue transition, i.e. $^1S_0\rightarrow{}^1P_1$, with linewidth $\sim 30\,\mathrm{MHz}$ and Doppler temperature of $\sim 0.7\,\mathrm{mK}$ and one red intercombination transition, i.e. $^1S_0\rightarrow{}^3P_1$, with linewidth $\sim 7.4\,\mathrm{kHz}$ and a Doppler temperature of only $\sim 0.2\,\mu\mathrm{K}$ [68, 69], roughly half of the photon-recoil temperature. Thus, the strategy for efficient production of ultracold Rb-Sr mixtures is to transfer the excellent cooling properties of Sr to Rb. This is accomplished by sympathetically cooling Rb atoms with colder Sr atoms, which serve as a refrigerant. In the following we will briefly describe the preparation of ultracold Sr gases [44] and, afterwards, Rb-Sr gas mixtures [34].

Preparation of a single-species Sr sample

To prepare a single-species Sr sample, the experimental sequence starts with Zeeman slowing the atomic beam exiting the oven on the broad blue transition at 461 nm. After the Zeeman slowing stage, the atoms are slow enough to be captured in the glass cell by a first 3D MOT, operating on the same broad transition with Doppler temperature $\sim 0.7\,\mathrm{mK}$. During the MOT, since the $^1S_0\rightarrow{}^1P_1$ transition is not perfectly cycling due to the presence of an intermediate $^1D_2$ state, Sr atoms accumulate in the metastable $^3P_2$ state, which is magnetically trapped by the existing quadrupole magnetic field. The shelved atoms are subsequently optically re-pumped into the ground state and re-captured by a second 3D MOT, operating on the narrow red transition, for which Doppler and recoil limit are almost equivalent. More than half of the resulting $\sim 1\mu\mathrm{K}$ cold cloud is loaded into the horizontal science ODT, see Fig. 2.1. Finally, in order to increase the density of the atoms, we ramp on a vertical near-infrared dipole trap beam, ending with atoms in a crossed ODT with density-averaged densities up to $10^{13}\,\mathrm{cm}^{-3}$. Although the basic cooling mechanisms are equivalent for all isotopes, the narrow-line 3D MOT for fermionic ^{87}Sr is more involved due to the presence of a nuclear moment in ^{87}Sr and requires use of an additional stirring laser beam [70], see Fig. 2.3. ^{84}Sr instead, due to the low abundance, requires transverse cooling by 2D optical molasses before the ZS, in order to increase the atomic flux captured by the MOT.

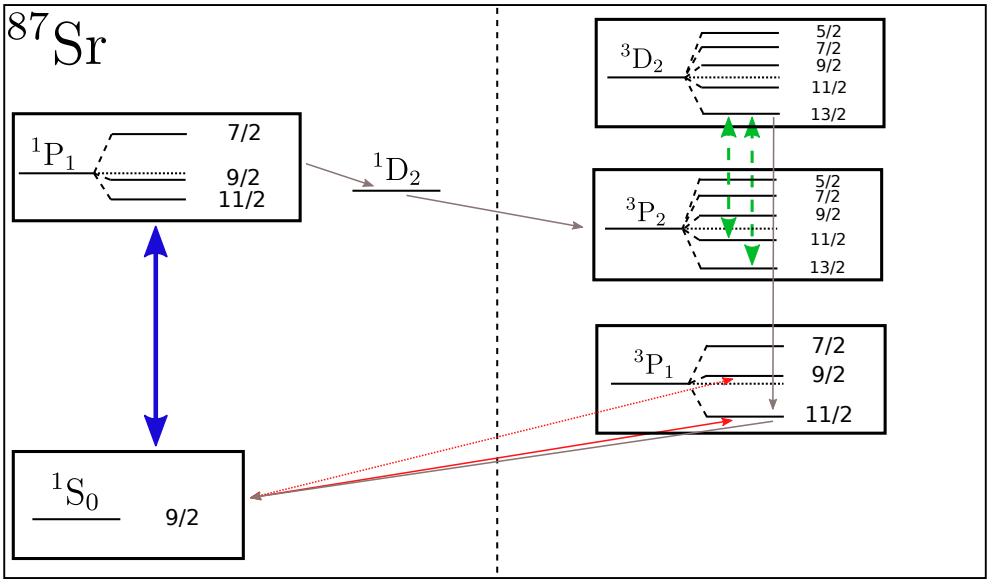

FIGURE 2.3: Subset of energy levels of fermionic ^{87}Sr. Lines with double arrows represent optical transitions addressed by lasers with a color representative of the corresponding wavelength. Solid lines are cooling transitions, dotted lines are "stirring" transitions, dashed lines are optical-pumping transitions. Grey lines with single arrow represent spontaneous emission processes of relevance. The fraction on the right side of an energy level is the hyperfine quantum number f. Energy splittings not on scale.

Preparation of a Rb-Sr mixture

Since Rb and Sr differ in their optical and magnetic properties and the apparatus has a single ZS section, they undergo the Zeeman slowing stage sequentially. We start by setting the laser and coil configurations to slow down Rb atoms, accumulate them in a MOT and then transfer them into a storage ODT, Fig. 2.1. Then we change the experimental parameters to laser cool Sr. In the following, we will give more details on the experimental sequence.

After being Zeeman slowed on the D_2 $f^{Rb} = 2 \rightarrow f^{Rb} = 3$ transition, Rb atoms are slow enough to be trapped in the 3D MOT operated in the glass cell on the same atomic transition. Unlike Sr, the Rb ground state is a hyperfine doublet, and during laser cooling, atoms can be optically pumped into the $f^{Rb} = 1$ hyperfine ground state, where they are not anymore addressed by the laser cooling light, which leads to a loss of atoms. To solve this problem we shine a "repump" laser addressing the D_2 $f^{Rb} = 1 \rightarrow f^{Rb} = 2$ line onto the atoms. Before trapping Rb in the storage ODT we further cool it down by polarization-gradient cooling in an optical molass, realized by the same MOT light in the absence of the MOT quadrupole field, which reduces the cloud temperature from $\sim 150\,\mu$K to $\sim 15\,\mu$K. Rb atoms are then loaded into the storage ODT using the dark-spot technique. The near-infrared laser beam, which constitutes the ODT, is shone onto the central region of the Rb cloud, and the repump laser beam is toggled to a path where a wire is imaged on the ODT, resulting in a dark spot in which no repump light is present, thus locally reducing scattering of the cooling laser. In this way, we can capture a good fraction ($\sim 20\%$) of the atoms and store them in the storage ODT at a temperature of $\sim 20\,\mu$K.

After Rb is stored in the storage ODT we load two narrow-line red Sr MOTs. The first MOT consists of ^{88}Sr and is used to sympathetically cool Rb. The second Sr MOT consists of the Sr isotope desired in a mixture with Rb to perform experiments. We always use the ^{88}Sr isotope to sympathetically cool Rb because of both its high natural abundance (83%) and the favorable Rb-Sr scattering properties. In case the ^{87}Rb-^{88}Sr mixture is desired, two ^{88}Sr MOTs are loaded, of which the first is used only for sympathetic cooling of Rb and the second provides the atoms for the mixture that will be investigated. After Rb is in the storage ODT, the experimental sequence proceeds with the steps described for single-species Sr samples, up to the metastable-state shelving, applied to ^{88}Sr and right after that, applied to the Sr isotope of interest for experiments. After the two isotopes are magnetically trapped in the metastable $^3P_2$ state, they are optically repumped into the ground state and captured by two simultaneous red MOTs. The first red MOT is then overlapped with the Rb cloud in the storage ODT to provide sympathetic cooling, bringing the temperature of Rb down to $\sim 3\,\mu$K and increasing the Rb phase-space-density by a factor ~ 200. Rb

can then be transferred to the science ODT optimized on the loading of Sr atoms. In case the "second" isotope is different from ^{88}Sr, any eventual trace of ^{88}Sr is eliminated from the science ODT by decreasing its depth. Finally, the second Sr red MOT is overlapped and loaded into the science ODT, resulting in an ultracold Rb-Sr mixture at $1 - 2\,\mu$K temperature. Finally, in order to increase the density of the atoms, we apply a vertical near-infrared ODT, reaching density-averaged densities of $10^{12} - 10^{13}\,\mathrm{cm}^{-3}$ for both species.

2.2.2 Preparation of quantum degenerate atomic samples

In order to maximize the efficiency of molecule production, we realize high phase-space density atomic samples in the form of BECs [71, 72, 73, 74] and MIs [75, 76, 8].

Bose-Einstein condensates

We obtain BECs [77, 78, 79] of dilute Sr and Rb gases by applying forced evaporative cooling [80] on the ultracold samples in the science ODT. Forced evaporation means that the ODT depth is slowly reduced over time, leading to the evaporation of ever colder atoms. Without reduction of the ODT depth the rate at which atoms evaporate lowers as the gas gets colder, rendering evaporative cooling unable to overcome undesirable but always present heating effects. Forced evaporation is executed by lowering the depth of the horizontal science ODT. The density and thus the thermalization rate is mostly determined by the vertical ODT. We obtain BECs with density-averaged densities in excess of $10^{14}\,\mathrm{cm}^{-3}$ for both species. In our research ^{84}Sr BECs [81] and ^{87}Rb-^{84}Sr double BECs [33] were used to investigate possible molecule production schemes, see chapters 4 and 5.

Mott insulators in optical lattice

Atomic MIs can be realized in an optical lattice resulting from the standing-wave interference pattern produced by pairs of retro-reflected laser beams. The MI phase corresponds to commensurate filling of the lattice sites and to a gapped excitation spectrum, i.e. to an insulator at low enough temperature. The quantum phase transition between a superfluid to a MI, predicted by the Bose-Hubbard model of lattice confined bosons [76], is induced by varying the ratio between the on-site repulsive interaction strength and the hopping amplitude between neighboring lattice sites. The crossing of the phase transition can be experimentally controlled by varying the lattice laser intensity. Indeed, for increasing laser intensity the on-site Wannier wavefunction becomes more localized and, while the on-site interaction increases, the tunneling

rate decreases, hence their ratio can be experimentally tuned over a wide range. In practice, the BEC is adiabatically loaded into the optical lattice by slowly increasing the intensity of the laser beams up to a critical value, at which the SF-MI phase transition occurs [82]. The scattering properties are favorable for the creation of both ^{84}Sr MIs [44] and ^{87}Rb-^{84}Sr double MIs [34], i.e. simultaneous MIs of both elements, see chapters 3 and 5. MIs with exactly two atoms per site, e.g. two Sr atoms or one Rb and one Sr atom, with average on-site densities up to $10^{15}\,\mathrm{cm}^{-3}$ are ideal starting conditions for associating those atom pairs into molecules.

2.2.3 Experimental methods for molecule production

We perform optical and magnetic spectroscopy on ultracold gases and study molecule production techniques using quantum gases. While spectroscopy and molecule production both rely on the resonant coupling of an atom-pair state with a bound molecular level, the former only uses it to *detect* the molecular level, while the latter exploits it to controllably *populate* that level. Although spectroscopy intrinsically involves a population transfer, such a transfer can be transient in time and small in magnitude, and still result in *detection*. The goal of molecule production, instead, is to create a controllable molecular sample to be further used or investigated, and requires an efficient and steady-state *population* of the molecular level.

Photoassociation spectroscopy: one- and two-color resonance

In photoassociation (PA) spectroscopy the coupling between the initial atomic state and the final molecular level [1] is optical and is induced by laser radiation. In particular, one-color spectroscopy requires a single-photon coupling, induced by a single laser, while two-color spectroscopy relies on a two-photon coupling and requires two tunable lasers [83, 84, 85, 86].

In one-color (or one-photon) spectroscopy the PA laser couples the initial continuum state $|a\rangle$ to bound molecular levels, hence the laser is called free-bound laser and denoted by L_{FB} in the following, see Fig. 2.4. By scanning the frequency of L_{FB}, the one-photon coupling between the initial state and a single excited rovibrational level $|e\rangle$ can be made resonant and cause population transfer. The resulting molecules spontaneously decay to lower lying states, and depending on their properties, either remain trapped or escape [87, 88]. Both these cases result in atom loss and lead to *detection* of the molecular level by atom loss revealed by standard absorption imaging,

[1] In the following the word *state* will refer both to atoms and molecules. For the latter, it will be implicitly referred to the electronic degrees of freedom. The word *level* will only be used for bound molecular levels.

see section 2.2.4. The energy of $|e\rangle$ is given by the frequency of L_{FB}, referenced to the dissociation threshold of the investigated molecular state, i.e. the binding energy. For an application of this method to RbSr see chapter 5.

In two-color (or two-photon) spectroscopy a second PA laser L_{BB} that couples $|e\rangle$ to molecular levels of a different molecular state is shone on the atoms together with L_{FB}, see Fig. 2.4. In our experiments these levels are supported by the molecular ground-state potential, and two-color spectroscopy is the same as stimulated Raman spectroscopy. By scanning the frequency of L_{BB}, with L_{FB} fixed on one-color resonance, the one-photon coupling between $|e\rangle$ and a single ground-state rovibrational level $|m\rangle$ can be made resonant. A significant light shift, corresponding to the Autler-Townes effect [89, 90], pushes L_{FB} out of one-color resonance. The loss induced by L_{FB} is then suppressed, resulting in a peak in atom number leading to *detection* of the molecular level [91, 92]. The energy of $|m\rangle$ referenced to the energy of $|a\rangle$, i.e. the binding energy, is given by the frequency difference between L_{BB} and L_{FB} at that peak. For an application of this method to RbSr see chapter 6. This type of two-color spectroscopy does not require phase coherence between L_{BB} and L_{FB}. However, for sufficient coherence, the two-color resonance results in the formation of a "dark" state superposition between $|a\rangle$ and $|m\rangle$ and, for low intensity of L_{BB} [93], to the observation of a "dark" resonance, which can also be used to *detect* a molecular level [94]. Since the width of the dark resonance is independent of the lifetime of $|e\rangle$ and typically limited by temperature and the much longer lifetime of $|a\rangle$ or $|m\rangle$, it can be used for a more precise measurement of the energy of $|m\rangle$ [95, 96, 26]. This phenomenon, also known as electromagnetically induced transparency, is particularly useful to *populate* the level $|m\rangle$, see subsection "Molecule production" later in this section.

PA spectroscopy is also a powerful tool for the investigation of atomic scattering properties. These properties only depend on the zero-energy semi-classical action and the universal long-range behavior of the interaction potential [97, 98, 99], which can both be inferred from the weakly-bound spectrum of the molecule. As explained above, PA allows for precision measurement of the energy of weakly-bound states, hence its importance. Finally, optical one- and two-color resonances, just as Fano-Feshbach resonances discussed in the next sub-section, can be interpreted in terms of scattering resonances arising from a quasi-bound state embedded in a continuum [100, 101, 102] and allow for tuning of the atomic collisions [103, 104, 105, 106]. However, the short lifetime of the excited molecular level in the optical case often results in losses and limited tuning of the elastic-scattering cross-section [107, 106] and makes magnetic Fano-Feshbach resonances, if present, preferred for this application.

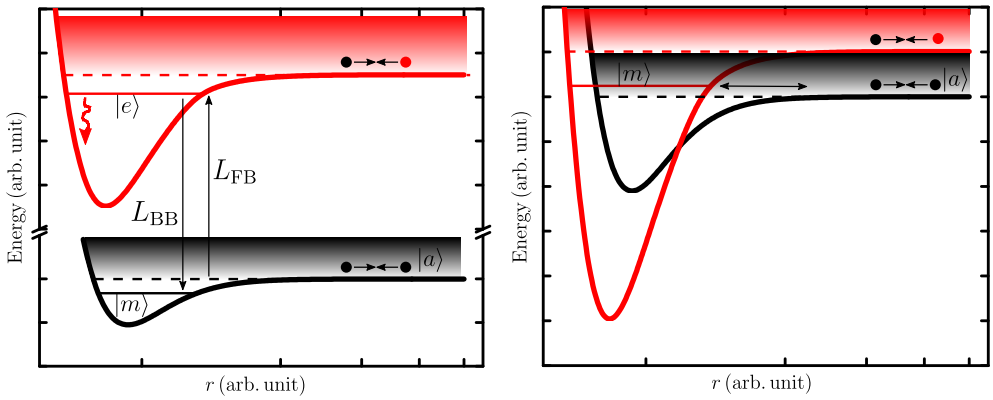

FIGURE 2.4: Pictorial representation of (left) (1)2-color and (right) Fano-Feshbach resonance. (left panel) The black (red) solid thick line represents the electronic ground(excited)-state molecular potential, the black (red) solid thin line represents the ground(excited)-state molecular level, the dashed lines represent dissociation thresholds. (right panel) The black and red solid thick lines represents two electronic ground-state molecular potentials, the red solid thin line represents a molecular level supported by the red potential, the dashed lines represent dissociation thresholds. Shaded areas represent the continuum term of the spectra. Symbols defined in text.

Magnetic spectroscopy: Fano-Feshbach resonances

In magnetic spectroscopy the coupling between the initial atomic state and the final molecular level is typically either the isotropic spin-exchange interaction, weaker relativistic spin-dependent interactions or magnetic dipole-dipole interactions [108, 109, 107, 110]. By scanning the external magnetic field, the coupling between the atom pair and a ground-state molecular level with suitable magnetic moment can be made resonant, see Fig. 2.4. This can in turn strongly enhance the probability of either inelastic scattering of a cold atom pair into a hotter atom pair with different internal states or reactive scattering of three cold atoms into a hotter dimer-atom pair. Although these processes involve different dynamics from two- or three-body physics, they both lead to atom loss and therefore *detection* [107]. In the field of atomic physics people call this detection method Fano-Feshbach or simply Feshbach spectroscopy. Fano-Feshbach resonances proved to be an invaluable tool for manipulation of ultracold atom collisions [111, 112]. Indeed, as for one- and two-color resonances, they can be interpreted in terms of scattering resonances arising from a quasi-bound state in the collision continuum and, because of the lack of radiative decay, typically result in tunability of elastic scattering amplitudes over a wide range compared to the background value. For an application of this method to RbSr see chapter 7.

Molecule production: STIRAP

In order to produce ground-state molecules efficiently, we need to *populate* a target ground-state molecular level efficiently. Although magneto-association via adiabatic magnetic field sweep across a Fano-Feshbach resonance has been successfully applied in alkali dimers [113, 114, 115], its applicability to species involving one alkaline-earth metal is not yet proven. Indeed, in AE-AE systems, these resonances do not exist, while in the case of A-AE systems, they were predicted but not yet experimentally observed before the start of this work, the first observation being reported in chapter 7. As a consequence, the more general optical production scheme of STIRAP is investigated here.

STIRAP is an acronym for Stimulated Raman Adiabatic Passage, where stimulated Raman represents the physical coupling mechanism and adiabatic passage refers to the population transfer generated by it. This technique exploits the same Λ scheme as two-color spectroscopy, coupling states $|a\rangle$, $|e\rangle$, and $|m\rangle$ by lasers L_{FB} and L_{BB}. The population transfer is based on the existence of a "dark" state between a colliding atom pair state and a ground-state molecular level, which is not coupled by

light to state $|e\rangle$, hence it does not suffer from radiative losses [2]. For a stationary "dark" state to exist, the detuning between L_{FB} and L_{BB} must match the energy difference between $|a\rangle$ and $|m\rangle$ and the two lasers must have a sufficient degree of phase coherence. With careful choice of time-dependent couplings induced by L_{FB} and L_{BB}, i.e. their intensities over time, the dark state can be adiabatically moved from $|a\rangle$, populated at the beginning, to $|m\rangle$, and therefore transfer population with vanishingly small losses. While "dark" resonances between atom-pairs and dimers have been experimentally observed in thermal gases [95, 94], STIRAP has not been performed [3]. The main experimental limitation to STIRAP efficiency comes from the weak coupling between $|a\rangle$ and $|e\rangle$ due to small Franck-Condon overlap. This can be improved, exploiting the quantized motion of the atoms and the high spatial density, either in optical lattices, see [26], or in BEC. For applications of this method to Sr_2 see chapters 3 and 4.

2.2.4 Atom detection

The samples are quantitatively characterized via absorption imaging, which is a simple and widely used imaging technique [46, 74], and it is the only imaging technique used in this thesis. Absorption imaging is based on the absorption and subsequent re-emission, i.e. scattering, of light from the probed particles illuminated by resonant radiation. For a resonant laser beam hitting the sample, the output intensity is reduced compared to the input intensity by an amount that is a function of the integrated particle density along the imaging direction and the total scattering cross-section. As a consequence, by collecting the laser light in presence and absence of the sample, the column density and the total particle number can be derived. If the atomic cloud is imaged *in situ*, i.e. in the presence of the ODT, the spatial density distribution is measured. The atoms can also be measured a certain time-of-flight (TOF) after release of the cloud from the trap, in which case the momentum distribution of the cloud at the moment of the imaging flash is measured. This momentum distribution corresponds in many cases quite well to the momentum distribution of the trapped cloud. This technique is especially efficient for strong cycling transitions, thus typically the ${}^1S_0 \rightarrow {}^1P_1$ transition is used for Sr and the D_2 $f^{Rb} = 2 \rightarrow f^{Rb} = 3$ transition for Rb. Rb atoms in $f^{Rb} = 1$ require a pulse of the repump laser prior to the imaging pulse. In absence of this pulse only $f^{Rb} = 2$ atoms are imaged. This fact can be exploited to make Rb imaging f-dependent. In case a measurement of the

[2] As such, this atom-dimer "dark" state should not be confused with atomic "dark" states used in laser cooling [116, 117, 94].

[3] By contrast, transfer of weakly-bound Feshbach molecules into the rovibrational ground state via STIRAP has been shown in a thermal gas [118].

populations of the internal degree of freedom is necessary, in other words resolution of the Zeeman substates is desired, we exploit the narrow $^1S_0 \rightarrow {}^3P_1$ transition for ^{87}Sr, and a combination of Stern-Gerlach separation and absorption imaging for Rb. A noteworthy case for which absorption imaging does not work due to absence of cycling transitions is that of molecules such as Sr_2. In order to detect molecules we therefore dissociate them into atoms and then detect atoms.

2.3 Experimental setup

The experimental setup we use in this work is a an ultracold Rb-Sr mixture machine that was built as a Sr quantum gas machine in 2008-2009 and upgraded to a multi-species machine in 2012. In December 2013 this machine was moved from Innsbruck (Austria) to Amsterdam (The Netherlands), where the present work was carried out [4]. Between 2008 and 2013, this machine was used to create the first Sr quantum gases, bring all stable Sr isotopes to quantum degeneracy [81, 119, 120, 121], create ground state Sr_2 dimers [26] and to obtain Bose-Einstein condensates by using only laser cooling to remove entropy from the gas [122]. In 2013, after the upgrade to Rb-Sr double-species operation, it was used to realize the first quantum degenerate Rb-Sr mixture [33]. Since the apparatus has been described in detail in previous theses of former group members [44, 34] we will limit ourselves to a brief overview of the setup. The setup can be conceptually divided into four parts: the vacuum system, already described in section 2.2.1, the magnetic-field coil system, the laser system and the control system.

2.3.1 Coil system

The coil system, identical to the one of [55], is composed of several electromagnets, connected to power supplies and mechanical relays located outside the laboratory. The coils have different designs depending on their purpose, with the high-current ones consisting of water-cooled copper tubes and the remaining ones of air-cooled copper wires. The coils are typically mounted on the optical table and do not touch the vacuum vessel. In particular all coils used to produce the magnetic fields in the science glass vacuum chamber sit in a glass-fiber reinforced PVC housing attached via posts to the optical table. Three pairs of coils used for cancellation of offset fields are mounted on a cubic cage with $\sim 1.5\,\mathrm{m}$ long edges centered around the glass cell. Details about the calibration of the coils generating the main offset field for Feshbach spectroscopy can be found in chapter 7.

[4] Website of the Sr quantum gas group in Amsterdam: http://www.strontiumbec.com/

2.3.2 Laser system

The laser system can be conceptually divided into a set of lasers necessary for laser cooling and tuned close to atomic transitions, another used for the creation of conservative potential traps from far-detuned radiation, and yet another for exploration of molecular physics via PA.

The lasers used for cooling the atoms are commercially available stabilized external-cavity diode lasers (ECDLs) and can be further divided into those used for cooling and trapping of Sr or Rb. For cooling and trapping of Sr we use a frequency-doubled laser with an additional slave laser addressing the blue $5s^2\,{}^1S_0 \rightarrow 5s5p\,{}^1P_1$ transition at 461 nm, a frequency-doubled laser addressing the $5s5p\,{}^3P_2 \rightarrow 5s5d\,{}^3D_2$ repump transition at 497 nm, and a cavity-stabilized 689 nm laser with three slave lasers addressing the red $5s^2\,{}^1S_0 \rightarrow 5s5p\,{}^3P_1$ transition, see [44, 45] and section 2.2.1. For the Rb we use two 780 nm lasers addressing the ${}^2S_{1/2} \rightarrow {}^2P_{3/2}$ D_2 line, in particular the $f^{Rb} = 2 \rightarrow f^{Rb} = 3$ and $f^{Rb} = 1 \rightarrow f^{Rb} = 1, 2$ hyperfine transitions, see [34, 66] and section 2.2.1.

The lasers used for the realization of ODTs are commercial high-power lasers. We use a 100-W, 1070-nm fiber laser (YLR-100-LP-AC-Y12 from IPG) for the realization of the storage ODT used for the first dipole trapping and storing of Rb, see section 2.2.1. A pair of 5-W, 1064-nm fiber lasers (YLD-5-LP from IPG) are used for the realization of horizontal and vertical science ODTs in crossed beam configuration. A single-frequency, 8-W, 532-nm laser (Verdi-V8 from Coherent) is exploited as source of the additional horizontal and vertical ODTs overlapped with the science ODTs in a bi-chromatic trap configuration. Finally, we derive the laser beams generating the optical lattice potential from a single-frequency, 48-W, 1064-nm laser (Mephisto MOPA from Innolight), see chapter 3.

The PA lasers are produced in two different ways, always referenced to the 689 nm master oscillator in a master-slave configuration. They are either derived from injection-locked slave diode lasers seeded by the master, or from a separate ECDL referenced to the master via beat-lock. The latter setup, which was used extensively for 1-color spectroscopy of RbSr, is described in detail in chapter 5.

2.3.3 Control system

The control system, developed by Florian Schreck, Todd Meyrath and Gerhard Hendl [123], is responsible for the automated functioning of the apparatus and is composed of a control program running on a personal computer, a digital output card, and the hardware electronics connected to the laser and coil systems. The overall experimental

sequence is referenced to the 50 Hz oscillation of the power lines to improve reproducibility. Many direct digital synthesizers and some commercial radio-frequency synthesizers are used to produce all required radio frequencies and are referenced to a Rb clock. The power supplies for most of the electronics are located outside the laboratory.

Chapter 3

Efficient production of long-lived Sr_2 molecules

Abstract

We associate Sr atom pairs on sites of a Mott insulator optically and coherently into weakly-bound ground-state molecules, achieving an efficiency above 80%. This efficiency is 2.5 times higher than in our previous work [S. Stellmer, B. Pasquiou, R. Grimm, and F. Schreck, Phys. Rev. Lett. **109**, 115302 (2012)] and obtained through two improvements. First, the lifetime of the molecules is increased beyond one minute by using an optical lattice wavelength that is further detuned from molecular transitions. Second, we compensate undesired dynamic light shifts that occur during the stimulated Raman adiabatic passage (STIRAP) used for molecule association. We also characterize and model STIRAP, providing insights into its limitations. Our work shows that significant molecule association efficiencies can be achieved even for atomic species or mixtures that lack Feshbach resonances suitable for magnetoassociation.

3.1 Introduction

Over the last fifteen years considerable experimental effort has been invested into the realization of ultracold molecular samples. Ultracold molecules hold promise for unveiling novel phases of matter near quantum degeneracy, implementing quantum information protocols, and enabling precision measurements beyond atomic physics [12, 15, 17]. Ultracold dimers in their rovibrational ground state can be created in a two-step process from ultracold atoms. In the first step, atom pairs are associated into weakly-bound molecules and in the second step, the molecules are transferred from a

weakly-bound state to the rovibrational ground state [21, 124]. So far the first step in these experiments has relied on the existence of magnetically tuneable Feshbach resonances [125, 126]. By ramping an external magnetic field adiabatically across such a resonance, a coherent transfer between a pair of free atoms and a molecular bound state can be accomplished. Such magneto-association is hard or even impossible for a vast class of atomic systems of interest, for instance combinations of an alkali metal and an alkaline-earth metal or pairs of alkaline-earth metal atoms. The former systems possess only extremely narrow magnetic Feshbach resonances [35, 127], the latter none at all.

Production of ultracold weakly-bound ground-state Sr_2 molecules was achieved in our previous work [26] and in [27], relying respectively on coherent and non-coherent optical transfer schemes, thus overcoming the absence of magnetic Feshbach resonances in the non-magnetic ground state of these atoms. More recently, two-photon coherent transfer of cold Rb atom pairs into ground-state Rb_2 molecules was demonstrated using a frequency-chirped laser pulse [128]. The coherent population transfer of [26] was stimulated Raman adiabatic passage (STIRAP), which evolves a dark state from a pair of atoms into a molecule [129, 130]. Unfortunately, because of losses by non-adiabatic coupling and short lifetime of the molecules, the molecule association efficiency was only 30%, far below the efficiency potentially achievable by STIRAP. Moreover, the short lifetime hindered further usage of the molecular sample.

In this article we show how to overcome these limitations. As in [26] we investigate the production of $^{84}Sr_2$ ultracold ground-state molecules by STIRAP starting from a Mott insulator (MI). We increase the lifetime of the molecules to over one minute by using an optical lattice wavelength that, unlike before, is far detuned from any molecular transition. We identify that the resulting STIRAP efficiency of slightly above 50 % is limited by the finite lifetime of the dark state arising from unwanted light shifts. We show how to overcome these light shifts with the help of an additional compensation beam [131], leading to a STIRAP efficiency above 80 %. Our work validates a general way of producing large samples of weakly-bound molecules without relying on Feshbach resonances. This will open the path for new classes of ultracold dimers useful for metrology experiments [132, 133, 134], for ultracold chemistry [135, 136] and for quantum simulation experiments relying on a strong permanent electric dipole moment [32, 137, 138].

This article is organized as follows. In Sec. 3.2 we present an overview of our experimental strategy. In Sec. 3.3 we introduce the model used to describe the STIRAP and we discuss the constraints imposed on the relevant experimental parameters when high transfer efficiency is required. In Sec. 3.4 we describe the experimental sequence leading to the initial atomic sample and the optical scheme for the creation of photoassociation (PA) laser light. In Sec. 3.5.1, we measure relevant parameters of the

system and we show the effect of the lattice on the free-bound Rabi frequency. In Sec. 3.5.2 we use STIRAP to associate atom pairs into molecules, achieving a transfer efficiency of $\sim 50\,\%$, and we show that this process is limited by the finite lifetime of the dark state, arising from unwanted light shifts on the binding energy of the ground-state molecule. This challenge is overcome in Sec. 3.5.3 by modifying the standard scheme with the addition of a light-shift compensation beam, reaching an efficiency higher than $80\,\%$. Finally, in Sec. 3.5.4 we characterize the effects of the lattice light shifts on STIRAP and we measure the molecule lifetime.

3.2 Experimental strategy

We will now discuss how one can optically and coherently associate pairs of atoms into ground-state molecules. We will explain how STIRAP works and can reach near-unit molecule association efficiency. We motivate the use of a MI as initial atomic sample and specify the STIRAP implementation used here.

To optically transfer a pair of atoms in state $|a\rangle$ into the molecular state $|m\rangle$, we use a Λ scheme, including an optically excited molecular state $|e\rangle$, see Fig. 3.1. States $|a\rangle$ and $|e\rangle$ are coupled with Rabi frequency Ω_{FB} by the free-bound laser L_{FB} and $|e\rangle$ is coupled to $|m\rangle$ with Rabi frequency Ω_{BB} by the bound-bound laser L_{BB}.

The conceptually simplest method for coherent molecule association are two consecutive π pulses, the first between $|a\rangle$ and $|e\rangle$ and the second between $|e\rangle$ and $|m\rangle$. To provide efficient transfer, this scheme needs to be executed much faster than the lifetime of the excited state $|e\rangle$, τ_e, which requires high Rabi frequencies ($\Omega_{\mathrm{FB,BB}} \gg \gamma_e = 1/\tau_e$). Since the Franck-Condon factor (FCF) of the free-bound transition is small, satisfying the condition $\Omega_{\mathrm{FB}} \gg \gamma_e$ is experimentally very challenging.

STIRAP overcomes this limitation by minimizing losses from $|e\rangle$ and provides coherent population transfer even when the condition $\Omega_{\mathrm{FB,BB}} \gg \gamma_e$ is not satisfied. To simplify the discussion we first introduce STIRAP without loss from the excited state ($\gamma_e = 0$) and with lasers L_{FB} and L_{BB} on resonance with the transitions $|a\rangle - |e\rangle$ and $|m\rangle - |e\rangle$, respectively. In this system a dark state exists, namely an eigenstate orthogonal to $|e\rangle$. If only one of the two lasers (L_{FB} or L_{BB}) is on, then the dark state coincides with one of the eigenstates in the absence of light ($|m\rangle$ or $|a\rangle$, respectively). When both lasers are on, the dark state is $|\mathrm{dark}\rangle = \cos(\theta)\,|\mathrm{a}\rangle - \sin(\theta)\,|\mathrm{m}\rangle$ with $\theta = \arctan\left(\Omega_{\mathrm{FB}}/\Omega_{\mathrm{BB}}\right)$. If the tuning knob θ is varied in time from 0 to $\pi/2$, then the dark state is moved from $|a\rangle$ to $|m\rangle$. Experimentally this is realized by changing the intensities $I_{\mathrm{FB,BB}}$ of $L_{\mathrm{FB,BB}}$, first switching on L_{BB}, then increasing I_{FB} while ramping off I_{BB}, and finally switching off L_{FB}. Since an energy gap exists

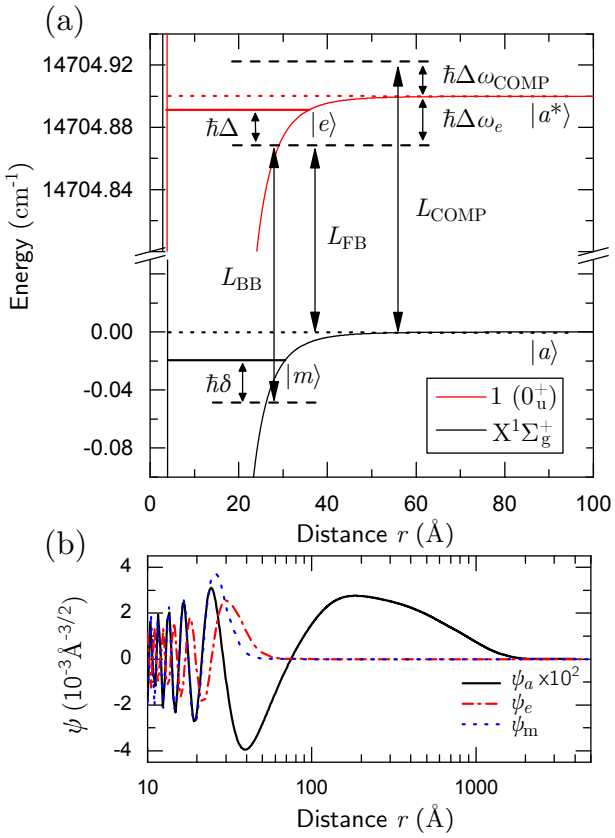

FIGURE 3.1: (color online) (a) $^{84}Sr_2$ molecular potential for the electronic ground state $X^1\Sigma_g^+$ ($J = 0$) and the optically exited state $1(0_u^+)$ ($J = 1$). The energy is referenced to the ground-state asymptote. The Λ scheme ($|a\rangle, |e\rangle, |m\rangle$) used for STIRAP is indicated along with the coupling laser fields $L_{\rm FB}$ and $L_{\rm BB}$ and their one- and two-color detunings Δ and δ. The laser field $L_{\rm COMP}$ with detuning $\Delta\omega_{\rm COMP}$ from the $|a\rangle - |a^*\rangle$ atomic transition is added for light-shift compensation in Sec. 3.5.3. In the situation shown Δ, δ, $\Delta\omega_{\rm COMP} > 0$ and $\Delta\omega_e < 0$. (b) Probability amplitude for the nuclear wavefunction of state $|a\rangle$, $|e\rangle$ and $|m\rangle$. The effect of an external harmonic confinement is taken into account to determine ψ_a, see Sec. 3.5.2.

between the dark state and the other two instantaneous eigenstates of the system, the adiabatic theorem of quantum mechanics applies [139, 140], provided that the change in the Hamiltonian is slow enough compared to the energy gap. This means that the population is kept in the dark state, providing unit transfer efficiency. State $|e\rangle$ is only used to induce couplings but never significantly populated. As a consequence this scheme works even in the presence of dissipation ($\gamma_e \neq 0$) as will be explained in Sec. 3.3.

In order to detect that atoms have been associated to molecules, we exploit the fact that STIRAP is reversible. After the association STIRAP (aSTIRAP) described above, we push remaining free atoms away with a pulse of resonant light. Molecules are barely affected by this light pulse because they do not have any strong optical transition close in frequency to the atomic transition used. To detect the molecules, we dissociate them by a time-mirrored aSTIRAP, which we call dissociation STIRAP (dSTIRAP), and detect the resulting atoms by absorption imaging. The sequence "aSTIRAP — push pulse — dSTIRAP" constitutes a STIRAP cycle and will be used to prepare samples with homogeneous conditions for molecule association and to measure the STIRAP efficiency, see Sec. 3.5.2.

We exploit a deep optical lattice to create a MI of doubly occupied sites with high on-site peak density. The reason for this is twofold. Firstly, the optical lattice increases the free-bound Rabi frequency, see Sec. 3.5.1, leading to an increase in the STIRAP efficiency. Secondly, the lattice increases the molecule lifetime by suppressing collisional losses, see Sec. 3.5.4, leading both to an increase in the STIRAP efficiency and to a longer lifetime of the resulting molecular sample.

The Λ scheme used here is the same as the one employed in our previous work [26]. The relevant potential energy curves of $^{84}Sr_2$ are shown in Fig. 3.1. The electronic ground state is a $X^1\Sigma_g^+$ ($J = 0$) state, asymptotically correlating to two ground-state Sr atoms ($^1S_0$), and the excited state is a $1(0_u^+)$ ($J = 1$) state, correlating to one Sr atom in the ground state and one in the optically excited state $^3P_1$. The initial state $|a\rangle$ consists of two atoms in the lowest vibrational level of an optical lattice well. At short range, their relative-motion wavefunction is proportional to a scattering state above the dissociation threshold of $X^1\Sigma_g^+$ ($J = 0$). Our target state $|m\rangle$ is the second to last vibrational level ($\nu = -2$) supported by this potential, with binding energy $E_m = h \times 644.7372(2)\,\mathrm{MHz}$, where h is the Planck constant. As intermediate state $|e\rangle$ we chose the $\nu = -3$ vibrational level of the $1(0_u^+)$ potential, with binding energy $E_e = h \times 228.38(1)\,\mathrm{MHz}$. The STIRAP lasers are appropriately detuned from the $^1S_0 - {}^3P_1$ transition of Sr at 689 nm, which has a linewidth of $\Gamma_{^3P_1} = 2\pi \times 7.4\,\mathrm{kHz}$. For the push beam we use the $^1S_0 - {}^1P_1$ transition at 461 nm, which has a linewidth of $\Gamma_{^1P_1} = 2\pi \times 30.5\,\mathrm{MHz}$.

3.3 Theory

In this section we will introduce a model for molecule association via STIRAP. We will discuss the conditions on experimental parameters under which STIRAP is efficient. An important insight will be that finite two-color detuning δ can lead to a significant reduction in the dark state lifetime and therefore efficiency. We give an overview of the sources for this detuning in our experiment and ways to overcome it.

3.3.1 Model

A model for STIRAP starting from two atoms in the ground state of an optical lattice is given by the time-dependent Schrödinger equation applied to the three relevant states, which in the rotating wave approximation takes the form [141, 142]

$$i\frac{d}{dt}\begin{pmatrix} a \\ e \\ m \end{pmatrix} = -\frac{1}{2}\begin{pmatrix} i\gamma_a & \Omega_{\mathrm{FB}} & 0 \\ \Omega_{\mathrm{FB}} & i\gamma_e - 2\Delta & \Omega_{\mathrm{BB}} \\ 0 & \Omega_{\mathrm{BB}} & i\gamma_m - 2\delta \end{pmatrix}\begin{pmatrix} a \\ e \\ m \end{pmatrix}. \tag{3.1}$$

The amplitudes $a(t)$, $e(t)$, and $m(t)$ correspond to the states $|a\rangle$, $|e\rangle$, and $|m\rangle$, respectively. Losses from these states are described by γ_a, γ_e and γ_m, which are responsible for the coupling of the three-level system to the environment. When loss rates are set to zero, the normalization condition is $|a|^2 + |e|^2 + |m|^2 = 1$. Finally, Δ and δ are the one- and two-color detunings, see Fig. 3.1. In the remainder of this section we will study the STIRAP efficiency under the following assumptions. STIRAP is executed during the time interval $[0, T]$, outside of which the two Rabi frequencies $\Omega_{\mathrm{FB,BB}}$ are zero. For times $t \in [0, T]$ the Rabi frequencies are described by (co)sine pulses of identical amplitude Ω_m, $\Omega_{\mathrm{BB}} = \Omega_m \cos(\theta)$ and $\Omega_{\mathrm{FB}} = \Omega_m \sin(\theta)$, with $\theta = \pi t/2T$. The scattering rate γ_e is the dominant loss term in the system, i.e. $\gamma_e \gg \gamma_{a,m}$. The two-color detuning depends on time only through θ, i.e. $\delta = \delta(\theta) = \delta_m f(\theta)$, where δ_m is the (signed) extremum of $\delta(\theta)$ with highest amplitude, and $f(\theta)$ describes the time variation caused by the time-dependent light shifts discussed in Sec. 3.3.3. Finally, unless stated otherwise, we will assume $\Delta = 0$.

3.3.2 Parameter constraints

We now analyse the constraints on the (experimentally controllable) detunings and Rabi frequencies under which STIRAP associates molecules with near-unit efficiency. We will first consider the resonant case (zero detunings) and derive the parameter constraints analytically, following Ref. [141]. We will then study the effects of deviations from two-color resonance, where an approximate solution and new parameter

constraints will be presented. Finally, the effects of one-color and two-color detunings will be compared.

We analyse the problem in the experimentally relevant case of strong dissipation $\Omega_m \lesssim \gamma_e$, in which STIRAP has the potential to outperform two appropriate consecutive π-pulses. Here dissipation leads to a strong non-hermitian contribution in the hamiltonian [143]. By adiabatically eliminating the variable $e(t)$ as in Ref. [141], we derive the effective Hamiltonian $\widetilde{H}_{\text{eff}}$ for the subspace $\{|a\rangle, |m\rangle\}$,

$$\widetilde{H}_{\text{eff}} = -i\frac{\tilde{\gamma}}{2}\begin{pmatrix} \sin(\theta)^2 & \sin(\theta)\cos(\theta) \\ \sin(\theta)\cos(\theta) & \cos(\theta)^2 + 2iAf(\theta) \end{pmatrix}, \tag{3.2}$$

where $\tilde{\gamma} = \Omega_m^2/\gamma_e$ and $A = \delta_m/\tilde{\gamma}$.

We first examine the case $\delta = \Delta = 0$ and we will show that adiabatic evolution ensures near-unit transfer efficiency [141]. Despite the strong dissipation, this system supports the same dark state as before, the eigenstate $|\text{dark}\rangle = \cos(\theta)\,|a\rangle - \sin(\theta)\,|m\rangle$. The orthogonal lossy state is the bright state $|\text{bright}\rangle$. In order to gain some insight, we work in the adiabatic representation, i.e. in the instantaneous eigenbasis $\{|\text{dark}\rangle, |\text{bright}\rangle\}$ of the Hamiltonian (3.2). A wavevector $|\Psi, t\rangle$ in the basis $\{|a\rangle, |m\rangle\}$ is written $|\Psi', t\rangle = \widetilde{U}(t)|\Psi, t\rangle$ in this new basis, with the appropriate unitary transformation $\widetilde{U}$. The time-dependent Schrödinger equation reads $i\frac{d}{dt}|\Psi'\rangle = \widetilde{U}\widetilde{H}_{\text{eff}}\widetilde{U}^{-1}|\Psi'\rangle + i\left(\frac{d}{dt}\widetilde{U}\right)\widetilde{U}^{-1}|\Psi'\rangle = \widetilde{H}'|\Psi'\rangle$, where $\widetilde{U}\widetilde{H}_{\text{eff}}\widetilde{U}^{-1}$ is diagonal and $\left(\frac{d}{dt}\widetilde{U}\right)\widetilde{U}^{-1}$ gives rise to non-adiabatic couplings. If we take $s = t/T \in [0, 1]$ as our independent variable, the Schrödinger equation becomes $i\frac{d}{ds}|\Psi'\rangle = T\widetilde{H}'|\Psi'\rangle$. In the case of zero detunings, $T\widetilde{H}'$ is independent of s and the equation is exactly solvable. The solution for the dark-state amplitude $d(s)$ is $d(s) = B_- e^{-i\lambda_- s} + B_+ e^{-i\lambda_+ s}$, where $\lambda_{-,+}$ are respectively the most and least dissipative eigenvalues of $T\widetilde{H}'$, and $B_{-,+}$ are constants. In the adiabatic regime, characterized by $\alpha = \tilde{\gamma}T \gg 1$, we have $\text{Im}\,(\lambda_-) \simeq -\alpha/2$ and $\text{Im}\,(\lambda_+) \simeq -\pi^2/2\alpha$. The transfer efficiency η is then given by $\eta = |d(s=1)|^2 \simeq |B_+|^2 e^{2\lambda_+} \simeq e^{-\pi^2/\alpha}$. Thus, STIRAP with near-unit efficiency requires $\alpha \gg \pi^2$, which can be interpreted as the adiabaticity condition.

Next we examine the case of non-zero two-color detuning, i.e. $\delta \neq 0$, and we show that adiabatic evolution does not guarantee high transfer efficiency. Going from zero to finite δ, the initially dark state is mixed with $|e\rangle$, resulting in a finite lifetime. For simplicity we all the same continue to use the label "dark state" for this state and, similarly, keep using "bright state" for the other eigenstate. We apply the same method as used previously, with $\widetilde{U}$ being this time the appropriate non-unitary transformation. The time evolution of the system is determined by $T\widetilde{H}'$, which now

depends on s and the solution is not trivial. However, since we are only interested in small δ and the populations at the end of the pulse, we replace $T\widetilde{H}'$ with its time average. The imaginary parts of the most and least dissipative eigenvalues are, to leading order in A^n/α^m, $\mathrm{Im}\,(\lambda_-) \simeq -\alpha/2$ and $\mathrm{Im}\,(\lambda_+) = -1/2(\pi^2/\alpha + CA^2\alpha)$, where $C = \frac{8}{\pi}\int_0^{\pi/2} f(\theta)^2 \sin(\theta)^2 \cos(\theta)^2 d\theta$. Thus, the transfer efficiency is approximately given for $\alpha \gg 1$, $|A| \ll 1$ by

$$\eta \simeq e^{-(\pi^2/\alpha + CA^2\alpha)}, \tag{3.3}$$

which is only a function of the parameters α and A. We identify two regimes depending on the value of $|A|\,\alpha = |\delta_m|T$. For $|\delta_m|T \ll \pi/\sqrt{C}$, the transfer efficiency is limited by non-adiabatic transitions of the dark state to the bright state. For $|\delta_m|T \gg \pi/\sqrt{C}$, the main limitation arises from the now finite lifetime of the dark state. For a non-zero detuning δ, the transfer efficiency features a maximum when varying pulse time T, which is determined only by the parameter $|A| = |\delta_m|/\tilde{\gamma}$, and the maximum efficiency is approximately $\eta_{\max} = e^{-2\pi\sqrt{C}|A|}$.

We now address the case of non-zero one-color detuning $\Delta \neq 0$, but zero two-color detuning $\delta = 0$, and we show that, as for $\delta = \Delta = 0$, adiabatic evolution ensures near-unit transfer efficiency. In this case, the Hamiltonian (3.1) supports a dark state, and by following the method used for $\delta = \Delta = 0$, it can be shown that $T\widetilde{H}'$ is independent of s. The eigenvalues of $T\widetilde{H}'$ are, to leading order in $1/\alpha$, given by $\mathrm{Im}\,(\lambda_-) \simeq -\alpha/2\left(1 + 4(\Delta/\gamma_e)^2\right)$ and $\mathrm{Im}\,(\lambda_+) \simeq -\pi^2/2\alpha$. This implies that, even for $\Delta \neq 0$, we can have $|\mathrm{Im}\,(\lambda_+)| \ll 1$ and thus $\eta \simeq 1$ for large enough values of α. To compare the effects of one-color and two-color detunings, we analyze the conditions to ensure high transfer efficiency at large but fixed α. For a constant one-color detuning we derive $\Delta \ll \gamma_e\alpha/2\pi$, while for a constant two-color detuning we have $|\delta_m| \ll \tilde{\gamma}\sqrt{2/\alpha} \lesssim \gamma_e\sqrt{2/\alpha}$, which is a much stronger constraint. The STIRAP efficiency is therefore much more sensitive to the two-color detuning than to the one-color detuning, which is also expected from energy conservation.

It is noteworthy to point out that population transfer between $|a\rangle$ and $|m\rangle$ can be obtained by exploiting the coherent dark state superposition in a *diabatic* evolution, i.e. projection, as opposed to STIRAP. However the efficiency in this case is bound to be at most $\eta_{\mathrm{proj}} = 25\,\%$, which is the value for equal free-bound and bound-bound Rabi frequencies, as obtained from $\eta_{\mathrm{proj}} = |\langle \mathrm{dark}|a\rangle|^2 \times |\langle m|\mathrm{dark}\rangle|^2 = \left(1 - \sin(\theta)^2\right)\sin(\theta)^2 \leq 1/4$. As a consequence surpassing the maximum possible efficiency of η_{proj} can be regarded as a requirement for STIRAP to be relevant.

3.3.3 Improving STIRAP efficiency

Finally, we discuss how we can improve the molecule production efficiency based on this theoretical description. We will focus on the limitations arising from light shifts induced on the states of the Λ scheme that contribute to δ and Δ. We distinguish between *static* and *dynamic* light shifts, where static and dynamic refer to their behavior during the STIRAP sequence. The lasers L_{FB} and L_{BB}, whose intensities vary during STIRAP, induce time- and space-dependent shifts Δ_{FB} and Δ_{BB} on the free-bound transition. In a similar way, these lasers also induce shifts δ_{FB} and δ_{BB} on the two-photon transition. These shifts correspond to changes $-\hbar\delta_{\mathrm{FB,BB}}$ of the binding energy of molecules in state $|m\rangle$, which is the energy difference between $|a\rangle$ and $|m\rangle$. The optical lattice, which provides the external confinement, induces only the static, space-dependent light shifts $\Delta_{\mathrm{Lattice}}$ and $\delta_{\mathrm{Lattice}}$, respectively, onto the free-bound transition and the two-photon transition. Thus, we decompose Δ and δ into $\Delta = \Delta_{\mathrm{Lattice}} + \Delta_{\mathrm{FB}} + \Delta_{\mathrm{BB}} + \Delta_0$ and $\delta = \delta_{\mathrm{Lattice}} + \delta_{\mathrm{FB}} + \delta_{\mathrm{BB}} + \delta_0$. The offsets Δ_0 and δ_0 can be freely adjusted by tuning $L_{\mathrm{FB,BB}}$ and depend neither on space nor on time.

These light shifts can influence the molecule production efficiency η. In our system the effect of Δ on η is negligible, see Sec. 3.5.3, justifying the approximation $\Delta = 0$. Since we also fulfill $\gamma_{a,m} \ll \gamma_e$ (see Sec. 3.5.1 and 3.5.4), we can use Eqn. 3.3, which shows that the maximum transfer efficiency for optimal pulse time depends only on $|A| = |\delta_m|/\tilde{\gamma}$. The efficiency is highest for small $|A|$, which means we have to achieve low $|\delta_m|$. The contribution $\delta_{\mathrm{Lattice}}$ to δ_m could be reduced by increasing the lattice beam diameter and adjusting δ_0 to compensate for the average remaining light shift across the sample. However in this work we reduce the inhomogeneity by simply removing atoms on sites with large light shift using a STIRAP cycle, see Sec. 3.5.2 and Sec. 3.5.3. The contribution δ_{FB} is proportional to $I_{\mathrm{FB}} \propto \sin(\theta)^2$. Lowering $A = \delta_m/\tilde{\gamma}$ by lowering I_{FB} is not possible since also $\tilde{\gamma} \propto I_{\mathrm{FB}}$. A straightforward way to half the effect of this contribution is to adjust δ_0 such that $\delta = \delta_m(\sin(\theta)^2 - 1/2)$. To go further and essentially cancel δ_{FB} we demonstrate in Sec. 3.5.3 the use of an additional laser beam (L_{COMP}) that produces the exact opposite light shift of L_{FB}. The last light shift, δ_{BB}, can be neglected in our case because L_{BB} has low intensity.

3.4 Experimental setup and creation of the Mott insulator

We will now describe the experimental setup and the procedure used to prepare the atomic sample that is the starting point for molecule creation, and describe the laser

system that generates the PA light.

The experimental apparatus is our Sr quantum gas machine, which is described in depth in [121]. The experimental sequence leading to a Bose-Einstein condensate (BEC) of ^{84}Sr starts with a magneto-optical trap operating on the $^1S_0 - ^1P_1$ transition, capturing atoms coming from a Zeeman slower. We further cool the atomic cloud by exploiting the intercombination transition $^1S_0 - ^3P_1$ at 689 nm, reaching a temperature of 1.0 μK. We then load the atoms into a crossed-beam dipole trap (DT), consisting of one horizontal beam with vertical and horizontal waists of 20 μm and 330 μm, respectively, and one near-vertical beam with a waist of 78 μm. After evaporative cooling we obtain a BEC of about 3.5×10^5 atoms, with a peak density of $6.0(5) \times 10^{13}\,\mathrm{cm}^{-3}$. The trapping frequencies are $\omega_x = 2\pi \times 16\,\mathrm{Hz}$, $\omega_y = 2\pi \times 11\,\mathrm{Hz}$, $\omega_z = 2\pi \times 95\,\mathrm{Hz}$, where the y-axis points along the horizontal DT beam and the z-axis is vertical. The Thomas-Fermi radii are $R_x = 23\,\mu$m, $R_y = 35\,\mu$m and $R_z = 4.1\,\mu$m, and the chemical potential is $\mu = 30(2)$ nK. These parameters are chosen to maximize the number of doubly-occupied sites in the optical lattice.

The Mott insulator (MI) is realized by adiabatically loading the BEC into a 3D optical lattice, whose standing-wave interference pattern is obtained from three orthogonal, retro-reflected laser beams, with waists of 78 μm, 206 μm and 210 μm, derived from a single-mode laser with $\lambda_{\mathrm{Lattice}} = 1064$ nm wavelength (Innolight Mephisto MOPA). Orthogonal polarizations and frequency offsets of about 10 MHz between the three laser beams ensure that the optical potential experienced by the atoms can be well described by the sum of three independent 1D lattices. The lattice depth is calibrated through Kapitza-Dirac diffraction [144].

The BEC is adiabatically loaded into the optical lattice by increasing the lattice potential in three consecutive exponential ramps. A first ramp of 500 ms duration is used to reach a depth of about 5 $\mathrm{E_r}$ in each lattice direction, where $\mathrm{E_r} = h \times 2.1\,\mathrm{kHz}$ is the recoil energy. During the second ramp, which takes 150 ms and reaches 20 $\mathrm{E_r}$, the system undergoes the superfluid to MI phase transition. We then switch off the crossed-beam DT. The final ramp increases the trap depth to 200 $\mathrm{E_r}$ in 5 ms in order to reduce the size of the lattice site ground-state wavefunction, which in turn increases the free-bound Rabi frequency, see Sec. 3.5.1.

Since only atoms in doubly occupied sites will contribute to molecule formation, we maximize that number by varying initial atom number and DT confinement. To determine the number of doubly-occupied sites, we exploit three-body recombination and photoassociation. After loading the lattice, three-body recombination empties triply-occupied sites on a $1/e$ timescale of 104(15) ms. After 200 ms of wait time, we also empty the doubly-occupied sites by PA using L_{FB}. The difference in atom number before and after the PA pulse is twice the number of doubly-occupied sites. Measuring the atom number also directly after the loading sequence we derive the

occupation fractions 47(9) %, 30(5) % and 23(4) % for the occupation numbers $n = 1$, $n = 2$ and $n = 3$, respectively, where we assumed that the number of sites with more than three atoms is negligible. To prepare samples for molecule association by STIRAP, we wait 200 ms after loading the lattice, thereby removing most sites with three or more atoms.

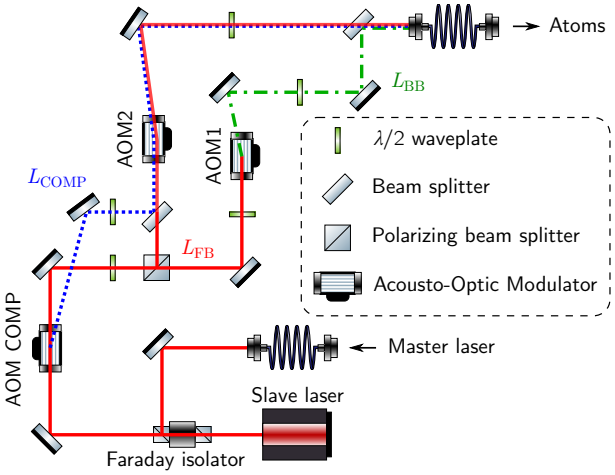

FIGURE 3.2: (color online) Optical setup used to produce photoassociation light and to compensate the light shift δ_{FB} in both space and time.

We now describe the laser setup used to illuminate the atoms with PA light, see Fig. 3.2, which also generates the light-shift compensation beam L_{COMP}, see Sec. 3.5.3. The two laser fields L_{FB} and L_{BB} are derived, by free-space splitting and recombination, from a single injection-locked slave laser seeded by a master oscillator with linewidth of less than $2\pi \times 3$ kHz. The frequencies of the laser fields are tuned by acousto-optical modulators (AOMs) and the beams are recombined into the same single-mode fiber with the same polarization, so that the main differences on the atomic cloud are their frequency and intensity. This setup ensures a good coherence between the two laser fields, which must match the Raman condition, which means that the frequency difference between the lasers must be equal to the binding energy of state $|m\rangle$ divided by h. The quality of the beat note of L_{FB} with L_{BB} is essentially set by the electronics controlling the AOMs. In the spectrum of the beat note, recorded on a photodiode and analyzed with a bandwidth of $2\pi \times 3$ Hz, the beat signal rises by ~ 60 dB above the background and has a width of $2\pi \times 60$ Hz. This narrow width can

be neglected on the time scale of the experiment (hundreds of μs) and doesn't need to be taken into account in our theoretical model of STIRAP. Frequency fluctuations of the master laser do not change the two-color detuning δ. They only change the one-color detuning Δ to which the STIRAP efficiency has low sensitivity, see Sec. 3.3.2. Finally, all laser fields used for PA are contained in one beam, which is sent onto the atomic cloud horizontally, under an angle of 30 ° from the y-axis. The waist of the beam at the location of the atoms is 113(2) μm. The polarization is linear and parallel to a vertically oriented guiding magnetic field of 5.30(5) G, which means that only π transitions can be addressed. The magnetic field splits the Zeeman levels of the state $|e\rangle$ by $2\pi \times 1.65(1)$ MHz $\gg \gamma_e$.

3.5 Molecule creation

We will now discuss molecule creation via STIRAP. First, we will characterize the parameters that can be measured before attempting STIRAP (PA Rabi frequencies, dynamic light shifts from PA light, and static light shifts from the lattice), see Tab. 3.1. We will then apply STIRAP on our sample and identify the finite lifetime of the dark state arising from the light shift δ_{FB} as the main limitation to the STIRAP efficiency. We will show how to overcome this limitation by minimizing δ_{FB} using a compensation beam and we will examine the effects of this compensation scheme on STIRAP. Finally we will characterize the spectral properties of the initial atomic sample and the lifetime of the molecular sample.

3.5.1 Parameter characterization

Rabi frequencies

We measure the bound-bound Rabi frequency Ω_{BB} through loss spectroscopy by probing the Autler-Townes splitting induced by Ω_{BB} with the free-bound laser [89]. We derive from our measurements $\Omega_{\mathrm{BB}} = 2\pi \times 234(5)\,\mathrm{kHz}/\sqrt{\mathrm{W/cm^2}}$.

To measure the free-bound Rabi frequency Ω_{FB} we shine L_{FB} on the MI and detect the resulting decay of atom number as a function of time. The observed decays are well described by exponentials with time constants τ. We measure τ for several lattice depths and intensities of L_{FB}. The variation of the atom number $N_a \propto |a|^2$ is determined by $\dot{a} = -\frac{\Omega_{\mathrm{FB}}^2}{2\Gamma_e}\, a$, which is obtained by adiabatic elimination of variable e in model (3.1) and by using the natural linewidth Γ_e of the free-bound transition as γ_e. Thus the measured decay time constant τ can be related to the Rabi frequency by $\Omega_{\mathrm{FB}} = \sqrt{\Gamma_e/\tau}$. The measurement of Γ_e is explained in Sec. 3.5.4. Figure 3.3 shows the

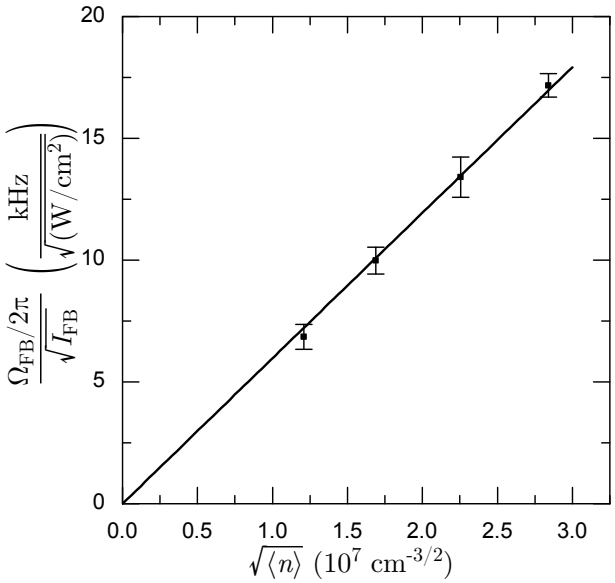

FIGURE 3.3: Free-bound Rabi frequency $\Omega_{\rm FB}$ as function of $\sqrt{\langle n\rangle}$, where $\langle n\rangle$ is the average on-site density of a single atom. The line is a linear fit to the data, justified in the text.

free-bound Rabi frequency $\Omega_{\rm FB}$ as a function of $\sqrt{\langle n\rangle}$, where n is the on-site density of a single atom and $\langle\cdot\rangle$ is the spatial average over one site. We observe that $\Omega_{\rm FB}$ is proportional to $\sqrt{\langle n\rangle}$, and we derive $\Omega_{\rm FB} = 2\pi \times 6.0(1)\, 10^{-7}\,\mathrm{kHz\,cm^{3/2}}/\sqrt{\mathrm{W/cm^2}}$.

We now present an argument that explains the observed linear relationship between $\Omega_{\rm FB}$ and $\sqrt{\langle n\rangle}$ [145, 146, 147]. The free-bound Rabi frequency depends on the Franck-Condon factor as $\Omega_{\rm FB} \propto \mathrm{FCF_{FB}} \propto \int_0^\infty \psi_e^*(r)\psi_a(r)r^2dr$, where ψ_e and ψ_a are the radial nuclear wavefunctions of the excited bound state and the initial atomic state, see Fig 3.1b. ψ_a is determined at short inter-particle distances by the molecular potential, and at long distances by the external harmonic confinement. ψ_e is non negligible only at short distances, and determined by the excited molecular potential. Therefore the value of $\mathrm{FCF_{FB}}$ is only determined by ψ_e and the short-range part of ψ_a. We vary $\sqrt{\langle n\rangle}$ by changing the external confinement provided by the lattice, which affects strongly the long-range part of ψ_a. We now need to determine how this change affects both the shape and the amplitude of the short-range part of ψ_a.

The short-range length scales $l_{a,e}$ of $\psi_{a,e}$ are set by the location of the wavefunction

node with largest internuclear distance and here $l_{a,e} < 10\,\mathrm{nm}$. Since in our case the two atoms described by ψ_a are both in the ground state of a lattice well, the total extent R of ψ_a is on the order of the harmonic oscillator size, which here means $R \gtrsim 100\,\mathrm{nm}$. A modification of the wavefunction at large distance by a change in the lattice confinement can affect the shape of the short-range wavefunction through a phase shift of order $\delta_\phi \simeq (l_a - a_s)k$, where $a_s = 6.6\,\mathrm{nm}$ is the s-wave scattering length and $k \simeq 1/R$ is the relative wavevector at long distance. Since $R \gg l_a$ and $R \gg a_s$, the phase shift δ_ϕ is negligible and does not affect the value of the integral $\mathrm{FCF}_{\mathrm{FB}}$. The relative wavefunction of two non-interacting particles in the external potential, $\phi_0(r)$, is a good approximation of $\psi_a(r)$ for $r \gg l_a$. Since $l_a \ll R$ we can choose r such that $\psi_a(r) \simeq \phi_0(r) \simeq \phi_0(0)$. As the external trap is changed, the amplitude at short distance is then simply scaled by a factor $\phi_0(0) \propto \sqrt{\langle n \rangle}$, thus leading to $\Omega_{\mathrm{FB}} \propto \mathrm{FCF}_{\mathrm{FB}} \propto \sqrt{\langle n \rangle}$.

Light shifts and loss by $L_{\mathrm{FB,BB}}$ light

We now characterize the parameters δ_{FB} and δ_{BB}, which are the time- and space-dependent light shifts contributing to the two-color detuning δ that are induced by the free-bound laser L_{FB} and the bound-bound laser L_{BB}, respectively. These detunings correspond to binding energy changes $-\hbar\delta_{\mathrm{FB,BB}}$ of molecules in state $|m\rangle$. We measure δ_{FB} (δ_{BB}) by two-color dark-state spectroscopy for different intensities of L_{FB} (L_{BB}) at fixed intensity of L_{BB} (L_{FB}). We obtain $\delta_{\mathrm{FB}} = 2\pi \times 18.3(6)\,\mathrm{kHz}/(\mathrm{W/cm^2})$ and $\delta_{\mathrm{BB}} = -2\pi \times 10(10)\,\mathrm{kHz}/(\mathrm{W/cm^2})$. These values agree with a simple theoretical estimation, which takes into account only transitions toward the optically excited atomic state $|a^*\rangle = {}^3P_1(m_J = 0)$. Indeed the light shift induced by $L_{\mathrm{FB,BB}}$ on $|m\rangle$ is weak because $L_{\mathrm{FB,BB}}$ do not couple this state to any other bound state out of the Λ scheme and because the coupling of $|m\rangle$ to $|a^*\rangle$ has to be scaled by a free-bound FCF. By contrast the light shift on $|a\rangle$ is substantial because of the atomic transition $|a\rangle - |a^*\rangle$, and therefore dominates the light shift of δ. To calculate the light shifts, we note that for our parameters the Rabi frequencies $\Omega^{\mathrm{FF}}_{\mathrm{FB,BB}}$ induced on the atomic transition by $L_{\mathrm{FB,BB}}$ are much smaller than the detunings of the lasers from the atomic transition. Taking also into account that two atoms contribute, the light shift of the binding energy can be approximated by $\delta_{\mathrm{FB}} \approx \hbar\Omega^{\mathrm{FF}^2}_{\mathrm{FB}}/2E_e = 2\pi \times 20.0\,\mathrm{kHz}/(\mathrm{W/cm^2})$ and $\delta_{\mathrm{BB}} \approx \hbar\Omega^{\mathrm{FF}^2}_{\mathrm{BB}}/2(E_e - E_m) = -2\pi \times 11.0\,\mathrm{kHz}/(\mathrm{W/cm^2})$, which is close to the measured values.

The coupling lasers L_{FB} and L_{BB} also induce time- and space-dependent light shifts Δ_{FB} and Δ_{BB} on the free-bound transition. We neglect Δ_{BB} because L_{BB} has low intensity. To determine Δ_{FB}, we perform one-color spectroscopy at several intensities of L_{FB}. We derive $\Delta_{\mathrm{FB}} = 2\pi \times 21(1)\,\mathrm{kHz}/(\mathrm{W/cm^2})$. The same reasoning

as above shows that the one-color shift is also dominated by the light shift of $|a\rangle$ and that $\Delta_{\mathrm{FB}} \approx \delta_{\mathrm{FB}}$, consistent with the measurement.

Significant atom loss is caused by L_{FB} through off-resonant scattering of photons on the ${}^1S_0 - {}^3P_1$ transition, which is the main contribution to γ_a. We measure this scattering rate by illuminating an atomic sample in a Mott insulator with L_{FB} detuned from the free-bound resonance by a few MHz. Since the system is in the Lamb Dicke regime, losses occur only through light-assisted inelastic collisions in sites with at least two atoms. We derive an effective natural linewidth for the free-atom transition of $\Gamma_a = 1.90(8)\,\Gamma_{{}^3\mathrm{P}_1}$, where $\Gamma_{{}^3\mathrm{P}_1}$ is the natural linewidth of the intercombination line. This is consistent with superradiant scattering, which is expected since the harmonic oscillator length is much smaller than the wavelength of L_{FB}.

Light shifts from lattice light

The lattice light induces static, space-dependent shifts of the two-color detuning ($\delta_{\mathrm{Lattice}}$) and of the free-bound transition ($\Delta_{\mathrm{Lattice}}$), which we now analyze experimentally and theoretically. We measure shifts $\delta_{\mathrm{Lattice}}$ up to a common offset through dark-state spectroscopy for several lattice depths, keeping the lattice well isotropic with $\omega_{x,y,z}$ within 10 % of each other. Similarly we measure shifts $\Delta_{\mathrm{Lattice}}$ through one-color spectroscopy up to a common offset. Both shifts are shown in Fig. 3.4 as a function of the average trap frequency of the central well. As before, the detuning $\delta_{\mathrm{Lattice}}$ corresponds to a change of the molecular binding energy of $-\hbar\delta_{\mathrm{Lattice}}$.

In the following we identify two independent components of the shifts by separating the two-body problem into its center-of-mass (CM) motion and its relative motion (rel), neglecting mixing terms if present. The first component is induced on the CM by the difference in polarizability of atom pairs and molecules. The second component is induced on the eigenenergies of the relative motion Hamiltonian by the external confinement and enables us to measure the zero-point energy of the lattice wells.

We start by deriving the two components of $\delta_{\mathrm{Lattice}}$. Firstly, the difference in polarizability of state $|a\rangle$ and $|m\rangle$ leads to a differential shift $\delta^{\mathrm{CM}}_{\mathrm{Lattice}} \propto \left(2\alpha_{({}^1S_0)} - \alpha_m\right) I_{\mathrm{Lattice}}$ as the external potentials experienced by the CM differ, where $\alpha_{({}^1S_0)}$ is the polarizability of a ground-state atom and α_m the polarizability of a molecule in state $|m\rangle$. Since the polarizability of weakly-bound molecules for far detuned light is close to the sum of the atomic polarizabilities of the constituent atoms we expect this shift to be small [148, 149]. Secondly, the external confinement induces a differential shift on the eigenenergies of the relative motion Hamiltonian, leading to $\delta^{\mathrm{rel}}_{\mathrm{Lattice}}$. The relative motion component of state $|a\rangle$ occupies the ground state of the lattice well potential with energy $E = 3\,\hbar\overline{\omega}_{\mathrm{Lattice}}/2 \propto I^{1/2}_{\mathrm{Lattice}}$, where $\overline{\omega}_{\mathrm{Lattice}}/2\pi = (\omega_x + \omega_y + \omega_z)/6\pi$ is the average trap frequency. By contrast, the energy of the relative motion component of

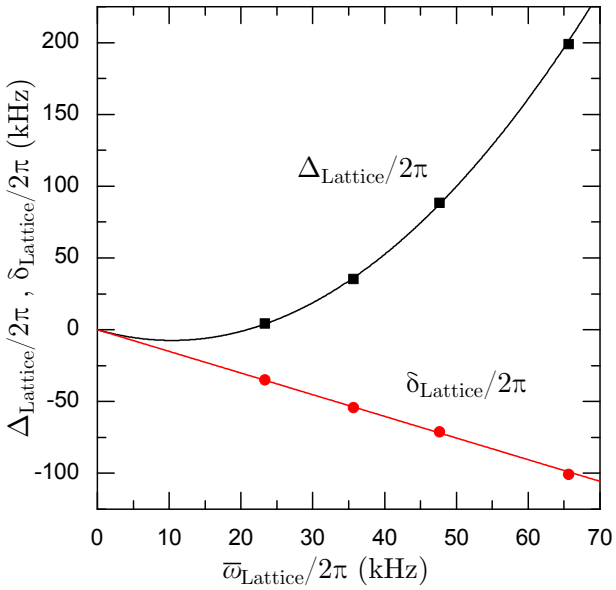

FIGURE 3.4: (color online) Shift $\delta_{\mathrm{Lattice}}$ of the two-color detuning (red disks) and shift $\Delta_{\mathrm{Lattice}}$ of the free-bound transition (black squares), as a function of the average trap frequency of the central well of the optical lattice. The measurements determine $\delta_{\mathrm{Lattice}}$ ($\Delta_{\mathrm{Lattice}}$) only up to a common offset, which is obtained by fits (curves) described in the text. The error bars of the measurements (i.e. excluding the error in the common offsets) are smaller than the symbol sizes.

state $|m\rangle$ is almost insensitive to the external confinement because the corresponding Condon point sets a volume scale which is less than 0.1 % of the ground-state oscillator volume. The light shift $\delta^{\mathrm{rel}}_{\mathrm{Lattice}}$ is therefore dominated by the behavior of $|a\rangle$, hence $\delta^{\mathrm{rel}}_{\mathrm{Lattice}} \propto I^{1/2}_{\mathrm{Lattice}}$. In contrast to $\delta^{\mathrm{CM}}_{\mathrm{Lattice}}$ this shift is even present for $\alpha_m = 2\alpha_{(^1S_0)}$. We neglect the density dependent interaction shift $\delta^{\mathrm{Coll}}_{\mathrm{Lattice}} \propto n \propto I^{1/4}_{\mathrm{Lattice}}$, because in our case it is small compared to $\delta^{\mathrm{rel}}_{\mathrm{Lattice}}$. The total light shift is then given by $\delta_{\mathrm{Lattice}} = \delta^{\mathrm{rel}}_{\mathrm{Lattice}} + \delta^{\mathrm{CM}}_{\mathrm{Lattice}} = a_1\, I^{1/2}_{\mathrm{Lattice}} + b_1\, I_{\mathrm{Lattice}}$, with a_1, b_1 being constants. We can thus distinguish the two contributions because of their different scaling with intensity.

The magnitude of the two components of $\delta_{\mathrm{Lattice}}$ can be determined from our

TABLE 3.1: Relevant parameters for molecule production.

Parameter	Units	Experiment	Theory
E_m/h	MHz	644.7372(2)	-
E_e/h	MHz	228.38(1)	-
Ω_{FB}	$\frac{\mathrm{kHz\,cm^{3/2}}}{\sqrt{\mathrm{W/cm^2}}}$	$2\pi \times 6.0(1)\,10^{-7}$	-
Ω_{BB}	$\frac{\mathrm{kHz}}{\sqrt{\mathrm{W/cm^2}}}$	$2\pi \times 234(5)$	-
Γ_e	kHz	$2\pi \times 17.0(1.5)$	$> 2\pi \times 14.8$
$\Gamma_a/\Gamma_{^3\mathrm{P}_1}$	-	1.90(8)	2
τ_{m}	ms	$6(2) \times t_{\mathrm{tunnel}}$	$\propto t_{\mathrm{tunnel}}$
γ_m^{FB}	$\frac{\mathrm{Hz}}{\mathrm{W/cm^2}}$	$2\pi \times 11(1)$	-
γ_m^{COMP}	$\frac{\mathrm{Hz}}{\mathrm{W/cm^2}}$	$2\pi \times 60(6)$	-
δ_{FB}	$\frac{\mathrm{kHz}}{\mathrm{W/cm^2}}$	$+2\pi \times 18.3(6)$	$+2\pi \times 20.0$
δ_{BB}	$\frac{\mathrm{kHz}}{\mathrm{W/cm^2}}$	$-2\pi \times 10(10)$	$-2\pi \times 11.0$
Δ_{FB}	$\frac{\mathrm{kHz}}{\mathrm{W/cm^2}}$	$+2\pi \times 21(1)$	$+2\pi \times 20.0$
$\delta_{\mathrm{Lattice}}$	$\overline{\omega}_{\mathrm{Lattice}}$	$-1.50(6)$	-1.5
$\Delta_{\mathrm{Lattice}}^{\mathrm{CM}}$	$\frac{\mathrm{Hz}}{\mathrm{W/cm^2}}$	$2\pi \times 2.13(2)$	$2\pi \times 2.98$
$\Delta_{\mathrm{Lattice}}^{\mathrm{rel}}$	$\overline{\omega}_{\mathrm{Lattice}}$	$-1.4(5)$	-1.5
$\tau_{\mathrm{DarkState}}$	ms	2.1(2)	-

experimental data. We fit the data as a function of $\overline{\omega}_{\mathrm{Lattice}} \propto I_{\mathrm{Lattice}}^{1/2}$, i.e. $\delta_{\mathrm{Lattice}} = a_2\overline{\omega}_{\mathrm{Lattice}} + b_2\,\overline{\omega}_{\mathrm{Lattice}}^2$, using also a common offset to all $\delta_{\mathrm{Lattice}}$ data points as fit parameter. The fit gives $a_2 = 1.5(3)$, which is consistent with the expected zero-point energy shift $3\hbar\,\overline{\omega}_{\mathrm{Lattice}}/2$. The fit result for b_2 yields an upper bound for the relative polarizability variation between atom pair and molecule of $|(2\alpha_{(^1S_0)} - \alpha_m)/2\alpha_a| < 1\,\%$. By assuming $\delta_{\mathrm{Lattice}}^{\mathrm{rel}}$ to dominate the shift and refitting while keeping $b_2 = 0$, we obtain $a_2 = 1.50(6)$. This measurement directly determines the variation of the harmonic oscillator zero point energy with trap frequency and was possible for two reasons: first, the negligible difference in polarizability between atom pairs and molecules and, second, the high precision achievable with dark-state spectroscopy.

We finally analyze the shift $\Delta_{\mathrm{Lattice}}$ of the free-bound transition. Analogous to $\delta_{\mathrm{Lattice}}^{\mathrm{CM}}$, the centre-of-mass component of the shift is given by $\Delta_{\mathrm{Lattice}}^{\mathrm{CM}} \propto \left(2\alpha_{(^1S_0)} - \alpha_e\right) I_{\mathrm{Lattice}}$, where now the molecular state is $|e\rangle$ with polarizability α_e. Again assuming that the molecular polarizability is the sum of atomic polarizabilities, we have $\Delta_{\mathrm{Lattice}}^{\mathrm{CM}} \propto \left(2\alpha_{(^1S_0)} - \left(\alpha_{(^3P_1)} + \alpha_{(^1S_0)}\right)\right) I_{\mathrm{Lattice}} = \left(\alpha_{(^1S_0)} - \alpha_{(^3P_1)}\right) I_{\mathrm{Lattice}}$. In contrast to before this shift is not small since the difference in polarizability of the $^1S_0$ and

$^3P_1$ ($m_J = 0$) states at the lattice wavelength is significant. A smaller shift is induced by changing lattice potentials on the CM zero point energy difference between $|a\rangle$ and $|e\rangle$, which we neglect. The relative motion component of the shift $\Delta^{\mathrm{rel}}_{\mathrm{Lattice}}$ is given by $\approx -3\,\overline{\omega}_{\mathrm{Lattice}}/2$, since also here the relative motion energy of molecular state $|e\rangle$ is barely influenced by the external potential. The two components add to the one-color detuning shift $\Delta_{\mathrm{Lattice}} = \Delta^{\mathrm{rel}}_{\mathrm{Lattice}} + \Delta^{\mathrm{CM}}_{\mathrm{Lattice}} = a_3\,\overline{\omega}_{\mathrm{Lattice}} + K\,\left(\alpha_{(^1S_0)} - \alpha_{(^3P_1)}\right)\overline{\omega}^2_{\mathrm{Lattice}}$, where a_3 is a free parameter, $K = 3m\lambda^2_{\mathrm{Lattice}}/(4\pi h\alpha_{(^1S_0)})$, m the mass of ^{84}Sr, and $\alpha_{(^1S_0)} = -234$ a.u. (atomic units, here 1 a.u. $= 4\pi\epsilon_0 a_0^3$, where ϵ_0 is the vacuum permittivity and a_0 the Bohr radius). Using a_3, $\alpha_{(^3P_1)}$, and a common offset to all data points as parameters, we fit this function to the data and retrieve $\alpha_{(^3P_1)} = -188(2)$ a.u. and $a_3 = -1.4(5)$. Since we experimentally vary the intensity for the three lattice beams together, we expect to obtain the mean value of the polarizability for the state $^3P_1$ ($m_J = 0$) calculated for the three different polarizations of the electric field for the three beams, which is -170.4 a.u. [150], roughly 10 % different from the experimental value. This deviation might be explained by our model neglecting the anisotropy in the trap frequencies.

3.5.2 STIRAP

We now apply STIRAP to our Mott insulator sample. We prove the association of molecules and measure the molecule association efficiency after optimization of the relevant parameters. We compare this efficiency with our theoretical model and find that dynamic light shifts of the binding energy limit the current scheme. This limit will be overcome in Sec. 3.5.3.

In order to demonstrate the production of molecules by STIRAP and to obtain a quantitative measurement of the single-path STIRAP efficiency, we apply a STIRAP cycle, see Sec. 3.2. Between aSTIRAP and dSTIRAP, we selectively remove all remaining atoms with a pulse of light resonant with the atomic $^1S_0 - {}^1P_1$ transition. Figure 3.8c shows the intensity profile used for the STIRAP lasers $L_{\mathrm{FB,BB}}$ and the push pulse. The push pulse doesn't affect molecules because their binding energy is much bigger than the linewidth of the transition $\Gamma_{^1\mathrm{P}_1} \simeq 2\pi \times 30$ MHz. Similarly, since absorption imaging is also performed using this transition, only atoms are imaged. Reappearance of atoms on images taken after the full STIRAP cycle is the experimental signature for the presence of molecules after the aSTIRAP. Assuming an equal efficiency for aSTIRAP and dSTIRAP, the single-path STIRAP efficiency is $\eta = \sqrt{N_f/N_i}$, where N_i and N_f are the atom numbers in doubly-occupied sites before and after the STIRAP cycle, respectively.

We optimize the STIRAP sequence by maximizing the number of Sr atoms retrieved after two STIRAP cycles, by varying independently the relevant parameters

TABLE 3.2: Optimized parameters used for STIRAP, without compensated two-color detuning (NO-COMP) or with (COMP).

Parameter	Units	NO-COMP	COMP
Ω_{FB}	kHz	$2\pi \times 32(2)$	$2\pi \times 38(2)$
Ω_{BB}	kHz	$2\pi \times 300(10)$	$2\pi \times 107(3)$
$A = \gamma_e \delta_{\mathrm{FB}}/\Omega_{\mathrm{FB}}^2$	-	$-1.4(3)$	$0.0(1)$
$\Delta\omega_{\mathrm{COMP}}$	MHz	-	$2\pi \times 197$
T_{pulse}	μs	400	400
n_{peak}	cm^{-3}	4.6×10^{15}	4.6×10^{15}
τ_{m}	ms	$> 10^5$	$> 10^5$
γ_e	kHz	$2\pi \times 44(13)$	$2\pi \times 44(13)$
$\tau_{\mathrm{DarkState}}$	ms	2.1(2)	2.1(2)
η	-	53.0(3.5) %	81(2) %

(Ω_{FB}, Ω_{BB}, T and $\langle n \rangle$). We choose to optimize the atom number after two cycles in order to reduce the influence of the inhomogeneous lattice light shift $\delta_{\mathrm{Lattice}}$ on the optimization result. During the first aSTIRAP only atoms on a subset of sites with similar light shift are successfully associated. The push pulse removes all remaining atoms, such that after dSTIRAP we are left with a sample of atom pairs on sites with similar lightshift. This purification of the sample is also evident when comparing the width of one-color PA spectra taken before and after the first STIRAP cycle, see Sec. 3.5.4. The second STIRAP cycle is used to measure the efficiency of STIRAP on this more homogeneous sample. The optimized parameters are reported in Tab. 3.2 in the column labeled NO-COMP. The best single-path STIRAP efficiency is $\eta_{\mathrm{exp}} = 53.0(3.5)\,\%$, which represents a considerable improvement compared to our previous work [26]. This improvement is made possible by a longer molecule lifetime, see Sec. 3.5.4.

To compare the performance of the experiment with the theoretical expectation, we model the aSTIRAP using Eq. (3.1). This model requires two not yet determined parameters, γ_e and γ_m, which can only be characterized employing STIRAP. Their measurement will be discussed in Sec. 3.5.3 and 3.5.4, respectively. Taking these and all previously determined parameters together with the pulse shape as input for the model, we predict that aSTIRAP has an efficiency of $\eta_{\mathrm{theory}} = 55(5)\,\%$, which is consistent with our measurements.

In order to discriminate whether the main limitation to the STIRAP efficiency is the adiabaticity of the sequence or the lifetime of the dark state we examine the

criterion $|A|\,\alpha = |\delta_m|T \gg \pi/\sqrt{C}$ derived from Eq. 3.3 for $\delta \approx \delta_{\mathrm{FB}}(\sin(\theta)^2 - 1/2)$ and $\Omega_m \approx \Omega_{\mathrm{FB}} \simeq \Omega_{\mathrm{BB}}$. The latter condition is not fulfilled in the experiment. However, the population transfer happens mainly in the time interval during which Ω_{FB} and Ω_{BB} are of the same order of magnitude, which makes the criterion approximately valid. We obtain $T = 400\,\mu\mathrm{s} \gg \pi/(\sqrt{C}\delta_{\mathrm{FB}}) = 88\,\mu\mathrm{s}$, suggesting that we are in the regime where the main loss mechanism is the dissipation from the finite lifetime of the dark state due to $\delta_{\mathrm{FB}} \neq 0$.

3.5.3 STIRAP with light-shift compensation

In order to improve the molecule creation efficiency we need to increase the dark-state lifetime. This lifetime is proportional to A^{-2}, where $A = \delta_m/\tilde{\gamma} \approx \gamma_e\delta_{\mathrm{FB}}/\Omega_{\mathrm{FB}}^2$, and efficient operation is ensured in the adiabatic regime only if $|A| \ll 1$. We cannot decrease $|A|$ by increasing the intensity of L_{FB}, because $\delta_{\mathrm{FB}} \propto \Omega_{\mathrm{FB}}^2$. In the following, we show how to compensate the shift δ_{FB} both in time and space by using an additional "compensation" laser beam. After optimization, the compensation scheme allows us to reach an efficiency of $\eta_{\mathrm{exp}} = 81(2)\,\%$.

Compensation beam

As explained in Sec. 3.5.1, the two-color detuning shift δ_{FB} is dominated by the light shift of $|a\rangle$ in presence of $\mathrm{L_{FB}}$ because of the atomic ${}^1S_0 - {}^3P_1$ transition, from which $\mathrm{L_{FB}}$ is red detuned by only $|\Delta\omega_e| = (E_e + \Delta)/\hbar \approx E_e/\hbar = 2\pi \times 228\,\mathrm{MHz}$. The resulting shift $\delta_{\mathrm{FB}} \approx \hbar\Omega_{\mathrm{FB}}^{\mathrm{FF}^2}/2E_e \propto I_{\mathrm{FB}}/\Delta\omega_e$ can be exactly cancelled by superimposing an additional compensation laser field L_{COMP} with $\mathrm{L_{FB}}$, creating the shift $\delta_{\mathrm{COMP}} = -\delta_{\mathrm{FB}}$ [131]. To cancel the shift, L_{COMP} has to be detuned by $\Delta\omega_{\mathrm{COMP}}$ to the blue of the atomic transition (see Fig. 3.1a) and must have an intensity $\frac{I_{\mathrm{COMP}}}{I_{\mathrm{FB}}} = |\frac{\Delta\omega_{\mathrm{COMP}}}{\Delta\omega_e}|$. This light-shift cancellation technique is similar to the SCRAP method [151], as it relies on tailoring the light shifts with an off-resonant beam.

Since I_{FB} varies in time during STIRAP the light-shift compensation needs to be dynamic as well [152]. Since we want to keep $\Delta\omega_{\mathrm{COMP}}$ and $\Delta\omega_e$ constant for convenience, I_{COMP} has to be varied proportionally to I_{FB} to always keep the light shift canceled. A simple technical solution to obtain such a coordinated change in intensity is to split the free-bound laser beam into two beams, impose on one of the beams a frequency offset $|\Delta\omega_e| + |\Delta\omega_{\mathrm{COMP}}|$ and recombine the beams with exactly the same polarization and spatial mode, before passing through an AOM to control the intensity of both frequency components in common. This composite beam is finally recombined with the bound-bound beam into one single mode fiber, from which PA

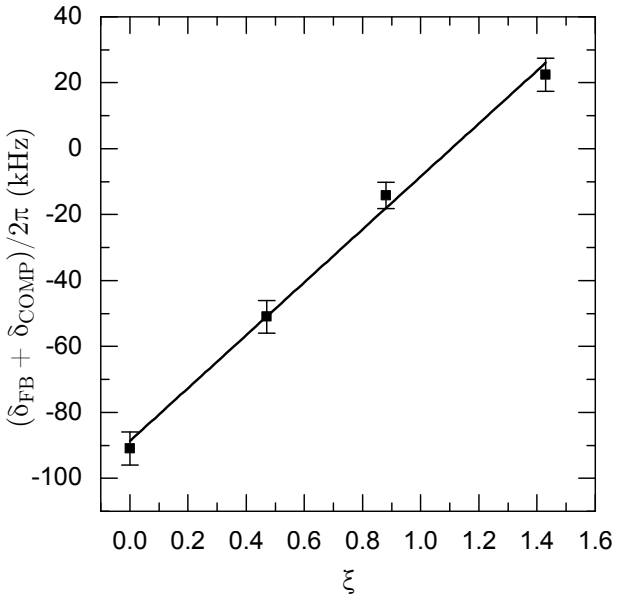

FIGURE 3.5: Light shift $\delta_{\mathrm{FB}} + \delta_{\mathrm{COMP}}$ induced by the free-bound laser L_{FB} and the compensation beam L_{COMP} as a function of the compensation level ξ. The solid line is a linear fit to the data.

light is shone on the atoms (see Fig. 3.2). This setup allows us to compensate the light shift δ_{FB} both in time and space.

To validate our technique we measure the light shift δ_{FB} induced by L_{FB} (referenced to the non-shifted extrapolated value for $I_{\mathrm{FB}} = 0\,\mathrm{W/cm^2}$) as a function of the compensation level defined as $\xi = \frac{I_{\mathrm{COMP}}}{I_{\mathrm{FB}}} |\frac{\Delta\omega_e}{\Delta\omega_{\mathrm{COMP}}}|$, where we expect perfect compensation for $\xi = 1$. The compensation level is varied by changing the intensity of the compensation beam before AOM 1 while keeping all other parameters fixed. For this measurement we use $\Delta\omega_{\mathrm{COMP}} = 2\pi \times 66\,\mathrm{MHz}$ and an intensity of $I_{\mathrm{FB}} = 5\,\mathrm{W/cm^2}$, which is of the order of the optimum intensity of L_{FB} for STIRAP. The measured δ_{FB} is plotted as a function of ξ in Fig. 3.5 together with a linear fit from which we obtain $\xi(\delta_{FB} = 0) = 1.1(1)$, which is consistent with our assumption of the light shift being dominated by the atomic ${}^1S_0 - {}^3P_1$ transition. To reduce the off-resonant scattering rate of photons on the atomic transition, we increase $\Delta\omega_{\mathrm{COMP}}$ to $2\pi \times 197\,\mathrm{MHz}$ in all further usages of the compensation beam.

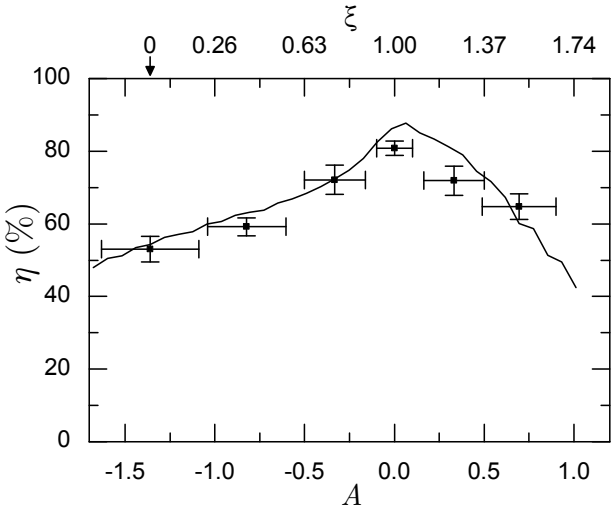

FIGURE 3.6: Maximum single-path STIRAP efficiency as a function of the parameter $A = \delta_m/\tilde{\gamma}$, varied by changing the intensity I_{COMP} of the compensation beam. Values of the compensation level ξ are given on the top axis for reference. Theoretical values (line) are obtained by simulating the STIRAP process with Eq. (3.1), using independently determined parameters and not performing any fit. The error bars represent one standard deviation.

STIRAP optimization and characterization

We characterize the effect of our dynamic optical compensation scheme on the STIRAP efficiency. For several compensation levels ξ we optimize STIRAP and show the efficiency achieved during the second STIRAP cycle in Fig. 3.6. The maximum efficiency rises from 53.0(3.5) % without compensation to 81(2) % and is obtained for $\xi = 1$, corresponding to $A = 0.0(1)$. This proves that a strong limitation to the STIRAP efficiency without compensation indeed originates from the space- and time-dependent light shift imposed on the binding energy by L_{FB} and that our scheme is able to compensate this undesired shift. The optimized parameters, shown in column "COMP" of Tab. 3.2, lead our theoretical model to describe the experimental data well. The model indicates that now, for $|A| \ll 1$, the limitations to the transfer efficiency are to similar amounts off-resonant scattering of photons from $|a\rangle$ and $|m\rangle$, and the finite dark-state lifetime resulting, e.g., from residual δ_{FB} and δ_{BB}. All STIRAPs discussed in the remainder of this article use the compensation beam with $\xi = 1$.

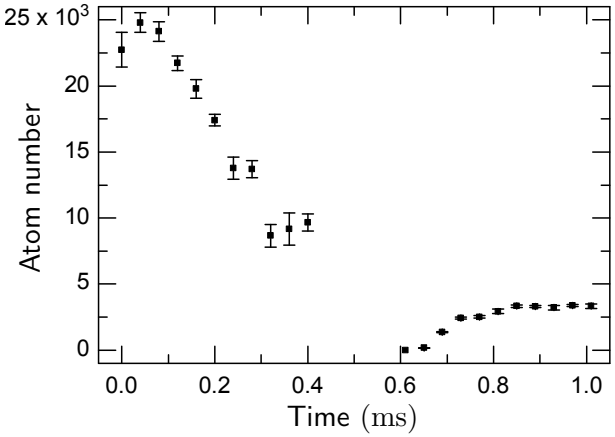

FIGURE 3.7: Time evolution of Sr atom number during the first STIRAP cycle, using light-shift compensation.

We next characterize the evolution of the atom number over several STIRAP cycles, showing the first cycle in Fig. 3.7 and subsequent cycles in Fig. 3.8a. We observe that the fraction of atoms reappearing after a STIRAP cycle compared to the atom number at the beginning of that cycle is $\sim 65\,\%$ for all but the first cycle, for which it is only $14\,\%$. Ignoring the first STIRAP cycle and assuming equal efficiencies of aSTIRAP and dSTIRAP within each cycle, we find that the single-path STIRAP efficiency is roughly $80\,\%$ and constant from the second cycle onwards.

The lower fraction of returning atoms of the first cycle can be explained by two effects, the existence of singly-occupied lattice sites and the lattice induced inhomogeneity of the molecular binding energy, which leads to a finite dark-state lifetime and therefore loss. An independent one-color spectroscopy measurement shows that our lattice contains 1.1×10^5 atoms on singly occupied sites, which matches the number of atoms remaining after the first aSTIRAP, letting us conclude that these atoms simply did not have partners to form molecules with. Following the first aSTIRAP these atoms are removed by the push beam pulse. The atom number reduction during the first aSTIRAP of 1.4×10^5 matches the number of atoms on doubly occupied sites. Assuming an $80\,\%$ single-path dSTIRAP efficiency as observed in STIRAP cycles beyond the first, the 3.5×10^4 atoms reappearing after dSTIRAP correspond to 4.4×10^4 atoms associated into molecules, which is only $30\,\%$ of the initial atom number on doubly occupied sites, not $80\,\%$ as during later STIRAP cycles. This difference can

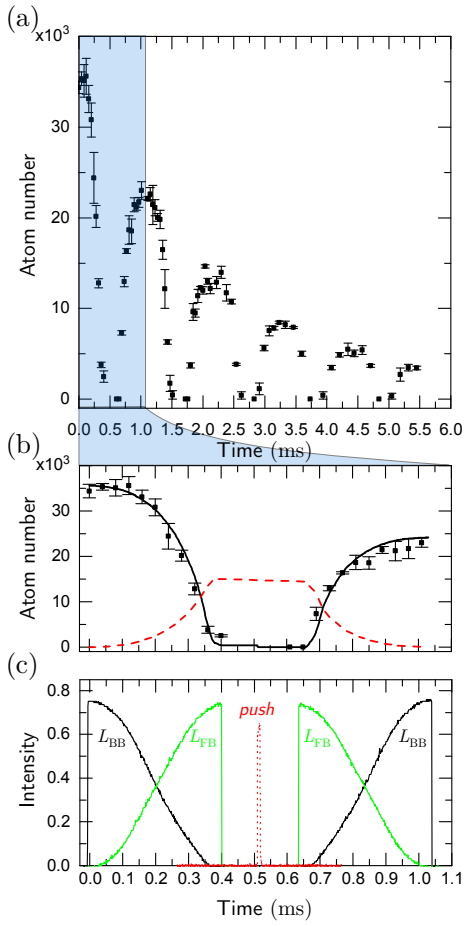

FIGURE 3.8: (color online) (a) Time evolution of the atom number during STIRAP cycles 2 to 5, using light-shift compensation. (b) Number of Sr atoms during the second STIRAP cycle as function of time. The lines are the theory curves based on Eq. (3.1) with no fitting parameter, representing the atom (black solid line) and molecule (red dashed line) number for the parameters given in Tab. 3.2.(c) Intensities of L_{FB}, L_{BB} and push pulse beam in arbitrary units. The intensity of L_{COMP} is not shown.

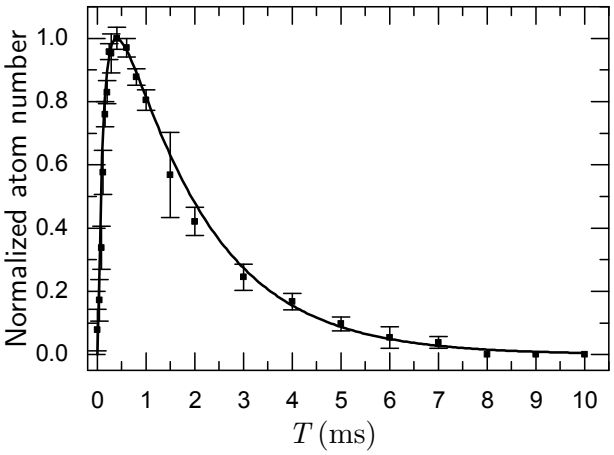

FIGURE 3.9: Number of atoms retrieved after two STIRAP cycles as a function of the pulse time T used for the second STIRAP. The line is a fit using our model, from which we obtain the parameter $\langle\delta\rangle$.

be explained by the decrease of STIRAP efficiency η with increasing two-color detuning δ, characterized in Sec. 3.5.3, in combination with the inhomogeneous spread of δ across the sample originating from the lattice light shift, estimated in Sec. 3.5.4. Both, $\eta(\delta)$ and the fraction of population on sites with detuning δ, $p(\delta)$, show peaks of similar width. The average STIRAP efficiency can be estimated by averaging $\eta(\delta)$ with weight $p(\delta)$ and is about half of the maximum efficiency, consistent with our observation. This indicates that the inhomogeneous shift of the binding energy by the lattice light shift is the main limitation to the fraction of lattice sites usable for molecule association. In future work this limit could be overcome by increasing the width of the lattice beams, while keeping the lattice depth constant. Here we simply use the first STIRAP cycle to remove atoms on sites with large two-color detuning δ and atoms on singly-occupied sites, providing us with an ideal sample to study STIRAP.

As first such study we trace the atom number during five consecutive STIRAP cycles in Fig. 3.8a, each identical to the first. The single-path STIRAP efficiency of the second cycle is 81(2) %. All cycles have efficiencies around 80 %, from which we can take two conclusions. First, the cleaning of the sample realized by the first STIRAP cycle is enough to decrease the binding energy inhomogeneity to a level that is negligible for the STIRAP efficiency. Second, it proves that our MI sample is not

heated significantly, which would have reduced the STIRAP efficiency with each cycle.

Next we study the dependence of STIRAP efficiency on pulse time, by recording the atom number after the second STIRAP cycle, see Fig. 3.9. Thanks to the light-shift compensation scheme, the pulse time for the STIRAP can be as high as a few ms while still resulting in substantial molecule production. For pulse times longer than 400 μs, we observe a decrease of the retrieved atom number on a $1/e$ time of ~ 2 ms. This decrease can neither be explained by the residual δ_{FB} nor by δ_{BB}, but it can be explained by the finite dark state lifetime of $\tau_{\mathrm{DarkState}} = 2.1(2)$ ms measured in Sec. 3.5.4. This finite lifetime could originate in laser noise or in a small but non-zero static Raman detuning $\langle\delta\rangle$ present during the STIRAP cycle. Fitting our data with the model Eq. (3.1) using a static Raman detuning as only free parameter we obtain $\langle\delta\rangle = 2\pi \times 2.4(5)$ kHz. A similar detuning would explain the observed dark-state lifetime.

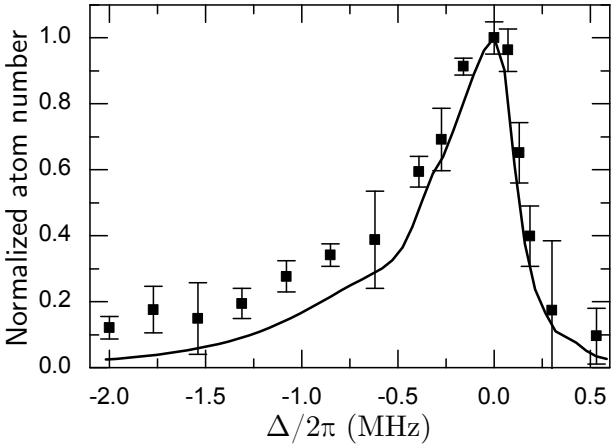

FIGURE 3.10: STIRAP efficiency in dependence of the one-color detuning Δ. The data points show the normalized number of atoms retrieved after two STIRAP cycles, depending on the value Δ used for the second STIRAP. The solid line is derived from Eq. (3.1) using no fit parameters.

Effect of Δ, δ on efficiency and determination of γ_e

We now analyze the efficiency of STIRAP in dependence of the one-color detuning Δ and the two-color detuning δ, see Fig. 3.10 and 3.11 respectively. To this end, we

keep the parameters of the first, purification STIRAP constant, and record the atom number N_2 after the second STIRAP for varying δ while keeping $\Delta = 0$, or *vice versa*. The STIRAP efficiency $\eta \propto \sqrt{N_2}$ exhibits peaks around zero detuning, which have a FWHM of $2\pi \times 0.5\,\mathrm{MHz}$ for $\eta(\Delta)$ and $2\pi \times 20\,\mathrm{kHz}$ for $\eta(\delta)$. The width of $\eta(\Delta)$ is much bigger than the broadened free-bound linewidth, see Sec. 3.5.4, so that the shift due to the inhomogeneous broadening induced by the lattice light on the free-bound transition can be neglected. However, as explained in Sec. 3.5.3, the width of $\eta(\delta)$ is comparable to the spread in δ, leading to a lower fraction of atoms in doubly occupied sites being associated during the first aSTIRAP compared to consecutive aSTIRAPs.

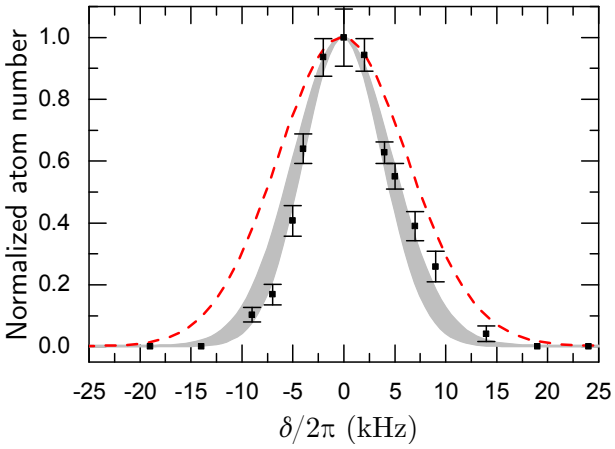

FIGURE 3.11: (color online) Dependence of STIRAP efficiency on the two-color detuning δ. The data points show the normalized number of atoms retrieved after two STIRAP cycles. The red dashed line is the shape determined by our model for $\gamma_e = \Gamma_e = 2\pi \times 17.0(1.5)\,\mathrm{kHz}$, while the grey area spans the widths between $2\pi \times 30\,\mathrm{kHz}$ and $2\pi \times 57\,\mathrm{kHz}$, which are the fitted values for the positive-detuning and the negative-detuning side, respectively.

From our measurement of $N_2(\delta)$ in Fig. 3.11, we are able to derive the loss term γ_e of Eq. (3.1), which describes the rate at which population is lost from state $|e\rangle$ because of coupling to states outside the subspace corresponding to our Λ scheme. It can be viewed as an indicator of how open our quantum system is. The value of γ_e relevant for STIRAP can be higher than the natural linewidth of the free-bound transition, i.e. $\gamma_e \geq \Gamma_e$, because of one- or two-photon processes induced by L_{FB}, L_{BB}, and L_{COMP} that introduce dissipation. To measure γ_e, we make use of the fact

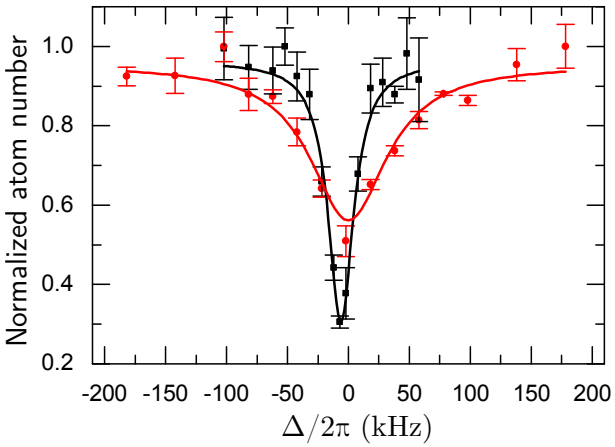

FIGURE 3.12: (color online) One-color molecular line and corresponding Lorentzian fits measured on an atomic sample in the lattice before (red disks) and after (black squares) the first STIRAP cycle. The narrower width of the latter signal is the result of the spectral selection imposed by the STIRAP pulse.

that the STIRAP efficiency is only high for small $A \approx \delta\gamma_e/\Omega_{\mathrm{FB}}^2$, see Sec. 3.3.2, which leads to a γ_e dependence of the $N_2(\delta)$ peak width. If we assume $\gamma_e = \Gamma_e$, where Γ_e is determined in Sec. 3.5.4, our model gives the dashed line shown in the figure, which is broader than the observed peak. Moreover, we observe a slight asymmetry in the data that is not reproduced by the model. We therefore fit the model independently to the data corresponding to positive and negative detunings using γ_e as the only fit parameter and derive $\gamma_e^+ = 2\pi \times 30(5)\,\mathrm{kHz}$ and $\gamma_e^- = 2\pi \times 57(8)\,\mathrm{kHz}$, respectively. In further uses of our model we fix γ_e to the average value $2\pi \times 44(13)\,\mathrm{kHz}$.

3.5.4 Sample characterization

Inhomogeneous light shifts by lattice light and dark state lifetime

In order to help understand the origin of the difference in STIRAP efficiencies between the first STIRAP cycle and the following cycles, we measure the lattice light shifts on the free-bound transition and on the binding energy of $|m\rangle$ for both initial and purified samples. We use PA spectroscopy for all measurements, but for the determination of the binding energy spread of the purified sample. Since this spread is below the

resolution of our two-color PA spectroscopy, we in this case measure the dark state lifetime and extract an upper bound of the binding energy spread from that.

In order to measure the inhomogeneous broadening induced by the lattice on the free-bound transition, we take one-color PA spectra using a MI sample, either directly after lattice loading or after one STIRAP cycle, see Fig. 3.12. These data sets are modelled by Eqs. (1), where γ_e is the fit parameter and all other quantities in the Hamiltonian, except for Ω_{FB}, are set to zero. We retrieve $\gamma_e = 63(8)\,\mathrm{kHz}$ and $17.0(1.5)\,\mathrm{kHz}$ for the free-bound transition linewidth before and after STIRAP, respectively. The latter value is consistent with our measurement of the natural linewidth of the molecular transition in a BEC [153], $\Gamma_e = 2\pi \times 19.2(2.4)\,\mathrm{kHz}$, while the former is roughly a factor of 4 wider. The reduction of the apparent linewidth after one STIRAP cycle is a result of the sample purification by the STIRAP cycle. Since both the free-bound transition shift and the binding energy shift are strongly dependent on the shift of state $|a\rangle$ by the lattice light, the STIRAP cycle not only reduces the spread in δ, but also the inhomogeneous broadening of the one-color PA line. Deconvolving the measured linewidths with twice the atomic ${}^1S_0 - {}^3P_1$ transition $2 \times \Gamma_{{}^3\mathrm{P}_1} = 2\pi \times 14.8\,\mathrm{kHz}$ [85, 27], we derive that the inhomogeneous differential light shifts on the free-bound transition of the initial and the final sample are $2\pi \times 61(10)\,\mathrm{kHz}$ and $2\pi \times 8(3)\,\mathrm{kHz}$, respectively.

In order to measure the inhomogeneous broadening induced by the lattice on the binding energy of $|m\rangle$, we perform two distinct measurements depending on the sample. We perform two-color spectroscopy on the initial sample using low intensity of $L_{\mathrm{FB,BB}}$, which ensures negligible light shifts from the PA light. The width of the dark resonance is then $\Delta\omega_{\mathrm{DarkState}} = 2\pi \times 18(4)\,\mathrm{kHz}$. To deduce an upper bound on the binding energy spread of the purified sample, we measure the dark-state lifetime. We prepare a roughly equal superposition of atomic and molecular state by applying only half of the second aSTIRAP pulse. We wait for a variable time while holding $L_{\mathrm{FB,BB}}$ at constant intensity, and finally apply the second half of the dSTIRAP. The measured lifetime is $\tau_{\mathrm{DarkState}} = 2.1(2)\,\mathrm{ms}$, and the experimental data agree with our model when adding a static two-color detuning of $\langle\delta\rangle = 2\pi \times 2.2(2)\,\mathrm{kHz}$. This value is an upper bound of the binding energy spread induced by the lattice on the purified sample.

The ratio of the free-bound transition linewidth and the two-color detuning spread is consistent with the light-shift calibration, both before and after STIRAP (see Tab. 3.1). Using this calibration, we conclude that the initial sample was populating lattice sites located off axis by up to $\simeq 30\,\%$ of the lattice beam waist.

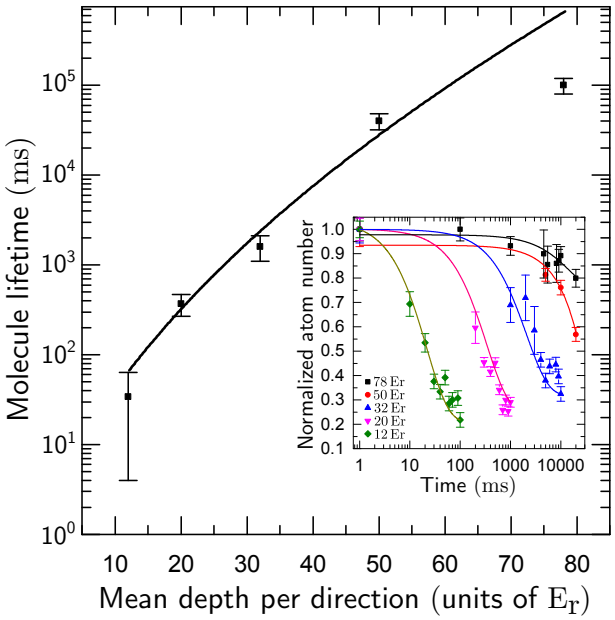

FIGURE 3.13: (color online) Molecule lifetime as function of the lattice depth averaged over the three directions in the central region of the lattice. The depth is that of the potential experienced by the molecules, expressed in units of recoil energies of the molecule $E_r/h = 8.4\,\mathrm{kHz}$. Inset: atom number decay as a function of hold time between association and dissociation STIRAP pulses for different lattice depths.

Molecule lifetime

The molecules produced in our experiment have a finite lifetime as a result of two loss mechanisms, inelastic collisions with other molecules in the lattice and dissipation caused by optical coupling of state $|m\rangle$ to states lying outside our Λ scheme. Thus, the lifetime is given by $\tau_m = 1/\gamma_m = 1/(\gamma_m^{\mathrm{coll}} + \gamma_m^{\mathrm{opt}})$, where γ_m^{coll} is the decay rate for collisional losses and γ_m^{opt} is the scattering rate for optically induced losses.

We measure the molecule lifetime $\tau_m^{\mathrm{coll}} = 1/\gamma_m^{\mathrm{coll}}$ that results from inelastic collisions by varying the hold time between the push pulse and the dSTIRAP at several lattice depths. During these measurements the lattice well potential is kept isotropic with $\omega_{x,y,z}$ within 10 % from each other. The molecule lifetime depends strongly on

the lattice depth, see Fig. 3.13. The observed change of four orders of magnitude over the lattice depth is consistent with loss of molecules by tunneling to neighboring sites followed by effectively instantaneous chemical reaction with the molecule already present on that site. Collisions between molecules and atoms do not play a role here since all atoms have been removed by the push pulse prior to lowering the lattice depth. Under these assumptions the lifetime is given by $\tau_m^{\mathrm{coll}} = D \times t_{\mathrm{tunnel}}$, where D is a constant and $t_{\mathrm{tunnel}} = h/\sum_i 2J_i$ is the total tunneling time, which depends on the tunneling rates along the 3 lattice directions $J_{1,2,3}$ [76, 154]. We fit the experimental data with this single-parameter model and retrieve $D = 6(2)$. We observe that the lifetime measured for our deepest lattice are lower than predicted by our model. This can be explained by loss through scattering of lattice photons becoming dominant over the low inelastic collision loss, since here the lattice light intensity is high and the tunnel time scale long.

For the deepest lattice the molecule lifetime is 100(20) s, representing a major improvement compared to our previous paper, where the lifetime was about 60 μs [26]. The main difference between this work and our previous work is the wavelength of the light used for the realization of the optical lattice. In our previous work, the lattice laser source was a Coherent Verdi at 532 nm wavelength, whereas here we use an Innolight Mephisto MOPA at 1064 nm. By shining 532-nm light derived from another Verdi laser on our sample, we confirm a strong reduction of the molecule lifetime within a factor of 10 of what was measured before. An explanation for the reduced lifetime is that the 532-nm light is close to molecular lines, thus inducing inelastic processes.

The second loss mechanism arises from optical couplings of molecules toward states outside our Λ scheme. One contribution is the scattering of lattice photons, as mentioned above. Other significant contributions arise from $L_{\mathrm{FB,COMP}}$, whereas the low intensity L_{BB} plays a minor role. We measure the scattering time $\tau_m^{\mathrm{opt}} = 1/\gamma_m^{\mathrm{opt}} = 1/(\gamma_m^{\mathrm{FB}} + \gamma_m^{\mathrm{COMP}})$ by shining L_{FB} and L_{COMP} on the molecules during the hold time between the push pulse and dSTIRAP, at several intensities of $L_{\mathrm{FB,COMP}}$. We derive $\gamma_m^{\mathrm{FB}} = 2\pi \times 11(1)\,\mathrm{Hz}/(\mathrm{W/cm^2})$ and $\gamma_m^{\mathrm{COMP}} = 2\pi \times 60(6)\,\mathrm{Hz}/(\mathrm{W/cm^2})$.

3.6 Conclusion and outlook

In conclusion, we have used STIRAP to associate pairs of Sr atoms in the ground state of lattice sites into weakly-bound ground-state molecules. This association process was efficient despite operating in the regime of strong dissipation $\Omega_{\mathrm{FB}} \lesssim \gamma_e$. By making use of a deep optical lattice using 1064-nm light, but without compensating dynamic light shifts created by the STIRAP lasers, we were able to reach a transfer

efficiency of roughly 50 %. The improvement from 30 % reached in our previous work [26] is mainly due to the increase in molecule lifetime from 60 μs up to 100(20) s, which was possible by using lattice light of 1064 instead of 532 nm. The lifetime is now proportional to the tunneling time in the lattice.

The efficiency of the STIRAP scheme without compensation beam is limited by the finite lifetime of the dark state. This lifetime is mainly the result of time-dependent light shifts induced by the free-bound laser on the binding energy of the ground-state molecule. We have identified the coupling to the atomic $^1S_0 - {}^3P_1$ transition as the main source of light shift, and we have shown how to cancel it with an auxiliary compensation beam, leading to an efficiency higher than 80 %. This efficiency is limited in equal parts by scattering from off-resonant light and finite dark-state lifetime. We have shown the effect of the time-independent inhomogeneous lattice light shifts on STIRAP. In further work these detrimental effects could be suppressed by using lattice beams with bigger waists, leading to larger molecular samples.

We thus demonstrated that, by use of STIRAP, we can optically associate atoms into molecules with an efficiency comparable to that obtained with magneto-association through a Feshbach resonance. This general technique can represent a valuable alternative for associating molecules containing non-magnetic atoms, and in particular for the creation of alkali — alkaline-earth dimers [40, 155, 156, 33]. Such dimers have been attracting great attention as they can allow fascinating quantum simulations, thanks to their permanent magnetic and electric dipole moments [32]. Finally, coherent, efficient and controlled creation of long-lived ultracold Sr_2 molecules in the ground state could be useful in metrology experiments, for instance as a probe for the time variation of the electron-to-proton mass ratio [13, 157].

Chapter 4

Observation of Bose-enhanced photoassociation products

Abstract

We produce $^{84}Sr_2$ molecules using Bose-enhanced Raman photoassociation. We apply the stimulated Raman adiabatic passage (STIRAP) technique on a Bose-Einstein condensate (BEC) to produce more than 8×10^3 ultracold molecules. This chemical reaction is only made possible because of the Bose enhancement of the optical transition dipole moment between the initial atomic state and an intermediate molecular state. We study the effect of Bose enhancement by measuring the transition Rabi frequency in a BEC and by comparing it with measurements for two atoms in sites of a Mott insulator. By breaking the dimers' bond and directly observing the separated atoms, we measure the molecular inelastic collision rate parameters. We discuss the possibility of applying Bose-enhanced STIRAP to convert a BEC of atoms into a BEC of molecules, and argue that the required efficiency for STIRAP is within experimental reach.

4.1 Introduction

The last decade has witnessed considerable progress in the study of chemical reactions at ultracold temperatures [85, 107, 135, 5, 158, 159]. While direct cooling and trapping of molecules is being developped [160, 161], so far ultracold chemistry relies on the formation of molecules from ultracold atoms. This process requires the existence of a coupling mechanism between a free-atom state and a bound molecular state. Feshbach resonances provide such coupling, and they have been exploited to produce

molecules starting from a variety of ultracold bosonic and fermionic atom gases [115, 162]. Moreover, Feshbach resonances have been used to convert a Bose-Einstein condensate (BEC) of atoms into a Bose-condensed gas of Feshbach molecules, a molecular BEC (mBEC) [163, 164]. However, suitable Feshbach resonances are only available in a limited number of systems, and they only allow the creation of molecules in high lying vibrational states, thus limiting experimental studies to a small class of chemical reactions. Another approach to the creation of a mBEC is Bose-enhanced stimulated Raman photoassociation (PA). This approach, which has been proposed in a number of theoretical works [165, 166, 167], involves the coupling by optical fields to an intermediate optically-excited molecular state. This technique requires the many-body Bose enhancement of the intrinsically weak coupling between the atomic state and the intermediate molecular state, and as such represents an example of *superchemistry*, i.e. "the coherent stimulation of chemical reactions via macroscopic occupation of a quantum state by a bosonic chemical species"[168]. The main limitation in this optical scheme are the losses caused by spontaneous emission from the intermediate state. Stimulated Raman adiabatic passage (STIRAP) has been proposed as a method to minimize these losses [168, 169, 170, 171, 172, 130].

Until now, no direct observation of molecules produced by Bose-enhanced stimulated Raman photoassociation has been reported. Molecule creation through stimulated Raman PA has been demonstrated via atom loss spectroscopy of a BEC, where the stimulated transition rate was much smaller than the molecular lifetime [173]. One-color PA of a BEC showing a non-classical association rate was reported in [174]. Notably, the work of [175] demonstrated reversible association by Rabi oscillations using a narrow one-color transition between atoms and molecules in a vibrational state born by an excited electronic potential. Moreover, the initial sample of [175] is a BEC, which is coupled to a mBEC. Due to the excited state of the molecule, the yet undetermined lifetime of such a mBEC is expected to be short, and likely shorter than typical ground-state molecule lifetimes. A STIRAP exploiting the Bose enhancement of the dipole moment of the free-bound transition between the atomic state and the intermediate molecular state, would be a two-photon process capable of producing a mBEC of ground-state molecules. As an important step, two-color PA using a BEC was reported in [96], showing the existence of atom-molecule dark states in a BEC, a necessary requirement for STIRAP.

In this paper, we report the optical production of ultracold ground-state $^{84}Sr_2$ molecules starting from a BEC of Sr atoms, via a STIRAP pulse sequence using optical transitions in the vicinity of a narrow intercombination line. This result requires the Bose enhancement of the free-bound transition Rabi frequency, which we investigate by comparing the free-bound Rabi frequency measured in this paper to that measured for two isolated atoms in a Mott insulator sample [176]. By disassociating the dimers

back into atoms, we directly observe that more than $8.1(0.7) \times 10^3$ Sr_2 molecules are produced. As a first study of the products of this chemical reaction, we measure the molecules inelastic collision rate parameters both with Sr_2 molecules and Sr atoms. Our experimental demonstration indicates that STIRAP from an atomic BEC into a BEC of ground-state molecules could be observed, provided the STIRAP has a higher transfer efficiency, for which we suggest several methods.

4.2 Experimental strategy

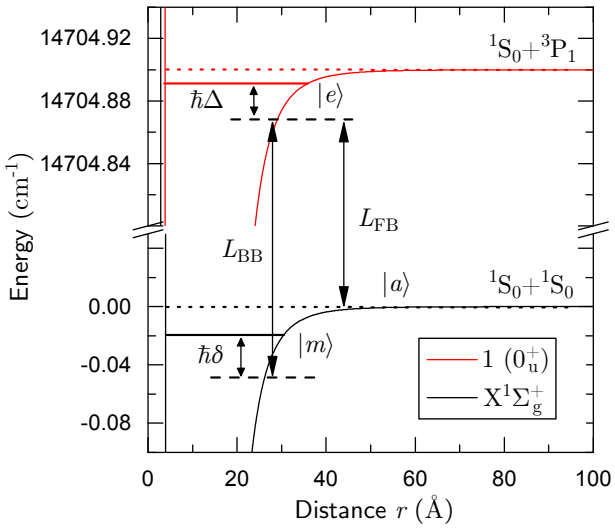

FIGURE 4.1: (color online) $^{84}Sr_2$ molecular potential for the electronic ground state $X^1\Sigma_g^+$ and the optically excited state $1(0_u^+)$. The energy is referenced to the ground-state asymptote. The laser fields $L_{\rm FB}$ and $L_{\rm BB}$ are given, along with the one- and two-photon detunings Δ and δ for the Λ scheme $\{|a\rangle, |e\rangle, |m\rangle\}$ used for STIRAP.

We apply a STIRAP sequence to convert Sr atoms in a BEC into molecules, using the Λ scheme that was adopted in our previous work [26]. Figure 4.1 shows the relevant potential energy curves of $^{84}Sr_2$ in the Born-Oppenheimer approximation. The initial sample is a BEC composed of atoms in the electronic ground-state $^1S_0$, and we label $|a\rangle$ the state associated with a pair of such atoms. The produced molecules populate the bound state $|m\rangle$, with binding energy $\Delta E_m = h \times 644.7372(2)$ MHz (with h being

the Planck constant), corresponding to the second to last vibrational state $\nu = -2$ of the potential $X^1\Sigma_g^+$, which asymptotically correlates to two Sr atoms in $^1S_0$. We couple these two states via a third state $|e\rangle$, a molecular bound state with binding energy $\Delta E_e = h \times 228.38(1)\,\mathrm{MHz}$, corresponding to the vibrational state $\nu = -3$ of the potential $1(0_u^+)$, which correlates to one atom in $^1S_0$ and one in the optically excited electronic state $^3P_1$. The states $|a\rangle$ and $|e\rangle$ are coupled with Rabi frequency Ω_{FB} by the free-bound laser L_{FB} and $|e\rangle$ is coupled to $|m\rangle$ with Rabi frequency Ω_{BB} by the bound-bound laser L_{BB}.

The STIRAP Λ scheme is coupled to the environment mainly through spontaneous emission from $|e\rangle$. The STIRAP sequence exploits the presence of a dark state, i.e. an eigenstate of the system orthogonal to $|e\rangle$, which can be adiabatically moved from $|a\rangle$ to $|m\rangle$ over the sequence time T, thus providing near-unit efficiency of atom-molecule conversion. The rotation of the dark state is controlled by the parameter $\Omega_{\mathrm{FB}}/\Omega_{\mathrm{BB}}$, which should be $\Omega_{\mathrm{FB}}/\Omega_{\mathrm{BB}} \ll 1$ at the initial time and $\Omega_{\mathrm{FB}}/\Omega_{\mathrm{BB}} \gg 1$ at time T. In a STIRAP sequence, the parameter $\Omega_{\mathrm{FB}}/\Omega_{\mathrm{BB}}$ is tuned by the temporal intensity profile of L_{FB} and L_{BB}.

In order to observe the molecules we produce, we disassociate them back into atoms. We first produce Sr_2 by a STIRAP sequence that induces the transfer $|a\rangle \rightarrow |m\rangle$. At the end of the STIRAP, we push away all remaining atoms by a pulse of light resonant with the $^1S_0 - {}^1P_1$ transition, therefore leaving only molecules in the trap. The molecules remain unaffected by this pulse, because their binding energy is much bigger than the transition linewidth $\Gamma_{^1P_1} \simeq 2\pi \times 30\,\mathrm{MHz}$. The reverse transfer $|m\rangle \rightarrow |a\rangle$ is obtained by the time-mirrored sequence of the laser beams intensity ramps used for STIRAP (see Fig. 4.2b). We image the atoms resulting from dissociated molecules by using absorption imaging on the $^1S_0 - {}^1P_1$ transition. Despite the time-symmetry of the laser intensity ramps, the dissociation sequence is not related to a STIRAP process. Indeed, if population transfer is mostly due to Bose-enhanced two-photon processes, the dissociation efficiency can be significantly lower than the association efficiency, and the enhancement depends on the population of state $|a\rangle$ surviving the push beam. We recover atoms by the dissociation sequence owing to both two-photon stimulated emission and spontaneous emission from $|e\rangle$. Therefore, the stated numbers of produced molecules are a conservative lower bound, which assumes an unrealistic 100 % dissociation efficiency.

We produce the initial BEC of ^{84}Sr as in [121]. The BEC contains typically $N \approx 3.0 \times 10^5$ atoms with a peak density of $n_{\mathrm{peak}} = 1.9(1) \times 10^{14}\,\mathrm{cm}^{-3}$. The trap frequencies are $\omega_x = 2\pi \times 34\,\mathrm{Hz}$, $\omega_y = 2\pi \times 22\,\mathrm{Hz}$ and $\omega_z = 2\pi \times 430\,\mathrm{Hz}$, where the z-axis is vertical. The Thomas-Fermi radii are $R_x = 20\,\mu\mathrm{m}$, $R_y = 31\,\mu\mathrm{m}$ and $R_z = 1.6\,\mu\mathrm{m}$, and the chemical potential is $\mu = 90(3)\,\mathrm{nK}$.

The beam containing both laser fields, L_{FB} and L_{BB}, used for PA is horizontal and

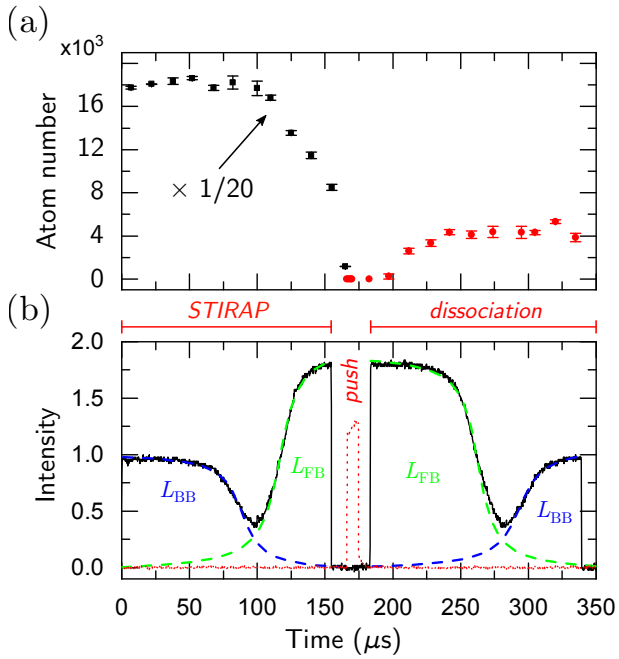

FIGURE 4.2: (color online) Typical time behaviour of the number of atoms, during a sequence composed of STIRAP ($|a\rangle \rightarrow |m\rangle$) — push pulse — dissociation ($|m\rangle \rightarrow |a\rangle$). (a) Atom number during the STIRAP (black squares) and dissociation (red circles). The atom number during STIRAP has been scaled by a factor 1/20 for clarity. The only atoms present after the dissociation transfer come from dissociated molecules. (b) Combined photoassociation laser intensities on the atomic sample (continuous black line). The dashed lines represent the contribution of L_{FB} and L_{BB}. The dotted red line gives the intensity of the push pulse between STIRAP and dissociation.

has a waist of 113(2) μm. The polarization is linear and parallel to a vertically oriented guiding magnetic field of 5.30(5) G and thus only π transitions can be addressed. This field splits the Zeeman levels of state $|e\rangle$ by $2\pi \times 1.65(1)$ MHz. Both L_{FB} and L_{BB} are derived from two injection-locked slave lasers seeded by the same master oscillator with a linewidth of less than $2\pi \times 3$ kHz. The frequencies of these laser fields are tuned by acousto-optical modulators and the beams are combined into a single-mode fiber

with the same polarization, so that the main difference on the atomic cloud are their intensity and frequency. This setup ensures good coherence between the two fields, whose beat note must match the Raman condition, i.e. the frequency difference must be equal to the binding energy of state $|m\rangle$.

4.3 Theory

The evolution of the population during the photoassociation sequence starting from a BEC is modelled by the set of equations [96, 169]

$$\begin{cases} i\,\dot{a} = -i\frac{\gamma_a}{2}\,a - \Omega_{\mathrm{FB}}\,a^*\,e\,, \\ i\,\dot{e} = -\frac{1}{2}(\Omega_{\mathrm{FB}}\,a^2 + \Omega_{\mathrm{BB}}\,m) + (\Delta - i\frac{\gamma_e}{2})e\,, \\ i\,\dot{m} = -\frac{1}{2}\Omega_{\mathrm{BB}}\,e + (\delta - i\frac{\gamma_m}{2})m\,, \end{cases} \tag{4.1}$$

where $a = a(t)$, $e = e(t)$ and $m = m(t)$ are the amplitudes corresponding respectively to the atomic condensate field, the excited molecular field and the ground-state molecular field in the semi-classical approximation. Losses are described by the parameters γ_a, γ_e and γ_m, which originate from the coupling of the three level system to the environment and which make the effective Hamiltonian non-Hermitian. In the absence of losses, the field amplitudes are normalized according to $|a|^2 + 2|e|^2 + 2|m|^2 = 1$. The free-bound Rabi frequency Ω_{FB} between the atomic field and the excited molecular field is given by $\Omega_{\mathrm{FB}} = d_{\mathrm{FB}}^{\mathrm{BEC}} \times E$, where E is the electric field amplitude and $d_{\mathrm{FB}}^{\mathrm{BEC}}$ is the Bose-enhanced transition dipole moment between the two fields. This quantity can be written as $d_{\mathrm{FB}}^{\mathrm{BEC}} = d_{\mathrm{FB}}^{\mathrm{Bare}} \times \sqrt{N}$, where $d_{\mathrm{FB}}^{\mathrm{Bare}}$ is the bare transition dipole moment calculated for a single atom pair of the condensate, and N is the number of atoms in the condensate [169]. Finally, the terms Δ and δ are respectively the one-photon and two-photon detunings shown in Fig. 4.1.

A criterion for a STIRAP transfer with near unit efficiency is to maintain the adiabaticity of the evolution of the dark state throughout the sequence. As discussed in [141, 176], this translates into the constraint $\alpha = \tilde{\gamma}T \gg 1$, with $\tilde{\gamma} = \Omega_{\mathrm{FB,BB}}^2/\gamma_e$. For realistic experimental conditions, the sequence time T is limited by the lifetimes of states $|a\rangle$ and $|m\rangle$, and the finite lifetime of the dark state. This puts a lower bound on the two Rabi frequencies $\Omega_{\mathrm{FB,BB}}$. A good choice of the pair of states $|e\rangle$ and $|m\rangle$ can ensure a suitably strong bound-bound Rabi frequency Ω_{BB}. On the contrary, the free-bound transition is intrinsically weak, due to the very small overlap between the wavefunction of a pair of atoms, whose characteristic length is determined by the trap, and the wavefunction of a single molecule, whose characteristic length is determined by the — much smaller — Condon point. Typically, for equal laser

intensity, the free-bound Rabi frequency is several orders of magnitude smaller than the bound-bound Rabi frequency, which would make STIRAP impossible for realistic experimental conditions. Since a BEC can contain on the order of 10^3 - 10^8 atoms [177], it has been predicted that the Bose-enhanced Ω_{FB} can lead to a near-unit STIRAP efficiency [169].

4.4 Bose-enhanced Rabi frequency

We experimentally determine the free-bound Rabi frequency Ω_{FB} for a BEC. This determination requires the knowledge of the natural linewidth of the excited state Γ_e, which we assume is in our case the only contribution to the losses described by γ_e, i.e. $\gamma_e = \Gamma_e$. In order to measure Γ_e, we shine L_{FB} on the BEC and record both the decay of the atom number over time and the spectral width of the loss signal. We make sure to use low intensities of the PA light in order to make light shifts irrelevant. In order to extract Γ_e from these data sets, we simplify our model by adiabatically eliminating the variable e from eq. (4.1), imposing $\dot{e} = 0$. The resulting equation for the atomic amplitude is $\dot{a} = -\frac{\Omega_{\mathrm{FB}}^2}{\Gamma_e}\, a^3$, which can be written in terms of the BEC atom number $\dot{N} = -K\, N^2$. We now first fit the data sets featuring the atom number decay with the function $N(t) = \frac{N_0}{1+KN_0t}$ and obtain $\frac{\Omega_{\mathrm{FB}}^2}{\Gamma_e} = \frac{KN_0}{2}$. Second, we fit the experimental spectral widths with the theoretical ones predicted by the model for a known value of $\Omega_{\mathrm{FB}}^2/\Gamma_e$, and thus obtain Γ_e. We derive the free-bound natural linewidth $\Gamma_e = 2\pi \times 19.2(2.4)\,\mathrm{kHz}$, which is consistent with measurements using a Mott insulator sample [176] and with values measured for $^{88}\mathrm{Sr}_2$ molecules [27]. The error in Γ_e is dominated by the error in the measured width in one-color PA spectra.

In order to determine Ω_{FB}, we next measure time-decay curves for a wide range of L_{FB} intensities, at the fixed density $n_{\mathrm{peak}} = 1.9 \times 10^{14}\,\mathrm{cm}^{-3}$ of the BEC. The experimental curve for Ω_{FB} as function of $\sqrt{I_{\mathrm{FB}}}$ presents deviations from linearity due to light shifts in the high power regime, and to inelastic processes at low Rabi frequencies and long pulse times. We derive a lower limit for the free-bound Rabi frequency of $\Omega_{\mathrm{FB}} = 2\pi \times 3.6(6)\,\mathrm{kHz}/\sqrt{\mathrm{W/cm^2}}$, from the experimental data sets corresponding to high L_{FB} intensities, where the effect of inelastic processes vanishes but the light shifts remain negligible.

In order to demonstrate the Bose enhancement of the dipole moment of the free-bound transition, we compare our measurement of Ω_{FB} with the one performed in a Mott insulator (MI) sample of doubly-occupied sites [176]. In Fig. 4.3 we show the free-bound Rabi frequency as a function of $\sqrt{\langle n \rangle}$, where $\langle \cdot \rangle$ represents the spatial average. For the measurement presented in this article, n is the density of the BEC calculated under the Thomas-Fermi approximation. For the measurements from [176],

n is the on-site density of a single atom. Moreover, the PA process is described by two different models in the case of a BEC (see eq. (4.1)) and in the case of a MI (see eq. (1) in [176]), so we need to be careful when comparing the free-bound Rabi frequencies. For this plot, we define Ω_{FB} by considering the atom decay rate W_a evaluated experimentally at the beginning of the PA pulse. As shown previously, in the BEC case the solution to the model is $\dot{a} = -\frac{\Omega_{\mathrm{FB}}^2}{\Gamma_e} a^3$, and therefore $W_a = -2\Omega_{\mathrm{FB}}^{\mathrm{BEC}\,2}/\Gamma_e$. In the MI case, the solution is $\dot{a} = -\frac{\Omega_{\mathrm{FB}}^2}{2\Gamma_e} a$, which gives the rate $W_a = -\Omega_{\mathrm{FB}}^{\mathrm{MI}\,2}/\Gamma_e$. This difference is a consequence of the different normalization used in the two models. In Fig. 4.3, we plot $\Omega_{\mathrm{FB}} = \sqrt{2}\Omega_{\mathrm{FB}}^{\mathrm{BEC}}$ for the BEC case (empty square).

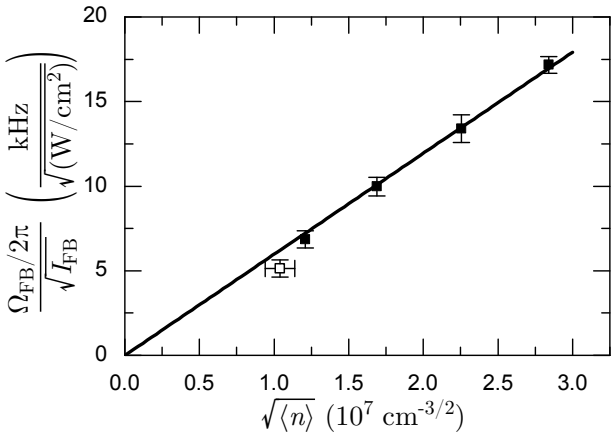

FIGURE 4.3: Free-bound Rabi frequency as a function of $\sqrt{\langle n\rangle}$, where $\langle n\rangle$ is the spatially averaged atomic density, measured in a BEC (empty square) and in a MI (filled squares). The line is a fit of the form $\Omega_{\mathrm{FB}} = c_1\sqrt{\langle n\rangle}$ to all data points.

To explain why our data demonstrates Bose enhancement, we first consider the BEC case and the MI case as two separate problems. We call n_{BEC} the BEC density and we call n_{MI} the on-site density in the MI. As discussed in detail in [176], the free-bound Rabi frequency for two atoms in a lattice site of the MI is $\Omega_{\mathrm{FB}}^{\mathrm{MI}} = c\sqrt{\langle n_{\mathrm{MI}}\rangle}$, where c is a constant that depends on the chosen free-bound PA line but not on the atomic density. We assume that this relation can be applied to the case of two atoms in a BEC, provided that we use $n_{\mathrm{MI}} = n_{\mathrm{BEC}}/N$, where N is the BEC atom number. The Rabi frequency for two atoms, i.e. the bare Rabi frequency, is then given by $\Omega_{\mathrm{FB}}^{\mathrm{Bare}} = c\sqrt{\langle n_{\mathrm{BEC}}/N\rangle}$, which, for our experimental conditions, is roughly three orders of magnitude smaller than $\Omega_{\mathrm{FB}}^{\mathrm{MI}}$. However in presence of Bose enhancement, which

features pair-wise constructive interference of the transition dipole moments, the bare Rabi frequency is multiplied by $\sqrt{N}$, and thus $\Omega_{\mathrm{FB}}^{\mathrm{BEC}} = \sqrt{N}\,\Omega_{\mathrm{FB}}^{\mathrm{Bare}} = c\sqrt{\langle n_{\mathrm{BEC}}\rangle}$. As a consequence, we fit the BEC data together with the MI data, using a function with the form $\Omega_{\mathrm{FB}} = c_1\sqrt{\langle n\rangle}$. The fitted function is shown in Fig. 4.3. The fit is successful, which demonstrates the Bose enhancement in the BEC case, and we derive $\Omega_{\mathrm{FB}} = 2\pi \times 5.9(2)\,10^{-7}\,\mathrm{kHz\,cm^{3/2}}/\sqrt{\mathrm{W/cm^2}}$.

4.5 STIRAP parameters

Before producing molecules by STIRAP, we first measure the other parameters relevant to the STIRAP transfer efficiency, which are necessary inputs to solve the model of eq. (4.1) numerically. The results of our measurements together with the theoretical estimates of these parameters are compiled in Tab. 4.1.

TABLE 4.1: Parameters of the chosen Λ scheme used for molecule creation from a BEC, measured experimentally and estimated theoretically. Symbols are defined in the text and illustrated in Fig. 4.1. The theoretical values of Ω_{FB} and Ω_{BB} are obtained by using mapped grid methods [178] and the WKB approximation with the potentials given in [179, 180].

Param.	Units	Experiment	Theory
Ω_{FB}	$\mathrm{kHz\,cm^{3/2}}/\sqrt{\mathrm{W/cm^2}}$	$2\pi \times 5.9(2)\,10^{-7}$	$2\pi \times 3.5\,10^{-7}$
Ω_{BB}	$\frac{\mathrm{kHz}}{\sqrt{\mathrm{W/cm^2}}}$	$2\pi \times 234(5)$	$2\pi \times 660$
Γ_e	kHz	$2\pi \times 19.2(2.4)$	$> 2\pi \times 14.8$
Δ_{FB}	$\frac{\mathrm{kHz}}{\mathrm{W/cm^2}}$	$+2\pi \times 21(1)$	$+2\pi \times 20.0$
δ_{FB}	$\frac{\mathrm{kHz}}{\mathrm{W/cm^2}}$	$+2\pi \times 17.0(2)$	$+2\pi \times 20.0$
Δ_{DT}	$\frac{\mathrm{kHz}}{\mathrm{W/cm^2}}$	$+2\pi \times 2.61(8)$	-
τ_{Dark}	ms	2.6(3)	-

The bound-bound Rabi frequency Ω_{BB} can be directly measured through loss spectroscopy, by probing the Autler-Townes splitting induced by Ω_{BB} with the free-bound laser L_{FB} [89]. We measure $\Omega_{\mathrm{BB}} = 2\pi \times 234(5)\,\mathrm{kHz}/\sqrt{\mathrm{W/cm^2}}$, where the measurement error is the standard deviation resulting from the fit.

In our approach, both the one-photon detuning Δ and the two-photon detuning δ depend on light shifts induced on the states of our Λ scheme. The free-bound laser

L_{FB}, whose intensity varies during STIRAP, induces a time- and space-dependent shift Δ_{FB} on the free-bound transition. It also induces a time- and space-dependent shift δ_{FB} on the binding energy of state $|m\rangle$. The light shifts from the weak L_{BB} laser are always negligible. We measure Δ_{FB} and δ_{FB} by performing one- and two-color spectroscopy for several intensities of L_{FB}, and obtain $\Delta_{\mathrm{FB}} = 2\pi \times 21(1)\,\mathrm{kHz}/\sqrt{\mathrm{W/cm^2}}$ and $\delta_{\mathrm{FB}} = 2\pi \times 17.0(2)\,\mathrm{kHz}/\sqrt{\mathrm{W/cm^2}}$. Both shifts are dominated by the shifts of state $|a\rangle$ induced by the off-resonant transition $^1\mathrm{S}_0 - {}^3\mathrm{P}_1$ ($m_J = 0$), as discussed in [176]. More precisely $\Delta_{\mathrm{FB}} \approx \delta_{\mathrm{FB}} \approx \hbar\Omega_{\mathrm{FF}}^2/2\Delta E_e$, where $\hbar$ is the reduced Planck constant and Ω_{FF} is the Rabi frequency induced on the atomic transition $^1\mathrm{S}_0 - {}^3\mathrm{P}_1$ by L_{FB}.

The DT induces space-dependent but time-independent light shifts Δ_{DT} and δ_{DT}, respectively on the free-bound transition and on the binding energy of state $|m\rangle$. We measure $\Delta_{\mathrm{DT}} = 2\pi \times 2.61(8)\,\mathrm{Hz}/(\mathrm{W/cm^2})$, while δ_{DT} is here negligible [176]. These time-independent shifts are compensated for by adapting the frequencies of the PA lasers. The remaining inhomogeneous energy spread originating from the finite size of the sample and the spatial profile of the trapping potential is too small to influence the STIRAP transfer efficiency and can be neglected. On the contrary, the time-dependent shifts Δ_{FB} and δ_{FB} are not compensated for at all times, and can limit the efficiency.

The lifetime of the dark-state superposition τ_{Dark} engineered during a STIRAP must be longer than the STIRAP sequence time in order to achieve a high transfer efficiency. We measure this lifetime by shining both L_{FB} and L_{BB} on the BEC, with $\Delta = \delta = 0$, and with $\Omega_{\mathrm{FB}} = 2\pi \times 3.5\,\mathrm{kHz}$ and $\Omega_{\mathrm{BB}} = 2\pi \times 10\,\mathrm{kHz}$. These Rabi frequencies are chosen in order for the dark state to have a significant overlap with the initial atomic state. We observe a first fast exponential decay of the atom number and a second slower one, with $1/e$ time constants of $100(20)\,\mu\mathrm{s}$ and $2.6(3)\,\mathrm{ms}$ respectively. The former time constant corresponds to scattering on the free-bound line, while the latter corresponds to the lifetime τ_{Dark}. Possible causes of this finite lifetime are the space dependent mean-field shift and multimode effects in the BEC[170, 181]. The former induces an average $\delta = 2\pi \times 0.37(5)\,\mathrm{kHz}$, giving a dephasing time of $2.7(4)\,\mathrm{ms}$.

As shown in measurements presented in the following paragraphs, the molecule lifetime is long compared to the STIRAP pulse duration, so we can neglect the effect of γ_m. Finally, the atomic loss term γ_a is dominated by off-resonant scattering on the atomic $^1\mathrm{S}_0 - {}^3\mathrm{P}_1$ line and can also be neglected.

4.6 Molecule production

We now apply STIRAP to a BEC and study its effects. We optimize the $|a\rangle \rightarrow |m\rangle$ transfer efficiency by varying the parameters Ω_{FB}, Ω_{BB}, T_{pulse} and n_{peak} while aiming for the maximum atom number after a STIRAP sequence followed by the push pulse and the dissociation transfer $|m\rangle \rightarrow |a\rangle$, see Fig. 4.2. We obtain the best efficiency for $\Omega_{\mathrm{FB}} = 2\pi \times 6.0(4)\,\mathrm{kHz}$, $\Omega_{\mathrm{BB}} = 2\pi \times 610(10)\,\mathrm{kHz}$, $T_{\mathrm{pulse}} = 150\,\mu\mathrm{s}$, and $n_{\mathrm{peak}} = 0.44(2) \times 10^{14}\,\mathrm{cm}^{-3}$. For this optimization, we also vary the frequencies of $L_{\mathrm{FB,BB}}$, but we keep them constant during the whole STIRAP+dissociation sequence. The maximum number of atoms having successfully undergone the $|a\rangle \rightarrow |m\rangle$ then $|m\rangle \rightarrow |a\rangle$ sequence is $16.2(1.4) \times 10^3$. Assuming a hypothetical 100 % efficiency for the $|m\rangle \rightarrow |a\rangle$ transfer, we derive a lower limit for the number of molecules produced of $N_{\mathrm{mol,MIN}} = 8.1(0.7) \times 10^3$. Under this assumption, the lower limit for the STIRAP efficiency is $\eta_{\mathrm{MIN}} = 5.1(6)\,\%$, which is orders of magnitude higher than the minute $3.1(8) \times 10^{-7}\,\%$ efficiency that is expected without Bose-enhancement of Ω_{FB}. For this reason, the non-zero number of atoms having successfully undergone the $|a\rangle \rightarrow |m\rangle$ then $|m\rangle \rightarrow |a\rangle$ sequence is proof of the Bose enhancement of the free-bound transition dipole moment. For the experimentally optimized parameters, our numerical model using eq. (4.1) predicts an efficiency of $\eta \simeq 9(2)\,\%$ for STIRAP, which gives $N_{\mathrm{mol}} = 14.4(3.5) \times 10^3$ molecules produced and a dissociation efficiency of 55(20) %. The error bars for this number comes from our measurements of all the relevant STIRAP parameters.

We measure the lifetime of the molecules we produced, which originates from inelastic collisions between two molecules or between a molecule and a Sr atom. We measure the molecular lifetime both in a pure Sr_2 sample and in a mixture $Sr_2 + Sr$, depending on when the push pulse is applied. The number of molecules as a function of the hold time is shown for both cases in Fig. 4.4, together with exponential fits. Assuming the STIRAP efficiency provided by our theoretical model, we measure a $1/e$ time $\tau_{\mathrm{Sr}_2} = 2.7(9)\,\mathrm{ms}$ for a pure Sr_2 sample containing $5(1) \times 10^3$ molecules, and $\tau_{\mathrm{Sr+Sr}_2} = 0.54(3)\,\mathrm{ms}$ for a mixture of $\simeq 170 \times 10^3$ Sr atoms and $4.5(8) \times 10^3$ molecules. From these lifetimes we can extract collision rate parameters considering losses that arise only from two-body inelastic collisions, when molecules are changing vibrational level and gaining enough kinetic energy to leave the trap [182]. Since the decay time is fast compared to the trapping frequencies, we assume the spatial distribution of Sr atoms to be the same as the one before STIRAP, and the Sr_2 distribution to coincide with the one describing the center of mass of an atom pair before STIRAP. We first fit the decay curve of the pure molecular sample and retrieve a two-body molecular collision rate parameter $K_{mm} = 3.4^{+2.3}_{-1.2} \times 10^{-10}\,\mathrm{cm}^3/\mathrm{s}$. We then fix this parameter and fit the molecule number decay in the mixture of both atoms and molecules. Neglecting

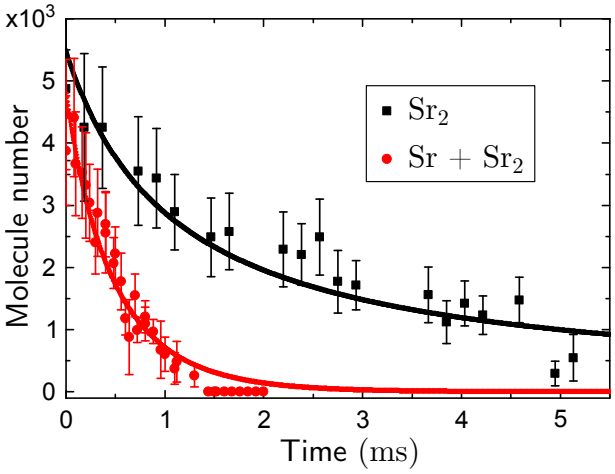

FIGURE 4.4: (color online) Decay of the number of Sr_2 molecules as a function of hold time, both in a pure sample of molecules (black squares) and in a mixture of atoms and molecules (red circles). The curves are the solutions to the collision rate equations using the fitted rate parameters.

the small variation of the atom number during the experiment time, we retrieve the atom/molecule two-body collision rate parameter $K_{ma} = 8.7^{+5.3}_{-3.5} \times 10^{-11}\,\mathrm{cm}^3/\mathrm{s}$. The stated uncertainties arise both from the statistical variation on the retrieved atoms number and from the measured uncertainties on the parameters presented in Tab. 4.1.

We can compare our measurements with the universal rate parameters for low-energy s-wave inelastic collisions given in [182, 183]. This model assumes unit probability of reaction at short range, and infers a universal collision rate parameter $K^{\mathrm{ls}} = 2g(h/\mu)\bar{a}$, where g is either 1 or 2 for distinguishable or indistinguishable particles, respectively. $\bar{a}$ is the van der Waals length, which for asymptotic dispersion potentials of the form $-C_6/r^6$ is $\bar{a} = 0.47799 \times (2\mu C_6/\hbar^2)^{1/4}$. The C_6 parameter is here the effective C_6 derived from the atomic coefficient C_6^a, i.e. $C_6 = 4C_6^a$ and $C_6 = 2C_6^a$ for molecule-molecule and molecule-atom collisions, respectively. For Sr this model predicts $K_{ma} = 6.8 \times 10^{-11}\,\mathrm{cm}^3/\mathrm{s}$ and $K_{mm} = 6.0 \times 10^{-11}\,\mathrm{cm}^3/\mathrm{s}$. The former value is consistent with our measurement, while the latter is roughly a factor of 5 smaller that the measured one. This could be due to an underestimation of the molecular density in our sample, or a departure from universality [182].

4.7 STIRAP limitations

We now analyse the STIRAP efficiency using the theory discussed in [170, 176]. Since our system fulfills $\Omega_{\mathrm{FB}} < \gamma_e$, we operate in a regime of strong dissipation. The three relevant parameters in the problem are then $\alpha = \tilde{\gamma}T$, $A = \delta/\tilde{\gamma}$, and T, where $\tilde{\gamma} = \Omega_{\mathrm{FB,BB}}^2/\gamma_e \approx \Omega_{\mathrm{FB}}^2/\Gamma_e$. We consider the light shift δ_{FB} induced by L_{FB} on the binding energy of state $|m\rangle$ as the only contribution to the two-photon detuning δ, therefore neglecting the time-dependent mean field shifts addressed in [170], which thus leads to $A \approx \delta_{\mathrm{FB}}/\tilde{\gamma}$. Indeed the optimized parameters for STIRAP lead to a shift $\delta_{\mathrm{FB}} = 2\pi\times 135\,\mathrm{kHz}$, which is much bigger than the mean-field shift of about $2\pi\times 1\,\mathrm{kHz}$, thus justifying this approximation. An efficient STIRAP requires $\alpha \gg \pi^2$, which ensures the adiabaticity of the transfer, $|A| \ll 1$, which ensures a long lifetime of the dark-state superposition, and $T \ll \tau_{\mathrm{Sr+Sr_2}}$, which ensures small losses from state $|m\rangle$. As discussed in detail in [176], the parameter A depends only on molecular physics and is here given by $|A| \approx |\delta_{\mathrm{FB}}|/\tilde{\gamma} \approx (\hbar\Omega_{\mathrm{FF}}^2/2\Delta E_e)\,\gamma_e/\Omega_{\mathrm{FB}}^2 = (\Omega_{\mathrm{FF}}/\Omega_{\mathrm{FB}})^2\,\hbar\gamma_e/2\Delta E_e = 1/(G^2\,N\,\mathrm{FCF}_{\mathrm{FB}}^2)\,\hbar\gamma_e/2\Delta E_e$, where N is the BEC atom number, and $\mathrm{FCF}_{\mathrm{FB}}$ and $G = 1/\sqrt{3}$ are respectively the Franck-Condon factor and the geometric factor of the free-bound transition [184]. From our measurements we derive $|A| \approx 18 \gg 1$ and $\alpha \simeq 4 < \pi^2$. We think the experimental constraint on α is imposed by the strong losses induced by the high $|A|$, which prevent a near-unit efficiency STIRAP. We conclude that the main limitation to the STIRAP efficiency in our system is the short lifetime of the dark state, due to the time-dependent light shift δ_{FB}.

One way to significantly increase the dark-state lifetime is to compensate δ_{FB} at all times during the STIRAP sequence. This has been achieved for our Λ scheme in the case of STIRAP on Sr atoms in a Mott insulator [176], allowing for a transfer efficiency higher than 80 %. By numerical simulation of eq. (4.1), we find that adapting this compensation technique to our case will allow us to reach an efficiency of 40 %. The remaining limitation will then be the short molecular lifetime, which will put an upper bound on the parameter α. However, since $\alpha \propto \mathrm{FCF}_{\mathrm{FB}}^2$, the STIRAP efficiency can be further increased by choosing a Λ scheme with a stronger free-bound transition, i.e. with a bigger Franck-Condon factor, if available. A STIRAP with near-unit efficiency applied on a BEC would ensure the coherent optical production of a molecular BEC [163, 164, 175]. In particular, the short molecular lifetime, which might prevent the sample from reaching thermal equilibrium, could be circumvented by a second STIRAP towards the potentially much more stable rovibrational groundstate [21, 124].

4.8 Conclusion and outlook

In conclusion, we have demonstrated the bosonic enhancement of the free-bound transition dipole moment in a Sr BEC and we have exploited it to coherently produce ultracold Sr_2 ground-state molecules using a STIRAP pulse sequence. We derive a STIRAP efficiency of 9(2) % and find it to be strongly limited by the finite lifetime of the dark-state superposition. However, we calculate that by optically compensating the time-dependent light shifts, as demonstrated in [176], an efficiency of 40 % should be achievable. Further increase in the efficiency is possible if stronger free-bound lines or faster transfer schemes are used [185]. We directly observe the products of this *superchemistry* reaction [168] and measure their inelastic collision rate parameters. Inelastic collisions result in lifetimes short but sufficient to allow a second STIRAP toward potentially more stable rovibrational ground-state molecules [21, 124]. Provided higher transfer efficiencies and longer lifetimes, it might be possible to produce a molecular sample that would be stable enough to reach thermal equilibrium and would feature a mBEC.

Chapter 5

1-color spectroscopy in ultracold Rb-Sr mixtures

5.1 Introduction

In this chapter we describe our high-resolution 1-color photoassociation (PA) spectroscopy in ultracold Rb-Sr mixtures. In section 5.2 we will give an overview of this type of spectroscopy and the overall experimental strategy. In section 5.3 we will describe our experiment in detail, including the atomic sample and laser setup in 5.3.1, our experimental methods for spectroscopy searches and line characterization in 5.3.2, and our analysis and results in 5.3.3. Finally, in section 5.4, we will explain the relationship between our results and possible Stimulated-Raman-Adiabatic-Passage (STIRAP) implementations to create weakly-bound ground-state RbSr molecules.

5.2 Overview of 1-color spectroscopy

We use 1-color spectroscopy to observe and characterize the weakly-bound spectrum of the optically excited states correlating to the Rb($^2S_{1/2}$)+Sr($^3P_1$) asymptote, see Fig. 5.1. By shining a laser beam L_{FB}, red-detuned to the atomic transition, on the atomic cloud, we induce an optical coupling between the initial atom-pair state and excited molecular levels. By scanning the frequency of L_{FB}, the coupling can be made resonant and cause population transfer from the initial state to a specific excited rovibrational level, producing RbSr* molecules. These molecules spontaneously decay to lower lying states, and depending on their dynamics, either remain trapped or escape the trap. Both these cases result in atom loss revealed by standard absorption imaging. In order to increase the excitation rate, samples with high interspecies density

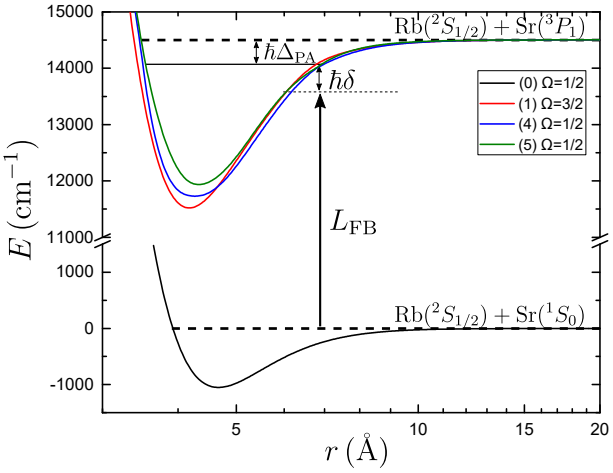

FIGURE 5.1: Born-Oppenheimer potential energy curves of RbSr as function of the internuclear distance. The potentials correlating to the $\mathrm{Rb}(^2S_{1/2})$+$\mathrm{Sr}(^1S_0)$ and $\mathrm{Rb}(^2S_{1/2})$+$\mathrm{Sr}(^3P_1)$ atomic threshold are shown in Hund case (c) representation. The curves are taken from [186].

are typically used for PA spectroscopy. Measuring the atom number in dependence of the L_{FB} frequency shows these PA loss features, corresponding to PA transitions (lines).

The experimental sequence for PA spectroscopy consists in the preparation of the ultracold Rb-Sr mixture with final excitation via L_{FB} and imaging, which differs from double MOT experiments, where the PA features are observed as a decrease of steady-state fluorescence as the frequency of L_{FB} is continuously swept, see [187]. Although this makes spectroscopy searches more time consuming, it benefits the precision and accuracy of our measurements in two ways. Firstly, it reduces Doppler broadening and shifts significantly, and secondly it allows for probing the optical transition for well-defined atomic internal states. Moreover, this experimental strategy provides higher atomic interspecies densities, which helps detecting weak transitions. In practice a μK mixture of unpolarized Rb together with a single Sr isotope is prepared in an optical dipole trap and illuminated by L_{FB} for PA. For detection, the cloud is released from the trap, the Rb Zeeman states are separated by a Stern-Gerlach field gradient, and finally the number of Rb and Sr atoms is measured via absorption imaging. The Rb atom numbers are normalized to their sum, resulting in the m_f^{Rb}-populations. The normalized m_f^{Rb} population will decrease if that m_f^{Rb} state is lost, but increase if any of the other states are lost because of the normalization to the sum of atoms in all m_f^{Rb} states. In the presence of a magnetic field PA transitions originating from neighboring m_f^{Rb} states occur at close magnetic fields. Therefore we often observe that the m_f^{Rb} population increases above the background level at a magnetic field slightly above or below the field at which the m_f^{Rb} population decreases. We call the corresponding signature of a PA transition a PA signal. We use PA signals for the detection of PA transitions because the m_f^{Rb}-populations have higher signal-to-noise ratio and stability compared to raw atom numbers. This is particularly useful for weak transitions and long spectroscopy searches.

In our PA experiments Rb plays the role of an impurity in a thermal bath of Sr atoms and a PA signal is directly associated with a RbSr* molecular PA line. This is so because the frequency of L_{FB} is far detuned from any Rb atomic transition and cannot influence Rb m_f^{Rb}-populations. The strategy for optimizing the PA signal has as goal to increase the ratio of atoms lost by PA compared to atoms lost by all other processes, e.g. three-body decay. The atomic sample is optimized by maximizing the phase-space density of both Rb, for good precision in m_f-resolved absorption imaging, and of Sr, for a large number of PA events. This results in the sample conditions given in Sec. 5.3.1. Laser excitation is optimized by maximizing the probability of PA events, which requires long L_{FB} pulse duration, high L_{FB} intensity, and selection of the L_{FB} polarization and magnetic field orientation to optimally drive the transition

of interest. Finally the presence of a homogeneous B-field on the atomic cloud of a few Gauss is necessary in order to enhance the PA signal. Without this field PA transitions for different Rb Zeeman substates are degenerate and loss features overlap, yielding constant Rb m_f^{Rb}-populations.

5.3 Experiment

In this section we describe our experimental setup, including atomic sample parameters and laser setup, we explain our experimental methods for PA spectroscopy searches and PA line characterization, and finally we show our analysis and results.

5.3.1 Experimental setup

Atomic sample

We prepare the ultracold mixture of the relevant isotopic combination of Sr and Rb as explained in previous works [33, 188, 189]. We store this mixture in a crossed-beam dipole trap formed by one 1064-nm (or 1070-nm) vertical beam with a waist of 78(2) μm (or 90(5) μm), and one 1064-nm horizontal elliptical beam with a vertical waist of 19(1) μm and a horizontal waist of 313(16) μm [1]. We prepare ^{87}Rb in its hyperfine ground state ($^2S_{1/2}, f^{\mathrm{Rb}} = 1$), with almost equal population of the Zeeman sub-states $m_f^{\mathrm{Rb}} = 0, \pm 1$, where f^{Rb} and m_f^{Rb} are the total angular momentum of Rb and its projection on the quantization axis, respectively. Bosonic Sr isotopes ^{84,86,88}Sr have zero nuclear magnetic moment leading to a structureless $^1S_0$ ground state. Fermionic ^{87}Sr has non-zero nuclear magnetic moment $i^{\mathrm{Sr}} = 9/2$ and is prepared in the stretched state $m_i^{\mathrm{Sr}} = 9/2$ or $m_i^{\mathrm{Sr}} = -9/2$ via optical pumping, where m_i^{Sr} is the projection of the nuclear magnetic moment on the quantization axis.

The atomic samples used to study bosonic isotopologues, i.e. ^{87}Rb $-^{84,86,88}$ Sr, have a temperature of 1.0(1) μK, density-averaged densities in the range $0.3 - 4 \times 10^{12}\,\mathrm{cm}^{-3}$ for Sr and $2 - 7 \times 10^{12}\,\mathrm{cm}^{-3}$ for Rb (including all m_f^{Rb} substates), and the trap frequencies $\{\omega_x, \omega_y, \omega_z\}$ are $2\pi \times \{66(6), 57(6), 560(50)\}$ Hz for Sr and $2\pi \times \{110(10), 95(9), 950(80)\}$ Hz for Rb [2], where z is vertical. The samples used to study the fermionic isotopologue, i.e. ^{87}Rb-^{87}Sr, have a temperature of 1.5(1) μK, density-averaged densities in the range $2 - 6 \times 10^{11}\,\mathrm{cm}^{-3}$ for Sr and $0.8 - 3 \times 10^{12}\,\mathrm{cm}^{-3}$ for Rb (including all m_f^{Rb} substates), and trapping frequencies in the range $\{\omega_x, \omega_y, \omega_z\} =$

[1] We add a 532-nm beam with horizontal (vertical) waist of 19(1) μm (219(4) μm) to increase the trap depth when studying ^{87}Sr, in order to capture more Sr atoms.

[2] The error bars on the trapping frequencies are dominated by the uncertainty on the waists previously stated.

$2\pi\times\{70-82,\ 57-72,\ 587-637\}$ Hz for Sr and $2\pi\times\{108-132,\ 97-123,\ 823-925\}$ Hz for Rb.

PA laser setup

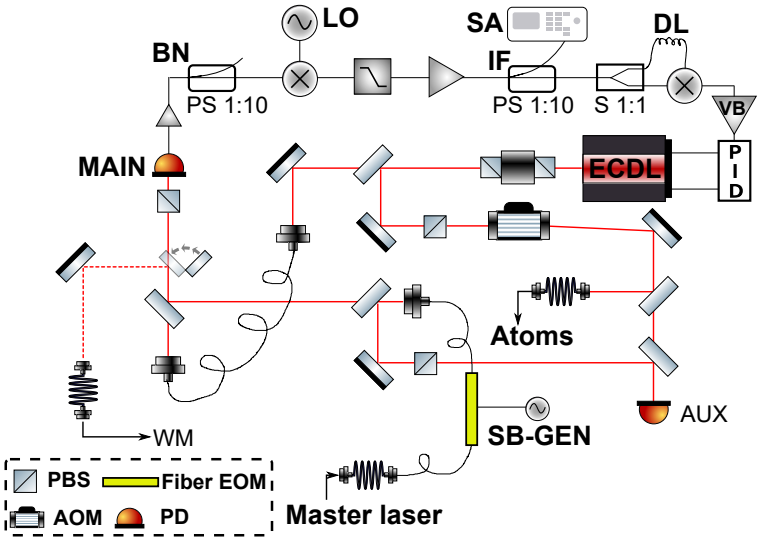

FIGURE 5.2: Schematic of the PA laser setup as explained in the text. The beat note (BN) between the PA laser and a sideband (SB) of the reference master laser, generated by a SB frequency generator (SB-GEN), is recorded by the main PD. The intermediate frequency (IF) output, resulting from the down-mixing of the BN with the local oscillator (LO), is continuously monitored via a spectrum analyzer (SA). A delay line (DL) of ~ 30 m is used for the generation of the error signal, which is sent through a voltage buffer (VB) to the PID. The PID controls the injection current of the laser diode and the voltage of the piezoelectric transducer in the ECDL. Waveplates and lenses are not shown.

L_{FB} is oriented horizontally at a $\sim 30°$ angle from the axis of the horizontal dipole trap and has a waist of $110(10)\,\mu$m. L_{FB} is derived from the master oscillator that provides light for the magneto-optical-trap operating on the $^1\mathrm{S}_0 \rightarrow {}^3\mathrm{P}_1$ intercombination

transition at 689 nm and has a linewidth smaller than 3.0 kHz [3].

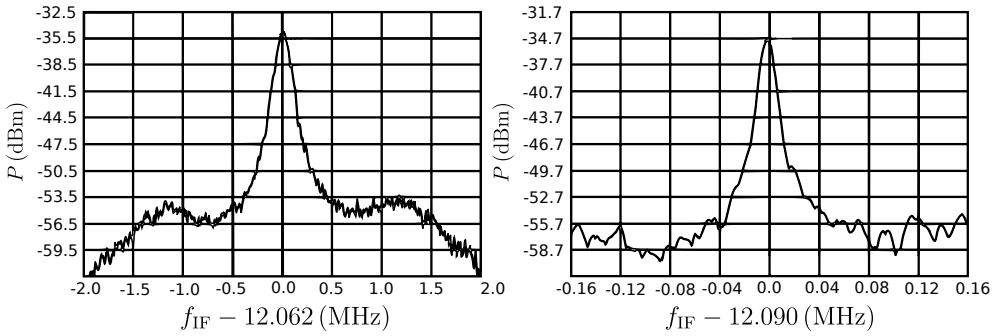

FIGURE 5.3: Power spectra of the IF, see Fig. 5.2. (a) Average spectrum over 20 sweeps for a resolution bandwidth of 100 kHz and sweep time of 20 ms without short-term stabilization. (b) Average spectrum over 20 sweeps for a resolution bandwidth of 10 kHz and sweep time of 66 ms with short-term stabilization.

The extensive spectroscopic searches were performed with the use of a separate ECDL, a Toptica DL PRO 100, stabilized on the light produced by the 689 nm master-oscillator. Since the full-width-at-half-maximum (FWHM) linewidth of this laser exceeds 200 kHz, we need both long-term and short-term stabilization for PA spectroscopy. We obtain both by use of an optimized version of a standard offset-locking technique [190]. The optical setup together with the electronics is depicted in Fig. 5.2. Since we require a scan range of order $10 - 20$ GHz able to cover the last 4-5 bound states of all isotopologues, the standard technique would force the use of an expensive photodiode (PD) operating in that frequency range to record the beat note (BN) between the reference light and L_{FB}. To reduce the required bandwidth of the PD we stabilize L_{FB} onto sidebands (SBs) derived from the reference light via a high-bandwidth fiber-coupled electro-optic modulator (EOM)[4]. Moreover, we optimized the offset-locking technique [190] to obtain the linewidth reduction needed in this work. The error signal, generated by the phase detector in Fig. 5.2, is proportional

[3] In initial spectroscopic searches L_{FB}, with a waist of $60(1)\,\mu$m, was produced via injection-lock of a slave laser onto the master oscillator light shifted by acusto-optical modulators (AOMs). This setup proved to be impractical, since it requires a cascade of AOMs to span the relevant vibrational splittings and isotope shifts, and it makes debugging of the experimental sequence, based on a reference spectroscopic line, non-trivial.

[4] The model PM-0K5-10-PFU-PFU-630 from EOSPACE was used. It is a 10 GHz bandwidth, fiber-coupled EOM based on lithium-niobate integrated optics technology.

to $\cos(\phi)$, with $\phi = 2\pi \times f_{\mathrm{IF}} \times L \times v^{-1}$, where $f_{\mathrm{IF}} = f_{\mathrm{BN}} - f_{\mathrm{LO}}$ is the intermediate frequency (IF) between the BN and the local oscillator (LO), L is the length of the delay line (DL) and v is the phase velocity of electromagnetic field in the coaxial cable constituting the DL [5], see [190]. The sensitivity of the error signal on the frequency of the PA laser is determined by the cable length L. By use of $\sim 30\,\mathrm{m}$ DL, we are able to produce an error signal with sufficient frequency sensitivity to feed a proportional-integral-derivative controller (PID controller; Toptica FALC 110) narrowing the laser FWHM linewidth to $\sim 20\,\mathrm{kHz}$, see Fig. 5.3. The SB frequency sent to the EOM is manually varied with large steps, while the finer scan of the LO is automated. The quality of the lock is continuously monitored with a spectrum analyzer (SA) via the IF, which is fixed during the scan, and is determined by the selected zero-crossing of the error signal $\propto \cos(\phi)$. The intensity of L_{FB} is finally controlled by an AOM. The beat-locked PA laser produces L_{FB} with absolute frequency $f_{\mathrm{FB}} = f_{\mathrm{Ref}} \pm n \times f_{\mathrm{SB}} \pm f_{\mathrm{LO}} \pm f_{\mathrm{AOM}} + f_{\mathrm{IF}}$, where f_{Ref} is the frequency of the reference laser, $n \times f_{\mathrm{SB}}$ is the frequency of the EOM sideband, f_{AOM} is the AOM frequency. The PA laser can be locked to obtain the desired sign of the different contributions, except for f_{IF}, whose sign is fixed by the PID polarity.

5.3.2 Experimental methods

We now describe the experimental methods used for our PA spectroscopy searches and subsequent characterization of specific 1-color PA lines.

Spectroscopy search

We first perform a low resolution scan to identify all 1-color PA lines to be later characterized. For each isotopologue we scan from slightly above the atomic threshold, i.e. a detuning $\Delta \simeq -10\,\mathrm{MHz}$, down to several GHz. Power ($10^{-3} - 10\,\mathrm{mW}$) and pulse time ($0.3 - 4\,\mathrm{s}$) of L_{FB} are set to provide a $70 - 90\%$ loss in Sr atom number. This loss level is not reachable for $\Delta > 3\,\mathrm{GHz}$, in which case we simply set the power to its maximum value. Correspondingly, we set the pulse time to a few seconds for ^{87}Rb-$^{84,\,86,\,88}$Sr, where inelastic losses are negligible, and to $0.4\,\mathrm{s}$ for ^{87}Rb-^{87}Sr, where inelastic losses are relatively strong. As explained in Sec. 5.2, we apply a homogeneous magnetic field B of a few Gauss to enhance the PA signal, see Fig. 5.4, in particular $B = 2.15\,\mathrm{G}$ for ^{87}Rb-^{84}Sr, $B = 4.61\,\mathrm{G}$ for ^{87}Rb-$^{86,\,88}$Sr, and $B = 2.15 - 2.73\,\mathrm{G}$ for ^{87}Rb-^{87}Sr. L_{FB} is parallel to the magnetic field and its polarization is circular in order to drive mostly $\sigma^{\pm}$ transitions. Unlike bosonic isotopes, fermionic ^{87}Sr has ten

[5] For the coaxial RG-58/U cable, in the relevant radio-frequency range we have $v \simeq 2/3 \times c$, where c is the velocity of light in vacuum.

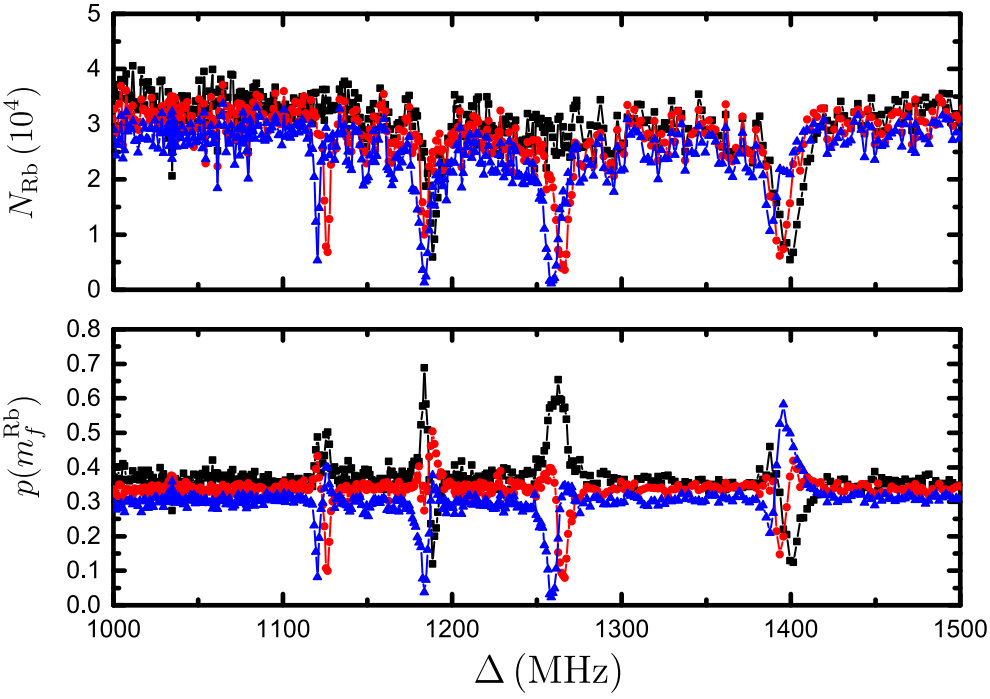

FIGURE 5.4: Example PA losses and PA signal for the ^{87}Rb^{86}Sr isotopologue. Top panel: The number of Rb atoms in $m_f^{\mathrm{Rb}} = -1$ (black squares), $m_f^{\mathrm{Rb}} = 0$ (red circles), and $m_f^{\mathrm{Rb}} = +1$ (blue triangles) as function of the detuning from the atomic transition Δ. Bottom panel: Rb m_f-populations, i.e. atom numbers normalized by the number of atoms in all m_f states, of $m_f^{\mathrm{Rb}} = -1$ (black squares), $m_f^{\mathrm{Rb}} = 0$ (red circles), and $m_f^{\mathrm{Rb}} = +1$ (blue triangles) as function of the detuning from the atomic transition Δ. Note how the Zeeman shift of a few MHz visible in the PA loss spectrum (top panel) results in a dispersive PA signal (bottom panel). The sensitivity is also improved, as shown from the transition at ~ 390 MHz, only clearly out of noise in the bottom panel.

Zeeman substates in its ground state and it is initially prepared in $m_i^{\mathrm{Sr}} = \pm 9/2$. Since Sr can be depolarized by off-resonant scattering events, reducing the PA signal, the best is working close to the Sr $^1S_0 \rightarrow {}^3P_1(f^{\mathrm{Sr}} = 11/2)$ transition and using circular polarization, driving $\sigma^{\pm}$ transitions. The frequency of L_{FB} is swept with uniform rate during the pulse time with a range of $0.5 - 2.0\,\mathrm{MHz}$ to increase the scan-range per experimental run. Finally we note that light polarization and sample preparation is of particular importance for the fermionic case, where the Sr nuclear spin should not be optically pumped into different m_i^{Sr} states by off-resonant scattering of photons during the PA pulse.

The spectroscopic search delivers more PA lines for some isotopologues than for others. In particular, we record the highest density of transitions for ^{87}Rb-^{87}Sr, followed by ^{87}Rb-^{88}Sr, ^{87}Rb-^{86}Sr, and finally ^{87}Rb-^{84}Sr. Although the highest density is expected for the fermionic isotopologue because of the presence of the Sr nuclear moment which can lift degeneracies, the bosonic isotopes have the same internal structure leading to similar densities of molecular levels. We believe this discrepancy is mostly due to strongly different Franck-Condon factors (FCFs), in particular to the short-range amplitude of the atomic scattering wavefunctions. Indeed, among bosonic combinations ^{87}Rb-^{88}Sr features the largest s-wave scattering amplitude and its p-wave counterpart is of the same order of magnitude. Because of these observations, we scan about 10 GHz for ^{87}Rb-^{87}Sr and ^{87}Rb-^{88}Sr and less for the other two isotopic combinations. The recorded spectra of all the investigated RbSr isotopologues are shown in Fig. 5.5.

In the case of ^{87}Rb-^{87}Sr, we observe only broad and weak features between the highest $\mathrm{Rb}(^2S_{1/2}, f^{Rb} = 1) + \mathrm{Sr}(^3P_1, f^{Sr} = 7/2)$ asymptote and the lowest $\mathrm{Rb}(^2S_{1/2}, f^{Rb} = 1) + \mathrm{Sr}(^3P_1, f^{Sr} = 11/2)$ asymptote. This is in strong contrast to the spectral region below the $\mathrm{Rb}(^2S_{1/2}, f^{Rb} = 1) + \mathrm{Sr}(^3P_1, f^{Sr} = 11/2)$ asymptote, where significantly narrower and stronger PA lines are found with high density. We attribute this difference to two possible causes. Firstly, the difference in the off-resonant scattering processes in these two regions. As mentioned in section 5.3.2 Sr is prepared in $m_i^{\mathrm{Sr}} = -9/2$, and for L_{FB} red detuned to the Sr $^1\mathrm{S}_0 \rightarrow {}^3P_1, f^{Sr} = 11/2$ transition, the PA signal is optimal for σ^- transitions, in which condition L_{FB} induces off-resonant scattering in a cycling transition conserving m_f^{Sr}, leaving Sr spin-polarized. However, for L_{FB} blue detuned to the Sr $^1\mathrm{S}_0 \rightarrow {}^3P_1, f^{Sr} = 11/2$ transition, the PA signal is optimal for σ^+ transitions, in which case L_{FB} induces scattering events that do not conserve m_f^{Sr}, depolarizing Sr. Secondly, this difference might also arise from pre-dissociation dynamics above the lowest lying hyperfine asymptote of the excited

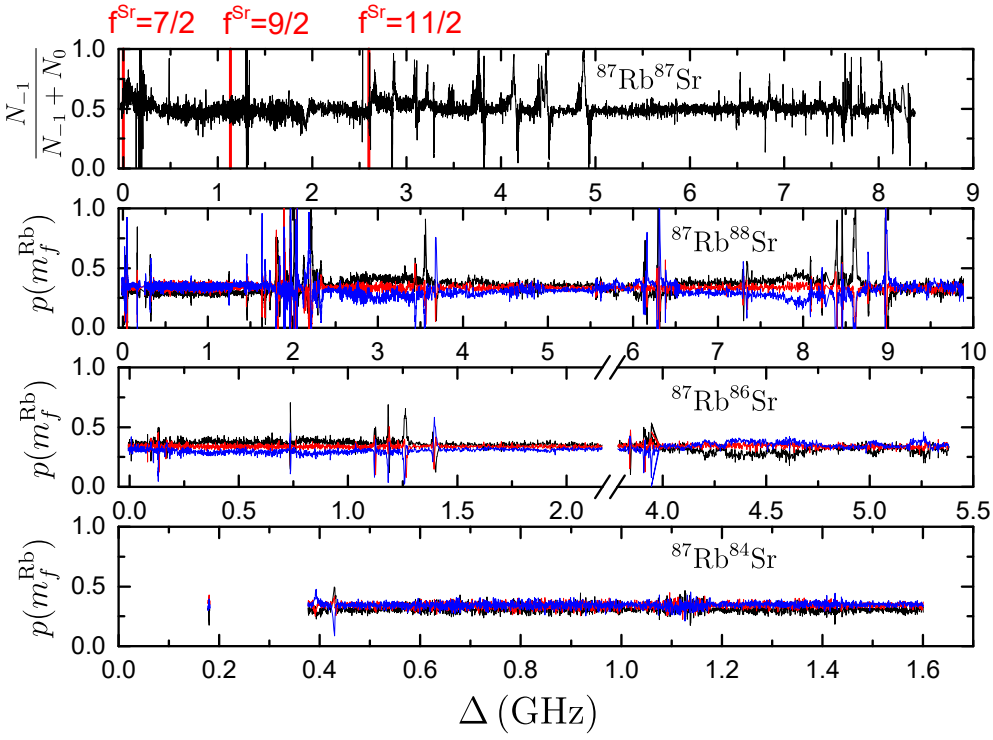

FIGURE 5.5: Results of spectroscopy searches. The PA signal of ^{87}Rb^{87}Sr, ^{87}Rb^{88}Sr, ^{87}Rb^{86}Sr and ^{87}Rb^{84}Sr is shown as function of the detuning to the Sr ^{1}S$_0 \rightarrow ^3P_1$ transition, where $f^{\mathrm{Sr}} = 9/2 \rightarrow ^{\mathrm{Sr}} = 7/2$ was chosen for Sr.

state manifold [191], although further investigation is needed to clarify this point [6]. We scan a total range of 8.6 GHz below the Rb($^2S_{1/2}, f^{Rb} = 1$)+Sr($^3P_1, f^{Sr} = 7/2$) asymptote, being only limited by the RF signal generator and not by decrease in 1-color line strength.

In the case of bosonic isotopologues we scan below the Rb($^2S_{1/2}, f^{Rb} = 1$)+Sr($^3P_1$) structureless asymptote and we report a drastic change in line strength between different isotopologues. As mentioned above, this is expected because different isotopic mixtures feature significantly different short-range amplitudes of the scattering state, hence different PA rates. In particular, in the case of ^{87}Rb-^{88}Sr we observe strong lines in the whole scan range of ~ 10.0 GHz and we stop because of limitations on the RF frequency generator, as for the fermionic species. We stress that molecular lines might not be detected in the window $\Delta = 2.3 - 3.6$ GHz because of a decrease in experimental sensitivity due to a strong Sr_2 line at $\Delta =\sim 2.6$ GHz. In the case of ^{87}Rb-^{86}Sr we scan over a range of ~ 4 GHz with a ~ 1.5 GHz gap due to the presence of a strong Sr_2 transition at $\Delta = 3.15(20)$ GHz, and we stop because of a drop in line strength. In the case of ^{87}Rb-^{84}Sr we scan only ~ 1.6 GHz because of the weakness of the observed lines. The plot shows a gap for this isotopologue around the $\Delta =\sim 175$ MHz transition. This gap was separately scanned with the same sample but different excitation conditions, resulting in no signal.

We check that a large number of PA signals recorded during the spectroscopic searches are indeed due to RbSr rather than Sr_2 or Rb_2 transitions, by verifying that loss of Rb occurs only if both elements are present. As expected, we observe no exception to this assumption. Indeed, Sr_2 transitions cause strong Sr losses and increase of Rb raw atom numbers but no PA signal, as observed for $^{88}Sr_2$ and $^{86}Sr_2$, whereas Rb_2 transitions, which would persist under exclusion of Sr atoms, are not observed, probably due to the low density of Rb_2 levels in this spectral region[7].

Line characterization

We proceed to characterize the PA transitions observed during the spectroscopy search explained in section 5.3.2. This characterization will allow us to precisely determine the energy of the excited rovibrational levels in absence of magnetic field and will inform any further investigation of the optical and magnetic properties of the PA lines.

[6] This might be related to our unsuccessful attempts at observing molecular levels above the $f^{\mathrm{Rb}} = 1$ asymptotes, i.e. supported by the potential correlating to the $f^{\mathrm{Rb}} = 2$ asymptote.

[7] The closest Rb_2 dissociation threshold above the investigated spectra range is Rb($^2S_{1/2}$)+Rb(^2D). Eventual Rb_2 levels would then be bound by $\sim 5 \times 10^3\,\mathrm{cm}^{-1}$ with a density of vibrational levels of the order of $\sim 1\mathrm{THz}^{-1}$.

The main purpose of the characterization is the determination of the spectrum, i.e. zero-magnetic-field resonance locations Δ_{PA}. For the fermionic isotopologue Δ_{PA} is referenced to the Sr $^1\mathrm{S}_0 \rightarrow {}^3P_1$, $f^{Sr} = 11/2$ transition, while for the bosonic isotopes it is referenced to the structureless Sr $^1\mathrm{S}_0 \rightarrow {}^3P_1$ transition. These positions are either directly measured or extrapolated. The former method consists in the measurement of the molecular transition frequency referenced to the Sr atomic transition in the absence of a magnetic field, i.e. $B < 20\,\mathrm{mG}$. In this case we do not use the PA signal described above, which carries no information since loss occurs in all m_f states at the same frequency (see Fig. 5.6), but the raw atom numbers. The latter method consists in a measurement of the magnetic moment of at least one magnetic substate by measuring the PA signal for several different magnetic fields. The first approach requires fewer runs of the experimental sequence but is limited by the stability of Rb and Sr atom numbers and cannot be applied in the case of weak transitions where the signal-to-noise ratio of the atom numbers is low. This method is applied mostly in the case of bosonic Sr isotopes. The second is more time consuming and requires extrapolation, but thanks to the better sensitivity of the PA signal it can detect weak transitions and results in both the energy and the magnetic moment. This method is used mostly for the ^{87}Rb-^{87}Sr mixture. As an example, the high-resolution spectrum of a triplet line in ^{87}Rb^{88}Sr, together with the effect of the magnetic field of one component, is shown in Fig. 5.6.

A secondary purpose of the characterization is the determination of the spontaneous and stimulated transition rates, i.e. γ and Γ, which are fundamental in attempts to molecule creation by STIRAP [176]. Given the large number of observed lines, we estimate the γ of each transition, under the assumption of negligible power-broadening, from the observed width Δf and loss fraction of the spectra recorded for the determination of Δ_{PA}. Although Γ can also be estimated from these measurements, we decide to record the atom number in dependence of the PA pulse duration for a small subset of transitions to improve our accuracy. This is done in order to quantify its range of variation as function of Δ_{PA} and isotopologue.

Finally, we investigate the magnetic properties of some rovibrational levels in order to gain information on the state corresponding to the rovibrational levels. The necessary measurements coincide with those needed to extrapolate Δ_{PA}. However, detection of a single magnetic substate is sufficient to obtain Δ_{PA}, while the study of magnetic properties requires investigation of more Zeeman substates. Since this is extremely time consuming, it was only carried out for a few levels of ^{87}Rb^{84,88}Sr, while for ^{87}Rb^{87}Sr we measure the magnetic moments of the stretched substates related to the strongest 1-color PA lines.

5.3.3 Analysis and Results

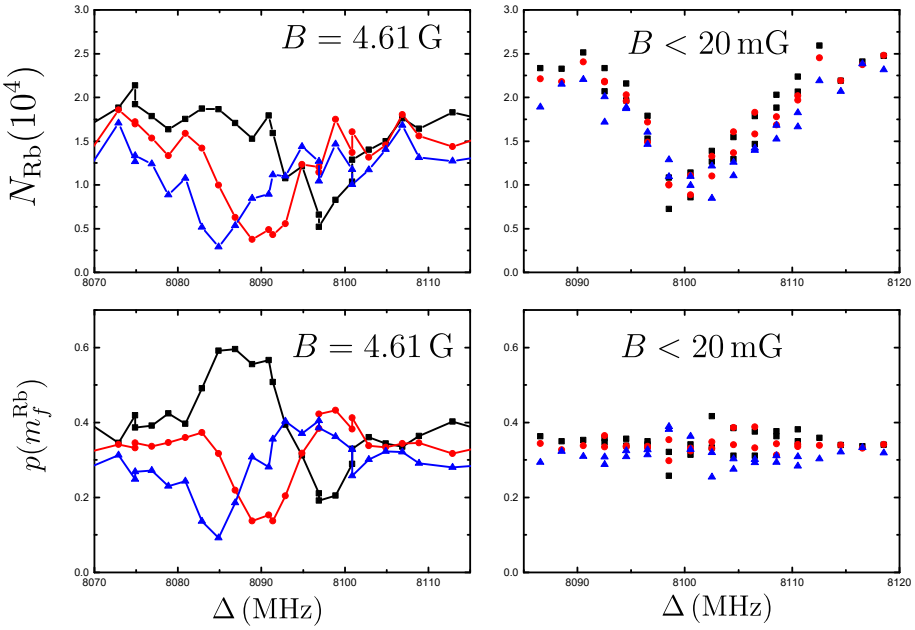

FIGURE 5.6: Example of the spectrum of the triplet line in ^{87}Rb^{88}Sr at $\Delta_{\mathrm{PA}} \sim 330\,\mathrm{MHz}$ with and without external magnetic field. The number of Rb atoms is shown as function of Δ_{PA} for $m_f^{\mathrm{Rb}} = -1, 0, 1$ in black squares, red circles, and blue triangles, respectively.

The zero-magnetic-field resonance locations Δ_{PA}, determining the location of molecular lines, are derived from the centers of Lorentzian fits to the PA losses and PA signals described above. We report the location of RbSr rovibrational levels Δ_{PA} in tables 5.1 and 5.2 for fermionic and bosonic isotopologues, respectively. In the case of the fermionic isotopologue, given the large number of observed lines, we fully characterize only the strongest ones, while for the rest we only estimate Δ_{PA} from the broad scan of our spectroscopy search and the measured average magnetic moment, see the end of this section. As a consequence, the error on Δ_{PA} is a few hundreds of kHz for fully characterized lines, while it is roughly an order of magnitude bigger for the others. In the case of bosonic isotopologues, which show a lower density of PA transitions, all observed lines were fully characterized. Finally, while the 1-color PA spectrum is typically strongly dominated by the s-wave atomic collisions for our

sample temperatures, ^{87}Rb^{88}Sr might represent an exception and its spectrum might involve contributions from p-wave collisions due to the anomalous large short-range amplitude of the corresponding wavefunction [189].

The investigation of the optical properties of the 1-color PA lines, i.e. γ and Γ, requires a well-defined model. Four main approximations can be made based on the conditions of our experiments, which substantially simplify our analysis. Firstly, since the PA time scale is much longer than the time scales set by the trapping frequencies, we will assume that PA events occur in an atomic mixture close to thermal equilibrium at temperature T, which is allowed to vary slowly in time $T = T(t)$ [192]. Secondly, since the temperature of our sample is about 1 μK, we assume that PA events happen in the s-wave channel [8]. Thirdly, as can be checked *a posteriori*, the PA transitions are far from saturation, i.e. $\Gamma \propto I$ where I is the intensity of L_{FB}. Fourthly, and last, since the number of Sr atoms is much bigger than the number of Rb atoms, it is, to first approximation, not affected by PA events. It can however contribute to non-negligible non-radiative losses of Rb that must be taken into account in order not to overestimate the independent contribution from PA.

The rate equation governing the density of Rb is [193, 84]:

$$-\frac{\partial}{\partial t} n_{\mathrm{Rb}} = K_{\mathrm{PA}} n_{\mathrm{Rb}} n_{\mathrm{Sr}} + K_{\mathrm{coll}}, \tag{5.1}$$

$$K_{\mathrm{PA}}(\gamma, \Gamma^0, \delta, I) \propto \frac{\gamma \Gamma^0}{\delta^2 + \left(\frac{\gamma}{2}\right)^2} \frac{I(\mathbf{x})}{I^0}, \tag{5.2}$$

where $n_{\mathrm{Rb,Sr}}(\mathbf{x})$ are the atomic densities, $K_{\mathrm{coll}}(\mathbf{x})$ is the loss rate due to all non-radiative processes, and K_{PA} is the PA rate coefficient function of the linewidth γ, the peak stimulated rate $\Gamma^0 = \Gamma(I^0)$, the detuning δ from 1-color resonance and the spatial intensity profile $I(\mathbf{x})/I^0$ of L_{FB}. Since we do not measure atomic densities, but only number of atoms, we need to rearrange Eqn. 5.1 to fit our data. By integrating both sides over the spatial coordinates we obtain:

$$-\frac{d}{dt} N_{\mathrm{Rb}} = K^0_{\mathrm{PA}} V_{\mathrm{PA}} N_{\mathrm{Rb}} N_{\mathrm{Sr}} + \int K_{\mathrm{coll}}(\mathbf{x}) d\mathbf{x}, \tag{5.3}$$

$$V_{\mathrm{PA}}(T) = \int \frac{n_{\mathrm{Rb}}(T, \mathbf{x})}{N_{\mathrm{Rb}}} \times \frac{n_{\mathrm{Sr}}(T, \mathbf{x})}{N_{\mathrm{Sr}}} \times \frac{I(\mathbf{x})}{I^0} \, d\mathbf{x}, \tag{5.4}$$

[8] As can be checked using the ground-state potential energy curve given in chapter 6, the short-range amplitude of the scattering wavefunctions with non-zero internuclear angular momentum is significantly smaller than that of s-wave scattering wavefunctions, with the only exception of ^{87}Rb-^{88}Sr.

where $N_{\mathrm{Rb,Sr}}(t)$ are atom numbers, $K^0_{\mathrm{PA}} = K_{\mathrm{PA}}(\gamma, \Gamma^0, \delta, I^0)$ is the peak PA rate coefficient, and $V_{\mathrm{PA}}(T)$ is the effective interaction volume given by the equilibrium thermal distributions of the atomic clouds and the intensity profile of L_{FB}. Under our assumptions and sufficiently far away from the atomic transition, i.e. $\delta \ll \Delta_{\mathrm{PA}}$, N_{Sr} does not depend on δ.

In order to study the contribution from non-radiative loss processes, we measure the atom number of Rb, trapped with Sr, in the absence of PA light for variable hold time in the ODT. Non-radiative losses are only observed in the case of ^{87}Rb^{87}Sr, as expected from the anomalously large inter-species s-wave scattering length. Although these losses are weaker than PA losses, and only provide a background to PA measurements, we include K_{coll} to improve the accuracy of K^0_{PA}. The main contributions to K_{coll} are three-body losses of either three Rb atoms, two Rb with one Sr atoms, or one Rb with two Sr atoms. As for bosonic isotopic combinations, the first contribution is negligible since we do not observe Rb losses without Sr. The two interspecies recombination processes are instead equally able to fit the Rb loss data in absence of PA light within experimental precision. Since the Rb loss rate induced by Rb-Sr-Sr collisions only slightly decreases during PA, we assume for simplicity this process as the dominant one, and we set $K_{\mathrm{coll}} = K_3 n_{\mathrm{Rb}} n^2_{\mathrm{Sr}}$, with K_3 being the fitted rate coefficient. Substitution into Eqn. 5.3 yields:

$$-\frac{d}{dt}N_{\mathrm{Rb}} = K^0_{\mathrm{PA}} V_{\mathrm{PA}} N_{\mathrm{Rb}} N_{\mathrm{Sr}} + K_3 V_3 N_{\mathrm{Rb}} N^2_{\mathrm{Sr}}, \tag{5.5}$$

$$V_3(T) = \int \frac{n_{\mathrm{Rb}}(T, \mathbf{x})}{N_{\mathrm{Rb}}} \times \left(\frac{n_{\mathrm{Sr}}(T, \mathbf{x})}{N_{\mathrm{Sr}}} \right)^2 d\mathbf{x}, \tag{5.6}$$

The natural widths γ of PA transitions is derived from the measurement of Rb atom number as function of frequency, with other experimental conditions fixed. As a consequence it requires fitting the Rb atom number after a fixed pulse time T. This number is the solution to Eqn. 5.5, and, in the limit of $\delta \ll \Delta_{\mathrm{PA}}$, is given by:

$$N_{\mathrm{Rb}}(T) \simeq N_{\mathrm{Rb}}(0) e^{-\frac{C_{\mathrm{PA}}}{\delta^2 + (\gamma/2)^2} - C_3}, \tag{5.7}$$

where $C_3 = \int_0^T K_3 V_3 N^2_{\mathrm{Sr}} dt$ is the background contribution from inelastic losses and $C_{\mathrm{PA}} = \int_0^T K_{\mathrm{PA}} V_{\mathrm{PA}} N_{\mathrm{Sr}} dt$ is the contribution from PA. Evidently only for $C_{\mathrm{PA}} \to 0$ can the PA contribution on the right-hand side of eqn. 5.7 be truncated to its first order Taylor expansion giving a spectrum with Lorentzian FWHM equal to γ. In practice, however the experimental conditions are optimized to obtain enough losses to have good signal-to-noise ratio on N_{Rb} and this makes the observed Lorentzian widths

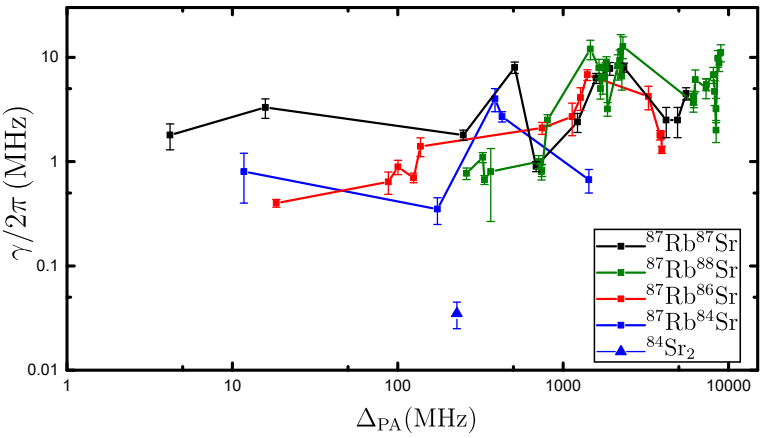

FIGURE 5.7: Natural linewidths of 1-color transitions as function of Δ_{PA} for RbSr isotopologues and for the reference $^{84}Sr_2$ line at ~ 228 MHz, see text.

systematically bigger [9]. To our experimental precision, we can estimate γ from the observed width Δf and the loss fraction on resonance. The results are reported in tables 5.1 and 5.2, and shown in Fig. 5.7.

The PA rate coefficients K^0_{PA} and the stimulated PA rates Γ^0 are derived from the measurement of Rb atom number as function of time, with other experimental conditions fixed, performed for a small subset of the observed 1-color PA lines. The solution N_{Rb} to Eqn. 5.5 is fitted to these data, with K^0_{PA} the only fit parameter. The resulting coefficient rates per unit of intensity $K_{PA}/I = K^0_{PA}/I^0$, assumed to be independent of temperature by virtue of the Wigner threshold law[84], are shown in Fig. 5.8. Finally Γ^0 is derived from the definition of the PA rate coefficient in terms of the scattering cross-section, i.e. $K_{PA} = \langle v\sigma \rangle$, which for s-wave collisions simplifies to [86, 194]:

$$\Gamma = \frac{\gamma K_{PA}}{4C_K(T)}, \tag{5.8}$$

$$C_K(T) = \frac{k_B T}{h}(2\pi\mu k_B T/h^2)^{-3/2}, \tag{5.9}$$

where $C_K(T)$ is a kinetic factor, T is the temperature of the mixture and μ is the

[9] Using the standard non-Hermitian 2-level model for PA and assuming the adiabatic approximation, see chapter 3, one obtains the same result.

reduced mass of RbSr. For the sake of comparison, since the functional dependence of Γ can be assumed to be given by the Wigner threshold law [84], we derive its value for the reference temperature of $T = 1.0\,\mu$K for all measurements. The resulting stimulated rates per unit of intensity $\Gamma/I = \Gamma^0/I^0$ are shown in Fig. 5.8.

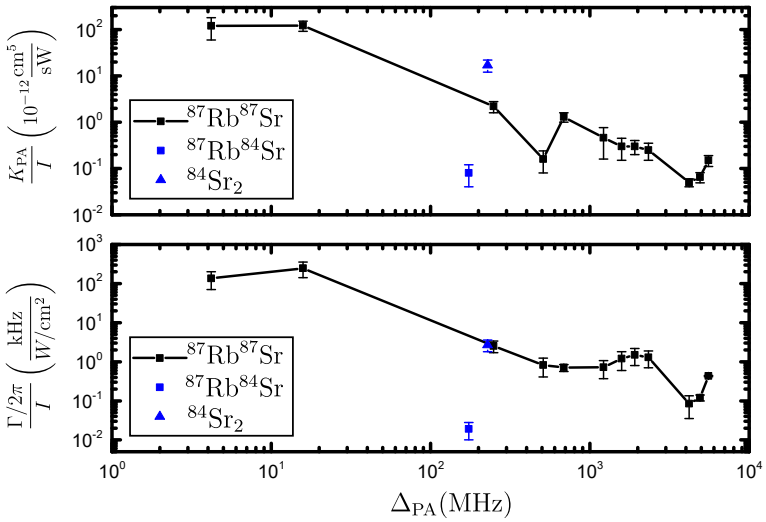

FIGURE 5.8: Optical properties. Top panel: PA rate coefficient over intensity is shown as function of Δ_{PA} for the investigated 1 color lines of $^{87}Rb^{84,\,87}Sr$ and $^{84}Sr_2$. Bottom panel: The extracted stimulated transition rate over intensity, referenced to $T = 1.0\,\mu$K, is shown as function of Δ_{PA} for the same molecular lines.

In order to corroborate our analysis, we carry out the same experiment on a Sr cloud, without the presence of Rb, to interrogate a well-known Sr_2 1-color PA line corresponding to a weakly-bound state below the $Sr(^1S_0)+Sr(^3P_1)$ asymptote at $\Delta_{PA} = 228\,$MHz. In this case the model reads:

$$-\frac{d}{dt}N_{Sr} = 2K^0_{PA}V_{PA}N^2_{Sr} + \frac{1}{\tau}N_{Sr}, \tag{5.10}$$

$$V_{PA}(T) = \int \left(\frac{n_{Sr}(T,\mathbf{x})}{N_{Sr}}\right)^2 \times \frac{I(\mathbf{x})}{I^0}\,d\mathbf{x}, \tag{5.11}$$

where $1/\tau$ is the loss rate due to off-resonant scattering. Since $\gamma \sim 1\,\mu$K, see [27]

and chapter 3, is of the order of the thermal width ($\sim 1.4\,\mu$K) and the Doppler width ($\sim 0.8\,\mu$K), we have taken into account the relevant correction factors given in [194, 180] in the derivation of γ and Γ from our measurements, which in this case only provide a correction of the order of our error. The extracted γ is shown in Fig. 5.7 and the extracted K_{PA}/I and Γ/I, always referenced to $T = 1.0\,\mu$K, are shown in Fig. 5.8. Using our method we obtain $\gamma/2\pi = 35(10)$ kHz, which is only 15 kHz larger than the one reported in literature, see [27] and chapter 3.

Finally the magnetic moments μ of the investigated levels of RbSr are derived from linear fits to the locations of PA lines as function of the magnetic field, already used in the previous section to extrapolate Δ_{PA}. They are reported in table 5.3 together with the number of Zeeman substates. For those levels whose number of magnetic substates has no uncertainty, the corresponding Landé factors $g_F\mu_{\mathrm{B}}$ are also reported. The measured μ of the rovibrational levels as function of Δ_{PA} are shown as data points in Fig. 5.9 together with the magnetic moments of the atom pair states corresponding to the dissociation threshold (red horizontal lines) for which $\Delta m_f^{\mathrm{Rb}} + \Delta m_f^{\mathrm{Sr}} = -0, \pm 1$. Although the detuning from the atomic transition, and consequently the corresponding binding energies, are extremely low compared to the potential depth, we observe a strong deviation of the observed molecular magnetic moments from the atomic counterparts, to which they must correlate asymptotically. This behavior implies the molecular fine and hyperfine interactions strongly affect the magnetic behavior in the investigated spectral region. A quantitative analysis of this phenomenon lies beyond the scope of the present work.

5.4 Implications on STIRAP to weakly-bound ground-state RbSr

RbSr ground-state molecules could coherently be optically associated from atom pairs confined in an optical lattice well via STIRAP, as already demonstrated for the case of Sr_2, see chapter 3. In this case a three-level system coupled by two phase-coherent lasers $L_{\mathrm{FB,BB}}$ in a Λ-scheme is exploited, see chapter 3. The three-level system consists of the initial atom-pair state $|a\rangle$, an excited molecular level $|e\rangle$, and ground-state molecular level $|m\rangle$, and the Λ-scheme consists of the optical couplings $|a\rangle \leftrightarrow |e\rangle$ and $|m\rangle \leftrightarrow |e\rangle$ induced by L_{FB} and L_{BB}, respectively. However, since the initial state is an atomic state and not a molecular level, the transfer efficiency is strongly dependent on the properties of the specific Λ-scheme, see chapter 3. In particular, in the case of equal maximum Rabi frequencies $\Omega = \Omega_{\mathrm{FB}} = \Omega_{\mathrm{BB}}$, induced by $L_{\mathrm{FB,BB}}$, the maximum attainable STIRAP efficiency depends, to first approximation, on a single parameter $A = \delta_m/\tilde{\gamma}$, where δ_m is the maximum light shift induced on the two-photon

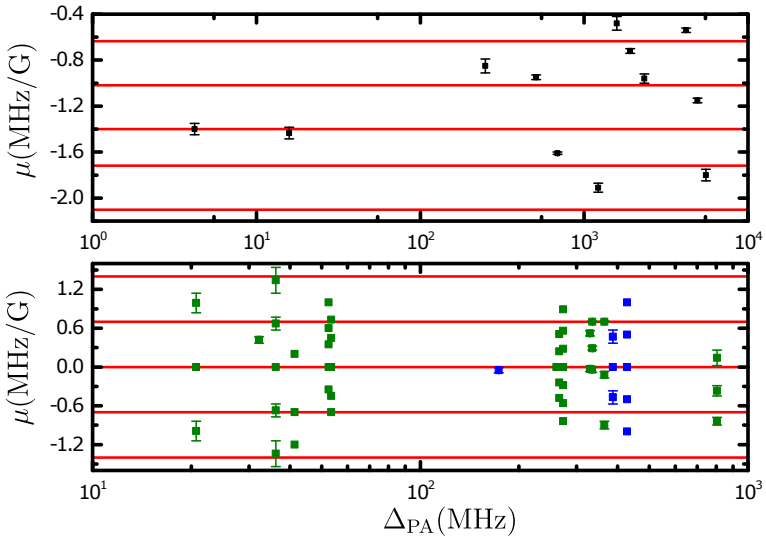

FIGURE 5.9: Magnetic properties. Top panel: Magnetic moments of excited molecular levels of ^{87}Rb^{87}Sr as function of Δ_{PA}. Bottom panel: Magnetic moments of excited molecular levels of ^{87}Rb^{88}Sr (green squares) and ^{87}Rb^{84}Sr (blue squares) as function of Δ_{PA}. The horizontal lines represent magnetic moments for atomic states obeying $\Delta m_f^{Rb} + \Delta m_f^{Sr} = -0, \pm 1$.

detuning and $\tilde{\gamma} = \Omega^2/\gamma$ is the effective coupling determined by the Rabi frequency Ω, see chapter 3. In practice Ω_{FB} and Ω_{BB} can be vastly different, but the maximum efficiency is limited by the weakest one, i.e. $\tilde{\gamma} = \Omega_{\mathrm{FB}}^2/\gamma$. Accordingly, since Ω_{FB} is much weaker than Ω_{BB}, its stimulation requires much higher intensities, therefore δ_m is essentially determined by L_{FB} and can be estimated from atomic optical properties. The maximum efficiency $\eta_{\max}$ depends exponentially on the parameter A according to $\eta_{\max} \simeq e^{-C|A|}$, where C is a constant depending on the temporal intensity profile of $L_{\mathrm{FB,BB}}$. The STIRAP efficiency is then maximized by minimizing $A = \delta_m\gamma/\Omega^2$, which can be regarded as a figure of merit. This analysis relies on the assumption that the main contribution to δ_m comes from the PA lasers themselves, and not from other effects, i.e. lattice inhomogeneity, which sets a time scale for STIRAP. Thus, in general one wants to maximize $\tilde{\gamma}$ and minimize A.

Since the strongest limitation in the intended STIRAP on RbSr is the interaction of our system with L_{FB}, our characterization measurements of γ and Γ are sufficient to discriminate the best candidate STIRAP scheme. This is evident from inspection of the stimulated transition rate, which is given by $\Gamma = 2\pi|\langle\phi_e|V_{\mathrm{rad}}(r)|\phi_i\rangle|^2$, where ϕ_i is the energy-normalized scattering wavefunction, ϕ_e is the excited molecular level wavefunction, and $V_{\mathrm{rad}}(r) \propto \sqrt{I}d(r)$ is the radiative coupling proportional to the square root of the laser intensity and the transition dipole moment $d(r)$ [86]. The free-bound Rabi frequency in the optical lattice well is $\Omega_{\mathrm{FB}} = 2\pi|\langle\phi_e|V_{\mathrm{rad}}(r)|\phi_0\rangle|$, where ϕ_0 is here the unit-normalized atom-pair wavefunction in the optical lattice well. As a consequence, the effective coupling for STIRAP in a lattice well $\tilde{\gamma}$ is proportional to $\Gamma/(I\gamma)$. The figure of merit $A = \delta_m/\tilde{\gamma}$, which should be minimized for optimum STIRAP, can be instead estimated as $\delta_m\gamma/(\Gamma/I)$. The values of $\Gamma/(I\gamma)$ and $\delta_m\gamma/(\Gamma/I)$ are shown as function of the detuning Δ_{PA} for different isotopic combinations and transitions in Fig. 5.10. We observe that, compared to the Sr_2 reference PA line, which was successfully used for efficient molecule production via STIRAP, the RbSr PA lines are orders of magnitude away in both parameters, corresponding to a much lower estimated STIRAP efficiency for RbSr. The $^{87}Rb^{84}Sr$ PA line investigated shows an increase of three orders of magnitude for $\delta_m\gamma/(\Gamma/I)$ and attempts to use this line for STIRAP were indeed unsuccessful [34]. In the case of the fermionic isotopologue we observe a clear improvement in both parameters compared to $^{87}Rb^{84}Sr$, although still far from Sr_2. However, unless precise interaction tuning via magnetic Fano-Feshbach resonances can be achieved, ^{87}Rb-^{87}Sr is not suitable for the realization of quantum gas mixtures or Mott insulators due to its anomalously large s-wave scattering length, see chapter 6.

We attribute the strong difference in the optical properties of 1-color transitions between Sr_2 and RbSr to the branching ratio of spontaneous decay from the weakly-bound levels of the excited state. This is based on two separate observations. Firstly,

the natural widths γ of molecular transitions in RbSr isotopologues are 1-2 orders of magnitude larger than those of Sr_2, which are close to the atomic intercombination linewidth, see [27] and chapter 3. Secondly, this increase in the natural width, i.e. in the coupling of excited weakly-bound levels to the electromagnetic field, is not accompanied by an increase of the stimulated rates Γ, which even for the fermionic isotope with extremely large scattering length, is of the same order of that in Sr_2. These two observations together imply that RbSr levels feature a strong bias in the branching ratio favoring spontaneous transitions to deeper bound ground-state levels. Although the dependence of the transition dipole moment on the internuclear distance was predicted for both molecules, it only induced a strong effect on weakly-bound levels of heteronuclear RbSr molecules, which might be due to the correlation with the unpaired valence electron of Rb. This analysis implies that the STIRAP efficiency of molecule formation in all RbSr isotopologues is expected to be significantly lower than in Sr_2. STIRAP between bound levels might instead be insensitive to this effect and it will require an independent investigation. This type of STIRAP, aiming at *state-transfer* rather than *molecule production*, could become relevant in the near future since magnetically-associated RbSr molecules, see chapter 7, can probably not be transferred to the groundstate in a single STIRAP.

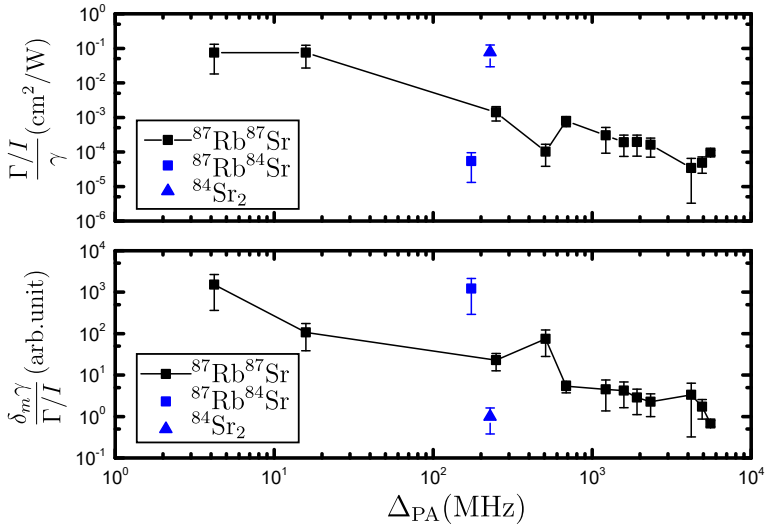

FIGURE 5.10: Effective coupling and figure of merit for STIRAP. Top panel: The effective coupling, analogous to $\tilde{\gamma}$ for the lattice case, is shown for the investigated RbSr lines as function of Δ_{PA} (higher is better). Bottom panel: The figure of merit, analogous to A in the lattice case, is shown for the investigated RbSr lines as function of Δ_{PA} (lower is better).

TABLE 5.1: 1-color PA spectrum and linewidths for the fermionic ^{87}Rb^{87}Sr isotopologue. Δ_{PA} is the zero-magnetic-field 1-color resonance location, FWHM is the observed Lorentzian FWHM, and $\gamma/2\pi$ is the derived natural width. All quantities are in units of MHz.

Δ_{PA}	Err	FWHM	Err	$\gamma/2\pi$	Err
4.20	0.50	–	–	1.80	0.50
15.84	0.32	4.50	1.00	3.30	0.70
65.22	3.50	–	–	–	–
249.30	0.40	2.56	0.41	1.80	0.20
260.40	3.47	–	–	–	–
275.00	3.63	–	–	–	–
288.40	2.82	–	–	–	–
458.00	3.01	–	–	–	–
483.00	3.48	–	–	–	–
509.90	0.50	9.10	1.30	8.00	1.00
573.90	2.87	–	–	–	–
611.00	3.53	–	–	–	–
622.00	3.59	–	–	–	–
686.79	0.23	1.24	0.13	0.90	0.10
799.22	2.97	–	–	–	–
829.22	3.64	–	–	–	–
1100.40	2.18	–	–	–	–
1160.90	3.07	–	–	–	–
1220.56	0.16	3.24	0.44	2.40	0.50
1492.90	3.00	–	–	–	–
1534.22	3.69	–	–	–	–
1569.00	3.41	–	–	–	–
1581.50	2.30	8.00	1.00	6.30	0.70
1799.00	2.99	–	–	–	–
1829.22	3.59	–	–	–	–
1863.00	3.37	–	–	–	–
1874.50	3.70	–	–	–	–
1913.40	0.60	9.80	1.30	7.80	1.10
2219.90	2.84	–	–	–	–
2270.90	3.53	–	–	–	–
2282.00	3.03	–	–	–	–
2335.40	0.60	10.80	1.40	8.00	0.80
3003.00	3.46	–	–	–	–
3013.90	3.26	–	–	–	–
3019.00	3.40	–	–	–	–
3670.00	3.18	–	–	–	–
3705.00	3.43	–	–	–	–
3730.00	3.18	–	–	–	–
3768.00	3.38	–	–	–	–
3892.49	3.10	–	–	–	–
3931.49	3.29	–	–	–	–
4199.20	0.30	3.00	1.00	2.50	0.80
4241.49	3.57	–	–	–	–
4385.49	3.49	–	–	–	–
4484.00	3.13	–	–	–	–
4625.49	3.06	–	–	–	–
4776.49	3.43	–	–	–	–
4850.49	3.05	–	–	–	–
4914.20	0.30	3.00	1.00	2.50	0.80
5021.49	3.06	–	–	–	–
5030.49	3.00	–	–	–	–
5076.49	3.51	–	–	–	–
5096.49	3.59	–	–	–	–
5114.49	2.73	–	–	–	–
5209.49	3.71	–	–	–	–
5281.49	3.11	–	–	–	–
5427.49	3.68	–	–	–	–
5500.00	3.13	–	–	–	–
5512.00	3.38	–	–	–	–
5546.20	0.40	5.50	1.00	4.50	0.60
5564.00	3.45	–	–	–	–
5653.22	3.48	–	–	–	–
5718.69	2.99	–	–	–	–

TABLE 5.2: 1-color PA spectrum and linewidths for the bosonic $^{87}Rb^{84,86,88}Sr$ isotopologues. Δ_{PA} is the zero-magnetic-field 1-color resonance location, FWHM is the observed Lorentzian FWHM, and $\gamma/2\pi$ is the derived natural width. All quantities are in units of MHz.

Δ_{PA}	Err	FWHM	Err	γ	Err
		$^{87}Rb^{84}Sr$			
11.74	0.60	-	-	0.80	0.40
173.50	0.20	-	-	0.35	0.10
387.40	0.50	-	-	4.00	1.00
427.80	0.20	4.80	0.60	2.70	0.30
1429.01	0.10	0.80	0.20	0.67	0.17
		$^{87}Rb^{86}Sr$			
18.44	0.08	0.79	0.07	0.40	0.03
87.80	1.00	0.79	0.19	0.64	0.15
100.20	1.00	1.10	0.17	0.89	0.14
124.70	1.00	1.10	0.12	0.70	0.07
137.13	0.08	1.72	0.35	1.40	0.29
746.96	0.13	3.49	0.46	2.10	0.27
1133.57	0.42	2.90	1.00	2.70	0.93
1195.08	0.87	> 10	–	–	–
1272.73	0.32	5.70	1.40	4.10	1.01
1401.66	0.32	10.40	1.22	6.80	0.79
3277.09	0.33	4.67	1.18	4.20	1.07
3849.53	0.07	2.86	0.30	1.80	0.19
3922.59	0.07	2.98	0.25	1.80	0.15
3956.95	0.05	1.95	0.16	1.30	0.10
5273.00	10.00	> 4	-	-	–
		$^{87}Rb^{88}Sr$			
20.70	1.80	-	-	-	–
32.23	0.60	-	-	-	–
36.26	0.50	-	-	-	–
41.39	0.60	-	-	-	–
52.54	0.30	-	-	-	–
53.50	0.40	-	-	-	–
260.54	0.05	1.33	0.17	0.77	0.1
265.58	0.05	1.57	0.61	-	–
272.91	0.07	0.86	0.52	-	–
326.93	0.04	1.80	0.20	1.10	0.12
329.34	0.03	1.37	0.19	-	–
334.99	0.10	1.27	0.12	0.67	0.07
364.81	0.05	1.50	1.00	0.80	0.53
712.18	0.11	1.40	0.20	1.00	0.14
738.85	0.05	1.20	0.20	0.80	0.13
743.53	0.05	1.50	0.20	0.83	0.11
804.26	0.02	4.13	0.51	2.50	0.31
1461.09	0.13	16.50	3.50	12.00	2.55
1646.00	0.20	9.37	1.95	7.90	1.65
1680.23	0.20	6.55	1.35	5.00	1.03
1733.59	0.20	8.70	2.78	6.50	2.08
1810.81	0.20	14.10	2.00	7.80	1.11
1828.91	0.20	13.52	1.72	9.00	1.15
1855.00	0.20	4.70	0.70	3.20	0.48
1910.07	0.03	9.91	2.09	-	–
1983.41	0.21	13.84	3.21	-	–
2029.72	0.12	6.66	1.15	-	–
2043.13	1.34	14.16	3.39	-	–
2060.59	0.12	3.91	0.64	-	–
2140.29	1.82	9.80	2.67	8.30	2.26
2198.35	0.20	14.81	3.82	9.30	2.40
2227.09	0.40	14.49	6.45	11.40	5.08
2265.70	1.00	7.50	2.00	6.60	1.76
2297.60	1.00	15.02	3.53	12.70	2.99
3454.60	1.00	>20.0	-	–	–
3566.50	1.00	>10.0	-	–	–
3691.40	1.00	>15.0	-	–	–
6137.02	0.29	5.10	1.00	3.70	0.73
6154.32	0.09	6.60	1.00	4.10	0.62
6174.03	0.08	6.15	0.96	3.90	0.61
6297.79	0.28	8.50	2.00	6.10	1.44
6309.98	0.33	10.99	2.88	-	–
6323.50	0.13	12.52	2.29	-	–
6394.35	0.10	6.31	0.93	-	–
7304.84	0.20	6.41	1.36	5.10	1.08
7352.34	0.24	7.32	0.98	5.50	0.73
8101.17	0.70	9.20	1.60	6.80	1.18
8229.85	0.39	6.09	1.62	4.70	1.25
8398.85	0.24	3.40	0.81	2.00	0.47
8411.47	0.18	4.45	1.16	3.20	0.83
8463.49	0.15	13.08	2.31	-	–
8475.82	0.52	13.41	2.59	-	–
8621.03	0.79	13.50	2.50	9.80	1.81
8774.85	0.54	11.74	2.01	8.80	1.51
8984.86	0.50	16.74	3.14	11.10	2.08

TABLE 5.3: Magnetic properties of the investigated 1-color PA lines of fermionic ^{87}Rb^{87}Sr and bosonic ^{87}Rb^{84,88}Sr isotopologues. Δ_{PA} is the zero-magnetic-field 1-color resonance location, # substates is the number of Zeeman substates, μ is the observed magnetic moment, $g_F\mu_B$ is the derived Landé g-factor times the Bohr magneton.

The quantities are expressed in units of MHz and Gauss.

Δ_{PA} (MHz)	# substates	μ(MHz/G)	$g_F\mu_B$ (MHz/G)
^{87}Rb^{87}Sr			
4.20	>1	-1.40(5)	–
15.84	>1	-1.44(5)	–
249.30	>1	-0.85(6)	–
509.90	>1	-0.95(2)	–
686.79	>1	-1.61(1)	–
1220.56	>1	-1.91(4)	–
1581.50	>1	-0.48(6)	–
1913.40	>1	-0.72(2)	–
2335.40	>1	-0.96(4)	–
4199.20	>1	-0.54(2)	–
4914.20	>1	-1.15(2)	–
5546.20	>1	-1.80(5)	–
^{87}Rb^{84}Sr			
173.50	1	-0.05(4)	0
387.40	3	–	0.47(17)
427.80	5	–	0.50(10)
^{87}Rb^{88}Sr			
20.70	>2	-0.99(15),0,0.99(15)	0.99(15)
32.23	1	0.42(5)	0.42(5)
36.26	5	-1.34(20),-0.67(10),0,0.67(10),1.34(20)	0.67(10)
41.39	3	-0.7,0.2,-1.1	0.90(20)
52.54	>4	-0.35,0,0.35,0.6,1.0	0.30(-)
53.50	>3	-0.70,-0.45,0,0.45,0.70	0.40(-)
260.54	1	0.01(5)	0.00(5)
265.58	5	-0.48,-0.24,0,0.24,0.48	0.24(7)
272.91	7	-0.84,-0.56,-0.28,0,0.28,0.56,0.84	0.28(8)
329.34	>1	0.52(4),-0.03(4)	–
334.99	>2	0.70(1),0.29(3),-0.04(4)	–
364.81	>2	0.70(1),-0.12(5),-0.90(6)	–
804.26	>2	-0.84(6),-0.37(8),0.14(12)	–
1733.59	>2	-0.61(13),0.00(1),0.61(20)	–

Chapter 6

The RbSr $^2\Sigma^+$ ground state investigated via spectroscopy of hot & ultracold molecules

Abstract

We report on spectroscopic studies of hot and ultracold RbSr molecules, and combine the results in an analysis that allows us to fit a potential energy curve (PEC) for the $X(1)^2\Sigma^+$ ground state bridging the short-to-long-range domains. The ultracold RbSr molecules are created in a μK sample of Rb and Sr atoms and probed by two-colour photoassociation spectroscopy. The data yields the long-range dispersion coefficients C_6 and C_8, along with the total number of supported bound levels. The hot RbSr molecules are created in a 1000 K gas mixture of Rb and Sr in a heat-pipe oven and probed by thermoluminescence and laser-induced fluorescence spectroscopy. We compare the hot molecule data with spectra we simulated using previously published PECs determined by three different *ab-initio* theoretical methods. We identify several band heads corresponding to radiative decay from the $B(2)^2\Sigma^+$ state to the deepest bound levels of $X(1)^2\Sigma^+$. We determine a mass-scalable high-precision PEC for $X(1)^2\Sigma^+$ by fitting all data using a single fit procedure. This PEC is consistent with all data, thus spanning short-to-long internuclear distances and bridging an energy gap of about $900\,\mathrm{cm}^{-1}$ still uncharted by any experiment. We benchmark previous *ab-initio* PECs against our results, and give the PEC fit parameters for both $X(1)^2\Sigma^+$ and $B(2)^2\Sigma^+$ states. As first outcomes of our analysis, we calculate the s-wave scattering properties for all stable isotopic combinations and corroborate the locations of Fano-Feshbach resonances between alkali Rb and closed-shell Sr atoms recently observed [Barbé *et al.*,

Nature Physics, Advance Online Publication (2018), doi:10.1038/s41567-018-0169-x]. These results and more generally our fit procedure should greatly contribute to the generation of ultracold alkali – alkaline-earth dimers, whose applications range from quantum simulation to product and reactant state-controlled quantum chemistry.

6.1 Introduction

Production of ultracold molecules composed of one alkali and one alkaline-earth(-like) atom is being pursued with increasing effort over the last years, boosted by the achievement of quantum degeneracy for gases of alkaline-earth atoms and atoms with similar electronic structure [81, 195, 196]. These heteronuclear open-shell molecules possess a $^2\Sigma$ electronic ground state. In their rovibrational ground state, they exhibit a non-zero electronic spin angular momentum and a strong permanent electric dipole moment. These properties make them suitable for quantum simulations of magnetic excitons [197] and topological quantum phases [32] mediated by the induced electric dipole-dipole interaction. Molecules with $^2\Sigma$ ground state could also be used as sensitive magnetic field sensors [198], quantum computing platforms [199], and probes of parity-violations [200] and variation of the proton-to-electron mass ratio [201]. If one can produce a quantum degenerate gas of molecules, where all degrees of freedom are under control, one can study quantum chemical reactions and their dynamics at the most fundamental level, with full control over the reactants, in dependence of electromagnetic fields, and detecting reaction products [202, 5, 203].

In order to create molecules at ultracold temperatures and to understand quantum chemistry processes, one needs an accurate molecular model. Recently *ab-initio* calculations for alkali – alkaline-earth(-like) molecules have provided potential energy curves (PECs), permanent electric dipole moments and transition dipole moments, but only a few attempts at benchmarking theories with experiments have been recorded so far [204, 205, 206, 207, 208, 209, 210]. The precision of *ab-initio* calculations is typically not enough to reliably predict the properties that need to be known to form ultracold molecules, such as molecular binding energies. Theory must therefore be complemented by spectroscopy experiments.

Different spectral ranges can be explored with the help of various spectroscopy types, two of which being relevant for the present work. Photoassociation (PA) spectroscopy of ultracold atoms provides data with precision and accuracy reaching down to the kHz level [85, 211]. PA spectroscopy favours the production of weakly-bound molecules, since their wavefunction has the best overlap with the large wavefunction describing colliding atoms. Knowledge of these weakly-bound levels is sufficient to determine the long-range behaviour of the PECs up to a short-range phase [38,

180]. Thermoluminescence and laser induced fluorescence (LIF) spectroscopy in high-temperature ovens provide spectra with many optical lines at a fraction of cm^{-1} precision [212, 213, 204]. Thermoluminescence and LIF spectra are usually dominated by the radiative decay towards the most bound levels of the ground-state potential and therefore allow to determine the behaviour of the PECs in a range of internuclear distances centred around the potential equilibrium distance.

In this paper we present two independent experimental investigations of alkali – alkaline-earth RbSr molecules, two-colour PA spectroscopy of ultracold Rb-Sr mixtures, and thermoluminescence/LIF spectroscopy of hot molecules, both carried out for the first time on this system. By combining the results from both experiments in a joint analysis and exploiting three previously reported state-of-the-art *ab-initio* calculations [186, 37], we can provide a PEC for RbSr ground-state molecules representing accurately all our experimental data and smoothly bridging the gap between the two spectral ranges investigated. We also determine the molecular constants of the $X(1)^2\Sigma^+$ and $B(2)^2\Sigma^+$ states, and dispersion coefficients of the $X(1)^2\Sigma^+$ state. We use these fitted PECs to benchmark the *ab-initio* calculations, which comes from three independent theoretical methods. Thanks to this analysis, we can infer the molecular spectra with sufficient accuracy to guide future experiments (e.g. STIRAP path towards rovibrational ground state [214, 36, 215]), as well as atomic properties such as scattering cross sections and Fano-Feshbach resonances.

This manuscript is structured as follows. In section 6.2, we summarize the experimental and theoretical information currently available on molecular RbSr, and we introduce the molecular potentials that we investigate. In section 6.3, we present two-colour PA spectroscopy of three RbSr isotopologues performed on μK atomic mixtures. We use the PA spectroscopy results to fit a model from which we extract the long-range dispersion coefficients C_6 and C_8 along with the zero-energy semi-classical action. Based on this spectroscopy type alone, we calculate the s-wave scattering properties of all isotopic combination of Rb and Sr, and explain the location of Fano-Feshbach resonances observed in previous work by some of the authors [188]. The Fano-Feshbach resonances are then included in the fit to provide a single comprehensive model. We corroborate this analysis by comparison with independent cross-thermalization experiments. In section 6.4, we present the thermoluminescence spectroscopy and LIF spectroscopy in a 1000 K heat-pipe oven. We detail the production of the molecular gas sample and its interrogation. We compare the recorded spectrum with three simulated spectra recreated starting from three *ab-initio* theory calculations. From this comparison we identify 24 band heads in the data and give the fitted Dunham coefficients, which describe the lowest vibrational energy levels of the ground and first excited $^2\Sigma^+$ states. In section 6.5, we use the results from both types of spectroscopy to refine the three *ab-initio* ground-state potentials via a

direct potential fit of an analytic function, and discuss the final results and how they compare with theory. In section 6.6, we conclude and give an outlook.

6.2 RbSr state of the art

We first introduce the molecular structure of RbSr and the results of previous studies. RbSr has recently been the subject of theoretical works [31, 186, 37, 216, 36], two of which [186, 37] cover the spectral region that we are investigating and provide state-of-the-art PECs based on *ab-initio* calculations. In the first reference, Żuchowski *et al.* [186] compare two different methods. The first is a full-configuration-interaction (FCI) treatment of RbSr, represented as a molecule with 3 valence electrons subject to an effective core potential (ECP) complemented with a core polarization potential (CPP), which is referred to as FCI-ECP+CPP. The second is a spin-restricted coupled-cluster (RCC) method, applied to a 19 electron problem subject to a fully-relativistic small-core ECP with single, double and triple excitations, referred to as RCCSD(T). In the second reference, Pototschnig *et al.* [37] have provided PECs obtained via multiconfigurational self-consistent field calculations, involving ECP and CPP, followed by second order multireference configuration interaction, which we label MRCI in the following. For all three methods, PECs of the non-rotating molecule were calculated without or with inclusion of the fine-structure Hamiltonian, resulting in Hund case (a,b)[1] or (c) representation, respectively.

Experimental investigation of RbSr has been restricted so far to Helium-nanodroplet-assisted spectroscopy [217, 218]. In these experiments a supersonic jet of He droplets is sequentially injected into pickup cells containing Rb or Sr, which can get caught on the droplet surface and reactively collide forming a RbSr molecule. In contact with superfluid He, RbSr further relaxes to its vibronic ground state, which greatly simplifies spectroscopic studies. Extensive spectroscopy data were collected via resonance-enhanced two-photon ionization, elucidating the electronic structure of RbSr in the spectral region $11600-23000\,\mathrm{cm}^{-1}$, where the precision was limited by line-broadening due to the coupling of RbSr to the He droplet. Remarkably, RbSr desorbed from the droplet upon laser excitation, allowing to record fluorescence of free RbSr molecules and to extract the harmonic constant of the ground state. The experimental value was consistent with theoretical predictions, however the measurement precision was not sufficient to discriminate between the three aforementioned high-precision theoretical PECs.

The electronic states relevant to the present work are those dissociating into the two lowest atomic asymptotes $\mathrm{Rb}(5s\ ^2S) + \mathrm{Sr}(5s^2\ ^1S)$ and $\mathrm{Rb}(5p\ ^2P) + \mathrm{Sr}(5s^2\ ^1S)$,

[1] Hund cases (a) and (b) are equivalent for non-rotating molecules.

see Fig. 6.1. Our thermoluminescence spectra are dominated by levels belonging to the $X(1)^2\Sigma^+$ and $B(2)^2\Sigma^+$ states. Two-colour PA spectroscopy explores the $X(1)^2\Sigma^+$ ground-state potential, by using intermediate molecular states supported by potentials dissociating into the lowest $Rb(5s\ ^2S) + Sr(5s5p\ ^3P)$ asymptote. From our combined measurements we therefore derive quantitative information about the $X(1)^2\Sigma^+$ and $B(2)^2\Sigma^+$ states. Since for both states the projection Λ of the electronic angular momentum $\widetilde{\Lambda}$ on the internuclear axis is zero, spin-orbit coupling vanishes and Hund case (b) is the appropriate representation for the rotating molecule [219]. The corresponding basis vectors are $|\Lambda, N, S, J\rangle$, where N is the momentum given by the coupling between $\widetilde{\Lambda}$ and the nuclear orbital momentum, S is the electron spin and J is the total electronic angular momentum. Moreover, we label F the total angular momentum of the molecule, and f the total angular momentum of the Rb atom.

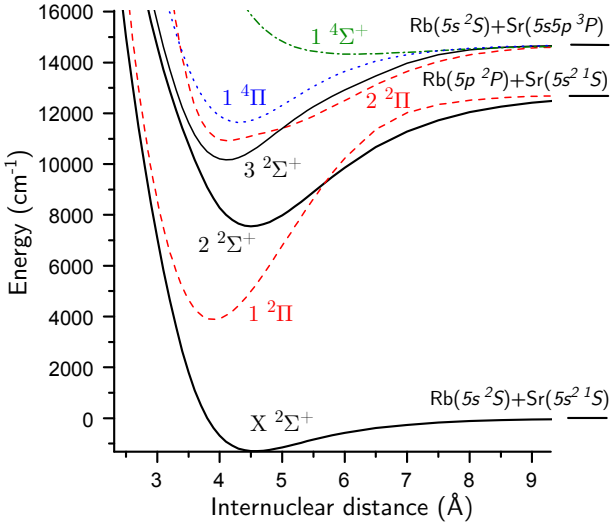

FIGURE 6.1: The potential energy curves calculated using the MRCI method [220] for all states correlating to the $Rb(5s\ ^2S) + Sr(5s^2\ ^1S)$, $Rb(5p\ ^2P) + Sr(5s^2\ ^1S)$ and $Rb(5s\ ^2S) + Sr(5s5p\ ^3P)$ asymptotes. The solid black lines denote $^2\Sigma^+$ states, the dashed red lines $^2\Pi$ states, the dotted blue line a $^4\Pi$ state and the dash-dotted green line a $^4\Sigma^+$ state.

6.3 PA spectroscopy of weakly-bound levels

In this section, we study the bound levels supported by the $X(1)^2\Sigma^+$ RbSr ground-state potential close to the dissociation threshold using μK atomic clouds. We first describe the two-colour photoassociation spectroscopy we use to observe and characterize weakly-bound RbSr molecular levels. We then present the characteristics of the atomic mixture samples studied here. We give the spectroscopy results and discuss their uncertainties. We detail our data analysis and discuss the physical quantities that can readily be extracted from this type of data, such as the zero-energy semi-classical action and the van der Waals dispersion coefficients, which determine the spectrum of weakly-bound levels and the atomic scattering properties. We use our findings to confirm the position and identification of recently observed Fano-Feshbach resonances [188], and include these data into our analysis. Finally, we corroborate the overall analysis by comparing the s-wave scattering lengths inferred by our model with the results of cross-thermalization measurements.

6.3.1 Overview of two-colour photoassociation spectroscopy

We carry out two-colour PA spectroscopy to observe weakly-bound $X(1)^2\Sigma^+$ levels and measure their energies referenced to the energy of the atomic scattering state $\mathrm{Rb}(^2S_{1/2}, f^{\mathrm{Rb}} = 1)+\mathrm{Sr}(^1S_0)$. Two-colour PA spectroscopy exploits the presence of an optically-excited molecular level e, which is coupled to an atom pair state a by the free-bound laser L_{FB} with frequency f_{FB}. When this laser is resonant with the a to e transition, pairs of colliding atoms a are transferred to e, from where they spontaneously decay to low-lying molecular levels, resulting in atom loss.[1] If an additional bound-bound laser L_{BB} with frequency f_{BB} is tuned on resonance with a molecular transition between e and a weakly-bound molecular level m of the $X(1)^2\Sigma^+$ ground state, a significant light shift pushes e out of resonance with L_{FB}. The loss induced by L_{FB} is then suppressed, resulting in an atom number peak when varying the frequency of L_{BB}, see the example in Fig. 6.2. The energy E of the molecular level m referenced to the energy of the atom pair a is directly given at that peak by $E = h \times (f_{\mathrm{BB}} - f_{\mathrm{FB}})$, where h is the Planck constant. In the limit of low temperature and small external fields, the molecular binding energy E_b is equal to E for levels with $F = 1$, and $E_b = E + E_{\mathrm{hf}}$ to within a few MHz for levels with $F = 2$, where E_{hf} is the Rb hyperfine splitting.

[1] We confirm that such loss originates from the formation of RbSr molecules and not Rb_2 or Sr_2 molecules, by verifying that the loss only occurs if both elements are present.

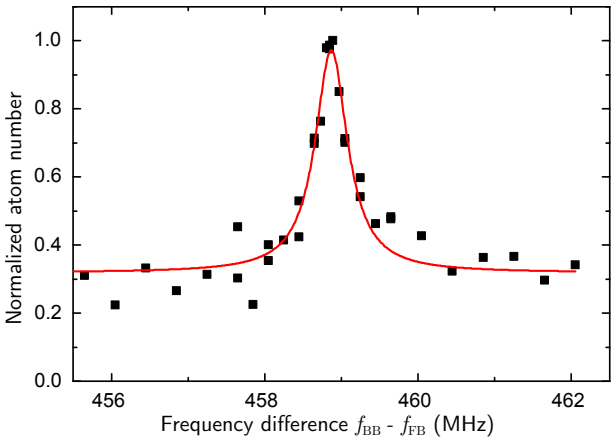

FIGURE 6.2: Typical two-colour photoassociation spectroscopy signal. The plot shows the number of Rb atoms in the $f^{\mathrm{Rb}} = 1$, $m_f^{\mathrm{Rb}} = 1$ level normalized to the atom number in other two $f^{\mathrm{Rb}} = 1$, m_f^{Rb} levels, as function of the frequency difference between L_{BB} and L_{FB}, recorded during a scan of the L_{BB} frequency, while L_{FB} is on resonance with an a to e transition. This signal corresponds to the $\{\nu = 66,\ N = 0,\ F = 1\}$ level of the ^{87}Rb-^{88}Sr ground-state potential, see Table 6.2.

In order to detect weakly-bound levels up to the least bound ones, we exploit similarly weakly-bound levels supported by the electronically excited potentials correlating to the $\mathrm{Rb}(5s\ ^2S_{1/2}) + \mathrm{Sr}(5s5p\ ^3P_1)$ asymptote [221, 186], see Fig. 6.1. These levels provide sufficient Franck-Condon factors between e and m, while the narrow linewidth of the nearby Sr intercombination transition results only in small losses and heating by off-resonant scattering of photons on Sr atoms.

6.3.2 Sample conditions and spectroscopy setup

We prepare the desired ultracold mixtures of Rb-Sr isotope as in our previous works [33, 34, 188]. We keep the mixture in a crossed-beam dipole trap formed by one 1064-nm horizontal elliptical beam with a vertical waist of 19(1) μm and a horizontal waist of 313(16) μm, and one 1064-nm (or 1070-nm) vertical beam with a waist of 78(2) μm (or 90(5) μm). When studying ^{87}Sr, we add a 532-nm beam with vertical (horizontal) waist of 19(1) μm (219(4) μm) to increase the trap depth, in order to capture more Sr atoms. We prepare ^{87}Rb in its hyperfine ground state ($^2S_{1/2}, f^{\mathrm{Rb}} = 1$) with almost

equal population of the Zeeman sub-levels $m_f^{\mathrm{Rb}} = 0, \pm 1$. During PA spectroscopy, we measure each m_f^{Rb} population separately via time-of-flight expansion in a Stern-Gerlach magnetic field gradient. Bosonic Sr isotopes ^{84}Sr and ^{88}Sr have zero nuclear magnetic moment leading to a structureless $^1S_0$ ground state. Fermionic ^{87}Sr has a non-zero nuclear magnetic moment of $i^{\mathrm{Sr}} = 9/2$ and is prepared in the stretched state $m_i^{\mathrm{Sr}} = 9/2$ or $m_i^{\mathrm{Sr}} = -9/2$ via optical pumping.

The atomic samples used to study ^{87}Rb^{84}Sr and ^{87}Rb^{88}Sr molecules have a temperature of $1.0(1)\,\mu$K, average densities of $0.3 - 4 \times 10^{12}\,\mathrm{cm}^{-3}$ for Sr and $2 - 7 \times 10^{12}\,\mathrm{cm}^{-3}$ for Rb (summing over all m_f^{Rb} levels), and the trap frequencies are $\{\omega_x, \omega_y, \omega_z\} = 2\pi \times \{66(6), 57(6), 560(50)\}\,\mathrm{Hz}$ for Sr and $2\pi \times \{110(10), 95(9), 950(80)\}\,\mathrm{Hz}$ for Rb,[2][3] where the z-axis is vertical. The samples used to study the fermionic ^{87}Rb^{87}Sr molecules have a temperature of $1.5(1)\,\mu$K, average densities in the range $2 - 6 \times 10^{11}\,\mathrm{cm}^{-3}$ for Sr and $0.8 - 3 \times 10^{12}\,\mathrm{cm}^{-3}$ for Rb, and trapping frequencies in the range $\{\omega_x, \omega_y, \omega_z\} = 2\pi \times \{70 - 80, 55 - 70, 590 - 640\}\,\mathrm{Hz}$ for Sr and $2\pi \times \{110 - 130, 95 - 125, 820 - 930\}\,\mathrm{Hz}$ for Rb.

The PA beam, containing both L_{FB} and L_{BB}, propagates horizontally at a $\sim 30°$ angle from the axis of the horizontal dipole trap and has a waist of either $60(1)\,\mu$m or $110(10)\,\mu$m, depending on the transition strength and the available laser power. L_{FB} and L_{BB} are derived from the same master oscillator, either via injection-lock or beat-lock, which ensures good coherence between them (typically below 100 Hz for injection-locked and $\sim 30\,$kHz for beat-locked lasers, which is a negligible contribution to the error on the determination of binding energies). We apply a homogeneous magnetic field in the range of 0 to 20 G. We vary the polarization and frequency of $L_{\mathrm{FB,BB}}$ as required to optimally detect a specific molecular transition or level. We adjust the pulse time and power of L_{FB} in order to induce 70 to 90 % loss of Sr atoms. The L_{BB} intensity is chosen such as to obtain a good signal-to-noise ratio for the two-colour PA signal, while not being limited by off-resonant scattering of photons on Sr atoms.

6.3.3 Experimental results

We have observed a total of 10 molecular levels via two-colour PA spectroscopy, of which we report the energies E in Table 6.1. We also report the one-colour PA line

[2]The error bars on the trap frequencies are dominated by the uncertainty on the waists previously stated.

[3]The sample used to find the ^{87}Rb^{88}Sr level at a binding energy of $h \times 459\,$MHz has a temperature of $1.5(1)\,\mu$K, average densities $6.4(2.2) \times 10^{12}\,\mathrm{cm}^{-3}$ for Sr and $8.4(3.0) \times 10^{11}\,\mathrm{cm}^{-3}$ for Rb, and trapping frequencies $\{\omega_x, \omega_y, \omega_z\} = 2\pi \times \{57(7), 8(1), 930(100)\}$ Hz for Sr and $2\pi \times \{97(10), 14(2), 1600(200)\}$ Hz for Rb.

used, the type of transition induced, the angular momentum projections involved and the bound-bound Rabi frequency, if characterized. Levels with negative values of E are necessarily levels with $F = 2$. The typical error of E_b is significantly larger than the uncertainty of $(f_{\mathrm{BB}} - f_{\mathrm{FB}})$, and is the result of several sources of uncertainty.

TABLE 6.1: Results of two-colour PA spectroscopy. The energy E is given by the two-colour frequency detuning $E/h = \nu_{L_{\mathrm{BB}}} - \nu_{L_{\mathrm{FB}}}$ at $B = 0\,\mathrm{G}$. Δ is the detuning of L_{FB} from the Sr $^1\mathrm{S}_0 - ^3\mathrm{P}_1$ transition for bosonic molecules and from the Sr $(^1\mathrm{S}_0, F = 9/2) - (^3\mathrm{P}_1, F = 11/2)$ transition for ^{87}Rb^{87}Sr molecules. The column labelled "Transition" shows the type of transition addressed by both L_{FB} and L_{BB}. The labels m_f^{at} and m_F^{mol} are the projections of the total angular momentum on the quantization axis, neglecting nuclear rotation and the nuclear spin of ^{87}Sr, for the atomic and molecular levels, respectively. For some excited levels $m_F^{mol,e}$ is not known. Such levels are all high-field seeking. The last column gives the bound-bound Rabi frequencies, if measured, between molecular levels m and e in the electronic ground and excited states

Isotopologue	E/h (MHz)	Δ (MHz)	Transition	m_f^{at}, $m_F^{mol,e}$, $m_F^{mol,g}$	$\Omega/2\pi$ (kHz/$\sqrt{\mathrm{mW/cm^2}}$)
^{87}Rb^{84}Sr	29.01(3)	173.5(2), 427.8(2)	π	0, 0, 0	-, 16(1)
	744.53(3)	173.5(2), 427.8(2)	π	0, 0, 0	6.7(3), 285(10)
^{87}Rb^{87}Sr	199.97(17)	686.79(23)	σ^-	-1,-,-1	6.0(5)
	287.27(18)	686.79(23)	σ^-	-1, -, -1	22.2(2.0)
	1950.24(11)	686.79(23)	σ^-	-1, -, -1	-
^{87}Rb^{88}Sr	$-6476.80(4)$	41.39(60)	$\sigma^\pm$	0, -, 0	0.31(6)
	$-4677.78(15)$	260.54(5)	$\sigma^\pm$	0, 0, 0	-
	356.99(3)	41.39(60)	π	0, -, 0	3.39(25)
	458.90(22)	53.5(4)	π	-1, -, -1	3.1(1.3)
	2153.83(15)	260.54(5)	π	0, 0, 0	0.59(13)

The first significant error contribution comes from the differential Zeeman shift between the atom pair a and the molecular level m. In order to minimize this contribution, we exploit the fact that, in the case of equal spin quantum numbers $F = f^{\mathrm{Rb}}$ and $m_F = m_f^{\mathrm{Rb}}$, this shift is vanishingly small for weak binding energy of the molecular level m, see the example of Fig. 6.3. We thus drive two-colour transitions between the atom pair in $f^{\mathrm{Rb}} = 1$ and molecular levels with $F = 1$ and $m_F = m_f^{\mathrm{Rb}}$. We derive a differential magnetic moment of $-2.0(2.0)\,\mathrm{kHz/G}$, resulting in a maximum systematic shift in the range 0.2-20.0 kHz for the measured points. For molecular levels with $F = 2$, we drive magnetically insensitive two-colour transitions with $m_F = m_f^{\mathrm{Rb}} = 0$. This results in a systematic shift of at the most 10 Hz for the measured points.

The second error contribution is the light shift on the two-colour transition arising from the spectroscopy lasers themselves. We have characterized it for some of the

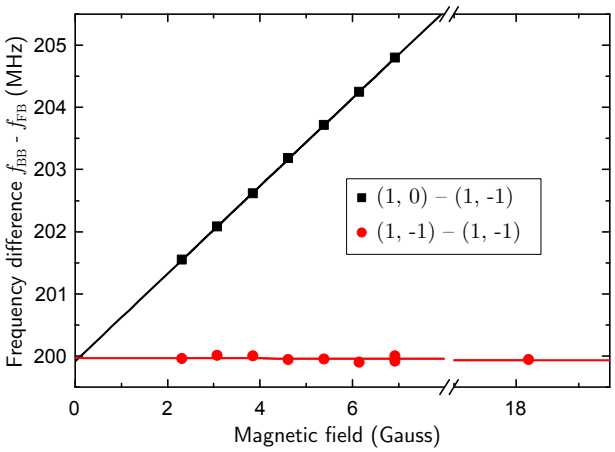

FIGURE 6.3: The plot shows the variation of molecular level energy $E/h = \nu_{L_{\mathrm{BB}}} - \nu_{L_{\mathrm{FB}}}$ as function of the magnetic field for the $(F, m_F) - (f^{\mathrm{Rb}}, m_f^{\mathrm{Rb}})$ transitions $(1,0) - (1,-1)$ (black squares) and $(1,-1) - (1,-1)$ (red disks) and corresponding linear fits. The error bars of the measurements are smaller than the symbol sizes.

points and estimated it for the others as explained in our previous work [176]. This amounts to shifts up to 100 kHz for the typical laser powers used here.

The third error contribution is the light shift on the two-colour transition arising from the dipole trap. Similarly to the previous error contribution, it is characterized for some of the points, and estimated for the others. Given the trap used here, only the differential polarizability between atoms and molecules affecting the centre-of-mass Hamiltonian is relevant. For Sr_2 we have shown that this effect is smaller than 1 % [176]. Here we use the conservative value of 5 % to estimate the errors when not characterized.

The last error contribution comes from thermal shifts and is typically negligible, as a temperature around 1 μK corresponds to an energy of about $h \times 20$ kHz.

6.3.4 Data analysis

Line attribution and estimation of physical quantities.

The first step in a quantitative analysis of the weakly-bound spectrum is a line attribution, by which we mean the assignment of quantum numbers to the atomic and

molecular levels used in the measurements of E. Angular momenta F and N of molecular levels are not known, and their proper assignment is crucial to the success of any model-fitting attempt. From the experiment, we partially know the angular momenta of atomic levels: we measure the Rb atomic spin angular momentum $f^{\mathrm{Rb}} = 1$ and its projection m_f, and for ^{87}Sr we measure the nuclear momentum projection m_i^{Sr}. On the other hand, despite the low temperature of the sample, the atomic relative orbital momentum is not known and all possible assignments of quantum numbers must be tested by the fit in order to find the best one.

Attributing quantum numbers to molecular levels is not trivial, especially in cases of sparse spectral data like the present one. In the spectral region considered here, i.e. for $E_b << D_e$ with D_e the molecular potential depth, only universal, model-independent properties are invoked in order to attribute quantum numbers without the help of any additional *a priori* information on the molecular potential. These properties are:

1. the asymptotic behaviour of the interaction potential V_g as $V_g(r) \to -C_6/r^6$ at large internuclear distance $r \gg R_L$, where R_L is the LeRoy radius;

2. the presence of a strong repulsive wall at the inner classical turning point, i.e. $|\frac{dV_g}{dr}(R_1)| \gg |\frac{dV_g}{dr}(R_2)|$, where R_1 and R_2 are the inner and outer classical turning points;

3. mass-scalability under the Born-Oppenheimer approximation, due to the presence of a single electronic state.

Property 1 implies that the semi-classical phase accumulation of the zero-energy scattering wavefunction $\Phi^0_{WKB} = \Phi_{WKB}(E_b = 0)$ is well defined. Moreover, because of both property 2 and the condition $E_b << D_e$, Φ_{WKB} is to a large extent model-independent [222]. Property 3 implies that a single-channel Hamiltonian, containing $V_g(r)$, explains all spectral data for different isotopologues via simple mass-scaling. Based on these considerations, a single well-defined value Φ^0_{WKB} referenced to an isotopologue of choice is sufficient to describe our system. In this work we choose the isotopologue with highest abundance ^{85}Rb^{88}Sr as our reference. As a consequence of these properties, we expect that two physical quantities Φ^0_{WKB} and C_6 can be extracted from our data by fitting our complete dataset and assigning the quantum numbers consistently. We employ a simple semi-classical approach to find the correct attribution of quantum numbers F and N [223].

We use this fitting strategy on the two-colour photoassociation spectroscopy data presented in Table 6.2 (labeled as "PA" in the "Method" column). Only a single attribution of quantum numbers delivers a satisfactory fit, which we report in Table 6.2 in

columns F and N. This simple fitting strategy is thus sufficient to provide an unambiguous attribution for these two quantum numbers. As expected, the vast majority of observed molecular levels are either $N = 0$ or $N = 2$. Even so, let us note the presence of two $N = 3$ levels for ^{87}Rb^{88}Sr, which might seem inconsistent with our ultracold sample temperature. However, due to the presence of a virtual near-threshold level in this isotopologue, the amplitude of the p-wave scattering wavefunction at the one-colour PA Condon point is less than a factor of 3 smaller than that of typical s-wave scattering states. The fit also provides a first estimation for Φ^0_{WKB} and C_6. We extract the zero-energy semi-classical action $\Phi^0_{WKB} = 67.42(1)$, which gives 67 bound levels for ^{87}Rb^{84}Sr and ^{87}Rb^{87}Sr, and 68 bound levels for ^{87}Rb^{88}Sr, and we extract the dispersion coefficient $C_6 = 1.78(2) \times 10^7$ Å^6 cm^{-1}. Both quantities are determined with better accuracy and precision in the following sections.

TABLE 6.2: List of observed molecular levels, with the experimentally determined binding energies E_b, the binding energies used to fit the data $\langle E_b \rangle$ and corresponding errors approximated by the theoretically estimated shift from the variation of the hyperfine splitting $\delta E_{\rm hf}$. The values E_b^{th} represent the binding energies given by the best fit in Sec. 6.3.4. The quantum numbers $\{\nu, N, F\}$ identifying each level are also shown. The vibrational quantum number ν is counted starting from the lowest level, which has $\nu = 0$

Isotopologue	E_b/h (MHz)	$\langle E_b \rangle/h$ (MHz)	$\delta E_{\rm hf}/h$ (MHz)	E_b^{th}/h (MHz)	ν	N	F	Method
^{87}Rb^{84}Sr	29.01(3)	29.01	0.094	28.93	66	0	1	PA
	744.53(3)	744.53	0.82	745.27	65	0	1	PA
^{87}Rb^{87}Sr	199.97(17)	199.97	0.34	199.90	66	2	1	PA,FFR
	287.27(18)	287.71	0.44	287.30	66	0	1	PA,FFR
	288.2(4)	287.71	0.44	287.30	66	0	2	FFR
	1950.24(11)	1950.24	1.56	1953.00	65	0	1	PA
	5991.8(1.4)	5991.8	3.30	5991.64	64	2	2	FFR
	6233.8(1.0)	6233.8	3.39	6232.14	64	0	2	FFR
^{87}Rb^{88}Sr	356.99(3)	357.43	0.50	357.21	66	2	1	PA
	357.87(4)	357.43	0.50	357.21	66	2	2	PA
	458.90(22)	458.9	0.59	459.12	66	0	1	PA
	2153.83(15)	2155.37	1.67	2158.40	65	3	1	PA
	2156.91(15)	2155.37	1.67	2158.40	65	3	2	PA
	7401.01(66)	7401.01	3.80	7397.47	64	0	2	FFR

Extraction of physical quantities.

Based on the quantum number attribution of F and N explained in the previous section, we check the consistency of our data with the universal long-range dispersion and extract the relevant physical quantities from a fit. We assess consistency with

our data using the reduced chi-square as figure of merit:

$$\widetilde{\chi}^2 = \frac{1}{\mathrm{DOF}} \times \sum_i \left(\frac{E_{b,i}^{exp} - E_{b,i}^{th}}{\Delta E_{b,i}^{exp}} \right)^2, \tag{6.1}$$

where DOF is the number of degrees of freedom in the fit,[1] i runs over the experimentally observed levels, $E_{b,i}^{exp}$ is the i^{th} measured binding energy (BE), $E_{b,i}^{th}$ is the i^{th} predicted BE and $\Delta E_{b,i}^{exp}$ is the experimental error of $E_{b,i}^{exp}$. We consider $\widetilde{\chi}^2$ to be good if close to unity, i.e. $\widetilde{\chi}^2 \lesssim 1$. Although probability levels can only be associated to confidence intervals if the experimental error distribution is known, we nevertheless state confidence intervals based on the absolute variation of $\widetilde{\chi}^2$, without quantitative knowledge of the associated probability level.

We fit a single-channel Hamiltonian model to our experimental data [223] in order to retrieve the relevant physical information, i.e. the zero-energy semi-classical action and dispersion coefficients. This means we require consistency between BEs measured via two-colour PA spectroscopy and the bound spectrum supported by the Hamiltonian:

$$\widetilde{H} = \widetilde{T} + \widetilde{V}_{int} + \widetilde{V}_{rot} = -\frac{\hbar^2}{2\mu}\frac{d^2}{dr^2} + V_g(r) + \frac{\hbar^2}{2\mu}\frac{N(N+1)}{r^2}, \tag{6.2}$$

where $\widetilde{T}$ is the kinetic energy operator, μ is the reduced mass, $\widetilde{V}_{rot}$ is the rotational energy operator and $\widetilde{V}_{int}$ is the interaction operator corresponding for the ground state to V_g, which obeys the properties enumerated in Sec. 6.3.4. For simplicity, we here use the generalized Lennard-Jones model for V_g:

$$V_{LJ}(r) = \frac{C_6}{r^6} \times \left(\left(\frac{\sigma}{r}\right)^6 - 1 \right) - \sum_{n\geq 2}^{N_{vdW}} \frac{C_{2(2+n)}}{r^{2(2+n)}}, \tag{6.3}$$

which contains the leading order dispersion coefficients $C_6, C_8, ..., C_{2(2+N_{vdW})}$. The maximum order N_{vdW} used in the long-range asymptotic expansion is chosen as the lowest number that is able to provide a good fit of our data by the weakly-bound spectrum supported by V_{LJ}. The parameter σ is used to tune the short-range phase accumulation.

Due to the presence of a single electronic ground-state in RbSr, the simple single-channel model (6.2) is sufficient to provide a quantum number attribution for our

[1] The DOF are defined as the number of experimental data points minus the number of fit parameters.

experimental data, as explained in Sec. 6.3.4. However, it is in general not sufficient to precisely fit high-resolution spectra. This is mostly due to the fact that the two $^2\Sigma^+$ PECs of $F = 1$ and $F = 2$ character are not exactly parallel [35]. At large nuclear separation r the splitting $E_{\rm hf}(r)$ between these PECs is the Rb atom hyperfine splitting, whereas it is reduced by about 10 % at the bottom of the PECs. This effect is due to the reduction of the electronic density at the Rb nucleus because of the bonding with Sr. Although extremely small, it is responsible for the strongest Fano-Feshbach resonances recently observed in RbSr [188]. In the present work, our precision and accuracy are enough to reveal hints for this effect, appearing as small differences in the BEs of levels with the same ν and N quantum numbers but different F, see the pairs of BEs of ^{87}Rb^{88}Sr $\{\nu = 66, N = 2\}$ and $\{\nu = 65, N = 3\}$ in Table 6.2. However, our data are not sufficient to extract this shift reliably and include it in our model.[1] We therefore keep a single-channel model and take this effect into account as a systematic error contribution to $\Delta E_{b,i}$. This contribution is estimated using the aforementioned differences in BEs and knowing that the change in hyperfine splitting scales as $\delta E_{\rm hf} \propto E_b^{2/3}$ close to the dissociation threshold [127]. These estimated shifts $\delta E_{{\rm hf},i}$, which dominate the errors $\Delta E_{b,i}$, are of the same order of magnitude as the shift predictions from *ab-initio* results [35], and are listed in Table 6.2. When BEs of both hyperfine states are measured, the mean binding energy $\langle E_b \rangle$ is used in the fit, see Table 6.2. The quality of this estimation is assessed a posteriori via the $\widetilde{\chi}^2$ of the best fit, i.e. $\widetilde{\chi}^2_{\rm min}$.

We fit the model Hamiltonian (6.2) to our PA spectroscopy data, using $\{\sigma, C_6, ..., C_{2(2+N_{vdW})}\}$ as independent fit parameters and we retrieve the zero-energy semi-classical action $\Phi^0_{WKB} = \Phi^0_{WKB}(\sigma, C_6, ..., C_{2(2+N_{vdW})})$. For $N_{vdW} = 1, 2, 3$ we obtain for the best fits $\widetilde{\chi}^2_{\rm min} = 41, 0.24, 0.32$, respectively. This shows that the inclusion of C_6 and C_8 terms is *necessary* and *sufficient* to model our data. We obtain the best fit parameters $\sigma = 5.012941656601387$ Å, $C_6 = 1.784438900566861 \times 10^7$ Å^6 cm^{-1}, $C_8 = 6.18126306008073 \times 10^8$ Å^8 cm^{-1} with DOF $= 5$. The fit gives the values $\sigma = 5.01(15)$ Å, $C_6 = 1.784(15) \times 10^7$ Å^6 cm^{-1}, $C_8 = 6.2(1.1) \times 10^8$ Å^8 cm^{-1}, and a corresponding $\Phi^0_{WKB} = 67.4379(12)$.[2] The errors stated in brackets correspond to, somewhat arbitrarily, the joint confidence region with $\Delta\widetilde{\chi}^2 = \widetilde{\chi}^2 - \widetilde{\chi}^2_{\rm min} = 1$. In Fig. 6.4 we show the configurations sampled by the fitting procedure that provide the

[1] The two observed shifts mentioned involve rotationally excited molecular states with unknown spin-rotation coupling, hence they do not directly yield the shift under discussion. The simplest experiment able to characterize this shift requires the measurement of pairs of rotationless states at different BEs.

[2] We stress that the number of vibrational levels is determined without uncertainty. All isotopologues have 67 vibrational levels, except for the two with the highest mass ^{87}Rb^{88}Sr and ^{87}Rb^{87}Sr, which have 68.

evaluation of the confidence regions. The dispersion coefficients are consistent with theoretical predictions [224, 225, 226, 35].

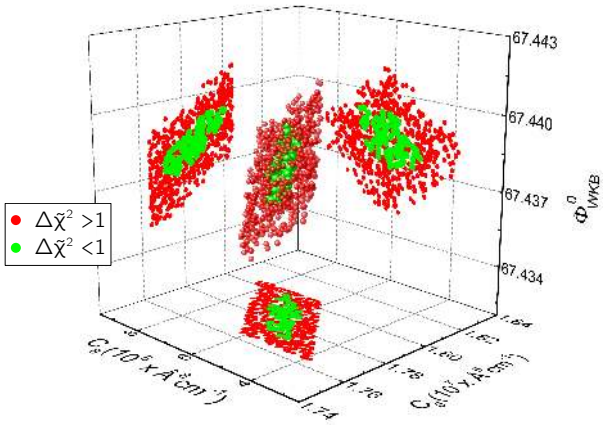

FIGURE 6.4: Confidence intervals. The plot shows $\widetilde{\chi}^2$ for configurations sampled close to the best fit configuration in the fit-parameter space, with its projections on the 2D coordinate planes. The total confidence regions corresponding to $\Delta\widetilde{\chi}^2 < 1$, used for error estimates, are indicated as green balls in the centre.

Atomic scattering properties at a given collisional energy and in the absence of external magnetic fields can be directly derived from the fitted PEC [223]. Scattering wavefunctions are obtained by integration of the nuclear Schrödinger equation for the appropriate relative angular momentum L, i.e. $\widetilde{H}(N)\psi_N(r) = E_{coll}\psi_N(r)$, where $\widetilde{H}(N)$ is the fitted Hamiltonian (6.2) with explicit N-dependence and $E_{coll} = \hbar^2k^2/2\mu$ is the collisional energy with wavevector k. Of particular interest for the cold atoms community are the scattering properties in the limit $E_{coll} \to 0$, which are dominated by s-wave scattering, i.e. $N = 0$. In this limit the scattering phase shift $\delta\phi \to -ka_s$ and the cross-section $\sigma_s \to 4\pi a_s^2$ are determined by a single parameter, the s-wave scattering length a_s, which we report in Table 6.3 for all stable isotopologues of RbSr.[2]. In Fig. 6.5 we show the s-wave scattering wavefunctions for a collision energy $E_{coll} = k_B \times 1.0\,\mu$K, with k_B the Boltzmann constant, where the effect of the scattering length on both the asymptotic phase shift and the short-range scattering

[2]The s-wave scattering length a_s is calculated by fitting ψ_0 at large r with the known asymptotic behaviour $\psi_0(r) \to \alpha r + \beta$, where α and β are fit parameters. a_s is then given by $a_s = -\beta/\alpha$ [98]

amplitude is evident. The s-wave scattering lengths derived from the fitted model for ^{87}Rb^{84}Sr and ^{87}Rb^{88}Sr are in good agreement with those extracted from the cross-thermalization measurements presented in Sec. 6.3.5, which corroborate the overall analysis carried out to this point.

TABLE 6.3: s-wave scattering lengths in units of the Bohr radius

	^{84}Sr	^{86}Sr	^{87}Sr	^{88}Sr
^{85}Rb	689(20)	90.6(0.2)	44.3(0.3)	−35.8(1.0)
^{87}Rb	92.7(0.2)	−43.0(1.1)	1421(98)	170.3(0.6)

Validation and inclusion of Fano-Feshbach spectroscopy.

The model described in the previous section is also *sufficient* to infer within a few Gauss the resonant magnetic field of the magnetically-tunable Fano-Feshbach resonances (FFRs) present in RbSr. Let us note that we can only derive FFR locations from the fitted PEC with experiment-level accuracy thanks to the extreme simplicity of the $^2\Sigma^+$ ground state of RbSr [223, 188]. The existence and observability of this novel type of FFRs was theoretically predicted a few years ago [35] and recently experimentally observed by some of the authors [188].

The best fit V_{LJ} in the previous section (see eqn (6.3)) predicts the location of FFRs for fermionic ^{87}Rb^{87}Sr within 10 G and has been used to infer with the same accuracy the location of one ^{87}Rb^{88}Sr FFR arising from the state $\{\nu = 64, N = 0, F = 2\}$, subsequently observed in our ultracold Rb-Sr mixture experiment [188]. The BEs and corresponding quantum number attribution of the bound levels inducing the FFRs derived from the experiment and our model are reported in Table 6.2, and marked with "FFR" in the "Method" column. As a complementary check, we apply the fitting procedure to the data set including both PA and FFRs, which results in the *same unique* solution. As in the case of two-colour PA spectroscopy data alone, inclusion of C_6 and C_8 is *necessary* and *sufficient* to model the complete data set. The best fit parameters are $\sigma = 5.02477864619132$ Å, $C_6 = 1.776513404206001 \times 10^7$ Å^6 cm^{-1}, $C_8 = 6.262096495696839 \times 10^8$ Å^8 cm^{-1}, with DOF = 8 and $\widetilde{\chi}^2_{\rm min} = 1.29$. The fit gives the values $\sigma = 5.02(19)$ Å, $C_6 = 1.777(18) \times 10^7$ Å^6 cm^{-1}, $C_8 = 6.3(1.3) \times 10^8$ Å^8 cm^{-1}, and a corresponding $\Phi^0_{WKB} = 67.4370(13)$. There is a significant increase in our figure of merit compared to Sec. 6.3.4, which we attribute primarily to the inclusion of deeper $F = 2$ states with rather large $\delta E_{\rm hf}$, and secondarily to the change in

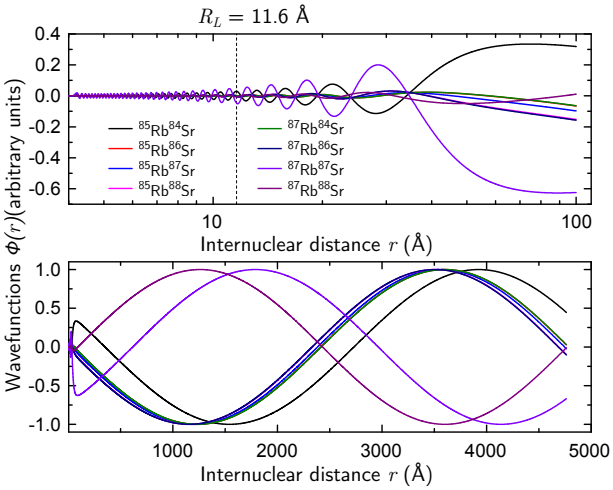

FIGURE 6.5: Atomic pair scattering wavefunctions. The top panel shows the scattering wavefunctions as function of the internuclear distance for all RbSr isotopes in the range of typical PA Condon points, which are only meaningful for $r > R_L$. The bottom panel shows the scattering wavefunctions at large distance where the phase shift encodes the short-range physics. We note that two pairs of isotopes have incidentally almost the same reduced mass, hence almost overlapping wavefunctions.

DOF. The inferred s-wave scattering lengths are consistent with those presented in Table 6.5.

The ability to predict FFRs with high accuracy is extremely valuable for mixtures with one open-shell and one closed-shell atom, due to the low density of resonances in these systems, in particular in the case of zero nuclear magnetic moment for the closed-shell atom, as in bosonic RbSr isotopologues [35, 227, 127]. As an example of the outcomes of our model, Fig. 6.6 shows the energy of the atomic scattering levels and molecular levels of ^{87}Rb^{84}Sr in dependence of magnetic field, and the locations of the predicted FFRs. Due to favourable scattering properties, this isotopic combination is a very good candidate for magneto-association [34].

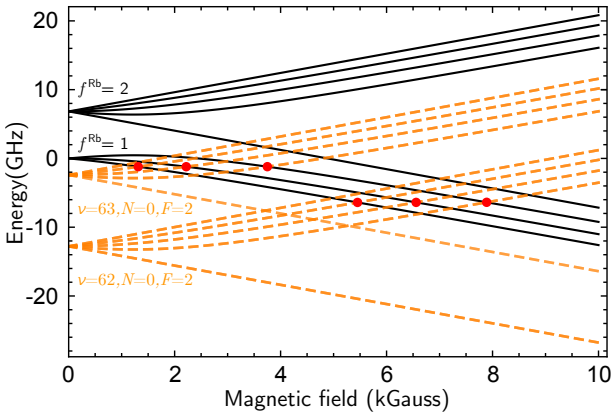

FIGURE 6.6: Zeeman sub-levels of ^{87}Rb^{84}Sr. The plot shows the energy of $f^{\mathrm{Rb}} = 1, 2$ atomic levels (black solid lines) and of $F = 2$ molecular levels (orange dashed lines) in dependence of magnetic field. The red dots mark the location of FFRs in this magnetic field range.

6.3.5 An independent check of quantum number assignment: inter-species thermalization

An improper quantum number attribution strongly affects the *accuracy* of the inferred scattering lengths. We therefore experimentally characterize the thermalization of Rb atoms with a Sr cloud to measure the Rb-Sr inter-species s-wave scattering lengths, and thus confirm our quantum number attribution. The values of scattering lengths obtained by thermalization experiments suffer from low *precision*, however they constitute a useful cross-check, as they rely on simple collisional physics and are independent from our PA and Fano-Feshbach spectroscopy experiments. We present thermalization experiments done with ^{87}Rb-^{84}Sr and ^{87}Rb-^{88}Sr. Trapped ultracold mixtures of ^{87}Rb-^{87}Sr show notably stronger 3-body losses, which limit the reliability of the data analysis for this particular mixture.

Experimental setup and sample conditions.

The starting point of the thermalization measurement is an ultracold mixture composed of ^{87}Rb and either ^{84}Sr or ^{88}Sr, prepared as for spectroscopy experiments, with the addition of evaporative cooling by lowering the dipole trap potential in 6 s, followed by a 1 s re-compression of the potential, which is used to tune the atomic

density and temperature. After this preparation sequence, the sample has a temperature between 200 and 400 nK and contains $1 - 1.7 \times 10^5$ atoms of ^{84,88}Sr and $50 - 70 \times 10^3$ atoms of ^{87}Rb. The typical shot-to-shot temperature fluctuation is 15 nK, while shot-to-shot atom number fluctuations are 15×10^3 and 5×10^3 for Sr and Rb, respectively. The trapping frequencies in our crossed-beam dipole trap are $\{\omega_x, \omega_y, \omega_z\} = 2\pi \times \{35 - 65, 20 - 55, 500(25)\}$ Hz for Sr and $\{\omega_x, \omega_y, \omega_z\} = 2\pi \times \{60 - 105, 35 - 90, 840(40)\}$ Hz for Rb, respectively. The frequency ranges in the horizontal x and y axes correspond to various trap re-compressions. The relative uncertainty on these frequencies is less than 5 %. The difference of trap frequencies between Sr isotopes is less than the uncertainty, hence negligible. The atomic densities used here are $n_{\mathrm{Sr}} = 0.3 - 3 \times 10^{12}\,\mathrm{cm}^{-3}$, $n_{\mathrm{Rb}} = 0.7 - 4.4 \times 10^{12}\,\mathrm{cm}^{-3}$ for the ^{87}Rb-^{84}Sr mixture and $n_{\mathrm{Sr}} = 1.7 - 4.4 \times 10^{12}\,\mathrm{cm}^{-3}$, $n_{\mathrm{Rb}} = 1.5 - 5.4 \times 10^{12}\,\mathrm{cm}^{-3}$ for the ^{87}Rb-^{88}Sr mixture. The Rb sample, just like for spectroscopy measurements, is not spin-polarized. Given the existence of a single electronic ground-state, a_s can be considered independent of f^{Rb} and m_f^{Rb}.

Measurement strategy.

In order to observe interspecies collisions, selectively excite the cloud of one species and observe the ensuing inter-species thermalization. Since the dipole trap is roughly three times deeper for Rb than for Sr, we excite the Rb cloud by scattering photons on Rb D_2 line for a few μs. After this excitation, the mixture is kept in the trap for a variable hold time t before a 17 ms time-of-flight expansion followed by absorption imaging. From the absorption images, we extract temperatures and atom numbers of both species. The main limitations to the precision of our measurement are shot-to-shot fluctuations in atom number and temperature.

Experimental results.

We measure the evolution of temperature and atom number for each species as functions of time. In Fig. 6.7 we show an example for each isotopic combination. The temperature of Sr smoothly evolves from the initial temperature $T_E^i = T_{\mathrm{Sr}}(t = 0)$ to the final equilibrium temperature $T_E^f = T_{\mathrm{Sr}}(t \to \infty)$. By contrast, the temperature of Rb shows a sharp decrease on a timescale of a few tens of ms from a temperature of a few μK down to $0.5 - 0.7\,\mu$K, after which the new equilibrium temperature $T_E^f = T_{\mathrm{Rb}}(t \to \infty) = T_{\mathrm{Sr}}(t \to \infty)$ is reached smoothly.

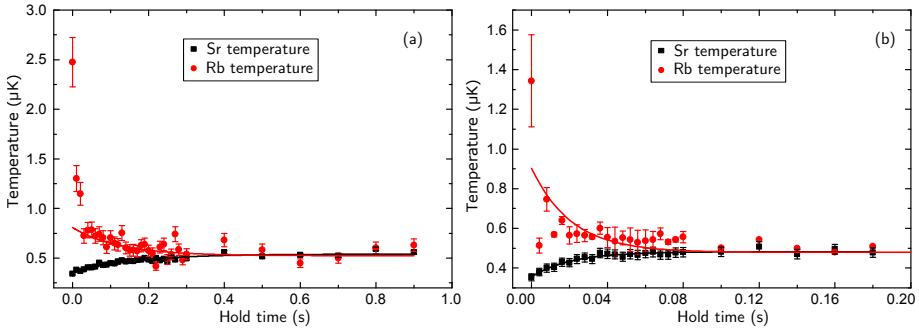

FIGURE 6.7: Inter-species thermalization. Evolution of Sr (black squares) and Rb (red circles) temperature as a function of the hold time during thermalization in (a) ^{87}Rb^{84}Sr mixture at an effective flux of $\Phi = 7.0 \times 10^{12}\,\mathrm{s}^{-1}\,\mathrm{cm}^{-2}$ and (b) ^{87}Rb^{88}Sr mixture at a flux of $\Phi = 1.9 \times 10^{13}\,\mathrm{s}^{-1}\,\mathrm{cm}^{-2}$. The lines are exponential fits to the data.

Extraction of collision cross sections.

We measure the thermalization time of both ^{87}Rb^{84}Sr and ^{87}Rb^{88}Sr mixtures. In the case of close-to-equilibrium dynamics, the evolution of temperatures $T_{1,2}(t)$ is described by exponential functions with the same well-defined time constant τ. We analyse the thermalization rate τ^{-1} using a well-known model [228, 229], which we detail in Appendix 6.7.1. This model gives the relation:

$$\tau^{-1} \approx \frac{1}{2.4}\,\sigma_{12} \times \Phi, \tag{6.4}$$

where $\sigma_{12} = 4\pi\, a_{12}^2$ is the collision cross section dependent on the inter-species s-wave scattering length a_{12}. The value 2.4 in the denominator represents the average number of collisions required for thermalization, when thermalization is fast compared to the trap frequencies. Φ is an effective flux that encompasses the kinematic contribution, see Appendix 6.7.1. We fit our data for various effective fluxes and extract values for τ, shown in Fig. 6.8.

The effective flux Φ is determined through the knowledge of the trap potential, atom cloud numbers and temperatures. All quantities are either measured or known from calibration, with the exception of the initial temperature T^i_{Rb} of the Rb sample right after excitation. Let us note that the excitation we apply experimentally is the injection of energy in the form of both heating and displacement of the cloud.

However, assuming the regime of close-to-equilibrium dynamics, we approximate the excitation to be solely an increase in temperature. The excitation energy of Rb can be derived with good precision from the atom numbers and the temperature evolution of Sr, since the system is isolated after the excitation. The trapping potential can be approximated at these low temperatures by a three dimensional harmonic oscillator potential giving $E = 3\,k_B T$ energy per particle. The final energy in the system E^f must be equal to the initial one E^i, and under our assumptions these are $E^f = 3\,k_B T_E^f (N_{\rm Sr} + N_{\rm Rb})$ and $E^i = 3\,k_B (N_{\rm Sr} T_E^i + N_{\rm Rb} T_{\rm Rb}^i)$. We thus derive $T_{\rm Rb}^i = T_E^f + \frac{N_{\rm Sr}}{N_{\rm Rb}} (T_E^f - T_E^i)$.

Fitting the data of Fig. 6.8 with eqn (6.4), we obtain the inter-species scattering lengths $|a_{^{87}\mathrm{Rb}-^{84}\mathrm{Sr}}| = 103^{+15}_{-10}\,a_0$ and $|a_{^{87}\mathrm{Rb}-^{88}\mathrm{Sr}}| = 215^{+50}_{-40}\,a_0$, where a_0 is the Bohr radius, and where the errors are estimated from the residual sum of squares 5-fold increase and their dependence on the choice of the equilibrium sample parameters (initial or final parameters). Let us note that the variation of the average number of collisions required for thermalization, within the meaningful range $2.4 - 3.0$ [229], leads to a variation of the scattering lengths smaller than the stated error.

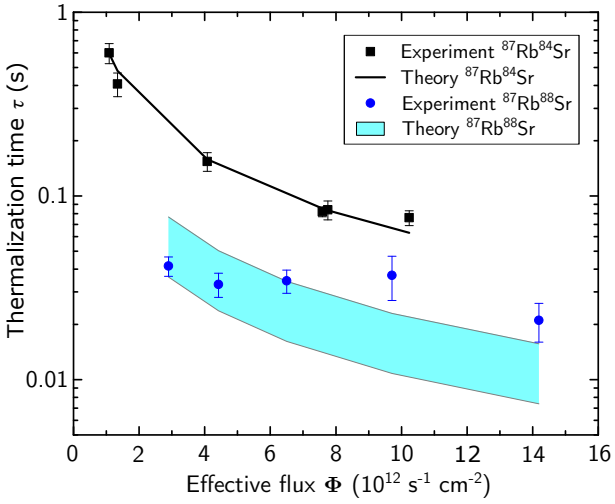

FIGURE 6.8: Thermalization time as function of the effective flux Φ (see main text) for both isotopic combinations. Black squares are data with ^{87}Rb^{84}Sr and blue circles with ^{87}Rb^{88}Sr. The solid black line shows the fit for ^{87}Rb^{84}Sr using the theory described in the text. The light-blue area shows the theoretical region corresponding to the uncertainty of the fitted scattering length for ^{87}Rb^{88}Sr.

While for ^{87}Rb-^{84}Sr the fit is satisfying, the fit of ^{87}Rb-^{88}Sr is worse because of the two points at highest Φ, which we include in the fit. For these two points the thermalization time is comparable with the initial fast time scale of the Rb temperature evolution (see Fig. 6.7), suggesting a strong deviation from the close-to-equilibrium case, as expected from the bigger inter-species scattering length. Nonetheless even in the latter case, a meaningful scattering length can be extracted with a correspondingly (larger) error. Finally, the ^{87}Rb-^{87}Sr mixture shows losses that we interpret as 3-body losses, which for similar densities are not observed in the other mixtures investigated. From this observation, we derive that $|a_{^{87}\mathrm{Rb}^{87}\mathrm{Sr}}| \gg |a_{^{87}\mathrm{Rb}^{88}\mathrm{Sr}}| \simeq 200\,a_0$.

The fitted (central) values of the inter-species scattering lengths are close to, but $10\,\% - 20\,\%$ higher than, the ones inferred from spectroscopy. This is expected since the initial densities of Rb are underestimated by our model, which assumes thermalization. A Monte-Carlo trajectory simulation would most likely improve the accuracy of the scattering lengths extracted from these thermalization measurements.

6.4 Thermoluminescence and LIF spectroscopy of deeply-bound levels

In a second experiment, we study the deeply-bound levels supported by the $B(2)^2\Sigma^+$ and $X(1)^2\Sigma^+$ state potentials via fluorescence spectroscopy of a 1000 K-hot gas mixture of Rb and Sr. In this section, we first describe the experimental setup we use to record the fluorescence from RbSr molecules in a heat-pipe oven. We then explain how we simulate theoretical spectra using three published sets of potential energy curves (PECs) produced by independent *ab-initio* methods. By comparing these spectra with our experimental data, we identify a few band heads, from which we extract Dunham coefficients describing the bottom parts of the $B(2)^2\Sigma^+$ and $X(1)^2\Sigma^+$ states. We repeat the comparison procedure until we identify 24 band heads and produce final sets of Dunham coefficients. Finally, we estimate by a Monte-Carlo method the uncertainty on the Dunham coefficients resulting from our analysis.

6.4.1 Experimental setup

The measurements at high temperatures were performed in two steps. In the first step, we record thermoluminescence spectra using the method and experimental setup described in detail by Szczepkowski *et al.*[204] We therefore provide here only information specific to this paper. We produce RbSr molecules in a dedicated dual-temperature heat-pipe oven. We place 10 g of metallic strontium in the central part of the oven, which is heated to $T_{Sr} = 1000$ K, and 8 g of metallic rubidium in the

outer part, heated to $T_{Rb} = 800\,\mathrm{K}$. Both metals have natural isotopic composition. To ensure the stability of the heat-pipe operation, we use a buffer gas of helium at a pressure of 30 Torr. At the applied temperatures the $B(2)^2\Sigma^+$ electronic state of RbSr is thermally populated, and we record the fluorescence towards the $X(1)^2\Sigma^+$ electronic ground state using a Bruker Vertex V80 Fourier Transform Spectrometer with a spectral resolution of $0.16\,\mathrm{cm}^{-1}$ limited by its aperture size.

In the second step, we obtain spectra via laser induced fluorescence (LIF). We employ a home-made 100 mW external-cavity diode laser whose wavelength is actively stabilized using a HighFinesse WS7 wavemeter. By tuning the laser frequency to the centre of selected band heads, we excite RbSr molecules to the $B(2)^2\Sigma^+$ state and record fluorescence to the ground state with the same spectrometer as before. To increase the contrast between LIF and thermoluminescence signals observed simultaneously, we reduce the temperature of the central part of the heat-pipe to $T_{Sr} = 900\,\mathrm{K}$.

6.4.2 Simulations of the recorded spectra

In order to interpret the experimental spectra, we first simulate fluorescence spectra using PECs and transition dipole moments computed theoretically, and compare theory and experiment. The simulations start from three sets of PECs, obtained independently with FCI-ECP+CPP [186], RCCSD(T) [186], and MRCI [37] methods. We calculate the energies of rovibrational levels of the $B(2)^2\Sigma^+$ and $X(1)^2\Sigma^+$ states by solving the radial Schrödinger equation with each of the three sets of PECs. All bound levels in the $X(1)^2\Sigma^+$ and $B(2)^2\Sigma^+$ states are included in the simulations. The contribution of the $A(1)^2\Pi$ state in this spectral region was found to be negligible. In our calculation we omit the fine structure splitting of molecular levels resulting from spin-rotational coupling. Indeed, the energy difference between fine structure components with low rotational quantum numbers N' contributing to a band head formation is expected to be smaller than the spectral resolution of the measurement [212]. We assume spectral lines having a Gaussian profile with FWHM $= 0.16\,\mathrm{cm}^{-1}$, which results from the Fourier Transform Spectrometer working parameters. Intensities of all spectral lines are calculated assuming thermal equilibrium in the central part of the heat-pipe. The simulation procedure has been described in detail by Szczepkowski *et al.*[204] including formulas necessary to perform the calculations.

The final step in the calculations is to average the simulated spectra of the most abundant isotopologues of RbSr, weighted by their natural abundances (59.6 % for $^{85}Rb^{88}Sr$, 22.9 % for $^{87}Rb^{88}Sr$, 7.1 % for $^{85}Rb^{86}Sr$, 5.1 % for $^{85}Rb^{87}Sr$, 2.7 % for $^{87}Rb^{86}Sr$ and 1.9 % for $^{87}Rb^{87}Sr$). As a result, we obtain three sets of "theoretical spectra" to be compared with the experimental data, shown in Fig. 6.9. The analysis of the spectra reveals that the positions of the observed band heads are defined by

the ^{85}Rb^{88}Sr isotope alone, and other isotopes influence mainly the band-head widths (broadened up to 0.08 cm^{-1}). Thus we only take into account the ^{85}Rb^{88}Sr isotope in the Dunham coefficients generation procedure described in the next subsection. The influence of other isotopes is included again during the error estimation process.

6.4.3 Results

In order to identify the observed band heads, we compare the thermoluminescence spectra of RbSr with the simulated spectra based on the three theoretical methods [186, 37]. Unfortunately, these simulations provide spectra of considerably different shapes for each theory (see Fig. 6.9) and only few experimental band heads can be identified unambiguously as they appear in all three simulations.

To address this issue we record additional LIF spectra by tuning the excitation laser frequency to the centres of already identified band heads. These new experimental data, shown in Fig. 6.10, confirm the validity of the assignment in the case of six band heads. Using the energy of experimental band heads and their assignment confirmed both by thermoluminescence and LIF spectroscopy, we fit preliminary Dunham coefficients for both X(1)$^2\Sigma^+$ and B(2)$^2\Sigma^+$ electronic states. The values of the ground state rotational constants (labelled $Y_{01} \equiv B_e$) were taken from theory for each set and fixed during the fit. We thus obtain three sets of fitted coefficients, each corresponding to one theoretical method. This procedure is described in detail by Szczepkowski *et al.* [204].

These fitted Dunham coefficients allow for a new prediction of the vibrational level energies in the X(1)$^2\Sigma^+$ and B(2)$^2\Sigma^+$ states, followed by an assignment of additional band heads in the thermoluminescence spectrum. With the improved assignment a correction of Dunham coefficients becomes possible, and we repeat the whole procedure until the final identification of 24 band heads, whose energies are given in Table 6.4 as a Deslandres table. To prevent mistakes in the assignment, only the 18 strongest band heads, whose energies are written in bold in the table and whose positions are marked in red in Fig. 6.9, were taken into account in the final fit of Dunham coefficients. As the outcome of this 1000 K-hot gas mixture spectroscopy, these fitted coefficients describe the energies of the six lowest vibrational levels $\nu'' = 0 - 5$ in the ground state and the nine lowest vibrational levels $\nu' = 0 - 8$ of the B(2)$^2\Sigma^+$ state. The final values for Dunham coefficients, given in Table 6.5, will be used in the next steps of our analysis described in the following section.

The uncertainties on the Dunham coefficients result mainly from the determination of the positions and widths of the band heads, as many lines corresponding to transitions between different rovibrational levels of the B(2)$^2\Sigma^+$ and X(1)$^2\Sigma^+$ states overlap in the spectra, and thus only the top parts of the band heads are observed in

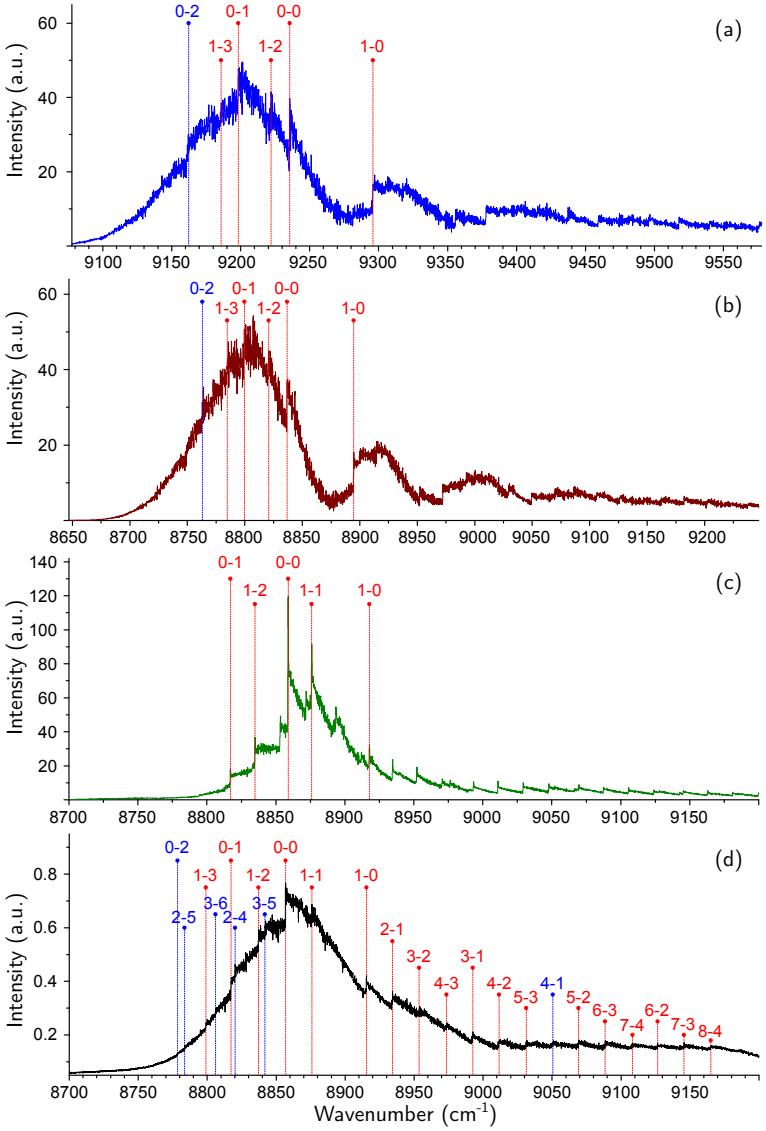

FIGURE 6.9: Thermoluminescence spectra simulated based on the three sets of theoretical PECs for the $X(1)^2\Sigma^+$ and $B(2)^2\Sigma^+$ states, calculated with (a) RCCSD [186], (b) FCI-ECP+CPP [186], and (c) MRCI [37], compared with the experimental data (d). The positions of identified band heads are marked with dashed lines and labelled with their vibrational quantum numbers $\nu' - \nu''$ (where primed and double primed symbols refer to $B(2)^2\Sigma^+$ and $X(1)^2\Sigma^+$, respectively). The wavenumber scales of theoretical spectra are adjusted in such a way that $0 - 0$ band heads are at the same position in all panels. The well-resolved band heads used in the final fit of Dunham coefficients are marked in red.

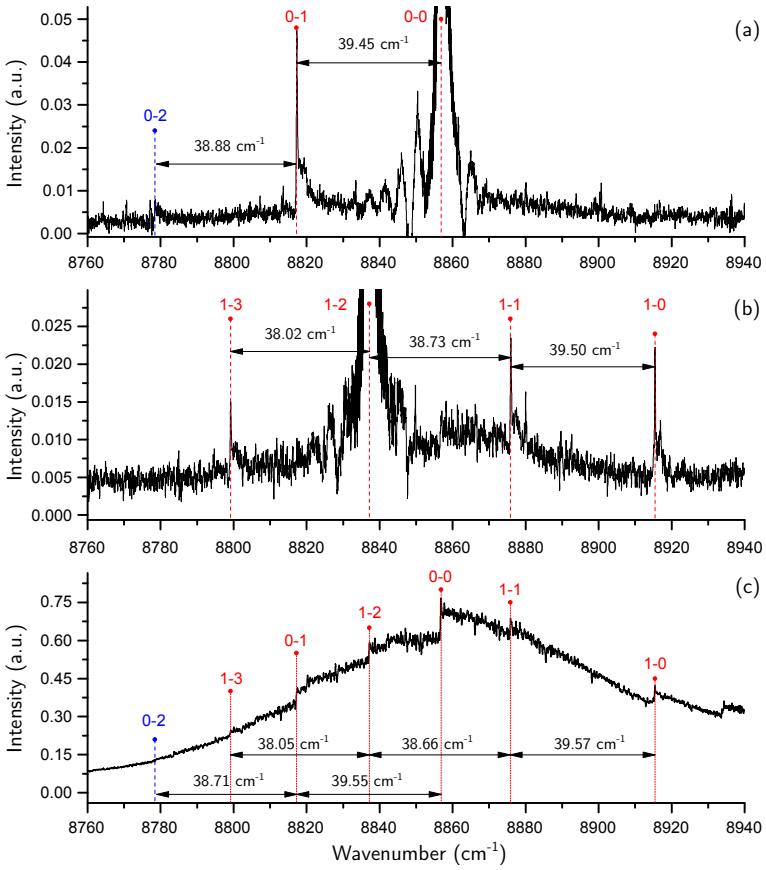

FIGURE 6.10: Comparison of band-head positions in the LIF (a) and (b), and thermoluminescence (c) spectra. The LIF spectra were obtained with the laser tuned to the centres of $\nu' - \nu''$ band heads: (a) $0 - 0$ and (b) $1 - 2$. The well-resolved band heads used in the preliminary fit of Dunham coefficients are marked in red.

TABLE 6.4: Deslandres table constructed for the observed band heads in the experimental thermoluminescence spectrum of RbSr. The wavenumbers of band heads are given in cm^{-1}. The energy of the 18 strongest band heads used in the final fit are written in bold

	$\nu'' = 0$		1		2		3		4		5		6
$\nu' = 0$	**8856.81**	39.55	**8817.26**	38.71	8778.55								
	58.63		58.61		58.66								
1	**8915.44**	39.57	**8875.87**	38.66	**8837.21**	38.05	**8799.16**						
			58.52										
2			**8934.39**						8820.25	36.6	8783.65		
			58.18								58.2		
3			**8992.57**	38.89	**8953.68**						8841.85	35.84	8806.01
			58.06		57.92								
4			9050.63	39.03	**9011.60**	37.97	**8973.63**						
					57.6		57.53						
5					**9069.2**	38.04	**9031.16**						
					57.34		57.35						
6					**9126.54**	38.03	**9088.51**						
							57.17						
7							**9145.68**	37.33	**9108.35**				
									56.82				
8									**9165.17**				

TABLE 6.5: The Dunham coefficients for the $B(2)^2\Sigma^+$ and $X(1)^2\Sigma^+$ states of the $^{85}Rb^{88}Sr$ molecule based on the LIF and thermoluminescence spectra. The three sets of coefficients for each state correspond to different values of the ground state equilibrium distance r_e taken from theoretical calculations. All values are in cm^{-1}

	MRCI[37]	FCI-ECP+CPP[186]	RCCSD(T)[186]
		$X(1)^2\Sigma^+$	
Y_{10}	40.39(0.72)	40.32(0.76)	40.31(0.76)
Y_{20}	−0.39(0.11)	−0.38(0.12)	−0.38(0.12)
$Y_{01} \times 10^2$	1.874[a]	1.84842[a]	1.79052[a]
$Y_{11} \times 10^4$	−0.8(0.6)	−1.1(1.1)	−0.9(1.2)
		$B(2)^2\Sigma^+$	
T_e	8847.92(0.80)	8847.66(0.80)	8847.66(0.80)
Y_{10}	58.96(0.38)	58.95(0.39)	58.95(0.39)
Y_{20}	−0.13(0.04)	−0.13(0.05)	−0.13(0.05)
$Y_{01} \times 10^2$	1.932(0.004)[b]	1.952(0.005)[b]	1.893(0.005)[b]
$Y_{11} \times 10^5$	−8.3(6.4)	−3.4(6.7)	−3.4(6.8)

[a] Values taken from theory and fixed during the fit.
[b] Values strongly correlated with Y_{01} of the $X(1)^2\Sigma^+$ state.

our experiment. We use a Monte-Carlo method to find the error associated with this problem. We randomly vary the positions of individual band heads within a range of $0.46\,cm^{-1}$. The choice for this range results from the band-head half-widths, assumed arbitrarily to be $0.3\,cm^{-1}$, combined with the maximum value of the isotopic shifts. We also vary the widths of individual band heads within $0.16\,cm^{-1}$, a value which influences the number of rovibrational lines taken into consideration in each case. We determine a set of Dunham coefficients for each random combination of positions and widths. We repeat the procedure until the average values of all coefficients becomes equal to the fitted values reported in Table 6.5. The final errors are defined for each Dunham coefficient as three times their standard deviation.

6.5 *Ab initio*-based PEC fit

We now combine the results from both types of spectroscopy, at μK and 1000 K temperatures, and perform a joint fit procedure in order to obtain a model representing the complete spectrum of the $X(1)^2\Sigma^+$ ground state of RbSr. In this section, we first describe the problem we will address. We then submit and motivate our choice of

representation for the potential energy curves. We next detail all steps of our fitting procedure. Finally, we present the results of our joint analysis and compare them with the three *ab-initio* theoretical methods we selected.

6.5.1 Statement of the problem

The goal of our data analysis is to provide a representation of the complete bound spectrum of the electronic ground state. This apparently contradicts the fact that, based on the independent analyses of the weakly- and deeply-bound levels, only 15 % of the vibrational levels, corresponding to less than 25 % of the well depth, were observed. Moreover, two-colour photoassociation spectroscopy has very high-accuracy and precision but only a few weakly-bound levels have been probed, while thermoluminescence spectroscopy explored a significantly bigger energy range but lacks rotational resolution and its precision is limited to $0.16\,\mathrm{cm}^{-1}$. To the knowledge of the authors, such a problem has not been addressed before and requires a novel method of analysis able to exploit all information present in the two data sets at our disposal.

An examination of the methods used in the previous sections shows how to overcome this problem. The weakly-bound spectrum was analysed, without the need for *ab-initio* PECs, via a direct potential fit of an analytic PEC, with the sole requirement of a correct long-range behaviour, see Sec. 6.3.4. The deeply-bound spectrum was analysed by a fit of Dunham expansion coefficients to band heads whose rovibrational composition was determined by the simulated spectrum based on *ab-initio* PECs, see Sec. 6.4.2 and 6.4.3. Since the fitted Lennard-Jones PEC and the Dunham expansion have no predictive power beyond the corresponding regions of definition, the results of those analyses are valid separately but cannot be extrapolated in the region with missing data. However, an *ab initio*-based model with an appropriate PEC for the $X(1)^2\Sigma^+$ state and a correlated $B(2)^2\Sigma^+$ state is expected to be a good representation of the complete data set, capable of predictive power for the $X(1)^2\Sigma^+$ state, and easily refined in the future by inclusion of new data.

6.5.2 Representation of the $X(1)^2\Sigma^+$ and $B(2)^2\Sigma^+$ state PECs

We now choose a suitable representation of the RbSr $X(1)^2\Sigma^+$ and $B(2)^2\Sigma^+$ states. A somewhat similar problem, albeit considerably more intricate, arose in the case of the excited $1^3\Sigma_g^+$ state in the homonuclear Li_2 molecule accessed via the $1^3\Sigma_g^+ \rightarrow a^3\Sigma_u^+$ system, see Dattani *et al.*[230] The authors were able to bridge a $5000\,\mathrm{cm}^{-1}$ gap in spectroscopy data, i.e. 70 % of the well depth, by performing direct potential fit

of Morse/Long-Range (MLR) functions to a rovibrationally resolved high-precision spectrum.[1].

The MLR function appears to be particularly suited to represent the RbSr ground state. Indeed, since the RbSr X(1)$^2\Sigma^+$ state is a single isolated electronic state and RbSr is a heavy molecule, the MLR PEC can easily represent the long-range tail, Born-Oppenheimer breakdown effects are expected to be small [232] [2], and damping functions are readily incorporated [235]. On the other hand, the B(2)$^2\Sigma^+$ state relevant for thermoluminescence spectroscopy is experimentally probed only close to its bottom, far from other electronic states, so it can be explicitly included in the analysis. However, compared to the case of Li_2, the precision of our thermoluminescence data is significantly lower and lacks rotational resolution. As a consequence, for different reasons compared to the case of Dattani *et al.* [230], the fit is non-trivial and a specific method must be devised.

The version of the MLR function used in this work is the same as in Dattani *et al.* [230]:

$$V_{\mathrm{MLR}}(r) = D_e \left[1 - \frac{u(r)}{u(r_e)} e^{-\beta(y_p(r), y_q(r))\cdot y_p(r)}\right]^2, \tag{6.5}$$

$$u(r) = \sum_{i=1}^{N_u} d_{m_i}(r) \cdot \frac{C_{m_i}}{r^{m_i}}, \tag{6.6}$$

$$y_x(r) = \frac{r^x - r_e^x}{r^x + r_e^x}, \tag{6.7}$$

$$\beta\left(y_p, y_q\right) = \ln\left(\frac{2D_e}{u(r_e)}\right) \cdot y_p(r) + (1 - y_p(r)) \cdot \sum_{i=0}^{N_\beta} \beta_i \left(y_q(r)\right)^i, \tag{6.8}$$

where D_e is the well depth, r_e is the equilibrium distance, $u(r)$ is the function describing the long-range behaviour, $y_x(r)$ is an x-order effective radial variable and $\beta\left(y_p, y_q\right)$ is the exponent coefficient of the radial variable y_p.[3] The functions $d_{m_i}(r)$, explicitly included in eqn (6.6), are Douketis-type [236] damping functions $D_m^s(r)$ with $s = -1$ and adapted to RbSr by scaling of the radial variable via atomic ionization potentials [237] as explained in Dattani *et al.* [230] The C_{m_i} coefficients in eqn (6.6) are the N_u lowest order dispersion coefficients.

[1] Successively, the binding energies extrapolated in the gap region were experimentally confirmed within $1.5\,\mathrm{cm}^{-1}$ [231].

[2] Adiabatic corrections are similar to those in Rb_2 [233, 234].

[3] Compared to Dattani *et al.* [230], the notation is simplified because we set $r_{ref} = r_e$, i.e. all effective radial variables are referenced to r_e.

In order to represent the theoretical PECs by MLR functions we choose a family of these functions and values of their parameters based on the available theoretical calculations. The family of the MLR functions is defined by the choice of N_u in eqn (6.6), N_β in eqn (6.8) and p, q. We use perturbation-theory results for C_6, C_8 and C_{10} available in the literature [224] and set $N_u = 3$. This choice implies $p > m_{last} - m_1 = 4$ and correspondingly $1 < q < p$ [230], with a contribution to the asymptotic long-range tail of order $r^{-m_1-p} = r^{-6-p}$. We resolve this indefiniteness, together with the one of N_β, by fitting the MLR function to the three point-wise representations of *ab-initio* PECs in the region $r \geq 3.0\,\text{Å}$, using the unweighted $\widetilde{\chi}^2$ as figure of merit, with errors set to $1.0\,\text{cm}^{-1}$. In all fitted cases we obtain $\widetilde{\chi}^2_{\text{min}} \simeq 1.0$ with "well-behaved" PECs, i.e. with a single inflection point, already for $N_\beta = 5$, and the best fits are obtained for low values of p, q. Hence, we eventually set $N_u = 3$, $N_\beta = 5$, $p = 5$ and $q = 2$, which we hold constant during later fits. Since our data on deeply-bound levels are not rotationally resolved and since weakly-bound levels, within our experimental precision, do not carry information on the equilibrium distance r_e, we set r_e equal to the equilibrium distances from the theoretical calculations and hold it fixed during fits. The remaining parameters D_e and β_i are fitted to the three point-wise representations of *ab-initio* PECs. This provides us with the three desired MLR functions representing the PECs from the three theoretical calculations, which we later use as starting conditions for fitting our experimental data. Since harmonic and first anharmonic contributions are sufficient to represent the data, see Sec. 6.4.3, only the parameters that strongly affect the lowest derivatives at $r = r_e$ need to be fitted to the thermoluminescence data. These are the coefficients β_i with lowest i. In summary, in the following fitting procedure of all experimental data, we will treat $\beta_{0 \leq i \leq 2}$, C_6, C_8 and D_e as the only fitting parameters, retaining in this way the theoretical shape of each PEC in the region where no data are available.

A well defined representation of the $\text{B}(2)^2\Sigma^+$ state is needed to simulate the thermoluminescence spectrum. We adopt a point-wise representation determined both by our experiment and by theoretical calculations in the region of missing data. This is realized by initializing the PEC with the *ab-initio* predictions and adapting it to fitted Dunham coefficients via the Inverted Perturbation Approach [238], see Sec. 6.5.3. The bottom part of the potential, determined by the experiment, and the upper part, determined by theory, are matched smoothly to provide a well depth referenced to that of the ground state. Within this representation the fitting parameters are the Dunham coefficients, which provide the link between the representations of the $\text{X}(1)^2\Sigma^+$ and $\text{B}(2)^2\Sigma^+$ states.

6.5.3 Fit Method

We fit our model of the $X(1)^2\Sigma^+$ and $B(2)^2\Sigma^+$ states to experimental data both from two-colour photoassociation and thermoluminescence/LIF spectroscopy. In particular, the fitted experimental quantities for two-colour PA are binding energies, while in the case of thermoluminescence/LIF they are band-head wavenumbers and, with lesser precision, the overall intensity profile. We recall that the fit parameters are those defining V_{MLR} for the $X(1)^2\Sigma^+$ state and the Dunham coefficients of the $X(1)^2\Sigma^+ - B(2)^2\Sigma^+$ system. While the weakly-bound spectrum and the band-head positions do not determine precisely the equilibrium distances, the intensity profile carries this information together with the overall potential shapes and can be used to adjust the equilibrium distance of the $B(2)^2\Sigma^+$ state with respect to that of the $X(1)^2\Sigma^+$ state. The initial values for the fit parameters in V_{MLR} are defined in Sec. 6.5.2 for each *ab-initio* model, while the initial values for the Dunham coefficients are those of Table 6.5. The figure of merit used in the fit is $\widetilde{\chi}^2$, see eqn (6.1). In the following, we outline a single iteration step of our fit, which is applied to each model, while a future work will provide a detailed explanation [223].

We first generate the rovibrational levels of $X(1)^2\Sigma^+$, using the fitted Dunham coefficients, for the range $v'' = \langle 0 - 6 \rangle$ for $N'' = 0$, and fit them together with the experimental weakly-bound energy levels, via a direct potential fit of our model MLR PEC [223]. We derive the $B(2)^2\Sigma^+$ state depth from the MLR D_e parameter and the Dunham coefficients. We then construct the $B(2)^2\Sigma^+$ PEC via the Inverted Pertubation Approach, using both the $B(2)^2\Sigma^+$ energy levels, generated with Dunham coefficients in the range $v' = \langle 0 - 8 \rangle$ for $N' = \langle 0 - 44 \rangle$, and the $B(2)^2\Sigma^+$ potential well depth. We simulate the thermoluminescence spectra using the resulting PECs, in order to check the agreement of the simulated band-head positions and intensity profiles with the experimental ones. Here the convergence of the fit algorithm is checked and, if met, the calculation is stopped. Otherwise, we optimize the equilibrium point of the $B(2)^2\Sigma^+$ state to maximize the agreement between the simulated intensity profile and the experimental one. During this optimization, for each change of the equilibrium point, the $B(2)^2\Sigma^+$ state is optimized against the $X(1)^2\Sigma^+$ state, which consists in fitting the Dunham coefficients of the $B(2)^2\Sigma^+$ state keeping those of the $X(1)^2\Sigma^+$ state fixed. With this new guess for the equilibrium distance of the $B(2)^2\Sigma^+$ state, we refit all Dunham coefficients of both states, see Sec. 6.4.3, and repeat the iteration step.

6.5.4 Results and discussion

The fit outlined above is performed separately starting with FCI-ECP+CPP, RCC SD(T) and MRCI *ab-initio* point-wise representations. In all cases we obtain satisfying agreement between our best-fit model and the binding energies and band-head positions. However, while in the case of MRCI and FCI-ECP+CPP potential energy curves, the $B(2)^2\Sigma^+$ state depth inferred after the first iteration is within $190\,\mathrm{cm}^{-1}$ of the *ab-initio* predictions, in the case of RCCSDS(T) the well depth is about $440\,\mathrm{cm}^{-1}$ away from the theoretical value. As a consequence, we observe that all *ab-initio* PECs give a sufficiently good representation of the RbSr ground state allowing for experimental fits, but only FCI-ECP+CPP and MRCI predictions are able to approximate the excited state well enough to permit its refinement by tuning its equilibrium distance. Best-fit parameters for the $X(1)^2\Sigma^+$ state MLR functions and refined point-wise representations of the $B(2)^2\Sigma^+$ state are reported in the Appendix 6.7.2. The derived Dunham coefficients for both $X(1)^2\Sigma^+$ and $B(2)^2\Sigma^+$ states are consistent with those in Table 6.5. A comparison between the initial MLR functions, fitted to *ab-initio* data, and the final MLR functions, based on *ab-initio* PECs and fitted to experimental data, is shown in Fig. 6.11.

The convergence of the three PECs towards a unique solution, as illustrated in Fig. 6.11, and the good agreement with our experimental data corroborate our fit method. In particular, we observe that our experimental information is enough to strongly constrain the depth of the ground state potential well to $D_e = 1152^{+9}_{-16}\,\mathrm{cm}^{-1}$.[1] The fitted PECs are consistent with the model-independent quantities derived in the previous sections up to residual model dependency. In particular, compared to those of Sec. 6.3.4, the dispersion coefficient C_6 and the semiclassical phase Φ^0_{WKB} are slightly bigger, which is mostly due to the inclusion of C_{10} in the MLR model,[2] while the C_8 is consistent within our relatively low precision. The fit quality of weakly-bound states can still be assessed by the $\widetilde{\chi}^2$ and DOF = 8 used in Sec. 6.3.4, since it is insensitive to β_i fitting parameters. We obtain 0.89, 0.53 and 0.99 for MRCI, FCI-ECP+CPP and RCCSD(T), respectively, which are all sufficiently good. We use the $\widetilde{\chi}^2$ with DOF = 10 error set to 0.16 cm^{-1} of the distance between band-head positions in experimental and simulated thermoluminescence spectra as a second benchmark of the fitted potential energy curves. We obtain 0.83, 0.5 and 1.78 for MRCI, FCI-ECP+CPP and RCCSD(T) respectively, which shows agreement within our experimental resolution.

[1] Although the depths derived from the FCI-ECP+CPP and RCCSD(T) methods are extremely close, we attribute to D_e the mean value of all three cases and the full uncertainty range.

[2] By fitting once more the weakly-bound spectrum with V_{LJ} including a C_{10} term fixed to the theoretical value, we obtain $C_6 = 1.7962010665716115 \times 10^7\,\mathrm{\AA}^6\,\mathrm{cm}^{-1}$, $C_8 = 5.792504377056786 \times 10^8\,\mathrm{\AA}^8\,\mathrm{cm}^{-1}$ and $\Phi^0_{WKB} = 67.4386$.

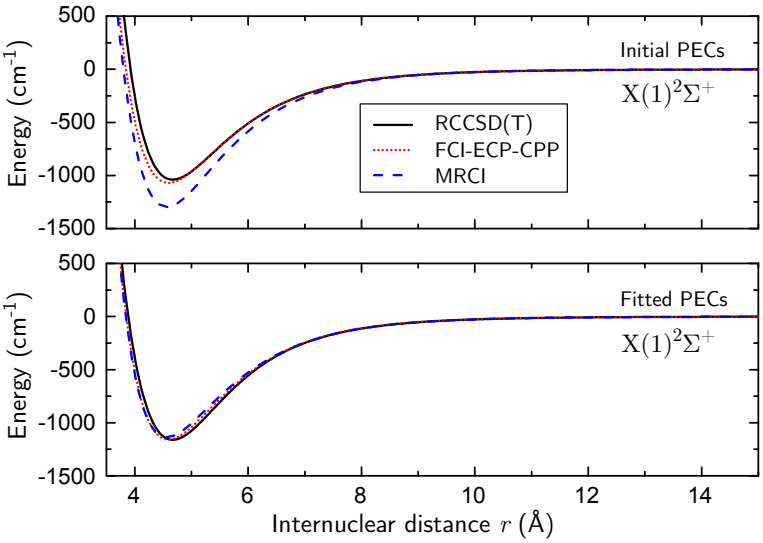

FIGURE 6.11: PECs of the $X(1)^2\Sigma^+$ state of RbSr. Top panel: theoretical PECs corresponding to the three different *ab-initio* calculations considered in this work. Bottom panel: PECs fitted to experimental data with initial fit parameters determined by each *ab-initio* method, see Sec. 6.5.3.

In Table 6.6 the experimental values of spectroscopic constants are compared with the theoretical ones. Also here the convergence of the described fitting procedure is remarkable. The final value of the vibrational constant ω_e does not depend on the starting *ab-initio* PECs used in the fit for both $X(1)^2\Sigma^+$ and $B(2)^2\Sigma^+$ states. However, the agreement between the experimental and theoretical ω_e values obtained is clearly the best for the FCI-ECP+CPP model. Similarly this model provides the best prediction of the potential well depths D_e of the investigated states and of the number of bound levels in the ground state. The experimental data also allow to determine the difference between equilibrium distances of the $X(1)^2\Sigma^+$ and $B(2)^2\Sigma^+$ electronic states, $\Delta r_e = r_{e\mathrm{B}} - r_{e\mathrm{X}}$, and the values obtained are almost identical when starting from theoretical PECs calculated with the FCI-ECP+CPP ($\Delta r_e = -0.086$Å) and MRCI ($\Delta r_e = -0.087$Å) methods.

Finally, we check in two ways the quality of the final fitted potential for the $X(1)^2\Sigma^+$ state. Firstly, we simulate the thermoluminescence spectrum by using the potential we obtained starting from the FCI-ECP+CPP potential, as it gives the

TABLE 6.6: Comparison of spectroscopic constants and dispersion coefficients for the $X(1)^2\Sigma^+$ and $B(2)^2\Sigma^+$ states of the $^{85}Rb^{88}Sr$ molecule. Units of energy and length are cm^{-1} and Å, respectively, while Φ^0_{WKB} is dimensionless. The final errors, defined as three times the standard deviation, are given in parenthesis

	D_e	ω_e	$B_e \times 10^2$	r_e [Å]	T_e	$C_6 \times 10^{-7}$	$C_8 \times 10^{-8}$	Φ^0_{WKB}
			$X(1)^2\Sigma^+$					
present[a]	1136	40.39(0.72)	1.874[e]	4.565[e]	0	1.81(2)	5.8(1.3)	67.4393
present[b]	1158	40.32(0.76)	1.848[e]	4.595[e]	0	1.80(2)	6.1(1.3)	67.4381
present[c]	1161	40.31(0.76)	1.791[e]	4.669[e]	0	1.81(2)	5.90(1.3)	67.4396
experimental[217]	–	42(5)	–	–	–	–	–	–
MRCI[37]	1298	42.5	1.874	4.565	0	–	–	70.7768
FCI-ECP+CPP[186]	1073.3	38.98	1.848	4.595	0	–	–	65.8890
RCCSD(T)[186]	1040.5	38.09	1.791	4.669	0	–	–	64.7252
ST[220]	1273	42.2	1.853	4.590	0	–	–	–
CCSD(T)[216]	916	36	1.75	4.72	0	–	–	–
Relativistic KR-MRCI[36]	1017.58	35.8	1.8	4.66	0	–	–	–
theory[224]	–	–	–	–	–	1.783	6.220	–
			$B(2)^2\Sigma^+$					
present[a]	5025	58.92(0.38)	1.946	4.478	8848.0(0.8)	–	–	–
present[b]	5047	58.94(0.39)	1.920	4.509	8847.6(0.8)	–	–	–
present[d]	5050	58.95(0.39)	1.893	–	8847.7(0.8)	–	–	–
MRCI[37]	5214	59.5	1.921	4.507	8830	–	–	–
FCI-ECP+CPP[186]	4982.9	58.37	1.975	4.445	8828	–	–	–
EOM-CC[186]	4609.6	60.20	1.925	4.503	9224	–	–	–
ST[220]	5078	58.5	1.899	4.533	8711	–	–	–
Relativistic KR-MRCI[36]	4683.56	58.1	1.98	4.43	9151	–	–	–
theory[224]	–	–	–	–	–	8.448	59.80	–

[a] based on MRCI[37] *ab-initio* calculation
[b] based on FCI-ECP+CPP[186] *ab-initio* calculation
[c] based on RCCSD(T)[186] *ab-initio* calculation
[d] based on RCCSD(T)[186] and EOM-CC[186] *ab-initio* calculation; parameters taken from Dunham coefficients listed in Table 6.5
[e] fixed during the fit at the theoretical value

best agreement between theoretical and experimental values of molecular constants. In Fig. 6.12 we show a comparison of this simulation with the experimental results. The agreement for the band head positions between the two spectra is almost perfect, and this allows the assignment of even more band heads. Secondly, we use the fitted $X(1)^2\Sigma^+$ state potential to calculate the positions of Fano-Feshbach resonances, which are listed in Tables 6.7 and 6.8. At the time of writing of this paper and thanks to these predictions, the resonances at about 1.3 kG for $^{87}Rb^{84}Sr$ and 1.0 kG for $^{87}Rb^{88}Sr$ have indeed been observed experimentally at the expected magnetic fields, which proves the high quality of the potential we obtained for the RbSr $X(1)^2\Sigma^+$ state.

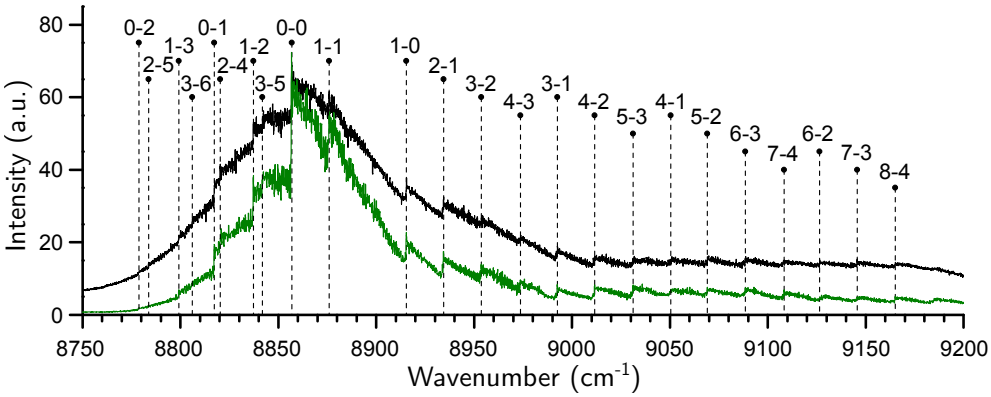

FIGURE 6.12: Comparison of the original experimental spectrum (upper curve, in black) with the spectrum simulated using the experimental potential employing the ground state r_e value from the FCI-ECP+CPP [186] calculations (lower curve, in green). The positions of identified band heads are marked with dashed lines and with the assigned vibrational quantum numbers $\nu' - \nu''$.

TABLE 6.7: Fano-Feshbach resonances for ^{85}Rb^{84,86,87,88}Sr isotopologues due to coupling between $N = 0$ molecular levels and $N = 0$ atomic scattering levels in the magnetic field region $B < 3.0$ kG. E_b is the binding energy of the bound state, f^{Rb}, m_f^{Rb}, F and m_F are the quantum numbers defined in the main text identifying the open and closed channel, respectively. B is the resonant magnetic field, $\Delta\mu$ is the differential magnetic moment, and ΔB is the width of the resonance calculated as the avoided crossing gap divided by $\Delta\mu$. The avoided crossing gap is calculated for the two-body problem in the species-independent external confinement provided by a potential well with $\omega = 2\pi \times 60$ kHz isotropic trapping frequency, by using first order perturbation theory and the *ab-initio* coupling matrix term [35]

BE (MHz)	f^{Rb}	m_f^{Rb}	F	m_F	B (G)	$\Delta\mu$ (MHz/G)	ΔB (mG)
^{85}Rb^{84}Sr							
6644.83	2	-2	3	-2	2950.99	-2.64	31.40
6644.83	2	-1	3	-1	2500.46	-2.53	35.06
6644.83	2	0	3	0	2108.76	-2.49	31.82
6644.83	2	1	3	1	1778.42	-2.53	24.94
6644.83	2	2	3	2	1506.91	-2.64	16.03
^{85}Rb^{86}Sr							
3421.32	2	-2	3	-2	1637.55	-2.10	5.37
3421.32	2	-1	3	-1	1029.72	-1.54	5.85
3421.32	2	0	3	0	562.87	-1.29	4.03
3421.32	2	1	3	1	307.68	-1.54	1.75
3421.32	2	2	3	2	193.47	-2.10	0.63
9308.75	2	1	3	1	2799.16	-2.67	4.71
9308.75	2	2	3	2	2499.41	-2.72	3.26
^{85}Rb^{87}Sr							
78.63	2	-1	2	-2	157.16	-0.53	0
78.63	2	0	2	-1	165.59	-0.48	0
78.63	2	1	2	0	174.48	-0.43	0
78.63	2	2	2	1	183.83	-0.39	0
78.63	3	-3	3	-2	149.40	-0.59	0
78.63	3	-2	3	-1	157.41	-0.53	0
78.63	3	-1	3	0	165.88	-0.47	0
78.63	3	0	3	1	174.82	-0.43	0
78.63	3	1	3	2	184.23	-0.39	0
78.63	3	2	3	3	194.10	-0.35	0
1071.24	2	-2	3	-3	1329.33	0.56	0
1071.24	3	-3	3	-2	995.37	-1.85	0
4227.19	2	-2	3	-2	1995.89	-2.37	-5.26
4227.19	2	-2	3	-1	1741.03	-2.22	0
4227.19	2	-1	3	-2	1740.39	-2.23	0
4227.19	2	-1	3	-1	1470.84	-2.06	5.63
4227.19	2	-1	3	0	1256.20	-1.98	0
4227.19	2	0	3	-1	1255.68	-1.99	0
4227.19	2	0	3	0	1049.46	-1.95	4.51
4227.19	2	0	3	1	889.86	-1.97	0
4227.19	2	1	3	0	889.49	-1.98	0
4227.19	2	1	3	1	748.80	-2.06	2.87
4227.19	2	1	3	2	642.03	-2.19	0
4227.19	2	2	3	1	641.79	-2.19	0
4227.19	2	2	3	2	551.81	-2.37	-1.46
4227.19	2	2	3	3	482.92	-2.57	0
4227.19	3	-3	3	-2	2314.53	-2.65	0
10827.35	2	2	3	3	2916.48	-2.77	0
^{85}Rb^{88}Sr							
5128.78	2	-2	3	-2	2364.10	-2.52	8.32
5128.78	2	-1	3	-1	1879.36	-2.33	9.05
5128.78	2	0	3	0	1474.80	-2.26	7.75
5128.78	2	1	3	1	1157.32	-2.33	5.57
5128.78	2	2	3	2	920.02	-2.52	-3.24

TABLE 6.8: Fano-Feshbach resonances for ^{87}Rb^{84,86,87,88}Sr isotopologues due to coupling between $N = 0$ molecular levels and $N = 0$ atomic scattering levels in the magnetic field region $B < 3.0$ kG. E_b is the binding energy of the bound state, f^{Rb}, m_f^{Rb}, F and m_F are the quantum numbers defined in the main text identifying the open and closed channel, respectively. B is the resonant magnetic field, $\Delta\mu$ is the differential magnetic moment, and ΔB is the width of the resonance calculated as the avoided crossing gap divided by $\Delta\mu$. The avoided crossing gap is calculated for the two-body problem in the species-independent external confinement provided by a potential well with $\omega = 2\pi \times 60$ kHz isotropic trapping frequency, by using first order perturbation theory and the *ab-initio* coupling matrix term [35]

BE (MHz)	f^{Rb}	m_f^{Rb}	F	m_F	B (G)	$\Delta\mu$ (MHz/G)	ΔB (mG)
^{87}Rb^{84}Sr							
9242.30	1	0	2	0	2218.82	-1.89	3.77
9242.30	1	1	2	1	1312.74	-2.15	1.69
^{87}Rb^{86}Sr							
12546.80	1	1	2	1	2726.72	-2.47	4.35
^{87}Rb^{87}Sr							
0.01	1	-1	1	0	0.18	0.70	0
0.01	1	0	1	1	0.18	0.70	0
0.01	2	-1	2	-2	0.18	0.70	0
0.01	2	0	2	-1	0.18	0.70	0
0.01	2	1	2	0	0.18	0.70	0
0.01	2	2	2	1	0.18	0.70	0
287.32	1	0	1	-1	397.14	-0.74	0
287.32	1	1	1	0	432.35	-0.62	0
287.32	2	-2	2	-1	366.06	-0.88	0
287.32	2	-1	2	0	398.65	-0.73	0
287.32	2	0	2	1	434.30	-0.62	0
287.32	2	1	2	2	473.02	-0.52	0
1952.06	2	-2	2	-1	1672.34	-1.70	0
6235.49	1	-1	2	-2	294.64	1.96	0
6235.49	1	-1	2	-1	1918.11	-0.88	-59.55
6235.49	1	-1	2	-1	519.45	0.88	16.13
^{87}Rb^{88}Sr							
7403.10	1	-1	2	-1	2804.54	-1.68	-8.73
7403.10	1	0	2	0	1014.50	-1.08	-5.70
7403.10	1	1	2	1	366.98	-1.68	-1.14

6.6 Conclusions and Outlook

We have performed two different types of spectroscopy in order to investigate the ground and second excited electronic states, both of $^2\Sigma^+$ symmetry, of the alkali – alkaline-earth RbSr molecule. We have presented a novel procedure to connect data from two-colour photoassociation measurements, which provide information on energy levels of the X(1)$^2\Sigma^+$ state near the dissociation threshold, and low-resolution data from thermoluminescence experiment, which allow to describe the bottom of

both $X(1)^2\Sigma^+$ and $B(2)^2\Sigma^+$ PECs. As the thermoluminescence spectra lack rotational resolution, the equilibrium distance between the Rb and Sr nuclei can not be determined from our measurements and must be taken from theoretical calculations. Therefore we use three different sets of theoretical PECs, resulting from state-of-the-art *ab-initio* calculations, as starting points for the fit of potential energy curves to the experimental data. We obtain three potentials derived for the $X(1)^2\Sigma^+$ state, but despite significant differences between the starting potentials, the three fitted ones converge to nearly the same curve shape. In the region of missing experimental data the shapes of the fitted PECs stay close to the starting theoretical potentials and this region awaits future spectroscopic investigation to be refined. Although in the case of the $B(2)^2\Sigma^+$ state, the experimental data provided only information about deeply-bound energy levels, our procedure is able to reject one theory that diverges too much from the experimental results.

We have demonstrated that our data analysis method is a powerful tool to obtain potential energy curves of heavy molecules, where achieving rotational resolution is difficult and investigation of mid-range spectrum challenging. This method may find a welcome use in the field of physical chemistry, since it shows, in the simple case of diatomic molecules, that several independent sources of information, both experimental and theoretical, can be synthesized successfully. The findings of our analysis may be of interest to physicists from various fields. Indeed, calculations performed with the fitted RbSr potentials demonstrated their power to predict the positions of unassigned band heads and intensity distribution of the spectra, but also the positions of Feshbach resonances, some of which have later been confirmed experimentally [188]. As a next step, we plan to further refine the PECs derived in this work via new LIF experiments with rotational resolution, and to account for effects from the hyperfine and spin-rotation couplings. We will also use the results of this work to provide an efficient STIRAP path for RbSr molecules towards the rovibrational ground level [36]. With such molecules available, one can study chemistry reactions with full control over both reactants and products at the quantum level [202, 5, 203].

6.7 Appendix

6.7.1 Theoretical model for inter-species thermalization

A rigorous analysis of the experimental data would require a Monte-Carlo trajectory simulation taking into account the initial atomic distributions, the subsequent excitation of Rb cloud and the elastic cross section, both inter-species and intra-species. However, we are here only interested in a confirmation of our ground-state potential model and for that we do not require precise values for the scattering lengths. Moreover we observe that, although during the thermalization the system is out of equilibrium, it might be close enough to equilibrium to apply a very simple collision model giving the cross-thermalization rate from equilibrium statistical physics [228]. This is suggested in our case by the very fast decrease in Rb temperature compared to the cross-thermalization time. In order to clarify the analysis, we review the model here.

The temperature difference is expected to decrease exponentially to zero with a inter-species thermalization rate given by:

$$\tau^{-1} = \frac{d(\Delta T)}{\Delta T dt} = \frac{d(\Delta T)}{\Delta T}\Gamma, \tag{6.9}$$

where ΔT is the temperature difference between species 1 and 2 and $dt = 1/\Gamma$ is the average collision time. The rate of interspecies collisions Γ is given by:

$$\Gamma = \sigma_{12} \times \bar{v} \times \int n_1(x)\, n_2(x)\, dx^3 =$$

$$= \sigma_{12} \times \bar{v} \times N_1 N_2 \int \rho_1(x)\, \rho_2(x)\, dx^3, \tag{6.10}$$

where $\sigma_{12} = 4\pi a_{12}^2$ is the interspecies cross section, $\bar{v}$ is the mean thermal relative velocity and $n_{1,2}(x)$, $\rho_{1,2}(x)$ are the atomic density distributions normalized to $N_{1,2}$ or 1, respectively. At thermal equilibrium with known trapping potential $U_{1,2}$, temperatures $T_{1,2}$, and atomic masses $m_{1,2}$, we know all the quantities in the equation above except the inter-species scattering length. In particular $\bar{v} = \sqrt{(8k_B/\pi) \times ((T_1/m_1) + (T_2/m_2))}$ and $n_{1,2}(x) \propto \exp^{-U_{1,2}(x)/k_B T_{1,2}}$.

From basic kinematics the energy transfer from species 1 to species 2 is given by:

$$\Delta E_{1\to 2} = \xi\, k_B \Delta T,$$

$$\xi = \frac{4m_1 m_2}{(m_1 + m_2)^2}, \tag{6.11}$$

where ξ accounts for the mass imbalance, and in our case $\xi \simeq 1$. From this we obtain:

$$d(\Delta T) = \frac{\xi}{3}\frac{N_1 + N_2}{N_1 N_2}\Delta T. \tag{6.12}$$

Substituting eqn (6.12) into eqn (6.9), we get the final result:

$$\tau^{-1} = \frac{\xi}{3}\frac{N_1 + N_2}{N_1 N_2}\Gamma = \frac{\xi}{3}\sigma_{12} \times (N_1 + N_2)\,\bar{v} \int \rho_1(x)\,\rho_2(x)\,dx^3 =$$

$$= \frac{\xi}{3}\sigma_{12} \times \Phi, \tag{6.13}$$

where the kinematic contribution to the rate is summarized in the effective flux Φ.

The value of 3 in the denominator of eqn (6.13) represents the average number of collisions for thermalization. Corrections to this number have been evaluated [229], and it is shown to vary within the range $2.4 - 3.4$, with 2.4 referring to fast thermalization compared to trap oscillation time and 3.4 to the opposite case.

6.7.2 Potential energy curves

In this part, we provide additional information about the fitted potentials. In Table 6.9, we give the best fit parameters for the MLR PEC describing the $X(1)^2\Sigma^+$ state. In Table 6.10 and Table 6.11 we give the point-wise representations of the fitted PECs for the $B(2)^2\Sigma^+$ state, fitted starting from the FCI-ECP+CPP and the MRCI methods, respectively. Finally, in Fig 6.13 we show a comparison of the potentials for the $B(2)^2\Sigma^+$ state before and after our fit procedure.

TABLE 6.9: Best fit parameters for the MLR PECs describing the $X(1)^2\Sigma^+$ state in the case of the three initial *ab-initio* representations. Units of energy and length are cm^{-1} and Å, respectively. The number of digits in the presented values of parameters is necessary from the numerical point of view, to reproduce band heads positions and weakly bound energy levels with the experimental uncertainty

	MRCI[37]	FCI-ECP+CPP[186]	RCCSD(T)[186]
p	5^a	5^a	5^a
q	2^a	2^a	2^a
N_u	3^a	3^a	3^a
N_β	5^a	5^a	5^a
D_e	1136.153957156767	1158.334744879383	1161.0696743991873
r_e	4.5645^a	4.59508^a	4.66879^a
$C_6 \times 10^{-7}$	1.808868014576728	1.795668695101867	1.8134615231939677
$C_8 \times 10^{-8}$	5.792504377056786	6.148308472469144	5.870256113661574
$C_{10} \times 10^{-10}$	2.2043858534998264^a	2.2043858534998264^a	2.2043858534998264^a
β_0	−1.2521217820591306	−1.2744532761179883	−1.2541965574219214
β_1	−2.7403962754860123	−2.6486718159733136	−2.324690124968812
β_2	−1.2388430923676004	−0.8587136858852784	−0.06921139967893859
β_3	0.8220377227516734^a	1.5773120878976061^a	0.9325813112428021^a
β_4	-2.710995726338915^a	-0.16154919058041997^a	-4.2183716802600495^a
β_5	-4.142301068756231^a	-0.8834374478517256^a	-5.290318777716273^a

[a] Held fixed during fit to experimental data.

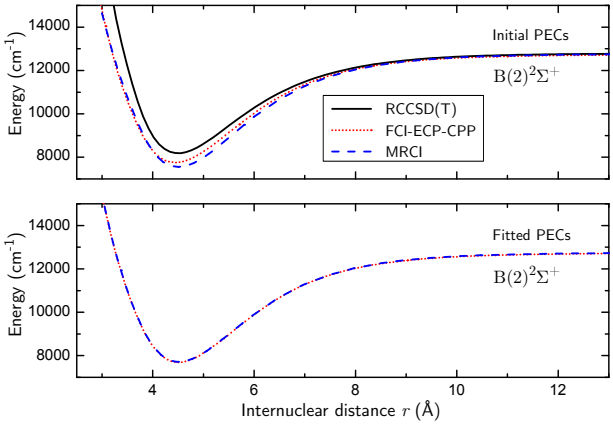

FIGURE 6.13: PECs of the $B(2)^2\Sigma^+$ state of RbSr. Top panel: theoretical PECs corresponding to the three different *ab-initio* calculations considered in this work. Bottom panel: PECs fitted to experimental data with initial fit parameters determined by each *ab-initio* method, see Sec. 6.5.3.

TABLE 6.10: The experimental pointwise potential energy curve of the $B(2)^2\Sigma^+$ state based on the theoretical curve calculated with the FCI-ECP+CPP method

r (Å)	E (cm^{-1})	r (Å)	E (cm^{-1})
2.68	19257.0300	8.18	12109.8735
2.78	17908.5708	8.29	12157.4315
2.89	16617.8234	8.39	12197.4666
3.00	15379.9026	8.50	12238.2371
3.10	14312.2244	8.60	12272.5381
3.21	13241.3574	8.71	12307.4494
3.31	12375.1023	8.82	12339.6227
3.42	11528.6439	8.92	12366.6696
3.52	10837.7736	9.03	12394.1795
3.63	10150.2670	9.13	12417.2977
3.74	9536.4284	9.24	12440.8047
3.84	9050.4423	9.35	12462.4492
3.95	8604.8603	9.45	12480.6336
4.05	8289.8226	9.56	12499.1204
4.16	8021.3425	9.66	12514.6521
4.27	7838.3481	9.77	12530.4436
4.37	7737.9870	9.87	12543.7127
4.48	7691.2318	9.98	12557.2074
4.58	7699.9253	10.09	12569.6388
4.69	7753.0775	10.19	12580.0904
4.79	7837.0308	10.30	12590.7265
4.90	7961.2580	10.40	12599.6736
5.32	8634.7155	10.51	12608.7842
5.43	8837.5343	10.62	12617.1902
5.54	9044.9495	10.72	12624.3507
5.64	9233.5924	10.83	12631.8586
5.75	9439.0045	10.93	12638.2067
5.85	9621.9672	11.04	12644.7041
5.96	9818.0546	11.14	12650.2014
6.06	9991.0355	11.25	12655.8314
6.17	10174.3255	11.36	12661.0571
6.28	10349.5430	11.46	12665.4829
6.38	10501.3856	11.57	12670.0202
6.49	10659.9119	11.67	12673.8658
6.59	10796.1676	11.78	12677.8112
6.70	10937.3983	11.89	12681.4802
6.81	11069.6823	11.99	12684.5934
6.91	11182.3688	12.10	12687.7911
7.02	11298.2776	12.20	12690.5065
7.12	11396.6341	12.31	12693.2978
7.23	11497.4813	12.41	12695.6701
7.33	11582.8320	12.52	12698.1107
7.44	11670.1576	12.63	12700.3871
7.55	11751.0295	12.73	12702.3241
7.65	11819.3069	12.84	12704.3196
7.76	11889.0220	12.94	12706.0191
7.86	11947.8194	13.05	12707.7714
7.97	12007.8007	13.16	12709.4095
8.08	12063.2037		

TABLE 6.11: The experimental pointwise potential energy curve of the $B(2)^2\Sigma^+$ state based on the theoretical curve calculated with the MRCI method

r (Å)	E (cm^{-1})	r (Å)	E (cm^{-1})
2.57	20015.9638	7.97	12039.5764
2.67	18623.1081	8.47	12260.0669
2.77	17378.0065	8.97	12412.7431
2.87	16227.5400	9.47	12513.9446
2.97	15164.7084	9.97	12581.4056
3.07	14191.0980	10.47	12626.6346
3.17	13301.5037	10.97	12657.3393
3.27	12484.9011	11.97	12693.3984
3.37	11729.7060	12.97	12711.7395
3.47	11028.5584	13.97	12721.6836
3.57	10381.0891	14.00	12721.9028
3.67	9791.4292	14.10	12722.6076
3.77	9271.8458	14.20	12723.2748
3.87	8816.5037	14.30	12723.9066
3.97	8486.8951	14.40	12724.5053
4.07	8191.1429	14.50	12725.0727
4.17	7968.0412	14.60	12725.6108
4.27	7821.7664	14.70	12726.1213
4.37	7739.7466	14.80	12726.6058
4.47	7711.9908	14.90	12727.0659
4.57	7729.6107	14.97	12727.3742
4.67	7784.9552	15.00	12727.5029
4.77	7871.4749	15.10	12727.9182
4.87	7983.6310	15.20	12728.3130
4.97	8116.4157	15.30	12728.6885
5.07	8265.5303	15.40	12729.0457
5.17	8430.3232	15.50	12729.3857
5.27	8609.5386	15.60	12729.7094
5.37	8792.9576	15.70	12730.0178
5.47	8981.4689	15.80	12730.3115
5.77	9548.1877	15.90	12730.5915
5.97	9908.3732	16.00	12730.8585
6.47	10690.4487	18.00	12734.2857
6.97	11287.8051	20.00	12735.7680
7.47	11725.8313		

Chapter 7

Observation of Feshbach resonances between alkali and closed-shell atoms

Abstract

Magnetic Feshbach resonances allow control of the interactions between ultracold atoms [107]. They are an invaluable tool in studies of few-body and many-body physics [239, 8], and can be used to convert pairs of atoms into molecules [240, 125] by ramping an applied magnetic field across a resonance. Molecules formed from pairs of alkali atoms have been transferred to low-lying states, producing dipolar quantum gases [9]. There is great interest in making molecules formed from an alkali atom and a closed-shell atom such as ground-state Sr or Yb. Such molecules have both a strong electric dipole and an electron spin; they will open up new possibilities for designing quantum many-body systems [32, 17] and for tests of fundamental symmetries [241]. The crucial first step is to observe Feshbach resonances in the corresponding atomic mixtures. Very narrow resonances have been predicted theoretically [35, 227, 127], but until now have eluded observation. Here we present the observation of magnetic Feshbach resonances of this type, for an alkali atom, Rb, interacting with ground-state Sr.

7.1 Main text

A magnetic Feshbach resonance arises when a pair of ultracold atoms couples to a near-threshold molecular state that is tuned to be close in energy by an applied

magnetic field. Magnetoassociation at such a resonance coherently transfers the atoms into the molecular state [162, 242]. In a few cases, near-threshold molecules formed in this way have been transferred to their absolute ground states [21, 243, 22], allowing exploration of quantum gases with strong dipolar interactions [9]. However, this has so far been achieved only for molecules formed from pairs of alkali atoms.

Mixtures of closed-shell alkaline-earth atoms with open-shell alkali atoms have been studied in several laboratories [40, 41, 208, 39, 244]. No strong coupling mechanism between atomic and molecular states exists in systems of this type, but theoretical work has identified weak coupling mechanisms that should lead to narrow Feshbach resonances, suitable for magnetoassociation [35, 227, 127]. In this letter we describe the detection of Feshbach resonances in mixtures of ^{87}Sr or ^{88}Sr with ^{87}Rb. The coupling between atomic and molecular states arises from two mechanisms previously predicted [35, 227, 127] and an additional, weaker mechanism that we identify here.

The experimental signature of a Feshbach resonance is field-dependent loss of Rb atoms. This may arise from either 3-body recombination or inelastic collisions, both of which are enhanced near a resonance. We perform loss spectroscopy using an ultracold Rb-Sr mixture, typically consisting of 5×10^4 Rb atoms mixed with 10^6 ^{87}Sr or 10^7 ^{88}Sr atoms at a temperature of 2 to 5 μK (see Methods). Figure 7.1 shows the observed loss features, eleven arising in the ^{87}Rb-^{87}Sr Bose-Fermi mixture and one in the ^{87}Rb-^{88}Sr Bose-Bose mixture. Ten loss features consist of a single, slightly asymmetrical dip with FWHM between 200 and 400 mG. The loss features labelled [1,0]a and [1,1]a each consist of several dips with a width of 20 to 60 mG at a spacing of 80 mG. We fit each dip with a Gaussian and give the resulting positions and widths in Tab. 7.1. None of these Rb loss features arises in the absence of Sr, proving that they depend on Rb-Sr interactions.

Both the atomic and molecular states are described by the total angular momentum of the Rb atom, f, and its projection m_f onto the magnetic field. Where necessary, atomic and molecular quantum numbers are distinguished with subscripts at and mol. In addition, the molecule has a vibrational quantum number n, counted down from $n = -1$ for the uppermost level, and a rotational quantum number L, with projection M_L. ^{88}Sr has nuclear spin $i_{\mathrm{Sr}} = 0$, whereas ^{87}Sr has $i_{\mathrm{Sr}} = 9/2$ and a corresponding projection $m_{i,\mathrm{Sr}}$.

The Rb-Sr atom-pair states and the near-threshold molecular states lie almost parallel to the Rb atomic states as a function of magnetic field [245]. We can therefore use the Breit-Rabi formula of Rb for both the atom-pair states and the molecular states. This allows us to extract zero-field binding energies E_{b} of the molecular states responsible for the resonances, giving the values in Tab. 7.2. The crossing atomic and

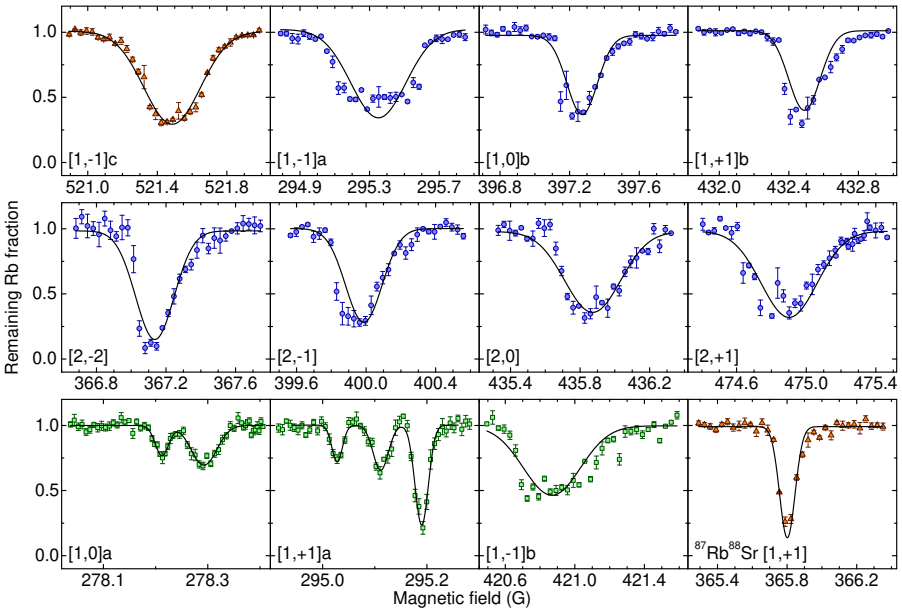

FIGURE 7.1: **Detection of Rb-Sr Feshbach resonances by field-dependent loss of Rb.** The fraction of Rb atoms remaining in state (f, m_f) after loss at each observed Feshbach resonance, normalised to unity far from the loss feature. Eleven loss features are observed in ^{87}Rb-^{87}Sr mixtures and one in ^{87}Rb-^{88}Sr (lower right panel). The loss features are labelled by $[f,m_f]j$, where $j \in$ {a,b,c} is an index used when losses due to several molecular states are observed at the same atomic threshold. Most loss features show a single dip in the atom number, whereas [1,0]a and [1,1]a show several. Each dip is fit by a Gaussian (black line), with results shown in Tab. 7.1. The color and shape of symbols indicates the coupling mechanism for the Feshbach resonance: mechanism I (orange triangles), II (blue circles), or III (green squares). The resonance near 521 G also has a contribution from mechanism II. The magnetic field uncertainty is 0.4 G and the noise is less than 40 mG. Error bars represent the standard error of three or more data points.

molecular levels are shown in Figs. 7.2 and 7.3, with filled symbols where we observe loss features.

To verify the bound-state energies and validate our model of Feshbach resonances, we use two-photon photoassociation (PA) spectroscopy. We detect the two $n = -2$ states (with $L = 0$ and 2) below the lower ($f = 1$) threshold of ^{87}Rb-^{87}Sr (states E and F in Tab. 7.2) at almost exactly the energies deduced from the resonance positions. All the states observed through Feshbach resonances (B to F) also arise to within 2 MHz in a more complete model of the Rb-Sr interaction potential, as described below.

Three different coupling mechanisms are responsible for the observed loss features. The first mechanism was proposed in ref. [35] and relies on the change of the Rb hyperfine splitting when the Rb electron distribution is perturbed by an approaching Sr atom. Its coupling strength is proportional to the magnetic field in the field region explored here [127]. The coupling conserves m_f and L and there are no crossings between atomic and molecular states with the same f and m_f. This mechanism therefore produces Feshbach resonances only at crossings between atomic states with Rb in $f = 1$ and molecular states with $f = 2$. We observe one such resonance for each of ^{87}Sr and ^{88}Sr.

The second mechanism involves hyperfine coupling of the Sr nucleus to the valence electron of Rb and was first proposed in ref. [227]. Since only fermionic ^{87}Sr has a nuclear magnetic moment, this can occur only in Rb-^{87}Sr collisions. This coupling conserves L and $m_f + m_{i,\mathrm{Sr}}$, with the selection rule $m_{f,\mathrm{at}} - m_{f,\mathrm{mol}} = 0, \pm 1$. Crossings that fulfil these conditions occur also for molecular states with the same f value as the atomic state, which makes them much more abundant than crossings obeying the selection rules of the first mechanism. Feshbach resonances belonging to different $m_{i,\mathrm{Sr}}$ are slightly shifted with respect to one another because of the weak Zeeman effect on the Sr nucleus and the weak Sr hyperfine splitting. However, since the shift is only ~ 10 mG for neighboring $m_{i,\mathrm{Sr}}$, much smaller than the width of the loss features of typically 300 mG, we do not resolve this splitting.

The third mechanism is the anisotropic interaction of the electron spin with the nucleus of either Rb or fermionic Sr. This mechanism can couple the s-wave atomic state to molecules with rotational quantum number $L = 2$. As usual, the total angular momentum projection (now $m_f + m_{i,\mathrm{Sr}} + M_L$) is conserved. If the Sr nucleus is involved, an additional selection rule is $\Delta m_f = \pm 1$. By contrast, if the Rb nucleus is involved, the selection rule is $\Delta m_f = -\Delta M_L$. These loss features are made up of many (m_f, M_L) components, split by several hyperfine terms [246]; in some cases the components separate into groups for different values of M_L. Three loss features are attributed to this mechanism and two of them ([1,1]a and [1,0]a) indeed show a structure of two or three dips.

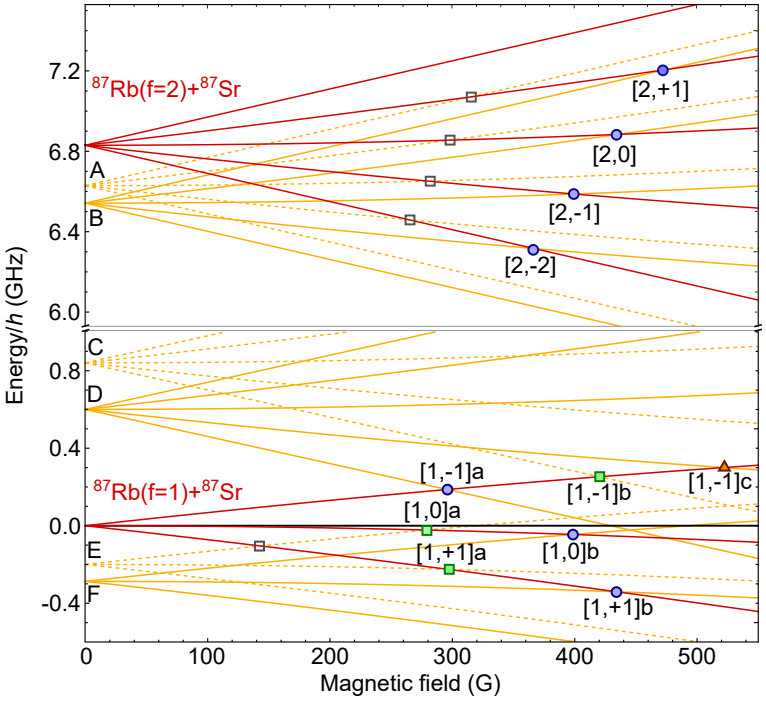

FIGURE 7.2: **Origin of the ^{87}Rb-^{87}Sr Feshbach resonances.** Energies of atomic (red) and molecular (orange) states as functions of magnetic field, shown with respect to the zero-field $f = 1$ atomic level. Molecular states are labelled as in Tab. 7.2 and shown dashed if rotationally excited ($L = 2$). Observed Feshbach resonances are labelled as in Fig. 7.1 and marked by filled symbols (orange triangles, blue circles or green squares for coupling mechanism I, II or III, respectively). Hollow symbols mark further, weak resonances predicted by our model, which could not be observed under our measurement conditions [245].

To create a model of the Rb-Sr Feshbach resonance locations we start with a RbSr ground-state potential that we have previously determined by electronic structure calculations [186]. This will be described in detail in a future publication [189]. We carry out a three-parameter fit to adapt the model potential to match the molecular binding energies determined by two-photon photoassociation in three Rb-Sr mixtures

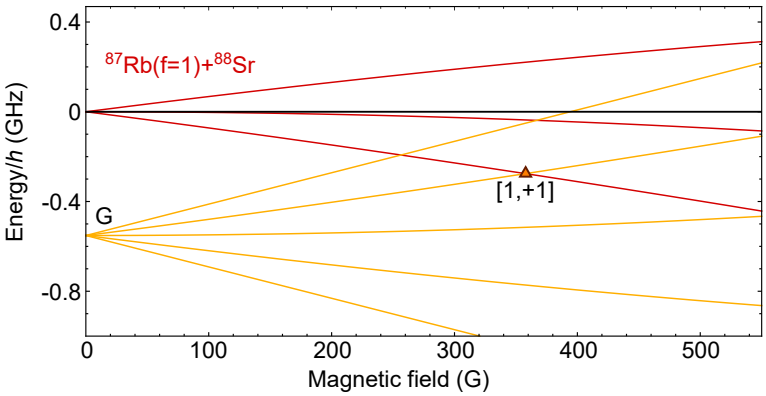

FIGURE 7.3: **Origin of the ^{87}Rb-^{88}Sr Feshbach resonance.** Energies of atomic (red) and molecular (orange) states as functions of magnetic field, shown with respect to the zero-field $f = 1$ atomic level. Only one Feshbach resonance has been observed, produced by coupling mechanism I. Since ^{88}Sr has zero nuclear spin, mechanism II is absent.

(^{87}Rb-^{84,87,88}Sr), supplemented by binding energies determined from the Feshbach resonance positions. The parameters adjusted are two long-range coefficients, C_6 and C_8, and a short-range well depth. The molecular bound states obtained from the model are within 2 MHz of the measured values, and the resonance positions are within 2 G. Scattering calculations on this potential give interspecies scattering lengths $a_{87,87} = 1600(+600, -450)$ a$_0$ and $a_{87,88} = 170(20)$ a$_0$ for ^{87}Rb-^{87}Sr and ^{87}Rb-^{88}Sr, where a_0 is the Bohr radius. Our model also predicts the background scattering lengths and Feshbach resonance positions for all other isotopic Rb-Sr mixtures. For example, we predicted the position of the ^{87}Rb-^{88}Sr resonance after initially fitting the model only on photoassociation results for three isotopic mixtures and ^{87}Rb-^{87}Sr Feshbach resonances. This resonance was subsequently observed within 10 G of the prediction.

An understanding of resonance widths is crucial to molecule formation. However, the widths δ of the experimental loss features are dominated by thermal broadening, with relatively little contribution from the true resonance widths Δ. We obtain theoretical widths Δ from the Golden Rule approximation [127] and include them in tab. 7.1. Δ depends on the amplitude of the atomic scattering function at short range; it is largest when the background scattering length a is large, and is proportional to a in this regime [127]. This effect enhances all the resonance widths for ^{87}Rb-^{87}Sr.

TABLE 7.1: **Properties of observed Feshbach resonances.** For resonances with many components, the theoretical width is the largest calculated value.

$[f, m_f]j$	(mol. state, m_f, M_L)	B (G)	δ (mG)	Δ (mG)	cpl. mech.
		^{87}Rb-^{87}Sr			
[2,+1]	(B, +2, 0)	474.9(4)	373(7)	0.095	II
[2,0]	(B, +1, 0)	435.9(4)	378(7)	0.14	II
[2,−1]	(B, 0, 0)	400.0(4)	247(4)	0.14	II
[2,−2]	(B, −1, 0)	367.1(4)	260(5)	0.095	II
[1,−1]a	(D, −2, 0)	295.4(4)	372(10)	0.73	II
[1,−1]b	(C, −2, mix)	420.9(4)	386(11)	0.025	III
[1,−1]c	(D, −1, 0)	521.5(4)	366(3)	3.5	I,II
[1,0]a	(E, −1, −1)	$B_1 = 278.2(4)$	30(3)	0.0012	III
	(E, −1, −2)	$B_1 + 0.081(2)$	58(4)	0.0015	III
[1,0]b	(F, −1, 0)	397.3(4)	207(4)	0.048	II
[1,+1]a	(E, 0, 0)	$B_2 = 295.0(4)$	24(3)	0.0002	III
	(E, 0, −1)	$B_2 + 0.083(2)$	35(3)	0.0014	III
	(E, 0, −2)	$B_2 + 0.162(2)$	30(1)	0.0016	III
[1,+1]b	(F, 0, 0)	432.5(4)	213(6)	0.048	II
		^{87}Rb-^{88}Sr			
[1,+1]	(G, +1, 0)	365.8(4)	105(2)	0.05	I

In summary, we have observed Feshbach resonances in mixtures of Rb alkali and Sr alkaline-earth atoms. Similar resonances will be ubiquitous in mixtures of alkali atoms with closed-shell atoms, particularly when the closed-shell atom has a nuclear spin. Magnetoassociation using resonances of this type should be feasible [245] and offers a path towards a new class of ultracold molecules, with electron spin and strong electric dipole moment. These molecules are expected to have important applications in quantum computation, many-body physics and tests of fundamental symmetries.

7.2 Methods

Sample preparation. We prepare ultracold ^{87}Rb-^{87}Sr Bose-Fermi mixtures by methods similar to those in our previous work [33]. We transfer Rb and ^{88}Sr from

magneto-optical traps into a horizontal "reservoir" dipole trap with a waist of 63(2) μm and a wavelength of 1070 nm. After Rb laser cooling we optically pump Rb into the $f = 1$ hyperfine state. By laser cooling Sr in the dipole trap on the narrow $^1S_0$-$^3P_1$ line we sympathetically cool Rb. We then transfer between 5×10^4 and 1×10^5 Rb atoms into the crossed-beam "science" dipole trap described below. We then ramp off the reservoir trap, discard ^{88}Sr atoms and transfer between 1×10^6 and 2×10^6 ^{87}Sr atoms in a mixture of all ten nuclear spin states into the science trap. The final temperature is typically 2 to 5 μK. In order to prepare Rb in an equal mixture of all three $f = 1$ m_f states we then randomize the distribution by non-adiabatic radiofrequency sweeps at a magnetic field of 130 G. To prepare Rb in the $f = 2$ hyperfine states we instead use optical pumping, which directly produces a nearly homogeneous distribution of Rb over the $f = 2$ m_f states. To prepare ^{87}Rb-^{88}Sr Bose-Bose mixtures we do not discard ^{88}Sr after transferring the gas into the science trap and we skip the loading of ^{87}Sr.

Science dipole trap. The science trap consists of two copropagating horizontal beams and one vertical beam, all with coinciding foci. The first horizontal beam has a wavelength of 1064 nm and a waist of 313(16) μm (19(1) μm) in the horizontal (vertical) direction. The second horizontal beam has a wavelength of 532 nm and a waist of 219(4) μm (19(1) μm). The vertical beam has a wavelength of 1070 nm and a waist of 78(2) μm. The horizontal 1064-nm beam is typically used at a power of 5.7 W to 6.2 W and dominates the trap potential. The 532-nm beam is operated at 0.2 W to 0.4 W. The vertical beam is operated at 0.7(1) W to measure loss feature [1,−1]b and is off otherwise. These operating conditions result in typical trap depths of 40 μK$\times k_B$ for Sr and 95 μK$\times k_B$ for Rb, taking account of gravitational sag.

Loss spectroscopy. We observe Feshbach resonances through field-dependent loss of Rb atoms. We submit the Rb-Sr mixture to a magnetic field of up to 550 G for a hold time of 1 to 10 s. Close to a Feshbach resonance, the rate of 2-body inelastic collisions or 3-body recombination is increased and atoms are lost. After the hold time we lower the magnetic field to near zero in 200 ms. During the next 10 ms, we ramp off the horizontal 532-nm beam and the vertical beam and decrease the power of the horizontal 1064-nm beam. This decrease lowers the evaporation threshold for Sr significantly, while Rb stays well trapped because its polarizability at 1064 nm is a factor of three higher. During the next 100 ms, Sr evaporates and cools Rb, which is advantageous for the subsequent imaging process.

At the end of the cooling stage, the science trap is switched off and a magnetic field gradient is applied to perform Stern-Gerlach separation of the Rb m_f states. After 14 ms of expansion, absorption images of Sr and Rb are taken. To reduce sensitivity to Rb atom number fluctuations, we normalize the atom number of the Rb m_f state of interest by the total atom number in m_f states that are not lost. We

verify that none of the loss features occurs in the absence of the Sr isotope concerned. For these verifications we need to retain a small amount of the other Sr isotope to allow sympathetic cooling.

Adaptation of experimental conditions. The width and depth of a loss feature depend on the measurement conditions. Thermal broadening sets a lower bound on the observable width, whereas hold time and peak densities affect the depth. For each resonance, we optimize the Sr density and hold time to maximize Rb loss without saturating the feature. We choose to use mixtures that contain much less Rb than Sr in order to obtain pronounced Rb loss features. Because of this atom number imbalance, and since most $m_{i,\mathrm{Sr}}$ states can contribute to a given loss feature, the fractional Sr loss during the hold time is small, which keeps the Rb loss rate high.

The resonances that we attribute to coupling mechanism II, with the exception of [1,−1]a, are recorded under identical conditions. The hold time is 5 s and the peak densities for Rb and ^{87}Sr are $2(1) \times 10^{11}\,\mathrm{cm}^{-3}$ and $9(5) \times 10^{11}\,\mathrm{cm}^{-3}$, respectively. The temperature of the Rb-Sr mixture before the hold time is $4.5(5)\,\mu$K.

The [1,−1]a and [1,−1]c resonances exhibit higher loss rates. For these we use hold times of 1.5 and 1 s, respectively. The peak densities for Rb and ^{87}Sr are $5(3) \times 10^{11}\,\mathrm{cm}^{-3}$ and $2(1) \times 10^{12}\,\mathrm{cm}^{-3}$. The temperature of the Rb-Sr mixture before the hold time is $3.0(1)\,\mu$K.

The resonances that we attribute to mechanism III exhibit much lower loss rates. Therefore we use a hold time of 10 s. To measure feature [1,−1]b we also add the vertical trapping beam to increase the gas densities. The peak densities for Rb are $2(1)\times10^{12}\,\mathrm{cm}^{-3}$, $4(2)\times10^{11}\,\mathrm{cm}^{-3}$ and $3(2)\times10^{11}\,\mathrm{cm}^{-3}$ for features [1,−1]b, [1,0]a and [1,+1]a respectively. The peak densities for Sr are $5(2) \times 10^{12}\,\mathrm{cm}^{-3}$, $2(1) \times 10^{12}\,\mathrm{cm}^{-3}$ and $4(2) \times 10^{12}\,\mathrm{cm}^{-3}$ respectively. The temperatures of the Rb-Sr mixture before the hold time are respectively $5(1)\,\mu$K, $3.2(2)\,\mu$K and $3.0(2)\,\mu$K.

The [1,+1] resonance observed in the Rb-^{88}Sr mixture exhibits a high loss rate, because we typically load one order of magnitude more ^{88}Sr atoms than ^{87}Sr atoms into the science trap due to the naturally higher abundance of ^{88}Sr. We use a hold time of 1 s and we do not use the 532-nm trapping beam. The peak densities for Rb and ^{88}Sr are $6(3) \times 10^{11}\,\mathrm{cm}^{-3}$ and $1.1(6) \times 10^{13}\,\mathrm{cm}^{-3}$. The temperature of the Rb-Sr mixture before the hold time is $2.2(1)\,\mu$K.

Magnetic field. We use three pairs of coils to produce a homogeneous magnetic field across the atomic sample. The primary coils create a field up to ~ 500 G with a resolution of 40 mG. These coils are used alone to record most of the loss features shown in Fig. 7.1. A second pair of coils is employed to resolve the substructure of the [1,0]a and [1,+1]a loss features, with the primary coils producing bias fields of 278 G and 294 G, respectively. The secondary coils create a low magnetic field with

a resolution of 3 mG. A third pair of coils is used to supplement the primary coils to observe the [1,-1]c loss feature, creating a bias field of 57 G.

We calibrate the magnetic field produced by the primary coils up to 290 G by spectroscopy on the narrow $^1S_0$-$^3P_1$ line of ^{88}Sr. We use a current transducer (LEM IT 600-S) to interpolate between the calibration points and to extrapolate to higher fields. We calibrate the secondary coils by recording one of the three [1,+1]a loss features for different values of the field from the primary coils.

The magnetic field precision is limited by the resolution and noise of the power supplies. The inductances of the coils reduce the power supply noise contribution to less than 40 mG from all three pairs of coils combined, which is confirmed by the observation of a loss feature with a width of only $\delta = 24$ mG. The accuracy is limited mainly by drifts in the ambient magnetic field. Monitoring the position of the ^{88}Sr MOT and the position of the loss feature due to a known Rb Feshbach resonance gives an upper bound of 350 mG for these drifts over the course of the present work. The calibration and statistical errors are typically one order of magnitude lower than the drifts. In addition, the positions of the loss maxima at finite temperature may differ from the positions of zero-energy Feshbach resonance positions. We account for this systematic error in the binding energies of Tab. 7.2 by adding an uncertainty of 4 times the root-mean-square width of the fitted Gaussian function.

7.3 Supplementary information

A magnetic Feshbach resonance arises when a pair of ultracold atoms couples to a near-threshold molecular state. All magnetic Feshbach resonances observed before our work occur for atomic pairs that interact to form multiple electronic states. This occurs if both atoms have electron spin or at least one of them is orbitally degenerate. Examples are alkali pairs [107] and mixtures of electronically excited (open-shell) Yb with either Li [247, 248] or ground-state Yb [249, 250]. Strong Feshbach resonances occur in these systems because the atom-pair state and the molecular state are different superpositions of the electronic states. By contrast the Rb-Sr system has only one relevant electronic state. There is also no magnetic dipole interaction, which can cause additional weak resonances between atoms such as alkalis, Cr [251], Er [252], and Dy [253]. The usual mechanisms that give rise to magnetic Feshbach resonances are therefore absent in Rb-Sr. Our work shows that all the same magnetic Feshbach resonances do occur. In the following we first discuss the unusual coupling mechanisms that give rise to these resonances. We then give details of our ground-state potential model, which fits the locations of the observed Feshbach resonances and predicts further resonances in all isotopic Rb-Sr mixtures. Finally we discuss the

suitability of Feshbach resonances in Rb-Sr for magnetoassociation of atom pairs into molecules.

7.3.1 Coupling mechanisms and resonance widths

The Hamiltonian for the interaction of Rb and Sr atoms may be written

$$\hat{H} = -\frac{\hbar^2}{2\mu R^2}\left[\frac{d^2}{dR^2} - \frac{\hat{L}^2}{R^2}\right] + \hat{H}_{\mathrm{asym}} + \hat{U}(R), \tag{7.1}$$

where R is the internuclear distance, μ is the reduced mass, and $\hat{L}^2$ is the operator for end-over-end rotation of the two atoms about one another. $\hat{H}_{\mathrm{asym}}$ is the asymptotic hyperfine Hamiltonian,

$$\hat{H}_{\mathrm{asym}} = \zeta_{Rb}\hat{\mathbf{i}}_{\mathrm{Rb}}\cdot\hat{\mathbf{s}} + (g_{\mathrm{Rb}}\mu_{\mathrm{N}}\hat{i}_{z,\mathrm{Rb}} + g_{\mathrm{Sr}}\mu_{\mathrm{N}}\hat{i}_{z,\mathrm{Sr}} + g_{\mathrm{e}}\mu_{\mathrm{B}}\hat{s}_z)B. \tag{7.2}$$

The operator $\hat{U}(R)$ includes all R-dependent interactions,

$$\begin{aligned}\hat{U}(R) = {} & \Delta\zeta_{\mathrm{Rb}}(R)\hat{\mathbf{i}}_{\mathrm{Rb}}\cdot\hat{\mathbf{s}} + \Delta\zeta_{\mathrm{Sr}}(R)\hat{\mathbf{i}}_{\mathrm{Sr}}\cdot\hat{\mathbf{s}} + t_{\mathrm{Rb}}(R)\sqrt{6}\,T^2(\boldsymbol{s},\boldsymbol{i}_{\mathrm{Rb}})\cdot T^2(C) \\ & + t_{\mathrm{Sr}}(R)\sqrt{6}\,T^2(\boldsymbol{s},\boldsymbol{i}_{\mathrm{Sr}})\cdot T^2(C) + V(R),\end{aligned} \tag{7.3}$$

where T^2 indicates a spherical tensor of rank 2. $T^2(C)$ has components $C^2_q(\theta,\phi)$, where C is a renormalised spherical harmonic and θ,ϕ are the polar coordinates of the internuclear vector. In Eq. (7.3) the first and second terms represent interaction-induced change of the scalar hyperfine coupling of the nuclear spins of Rb and Sr with the electron spin, the third and fourth terms represent the dipolar interaction between the electron spin and the nuclear spins of ^{87}Rb and ^{87}Sr, and the last term is the Born-Oppenheimer electronic interaction potential. The first two terms correspond to coupling mechanisms I and II discussed in the paper. The third and fourth terms correspond to mechanism III, though for RbSr the dipolar coupling involving the ^{87}Rb nucleus is very weak and the resonances due to this mechanism alone have not been observed. Note that $i_{\mathrm{Sr}} = 0$ for bosonic Sr isotopes (^{84,86,88}Sr), so that mechanism II is absent in Rb-Sr mixtures containing these isotopes. The couplings responsible for all three mechanisms were obtained from density-functional calculations of the molecular electronic structure using the same methods as in ref. [246].

The scattering length $a(B)$ around a narrow Feshbach resonance is described by

$$a(B) = a_{\mathrm{bg}}\left(1 - \frac{\Delta}{B - B_{\mathrm{res}}}\right), \tag{7.4}$$

where a_{bg} is the background scattering length, B_{res} is the resonance position and Δ is its width (in magnetic field). The width Δ is related to the width $\Gamma(k)$ (in the energy domain) of the state above threshold,

$$\Delta = \lim_{k\to 0} \frac{\Gamma(k)}{2ka_{\mathrm{bg}}\delta\mu_{\mathrm{res}}}, \tag{7.5}$$

where $k = \sqrt{2\mu E_{\mathrm{coll}}/\hbar^2}$ is the wavevector and $\delta\mu_{\mathrm{res}}$ is the difference between the magnetic moments of the atomic pair and the bound state. In the present work we obtain the width $\Gamma(k)$, from Fermi's Golden Rule,

$$\Gamma(k) = 2\pi|\langle\alpha' n|\omega_i(R)\hat{\Omega}_i|\alpha k\rangle|^2, \tag{7.6}$$

where $\omega_i(R)\hat{\Omega}_i$ is the coupling corresponding to one of mechanisms I to III, α and α' label eigenstates of H_{asym} and $|\alpha k\rangle$ and $|\alpha' n\rangle$ are the scattering and bound-state wavefunctions, respectively. Equation 7.6 factorizes into spin-dependent and radial parts [127],

$$\Gamma(k) = 2\pi I_{\alpha,\alpha'}(B)^2 I_{k,n}^2, \tag{7.7}$$

where

$$I_{\alpha,\alpha'}(B) = \langle\alpha'|\hat{\Omega}_i|\alpha\rangle; \tag{7.8}$$

and

$$I_{k,n} = \int_0^\infty \psi_n(R)\omega_i(R)\psi_k(R)dR. \tag{7.9}$$

The values of $I_{\alpha,\alpha'}(B)$ are obtained here as the off-diagonal matrix elements of the operators $\hat{\mathbf{i}}_{\mathrm{Rb}}\cdot\hat{\mathbf{s}}$, $\hat{\mathbf{i}}_{\mathrm{Sr}}\cdot\hat{\mathbf{s}}$ and $T^2(\hat{\mathbf{i}}_{\mathrm{Sr}},\hat{\mathbf{s}})$, transformed to the basis set of asymptotic eigenfunctions of H_{asym}, while $I_{k,n}$ was evaluated numerically for limitingly small values of k.

7.3.2 Predicted Feshbach resonances

Our model predicts further Feshbach resonances, in addition to the ones we have observed, in all isotopic Rb-Sr mixtures [189]. A few additional ^{87}Rb-^{87}Sr resonances occur in the magnetic field accessible to us ($< 550\,\mathrm{G}$), as indicated by hollow symbols in Fig. 7.2. We searched for loss features corresponding to those resonances, but found that they are not observable under our experimental conditions. The $L = 2$ Feshbach resonances in Rb $f = 2$ are quite weak and hard to observe for two reasons. First, they coincide with broad, known Rb Feshbach resonances [254]. Secondly, our Rb $f = 2$ samples have a lower atom number per m_f state and a shorter lifetime than

$f = 1$ samples. The Rb $f = 1$ resonance at 130 G is predicted to be two orders of magnitude narrower than the broadest coupling mechanism III resonance observed.

In addition, the large positive scattering length for ^{87}Rb-^{87}Sr will produce a least-bound molecular state with binding energy $h \times 25(15)$ kHz, which leads to Feshbach resonances at low magnetic field. However, bound states very near dissociation exist mostly at long range, and produce resonances with widths proportional to $|E_b|^{2/3}$ [127]. The widths of resonances due to the least-bound states are expected to be at least two orders of magnitude narrower than those due to deeper states. Therefore we do not expect to observe loss features corresponding to these resonances.

7.3.3 Prospect for magnetoassociation

Magnetoassociation uses magnetic Feshbach resonances to form molecules from pairs of atoms [107]. At a Feshbach resonance the atom-pair state $|a\rangle$ and the molecular state $|m\rangle$ couple, producing an avoided crossing. The strength of this crossing depends on the product $a_{bg}\Delta$. A common way to perform magnetoassociation is to ramp the magnetic field across the resonances such that $|a\rangle$ evolves adiabatically into $|m\rangle$. Even quite weak resonances, comparable in coupling strength to the strongest Rb-Sr resonances, have been used for magnetoassociation, starting from a BEC [255] or atom pairs on the sites of a lattice [256]. Our Rb-Sr Feshbach resonance model identifies several promising paths to form RbSr molecules from atoms, either in free space or in an optical lattice. We have already created a Mott insulator with 3×10^4 sites occupied by one atom of each, ^{87}Rb and ^{84}Sr [34]. Our model predicts suitable resonances in this and several other isotopic mixtures.

The experimental discovery of Feshbach resonances in Rb-Sr also validates the theory predicting Feshbach resonances in other mixtures of closed-shell atoms with alkalis. Several such mixtures are currently under experimental investigation, such as Li-Yb [40, 41], Rb-Yb [208, 39], and Cs-Yb [257]. It should be possible to identify magnetic Feshbach resonances in these mixtures using two-photon photoassociation and Feshbach spectroscopy. Identifying these resonances would give further opportunities to create molecules with a strong electric dipole and an electron spin.

TABLE 7.2: **Molecular states responsible for Feshbach resonances.** Binding energies obtained from observed Feshbach resonances, E_b^{FR}, and from two-photon photoassociation, E_b^{PA}. The experimental uncertainties in E_b^{FR} arise principally from the magnetic field measurement.

label	n	F	L	E_b^{FR}/h (MHz)	E_b^{PA}/h (MHz)
			^{87}Rb-^{87}Sr		
A	-2	2	2	-	-
B	-2	2	0	288.2(4)	-
C	-4	2	2	5992(1)	-
D	-4	2	0	6234(1)	-
E	-2	1	2	200.0(3)	200.0(3)
F	-2	1	0	287.3(3)	287.3(2)
			^{87}Rb-^{88}Sr		
G	-4	2	0	7401.0(7)	-

Chapter 8

Outlook

Our work was mainly focused, with few exceptions, on few-body physics. However, harnessing the underlying few-body physics of our molecules opens up much broader prospects. The experimental and theoretical studies stemming from our work can be divided into our three topic areas: metrology and precision measurements (PM), few-body physics and ultracold chemistry (FBP), and many-body physics and quantum simulation (MBP). We list in the following the prospects envisioned by the author, based on our results and recent developments in the field of ultracold atoms and molecules.

8.1 Metrology and Precision measurements

- A lattice clock with weakly-bound molecules [14]. Recent theoretical investigation of a molecular clock based on AE-AE dimers was recently carried out and showed good feasibility prospects. The proposed clock transition is between a weakly-bound ground-state molecular level and a weakly-bound excited-state level supported by the potential correlating to the $^1S_0 + ^3P_0$ atomic asymptote. For ^{84}Sr this asymptote must be first located via atomic optical spectroscopy exploiting the magnetically-induced radiative coupling between the atomic $^1S_0$ and the $^3P_0$ states [258]. Our $^{84}Sr_2$ MI appears to be an ideal sample to perform the subsequent search for the molecular clock transition. Optimal operation of the clock will require a magic-wavelength lattice to cancel the differential shifts from state-dependent center-of-mass motion. Related fundamental physics: physics beyond standard model and time variation of fundamental constants.

- A lattice clock with deeply-bound molecules [13]. This molecular clock would operate in the less explored frequency regime around 10 THz corresponding to Raman transitions between different rovibrational levels supported by the

ground-state potential. Bosonic AE-AE dimers, like Sr_2, are ideal candidates due to the insensitivity to external magnetic fields and lack of hyperfine structure. This work requires precision Raman spectroscopy and would be supported by existing extensive spectral data on Sr_2 [259]. Optimal operation of the clock will require a magic-wavelength lattice to cancel the differential shifts between different ground-state rovibrational levels. Related fundamental physics: time variation of electron-to-proton mass ratio.

- Observation and characterization of hyperfine molecular shifts induced by the weak coupling mechanisms in RbSr [35, 246]. Three coupling mechanisms, two isotropic and one anisotropic, have been considered responsible for the observed FF resonance, however the calculation of their absolute magnitude and dependence on the internuclear distance is challenging. Precise two-color spectroscopy informed by our fitted potential would shed light on these exotic coupling mechanisms. This would in turn further refine the molecular potential as the corresponding systematic shifts could be taken into account.

- Born-Oppenheimer breakdown effects and non-Newtonian gravity [260, 211]. Two color spectroscopy in a $^{84}Sr_2$ BEC or MI could be used to reach the required precision and accuracy of binding energies of weakly-bound and deeply-bound molecules.

8.2 Few-body physics and ultracold chemistry

- Production of weakly-bound $^{87}Rb^{84}Sr$ molecules in the electronic ground state in a deep optical lattice via the FF resonance at $B \simeq 1310\,\mathrm{G}$. The required atomic sample was already used in the present thesis, but only STIRAP was attempted since magnetic FF resonances were not yet experimentally observed nor the interaction potential known. In our 3D lattice with isotropic trapping frequency of $\sim 60\,\mathrm{kHz}$, the relevant avoided crossing gap is of order 2 mG, likely to be underestimated, and should allow magneto-association.

- Production of weakly-bound ground-state $^{87}Rb^{84}Sr$ in a double BEC via the same FF resonance at $B \simeq 1310\,\mathrm{G}$. Comparison to the lattice case. Investigation of *reactive* collisions similarly to our work on Sr_2.

- Interaction-tuning of the s-wave scattering length in RbSr via magnetic FF resonance induced by coupling mechanism I. Also in this case, $^{87}Rb^{84}Sr$ seems to be an ideal candidate. Indeed, the $B \simeq 1310\,\mathrm{G}$ FF resonance has no inelastic collision channel coupled to the entrance channel (the lowest atomic state).

This corresponds to a divergence in the scattering length on resonance. Other resonances, i.e. other magnetic-field locations and isotopic combinations, will instead be characterized by multiple inelastic channels and thus correspond to so-called "decayed" resonances, for which the scattering length does not show a divergence but rather a limited modulation (see also optical FF resonances). Although less useful for interaction tuning, investigation of these resonances could shed light on *inelastic* collisions near a FF resonance.

- Transfer of weakly-bound molecules to deeper levels. The necessary two-color spectroscopy can be performed using already known one-color transitions and exploiting the fitted ground-state potential. Efficient STIRAP can probably only provide transfer to levels bound by a few 100 GHz. A second spectroscopy search will inform the final STIRAP transfer to the rovibrational ground state.
- Investigation of a *d*-wave FF resonances in ^{87}Rb-^{84}Sr double BEC [261, 262]. Coupling mechanism III involving the ^{87}Rb nucleus could be observed and lead to *d*-wave resonances. Surface effects could be studied by shaping of the bichromatic trap to induce miscible and non-miscible phases [34].
- Ultracold molecules beyond dimers [263]. Optical spectroscopy and creation of trimer excited states, for instance in $^{84}Sr_3$*, exploiting the species-dependent superfluid-to-MI transition. So far trimers have only been observed in exotic systems composed of one Rydberg atom and two ground-state atoms trapped in the effective potential induced on them by the giant Rydberg electron wavefunction [264].

8.3 Many-body physics and quantum simulation

- Investigation of high-partial wave pairing in a ^{87}Rb-^{84}Sr double BEC via magnetic FF resonances [261]. Our optical lattice could be exploited to reduce losses from three-body recombinations [261].
- STIRAP from an atomic ^{84}Sr BEC to a molecular $^{84}Sr_2$ BEC [165, 166, 167]. Our investigation of molecule production in a Sr BEC did not benefit from the optimized STIRAP, developed later, which should allow for efficient and coherent molecule production. The measured lifetime of the molecular sample is long enough for the STIRAP from the weakly-bound to rovibrational ground-state molecules.
- Molecular BEC of RbSr via evaporative cooling [29]. Application of external electric and magnetic fields should allow to engineer repulsive van der Waalls

repulsion between RbSr molecules, thereby reducing reactive and inelastic collisions in favor of elastic collisions.

- Quantum simulation with RbSr ground-state molecules in optical lattice. The electronic spins of neighboring RbSr molecules can be coupled by exploiting the electric dipole interaction, which enables the exploration of lattice-spin models[32].

Finally, the methods we are establishing to produce and manipulate ultracold ground-state RbSr might be especially relevant for molecules suited for the search of the electron electric dipole moment, of physics beyond the standard model, and time variation of fundamental constants as the proton to electron mass ratio [265, 133, 266].

Bibliography

[1] P. W. Anderson, "More Is Different", *Science* 177, 393 (1972).

[2] P. Gill, "Is the time right for a redefinition of the second by optical atomic clocks?", *Journal of Physics: Conference Series* 723, 012053 (2016).

[3] R. H. Parker, C. Yu, W. Zhong, B. Estey, and H. Müller, "Measurement of the fine-structure constant as a test of the Standard Model", *Science* 360, 191 (2018).

[4] J. Bagdonaite, E. J. Salumbides, S. P. Preval, M. A. Barstow, J. D. Barrow, M. T. Murphy, and W. Ubachs, "Limits on a Gravitational Field Dependence of the Proton-Electron Mass Ratio from H_2 in White Dwarf Stars", *Phys. Rev. Lett.* 113, 123002 (2014).

[5] S. Ospelkaus, K.-K. Ni, D. Wang, M. H. G. de Miranda, B. Neyenhuis, G. Quéméner, P. S. Julienne, J. L. Bohn, D. S. Jin, and J. Ye, "Quantum-State Controlled Chemical Reactions of Ultracold Potassium-Rubidium Molecules", *Science* 327, 853 (2010).

[6] J. M. Hutson, "Ultracold Chemistry", *Science* 327, 788 (2010).

[7] J. L. Bohn, A. M. Rey, and J. Ye, "Cold molecules: Progress in quantum engineering of chemistry and quantum matter", *Science* 357, 1002 (2017).

[8] I. Bloch, J. Dalibard, and W. Zwerger, "Many-body physics with ultracold gases", *Rev. Mod. Phys.* 80, 885 (2008).

[9] S. A. Moses, J. P. Covey, M. T. Miecnikowski, D. S. Jin, and J. Ye, "New frontiers for quantum gases of polar molecules", *Nature Physics* 13, 13 (2016).

[10] B. Yan, S. A. Moses, B. Gadway, J. P. Covey, K. R. A. Hazzard, A. M. Rey, D. S. Jin, and J. Ye, "Observation of dipolar spin-exchange interactions with lattice-confined polar molecules", *Nature* 501, 521 (2013).

[11] B. Gadway and B. Yan, "Strongly interacting ultracold polar molecules", *Journal of Physics B: Atomic, Molecular and Optical Physics* 49, 152002 (2016).

[12] R. Krems, B. Friedrich, and W. C. Stwalley, *Cold Molecules: Theory, Experiment, Applications*, CRC Press, 2009.

[13] T. Zelevinsky, S. Kotochigova, and J. Ye, "Precision Test of Mass-Ratio Variations with Lattice-Confined Ultracold Molecules", *Phys. Rev. Lett.* 100, 043201 (2008).

[14] M. Borkowski, "Optical Lattice Clocks with Weakly Bound Molecules", *Phys. Rev. Lett.* 120, 083202 (2018).

[15] L. D. Carr, D. DeMille, R. V. Krems, and J. Ye, "Cold and ultracold molecules: science, technology and applications", *New Journal of Physics* 11, 055049 (2009).

[16] J. Wolf, M. Deiß, A. Krükow, E. Tiemann, B. P. Ruzic, Y. Wang, J. P. D'Incao, P. S. Julienne, and J. H. Denschlag, "State-to-state chemistry for three-body recombination in an ultracold rubidium gas", *Science* 358, 921 (2017).

[17] M. A. Baranov, M. Dalmonte, G. Pupillo, and P. Zoller, "Condensed Matter Theory of Dipolar Quantum Gases", *Chemical Reviews* 112, 5012 (2012).

[18] A. Kitaev, "Fault-tolerant quantum computation by anyons", *Annals of Physics* 303, 2 (2003).

[19] J. Levinsen, N. R. Cooper, and G. V. Shlyapnikov, "Topological $p_x + ip_y$ superfluid phase of fermionic polar molecules", *Phys. Rev. A* 84, 013603 (2011).

[20] E. B. Norrgard, D. J. McCarron, M. H. Steinecker, M. R. Tarbutt, and D. DeMille, "Submillikelvin Dipolar Molecules in a Radio-Frequency Magneto-Optical Trap", *Phys. Rev. Lett.* 116, 063004 (2016).

[21] N. K.-K., S. Ospelkaus, M. H. G. de Miranda, A. Pe'er, B. Neyenhuis, J. J. Zirbel, S. Kotochigova, P. S. Julienne, D. S. Jin, and J. Ye, "A High Phase-Space-Density Gas of Polar Molecules", *Science* 322, 231 (2008).

[22] T. Takekoshi, L. Reichsöllner, A. Schindewolf, J. M. Hutson, C. R. Le Sueur, O. Dulieu, F. Ferlaino, R. Grimm, and H.-C. Nägerl, "Ultracold Dense Samples of Dipolar RbCs Molecules in the Rovibrational and Hyperfine Ground State", *Phys. Rev. Lett.* 113, 205301 (2014).

[23] J. W. Park, S. A. Will, and M. W. Zwierlein, "Ultracold Dipolar Gas of Fermionic $^{23}Na^{40}K$ Molecules in Their Absolute Ground State", *Phys. Rev. Lett.* 114, 205302 (2015).

[24] M. Guo, B. Zhu, B. Lu, X. Ye, F. Wang, R. Vexiau, N. Bouloufa-Maafa, G. Quéméner, O. Dulieu, and D. Wang, "Creation of an Ultracold Gas of Ground-State Dipolar $^{23}Na^{87}Rb$ Molecules", *Phys. Rev. Lett.* 116, 205303 (2016).

[25] T. M. Rvachov, H. Son, A. T. Sommer, S. Ebadi, J. J. Park, M. W. Zwierlein, W. Ketterle, and A. O. Jamison, "Long-Lived Ultracold Molecules with Electric and Magnetic Dipole Moments", *Phys. Rev. Lett.* 119, 143001 (2017).

[26] S. Stellmer, B. Pasquiou, R. Grimm, and F. Schreck, "Creation of Ultracold Sr_2 Molecules in the Electronic Ground State", *Phys. Rev. Lett.* 109, 115302 (2012).

[27] G. Reinaudi, C. B. Osborn, M. McDonald, S. Kotochigova, and T. Zelevinsky, "Optical Production of Stable Ultracold $^{88}Sr_2$ Molecules", *Phys. Rev. Lett.* 109, 115303 (2012).

[28] A. V. Avdeenkov, M. Kajita, and J. L. Bohn, "Suppression of inelastic collisions of polar $^1\Sigma$ state molecules in an electrostatic field", *Phys. Rev. A* 73, 022707 (2006).

[29] G. Quéméner and J. L. Bohn, "Shielding $^2\Sigma$ ultracold dipolar molecular collisions with electric fields", *Phys. Rev. A* 93, 012704 (2016).

[30] G. Wang and G. Quéméner, "Tuning ultracold collisions of excited rotational dipolar molecules", *New Journal of Physics* 17, 035015 (2015).

[31] R. Guérout, M. Aymar, and O. Dulieu, "Ground state of the polar alkali-metal-atom–strontium molecules: Potential energy curve and permanent dipole moment", *Phys. Rev. A* 82, 042508 (2010).

[32] A. Micheli, G. K. Brennen, and P. Zoller, "A toolbox for lattice-spin models with polar molecules", *Nat. Phys.* 2, 341 (2006).

[33] B. Pasquiou, A. Bayerle, S. M. Tzanova, S. Stellmer, J. Szczepkowski, M. Parigger, R. Grimm, and F. Schreck, "Quantum degenerate mixtures of strontium and rubidium atoms", *Phys. Rev. A* 88, 023601 (2013).

[34] A. Bayerle, "Ultracold strontium and rubidium: mixtures, quantum gases and molecules", PhD thesis, Amsterdam: University of Amsterdam, 2017.

[35] P. S. Żuchowski, J. Aldegunde, and J. M. Hutson, "Ultracold RbSr Molecules Can Be Formed by Magnetoassociation", *Phys. Rev. Lett.* 105, 153201 (2010).

[36] T. Chen, S. Zhu, X. Li, J. Qian, and Y. Wang, "Prospects for transferring $^{87}Rb^{84}Sr$ dimers to the rovibrational ground state based on calculated molecular structures", *Phys. Rev. A* 89, 063402 (2014).

[37] J. V. Pototschnig, R. Meyer, A. W. Hauser, and W. E. Ernst, "Vibronic transitions in the alkali-metal (Li, Na, K, Rb) – alkaline-earth-metal (Ca, Sr) series: A systematic analysis of de-excitation mechanisms based on the graphical mapping of Frank-Condon integrals", *Phys. Rev. A* 95, 022501 (2017).

[38] F. Münchow, C. Bruni, M. Madalinski, and A. Görlitz, "Two-photon photoassociation spectroscopy of heteronuclear YbRb", *Phys. Chem. Chem. Phys.* 13, 18734 (2011).

[39] V. D. Vaidya, J. Tiamsuphat, S. L. Rolston, and J. V. Porto, "Degenerate Bose-Fermi mixtures of rubidium and ytterbium", *Phys. Rev. A* 92, 043604 (2015).

[40] H. Hara, Y. Takasu, Y. Yamaoka, J. M. Doyle, and Y. Takahashi, "Quantum Degenerate Mixtures of Alkali and Alkaline-Earth-Like Atoms", *Phys. Rev. Lett.* 106, 205304 (2011).

[41] A. H. Hansen, A. Khramov, W. H. Dowd, A. O. Jamison, V. V. Ivanov, and S. Gupta, "Quantum degenerate mixture of ytterbium and lithium atoms", *Phys. Rev. A* 84, 011606 (2011).

[42] A. Guttridge, M. D. Frye, B. Yang, J. M. Hutson, and S. L. Cornish, "Two-photon photoassociation spectroscopy of CsYb: ground-state interaction potential and interspecies scattering lengths", *arXiv:1806.00295* (2018).

[43] R.-C. project on Kleinert's group webpage, URL: `http://michaelakleinert.wixsite.com/amoatwu`.

[44] S. Stellmer, "Degenerate quantum gases of strontium", PhD thesis, Innsbruck: University of Innsbruck, 2012.

[45] S. Stellmer, F. Schreck, and T. C. Killian, "Degenerate Quantum Gases of Strontium", *Annual Review of Cold Atoms and Molecules*, vol. 2, World Scientific Publishing Co., 2014.

[46] H. J. Metcalf and P. van der Straten, *Laser cooling and trapping*, Graduate Texts in Contemporary Physics, Springer, 1999.

[47] C. Foot, *Atomic Physics*, Oxford Master Series in Physics, Oxford University Press, 2004.

[48] T. Hänsch and A. Schawlow, "Cooling of gases by laser radiation", *Optics Communications* 13, 68 (1975).

[49] Y. Castin, H. Wallis, and J. Dalibard, "Limit of Doppler cooling", *J. Opt. Soc. Am. B* 6, 2046 (1989).

[50] P. J. Ungar, D. S. Weiss, E. Riis, and S. Chu, "Optical molasses and multilevel atoms: theory", *J. Opt. Soc. Am. B* 6, 2058 (1989).

[51] J. Dalibard and C. Cohen-Tannoudji, "Laser cooling below the Doppler limit by polarization gradients: simple theoretical models", *J. Opt. Soc. Am. B* 6, 2023 (1989).

[52] C. Cohen-Tannoudji and W. Phillips, "New Mechanisms for Laser Cooling", *Physics Today* 43, 33 (1990).

[53] V. Vuletić, A. J. Kerman, C. Chin, and S. Chu, "Laser Cooling: Beyond optical molasses and beyond closed transitions", *Proceedings of the XVII. International Conference on Atomic Physics (ICAP 2000, Florence)*, 2001.

[54] F. Bardou, J. P. Bouchaud, O. Emile, A. Aspect, and C. Cohen-Tannoudji, "Subrecoil laser cooling and Lévy flights", *Phys. Rev. Lett.* 72, 203 (1994).

[55] E. Wille, "Preparation of an Optically Trapped Fermi-Fermi Mixture of ^{6}Li and ^{40}K Atoms and Characterization of the Interspecies Interactions by Feshbach Spectroscopy", PhD thesis, Innsbruck: University of Innsbruck, 2009.

[56] W. D. Phillips and H. Metcalf, "Laser Deceleration of an Atomic Beam", *Phys. Rev. Lett.* 48, 596 (1982).

[57] E. L. Raab, M. Prentiss, A. Cable, S. Chu, and D. E. Pritchard, "Trapping of Neutral Sodium Atoms with Radiation Pressure", *Phys. Rev. Lett.* 59, 2631 (1987).

[58] H. Metcalf, "Magneto-optical trapping and its application to helium metastables", *J. Opt. Soc. Am. B* 6, 2206 (1989).

[59] A. Kastler, "Quelques suggestions concernant la production optique et la détection optique d'une inégalité de population des niveaux de quantifigation spatiale des atomes. Application à l'expérience de Stern et Gerlach et è la résonance magnétique.", *J. Phys. Radium* 11, 255 (1950).

[60] C. Cohen-Tannoudji and A. Kastler, "I Optical Pumping", ed. by E. Wolf, vol. 5, Progress in Optics, Elsevier, 1966, 1.

[61] P. D. Lett, R. N. Watts, C. I. Westbrook, W. D. Phillips, P. L. Gould, and H. J. Metcalf, "Observation of Atoms Laser Cooled below the Doppler Limit", *Phys. Rev. Lett.* 61, 169 (1988).

[62] D. S. Weiss, E. Riis, Y. Shevy, P. J. Ungar, and S. Chu, "Optical molasses and multilevel atoms: experiment", *J. Opt. Soc. Am. B* 6, 2072 (1989).

[63] D. Boiron, C. Triché, D. R. Meacher, P. Verkerk, and G. Grynberg, "Three-dimensional cooling of cesium atoms in four-beam gray optical molasses", *Phys. Rev. A* 52, R3425 (1995).

[64] S. E. Hamann, D. L. Haycock, G. Klose, P. H. Pax, I. H. Deutsch, and P. S. Jessen, "Resolved-Sideband Raman Cooling to the Ground State of an Optical Lattice", *Phys. Rev. Lett.* 80, 4149 (1998).

[65] R. Grimm, M. Weidemüller, and Y. B. Ovchinnikov, "Optical Dipole Traps for Neutral Atoms", *Advances In Atomic, Molecular, and Optical Physics* 42, 95 (2000).

[66] D. A. Steck, *Rubidium 87 D Line Data*, URL: http://steck.us/alkalidata/.

[67] S. Rosi, A. Burchianti, S. Conclave, D. Naik, G. Roati, C. Fort, and F. Minardi, "Λ-enhanced grey molasses on the D_2 transition of Rubidium-87 atoms", *Scientific Reports* 8, 1301, 1301 (2018).

[68] H. Katori, T. Ido, Y. Isoya, and M. Kuwata-Gonokami, "Magneto-Optical Trapping and Cooling of Strontium Atoms down to the Photon Recoil Temperature", *Phys. Rev. Lett.* 82, 1116 (1999).

[69] K. R. Vogel, T. P. Dinneen, A. Gallagher, and J. L. Hall, "Narrow-line Doppler cooling of strontium to the recoil limit", *IEEE Transactions on Instrumentation and Measurement* 48, 618 (1999).

[70] T. Mukaiyama, H. Katori, T. Ido, Y. Li, and M. Kuwata-Gonokami, "Recoil-Limited Laser Cooling of ^{87}Sr Atoms near the Fermi Temperature", *Phys. Rev. Lett.* 90, 113002 (2003).

[71] Bose, "Plancks Gesetz und Lichtquantenhypothese", *Zeitschrift für Physik* 26, 178 (1924).

[72] A. Einstein, *Quantentheorie des einatomigen idealen Gases*, vol. 261, Akademie der Wissenshaften, in Kommission bei W. de Gruyter, July 1924.

[73] L. P. Pitaevskii and S. Stringari, *Bose-Einstein Condensation*, International Series of Monographs on Physics, Oxford University Press, 2003.

[74] W. Ketterle, D. S. Durfee, and S. D. M. Kurn, "Making, probing and understanding Bose-Einstein condensates", *Bose-Einstein Condensation in Atomic Gases (Proceedings of the International School of Physics "Enrico Fermi," Course CXL)*, ed. by M. Inguscio, S. Stringari, and C. E. Wieman, IOS Press, 1999.

[75] M. P. A. Fisher, P. B. Weichman, G. Grinstein, and D. S. Fisher, "Boson localization and the superfluid-insulator transition", *Phys. Rev. B* 40, 546 (1989).

[76] D. Jaksch, C. Bruder, J. I. Cirac, C. W. Gardiner, and P. Zoller, "Cold Bosonic Atoms in Optical Lattices", *Phys. Rev. Lett.* 81, 3108 (1998).

[77] M. H. Anderson, J. R. Ensher, M. R. Matthews, C. E. Wieman, and E. A. Cornell, "Observation of Bose-Einstein Condensation in a Dilute Atomic Vapor", *Science* 269, 198 (1995).

[78] C. C. Bradley, C. A. Sackett, J. J. Tollett, and R. G. Hulet, "Evidence of Bose-Einstein Condensation in an Atomic Gas with Attractive Interactions", *Phys. Rev. Lett.* 75, 1687 (1995).

[79] K. B. Davis, M. O. Mewes, M. R. Andrews, N. J. van Druten, D. S. Durfee, D. M. Kurn, and W. Ketterle, "Bose-Einstein Condensation in a Gas of Sodium Atoms", *Phys. Rev. Lett.* 75, 3969 (1995).

[80] H. F. Hess, "Evaporative cooling of magnetically trapped and compressed spin-polarized hydrogen", *Phys. Rev. B* 34, 3476 (1986).

[81] S. Stellmer, M. K. Tey, B. Huang, R. Grimm, and F. Schreck, "Bose-Einstein Condensation of Strontium", *Phys. Rev. Lett.* 103, 200401 (2009).

[82] M. Greiner, O. Mandel, T. Esslinger, T. W. Hänsch, and I. Bloch, "Quantum phase transition from a superfluid to a Mott insulator in a gas of ultracold atoms", *Nature* 415 (2002).

[83] H. R. Thorsheim, J. Weiner, and P. S. Julienne, "Laser-induced photoassociation of ultracold sodium atoms", *Phys. Rev. Lett.* 58, 2420 (1987).

[84] J. L. Bohn and P. S. Julienne, "Semianalytic theory of laser-assisted resonant cold collisions", *Phys. Rev. A* 60, 414 (1999).

[85] K. M. Jones, E. Tiesinga, P. D. Lett, and P. S. Julienne, "Ultracold photoassociation spectroscopy: Long-range molecules and atomic scattering", *Rev. Mod. Phys.* 78, 483 (2006).

[86] R. Napolitano, J. Weiner, C. J. Williams, and P. S. Julienne, "Line Shapes of High Resolution Photoassociation Spectra of Optically Cooled Atoms", *Phys. Rev. Lett.* 73, 1352 (1994).

[87] J. D. Miller, R. A. Cline, and D. J. Heinzen, "Photoassociation spectrum of ultracold Rb atoms", *Phys. Rev. Lett.* 71, 2204 (1993).

[88] W. I. McAlexander, E. R. I. Abraham, N. W. M. Ritchie, C. J. Williams, H. T. C. Stoof, and R. G. Hulet, "Precise atomic radiative lifetime via photoassociative spectroscopy of ultracold lithium", *Phys. Rev. A* 51, R871 (1995).

[89] S. H. Autler and C. H. Townes, "Stark Effect in Rapidly Varying Fields", *Phys. Rev.* 100, 703 (1955).

[90] C. Cohen-Tannoudji, "The Autler-Townes Effect Revisited", *Amazing Light*, ed. by C. R.Y., Springer, New York, NY, 1996.

[91] E. R. I. Abraham, W. I. McAlexander, C. A. Sackett, and R. G. Hulet, "Spectroscopic Determination of the s-Wave Scattering Length of Lithium", *Phys. Rev. Lett.* 74, 1315 (1995).

[92] C. C. Tsai, R. S. Freeland, J. M. Vogels, H. M. J. M. Boesten, B. J. Verhaar, and D. J. Heinzen, "Two-Color Photoassociation Spectroscopy of Ground State Rb_2", *Phys. Rev. Lett.* 79, 1245 (1997).

[93] P. M. Anisimov, J. P. Dowling, and B. C. Sanders, "Objectively Discerning Autler-Townes Splitting from Electromagnetically Induced Transparency", *Phys. Rev. Lett.* 107, 163604 (2011).

[94] M. Portier, M. Leduc, and C. Cohen-Tannoudji, "Fano profiles in two-photon photoassociation spectra", *Faraday Discuss.* 142, 415 (2009).

[95] R. Dumke, J. D. Weinstein, M. Johanning, K. M. Jones, and P. D. Lett, "Sub-natural-linewidth quantum interference features observed in photoassociation of a thermal gas", *Phys. Rev. A* 72, 041801 (2005).

[96] K. Winkler, G. Thalhammer, M. Theis, H. Ritsch, R. Grimm, and J. H. Denschlag, "Atom-Molecule Dark States in a Bose-Einstein Condensate", *Phys. Rev. Lett.* 95, 063202 (2005).

[97] L. D. Landau and E. M. Lifshitz, *Quantum Mechanics: Non-Relativistic Theory*, vol. 3, Butterworth-Heinemann, 1981.

[98] G. F. Gribakin and V. V. Flambaum, "Calculation of the scattering length in atomic collisions using the semiclassical approximation", *Phys. Rev. A* 48, 546 (1993).

[99] R. Côté, A. Dalgarno, Y. Sun, and R. G. Hulet, "Photoabsorption by Ultracold Atoms and the Scattering Length", *Phys. Rev. Lett.* 74, 3581 (1995).

[100] U. Fano, "Sullo spettro di emissione dei gas nobili presso il limite dello spettro d'arco", *Nuovo Cimento* 12, 154 (1935).

[101] U. Fano, "Effects of Configuration Interaction on Intensities and Phase Shifts", *Phys. Rev.* 124, 1866 (1961).

[102] H. Feshbach, "Unified theory of nuclear reactions", *Annals of Physics* 5, 357 (1958).

[103] P. O. Fedichev, Y. Kagan, G. V. Shlyapnikov, and J. T. M. Walraven, "Influence of Nearly Resonant Light on the Scattering Length in Low-Temperature Atomic Gases", *Phys. Rev. Lett.* 77, 2913 (1996).

[104] F. K. Fatemi, K. M. Jones, and P. D. Lett, "Observation of Optically Induced Feshbach Resonances in Collisions of Cold Atoms", *Phys. Rev. Lett.* 85, 4462 (2000).

[105] M. Theis, G. Thalhammer, K. Winkler, M. Hellwig, G. Ruff, R. Grimm, and J. H. Denschlag, "Tuning the Scattering Length with an Optically Induced Feshbach Resonance", *Phys. Rev. Lett.* 93, 123001 (2004).

[106] G. Thalhammer, M. Theis, K. Winkler, R. Grimm, and J. H. Denschlag, "Inducing an optical Feshbach resonance via stimulated Raman coupling", *Phys. Rev. A* 71, 033403 (2005).

[107] C. Chin, R. Grimm, P. Julienne, and E. Tiesinga, "Feshbach resonances in ultracold gases", *Rev. Mod. Phys.* 82, 1225 (2010).

[108] W. C. Stwalley, "Stability of Spin-Aligned Hydrogen at Low Temperatures and High Magnetic Fields: New Field-Dependent Scattering Resonances and Predissociations", *Phys. Rev. Lett.* 37, 1628 (1976).

[109] M. W. Reynolds, I. Shinkoda, R. W. Cline, and W. N. Hardy, "Observation of inverse predissociation of spin-polarized atomic hydrogen at low temperatures", *Phys. Rev. B* 34, 4912 (1986).

[110] E. Tiesinga, B. J. Verhaar, and H. T. C. Stoof, "Threshold and resonance phenomena in ultracold ground-state collisions", *Phys. Rev. A* 47, 4114 (1993).

[111] S. Inouye, M. R. Andrews, J. Stenger, H.-J. Miesner, D. M. Stamper-Kurn, and W. Ketterle, "Observation of Feshbach resonances in a Bose-Einstein condensate", *Nature* 392, 151 (1998).

[112] T. Weber, J. Herbig, M. Mark, H.-C. Nägerl, and R. Grimm, "Three-Body Recombination at Large Scattering Lengths in an Ultracold Atomic Gas", *Phys. Rev. Lett.* 91, 123201 (2003).

[113] E. A. Donley, N. R. Claussen, S. T. Thompson, and C. E. Wieman, "Atom-molecule coherence in a Bose-Einstein condensate", *Nature* 417, 529 (2002).

[114] J. Herbig, T. Kraemer, M. Mark, T. Weber, C. Chin, H.-C. Nägerl, and R. Grimm, "Preparation of a Pure Molecular Quantum Gas", *Science* 301, 1510 (2003).

[115] K. Xu, T. Mukaiyama, J. R. Abo-Shaeer, J. K. Chin, D. E. Miller, and W. Ketterle, "Formation of Quantum-Degenerate Sodium Molecules", *Phys. Rev. Lett.* 91, 210402 (2003).

[116] G. Alzetta, A. Gozzini, L. Moi, and G. Orriols, "An experimental method for the observation of r.f. transitions and laser beat resonances in oriented Na vapour", *Il Nuovo Cimento B (1971-1996)* 36, 5 (1976).

[117] E. Arimondo and G. Orriols, "Nonabsorbing atomic coherences by coherent two-photon transitions in a three-level optical pumping", *Lettere al Nuovo Cimento (1971-1985)* 17, 333 (1976).

[118] K. Aikawa, D. Akamatsu, M. Hayashi, K. Oasa, J. Kobayashi, P. Naidon, T. Kishimoto, M. Ueda, and S. Inouye, "Coherent Transfer of Photoassociated Molecules into the Rovibrational Ground State", *Phys. Rev. Lett.* 105, 203001 (2010).

[119] S. Stellmer, M. K. Tey, R. Grimm, and F. Schreck, "Bose-Einstein condensation of ^{86}Sr", *Phys. Rev. A* 82, 041602 (2010).

[120] M. K. Tey, S. Stellmer, R. Grimm, and F. Schreck, "Double-degenerate Bose-Fermi mixture of strontium", *Phys. Rev. A* 82, 011608 (2010).

[121] S. Stellmer, R. Grimm, and F. Schreck, "Production of quantum-degenerate strontium gases", *Phys. Rev. A* 87, 013611 (2013).

[122] S. Stellmer, B. Pasquiou, R. Grimm, and F. Schreck, "Laser Cooling to Quantum Degeneracy", *Phys. Rev. Lett.* 110, 263003 (2013).

[123] F. Schreck, T. Meyrath, and G. Hendl, *A Laboratory Control System for Cold Atom Experiments*, URL: `http://www.strontiumbec.com/control.html`.

[124] J. G. Danzl, E. Haller, M. Gustavsson, M. J. Mark, R. Hart, N. Bouloufa, O. Dulieu, H. Ritsch, and H.-C. Nägerl, "Quantum Gas of Deeply Bound Ground State Molecules", *Science* 321, 1062 (2008).

[125] T. Köhler, K. Góral, and P. S. Julienne, "Production of cold molecules via magnetically tunable Feshbach resonances", *Rev. Mod. Phys.* 78, 1311 (2006).

[126] C. Ospelkaus, S. Ospelkaus, L. Humbert, P. Ernst, K. Sengstock, and K. Bongs, "Ultracold Heteronuclear Molecules in a 3D Optical Lattice", *Phys. Rev. Lett.* 97, 120402 (2006).

[127] D. A. Brue and J. M. Hutson, "Prospects of forming ultracold molecules in $^2\Sigma$ states by magnetoassociation of alkali-metal atoms with Yb", *Phys. Rev. A* 87, 052709 (2013).

[128] J. L. Carini, S. Kallush, R. Kosloff, and P. L. Gould, "Enhancement of Ultracold Molecule Formation Using Shaped Nanosecond Frequency Chirps", *Phys. Rev. Lett.* 115, 173003 (2015).

[129] U. Gaubatz, P. Rudecki, S. Schiemann, and K. Bergmann, "Population transfer between molecular vibrational levels by stimulated Raman scattering with partially overlapping laser fields. A new concept and experimental results", *J. Chem. Phys.* 92, 5363 (1990).

[130] K. Bergmann, N. V. Vitanov, and B. W. Shore, "Perspective: Stimulated Raman adiabatic passage: The status after 25 years", *J. Chem. Phys.* 142, 170901 (2015).

[131] L. Yatsenko, R. Unanyan, K. Bergmann, T. Halfmann, and B. Shore, "Population transfer through the continuum using laser-controlled Stark shifts", *Opt. Commun.* 135, 406 (1997).

[132] E. R. Hudson, H. J. Lewandowski, B. C. Sawyer, and J. Ye, "Cold Molecule Spectroscopy for Constraining the Evolution of the Fine Structure Constant", *Phys. Rev. Lett.* 96, 143004 (2006).

[133] M. Kajita, G. Gopakumar, M. Abe, and M. Hada, "Characterizing of variation in the proton-to-electron mass ratio via precise measurements of molecular vibrational transition frequencies", *Journal of Molecular Spectroscopy* 300 Spectroscopic Tests of Fundamental Physics, 99 (2014).

[134] V. V. Flambaum and M. G. Kozlov, "Enhanced Sensitivity to the Time Variation of the Fine-Structure Constant and m_p/m_e in Diatomic Molecules", *Phys. Rev. Lett.* 99, 150801 (2007).

[135] R. V. Krems, "Cold controlled chemistry", *Phys. Chem. Chem. Phys.* 10, 4079 (2008).

[136] M. H. G. de Miranda, A. Chotia, B. Neyenhuis, D. Wang, G. Quemener, S. Ospelkaus, J. L. Bohn, J. Ye, and D. S. Jin, "Controlling the quantum stereodynamics of ultracold bimolecular reactions", *Nat. Phys.* 7, 502 (2011).

[137] R. Barnett, D. Petrov, M. Lukin, and E. Demler, "Quantum Magnetism with Multicomponent Dipolar Molecules in an Optical Lattice", *Phys. Rev. Lett.* 96, 190401 (2006).

[138] H. P. Büchler, E. Demler, M. Lukin, A. Micheli, N. Prokof'ev, G. Pupillo, and P. Zoller, "Strongly Correlated 2D Quantum Phases with Cold Polar Molecules: Controlling the Shape of the Interaction Potential", *Phys. Rev. Lett.* 98, 060404 (2007).

[139] M. Born and V. Fock, "Beweis des adiabatensatzes", *Z. Phys.* 51, 165 (1928).

[140] T. Kato, "On the Adiabatic Theorem of Quantum Mechanics", *J. Phys. Soc. Jpn.* 5, 435 (1950).

[141] N. V. Vitanov and S. Stenholm, "Population transfer via a decaying state", *Phys. Rev. A* 56, 1463 (1997).

[142] K. Winkler, F. Lang, G. Thalhammer, P. v. d. Straten, R. Grimm, and J. H. Denschlag, "Coherent Optical Transfer of Feshbach Molecules to a Lower Vibrational State", *Phys. Rev. Lett.* 98, 043201 (2007).

[143] G. Nenciu and G. Rasche, "On the adiabatic theorem for nonself-adjoint Hamiltonians", *J. Phys. A* 25, 5741 (1992).

[144] Y. B. Ovchinnikov, J. H. Müller, M. R. Doery, E. J. D. Vredenbregt, K. Helmerson, S. L. Rolston, and W. D. Phillips, "Diffraction of a Released Bose-Einstein Condensate by a Pulsed Standing Light Wave", *Phys. Rev. Lett.* 83, 284 (1999).

[145] F. H. Mies, E. Tiesinga, and P. S. Julienne, "Manipulation of Feshbach resonances in ultracold atomic collisions using time-dependent magnetic fields", *Phys. Rev. A* 61, 022721 (2000).

[146] D. Jaksch, V. Venturi, J. I. Cirac, C. J. Williams, and P. Zoller, "Creation of a Molecular Condensate by Dynamically Melting a Mott Insulator", *Phys. Rev. Lett.* 89, 040402 (2002).

[147] T. Busch, B.-G. Englert, K. Rzażewski, and M. Wilkens, "Two Cold Atoms in a Harmonic Trap", *Found. Phys.* 28, 549 (1998).

[148] L. W. Clark, L.-C. Ha, C.-Y. Xu, and C. Chin, "Quantum Dynamics with Spatiotemporal Control of Interactions in a Stable Bose-Einstein Condensate", *Phys. Rev. Lett.* 115, 155301 (2015).

[149] M. Cetina, M. Jag, R. S. Lous, J. T. M. Walraven, R. Grimm, R. S. Christensen, and G. M. Bruun, "Decoherence of Impurities in a Fermi Sea of Ultracold Atoms", *Phys. Rev. Lett.* 115, 135302 (2015).

[150] M. M. Boyd, PhD thesis, Boulder (USA): University of Colorado, 2007.

[151] L. P. Yatsenko, B. W. Shore, T. Halfmann, K. Bergmann, and A. Vardi, "Source of metastable H(2s) atoms using the Stark chirped rapid-adiabatic-passage technique", *Phys. Rev. A* 60, R4237 (1999).

[152] S. Guérin, L. P. Yatsenko, T. Halfmann, B. W. Shore, and K. Bergmann, "Stimulated hyper-Raman adiabatic passage. II. Static compensation of dynamic Stark shifts", *Phys. Rev. A* 58, 4691 (1998).

[153] A. Ciamei, A. Bayerle, B. Pasquiou, and F. Schreck, unpublished.

[154] W. Zwerger, "Mott-Hubbard transition of cold atoms in optical lattices", *Journal of Optics B: Quantum and Semiclassical Optics* 5, S9 (2003).

[155] A. Khramov, A. Hansen, W. Dowd, R. J. Roy, C. Makrides, A. Petrov, S. Kotochigova, and S. Gupta, "Ultracold Heteronuclear Mixture of Ground and Excited State Atoms", *Phys. Rev. Lett.* 112, 033201 (2014).

[156] C. Bruni and A. Görlitz, "Observation of hyperfine interaction in photoassociation spectra of ultracold RbYb", *Phys. Rev. A* 94, 022503 (2016).

[157] K. Beloy, A. W. Hauser, A. Borschevsky, V. V. Flambaum, and P. Schwerdtfeger, "Effect of α variation on the vibrational spectrum of Sr_2", *Phys. Rev. A* 84, 062114 (2011).

[158] S. Knoop, F. Ferlaino, M. Berninger, M. Mark, H. C. Nägerl, R. Grimm, J. P. D'Incao, and B. D. Esry, "Magnetically Controlled Exchange Process in an Ultracold Atom-Dimer Mixture", *Phys. Rev. Lett.* 104, 053201 (2010).

[159] J. Rui, H. Yang, L. Liu, D.-C. Zhang, Y.-X. Liu, J. Nan, B. Zhao, and J.-W. Pan, "Controlled state-to-state atom-exchange reaction in an ultracold atom-dimer mixture", *arXiv:1611.09066* (2016).

[160] J. F. Barry, D. J. McCarron, E. B. Norrgard, M. H. Steinecker, and D. DeMille, "Magneto-optical trapping of a diatomic molecule", *Nature* 512, 286 (2014).

[161] I. Kozyryev, L. Baum, K. Matsuda, B. L. Augenbraun, L. Anderegg, A. P. Sedlack, and J. M. Doyle, "Sisyphus Laser Cooling of a Polyatomic Molecule", *Phys. Rev. Lett.* 118, 173201 (2017).

[162] C. A. Regal, C. Ticknor, J. L. Bohn, and D. S. Jin, "Creation of ultracold molecules from a Fermi gas of atoms", *Nature* 424, 47 (2003).

[163] S. Jochim, M. Bartenstein, A. Altmeyer, G. Hendl, S. Riedl, C. Chin, J. Hecker Denschlag, and R. Grimm, "Bose-Einstein Condensation of Molecules", *Science* 302, 2101 (2003).

[164] M. Greiner, C. A. Regal, and D. S. Jin, "Emergence of a molecular Bose-Einstein condensate from a Fermi gas", *Nature* 426, 537 (2003).

[165] J. Javanainen and M. Mackie, "Coherent photoassociation of a Bose-Einstein condensate", *Phys. Rev. A* 59, R3186 (1999).

[166] P. D. Drummond, K. V. Kheruntsyan, and H. He, "Coherent Molecular Solitons in Bose-Einstein Condensates", *Phys. Rev. Lett.* 81, 3055 (1998).

[167] P. S. Julienne, K. Burnett, Y. B. Band, and W. C. Stwalley, "Stimulated Raman molecule production in Bose-Einstein condensates", *Phys. Rev. A* 58, R797 (1998).

[168] D. J. Heinzen, R. Wynar, P. D. Drummond, and K. V. Kheruntsyan, "Superchemistry: Dynamics of Coupled Atomic and Molecular Bose-Einstein Condensates", *Phys. Rev. Lett.* 84, 5029 (2000).

[169] M. Mackie, R. Kowalski, and J. Javanainen, "Bose-Stimulated Raman Adiabatic Passage in Photoassociation", *Phys. Rev. Lett.* 84, 3803 (2000).

[170] P. D. Drummond, K. V. Kheruntsyan, D. J. Heinzen, and R. H. Wynar, "Stimulated Raman adiabatic passage from an atomic to a molecular Bose-Einstein condensate", *Phys. Rev. A* 65, 063619 (2002).

[171] M. Mackie, A. Collin, and J. Javanainen, "Comment on "Stimulated Raman adiabatic passage from an atomic to a molecular Bose-Einstein condensate"", *Phys. Rev. A* 71, 017601 (2005).

[172] P. D. Drummond, K. V. Kheruntsyan, D. J. Heinzen, and R. H. Wynar, "Reply to "Comment on 'Stimulated Raman adiabatic passage from an atomic to a molecular Bose-Einstein condensate' "", *Phys. Rev. A* 71, 017602 (2005).

[173] R. Wynar, R. S. Freeland, D. J. Han, C. Ryu, and D. J. Heinzen, "Molecules in a Bose-Einstein Condensate", *Science* 287, 1016 (2000).

[174] C. McKenzie, J. Hecker Denschlag, H. Häffner, A. Browaeys, L. E. E. de Araujo, F. K. Fatemi, K. M. Jones, J. E. Simsarian, D. Cho, A. Simoni, E. Tiesinga, P. S. Julienne, K. Helmerson, P. D. Lett, S. L. Rolston, and W. D. Phillips, "Photoassociation of Sodium in a Bose-Einstein Condensate", *Phys. Rev. Lett.* 88, 120403 (2002).

[175] M. Yan, B. J. DeSalvo, Y. Huang, P. Naidon, and T. C. Killian, "Rabi Oscillations between Atomic and Molecular Condensates Driven with Coherent One-Color Photoassociation", *Phys. Rev. Lett.* 111, 150402 (2013).

[176] A. Ciamei, A. Bayerle, C.-C. Chen, B. Pasquiou, and F. Schreck, "Efficient production of long-lived ultracold Sr_2 molecules", *Phys. Rev. A* 96, 013406 (2017).

[177] K. M. R. van der Stam, E. D. van Ooijen, R. Meppelink, J. M. Vogels, and P. van der Straten, "Large atom number Bose-Einstein condensate of sodium", *Rev. Sci. Instrum.* 78, 013102 (2007).

[178] K. Willner, O. Dulieu, and F. Masnou-Seeuws, "Mapped grid methods for long-range molecules and cold collisions", *J. Chem. Phys.* 120, 548 (2004).

[179] A. Stein, H. Knöckel, and E. Tiemann, "The 1S+1S asymptote of Sr2 studied by Fourier-transform spectroscopy", *Eur. Phys. J. D* 57, 171 (2010).

[180] M. Borkowski, P. Morzyński, R. Ciuryło, P. S. Julienne, M. Yan, B. J. DeSalvo, and T. C. Killian, "Mass scaling and nonadiabatic effects in photoassociation spectroscopy of ultracold strontium atoms", *Phys. Rev. A* 90, 032713 (2014).

[181] J. J. Hope, M. K. Olsen, and L. I. Plimak, "Multimode model of the formation of molecular Bose-Einstein condensates by Bose-stimulated Raman adiabatic passage", *Phys. Rev. A* 63, 043603 (2001).

[182] Z. Idziaszek and P. S. Julienne, "Universal Rate Constants for Reactive Collisions of Ultracold Molecules", *Phys. Rev. Lett.* 104, 113202 (2010).

[183] J. Deiglmayr, M. Repp, R. Wester, O. Dulieu, and M. Weidemüller, "Inelastic collisions of ultracold polar LiCs molecules with caesium atoms in an optical dipole trap", *Phys. Chem. Chem. Phys.* 13, 19101 (2011).

[184] M. Machholm, P. S. Julienne, and K.-A. Suominen, "Calculations of collisions between cold alkaline-earth-metal atoms in a weak laser field", *Phys. Rev. A* 64, 033425 (2001).

[185] X. Chen and J. G. Muga, "Engineering of fast population transfer in three-level systems", *Phys. Rev. A* 86, 033405 (2012).

[186] P. S. Żuchowski, R. Guérout, and O. Dulieu, "Ground- and excited-state properties of the polar and paramagnetic RbSr molecule: A comparative study", *Phys. Rev. A* 90, 012507 (2014).

[187] A. Guttridge, S. Hopkins, M. Frye, J. McFerran, J. Hutson, and S. Cornish, "Production of ultracold Cs*Yb molecules by photoassociation", *arXiv:1804.07319* (2018).

[188] V. Barbé, A. Ciamei, B. Pasquiou, L. Reichsöllner, F. Schreck, P. S. Żuchowski, and J. Hutson, "Observation of Feshbach resonances between alkali and closed-shell atoms", *arXiv:1710.03093* (2017).

[189] A. Ciamei and et. al, *in preparation*.

[190] U. Schünemann, H. Engler, R. Grimm, M. Weidemüller, and M. Zielonkowski, "Simple scheme for tunable frequency offset locking of two lasers", *Review of Scientific Instruments* 70, 242 (1999).

[191] O. Dulieu, *private communication*.

[192] R. Wester, S. Kraft, M. Mudrich, M. Staudt, J. Lange, N. Vanhaecke, O. Dulieu, and M. Weidemüller, "Photoassociation inside an optical dipole trap: absolute rate coefficients and Franck–Condon factors", *Appl. Phys. B* 79, 993 (2004).

[193] J. Weiner, V. S. Bagnato, S. Zilio, and P. S. Julienne, "Experiments and theory in cold and ultracold collisions", *Rev. Mod. Phys.* 71, 1 (1999).

[194] R. Ciuryło, E. Tiesinga, S. Kotochigova, and P. S. Julienne, "Photoassociation spectroscopy of cold alkaline-earth-metal atoms near the intercombination line", *Phys. Rev. A* 70, 062710 (2004).

[195] S. Taie, R. Yamazaki, S. Sugawa, and Y. Takahashi, "An SU(6) Mott insulator of an atomic Fermi gas realized by large-spin Pomeranchuk cooling", *Nat. Phys.* 8, 825 (2012).

[196] S. Kraft, F. Vogt, O. Appel, F. Riehle, and U. Sterr, "Bose-Einstein Condensation of Alkaline Earth Atoms: ^{40}Ca", *Phys. Rev. Lett.* 103, 130401 (2009).

[197] J. Pérez-Ríos, F. Herrera, and R. V. Krems, "External field control of collective spin excitations in an optical lattice of $^2\Sigma$ molecules", *New J. Phys.* 12, 103007 (2010).

[198] S. V. Alyabyshev, M. Lemeshko, and R. V. Krems, "Sensitive imaging of electromagnetic fields with paramagnetic polar molecules", *Phys. Rev. A* 86, 013409 (2012).

[199] F. Herrera, Y. Cao, S. Kais, and K. B. Whaley, "Infrared-dressed entanglement of cold open-shell polar molecules for universal matchgate quantum computing", *New J. Phys.* 16, 075001 (2014).

[200] S. B. Cahn, J. Ammon, E. Kirilov, Y. V. Gurevich, D. Murphree, R. Paolino, D. A. Rahmlow, M. G. Kozlov, and D. DeMille, "Zeeman-Tuned Rotational Level-Crossing Spectroscopy in a Diatomic Free Radical", *Phys. Rev. Lett.* 112, 163002 (2014).

[201] M. Kajita, "Prospects of detecting m_e/m_p variance using vibrational transition frequencies of $^2\Sigma$-state molecules", *Phys. Rev. A* 77, 012511 (2008).

[202] J. Wolf, M. Deiss, A. Krükow, E. Tiemann, B. P. Ruzic, Y. Wang, J. P. D'Incao, P. S. Julienne, and J. H. Denschlag, "State-to-state chemistry at ultra-low temperature", *Science* 358, 921 (2017).

[203] T. Sikorsky, Z. Meir, R. Ben-shlomi, N. Akerman, and R. Ozeri, "Spin-controlled atom-ion chemistry", *Nat. Commun.* 9, 920 (2018).

[204] J. Szczepkowski, A. Grochola, P. Kowalczyk, O. Dulieu, R. Guérout, P. S. Żuchowski, and W. Jastrzebski, "Experimental and theoretical study of the B(2) X(1) system in the KSr molecule", *J. Quant. Spectrosc. Radiat. Transfer* 210, 217 (2018).

[205] J. V. Pototschnig, G. Krois, F. Lackner, and W. E. Ernst, "Investigation of the RbCa molecule: Experiment and theory", *J. Mol. Spectrosc.* 310, 126 (2015).

[206] M. Ivanova, A. Stein, A. Pashov, A. V. Stolyarov, H. Knöckel, and E. Tiemann, "The $X^2\Sigma^+$ state of LiCa studied by Fourier-transform spectroscopy", *J. Chem. Phys.* 135, 174303 (2011).

[207] E. Schwanke, H. Knöckel, A. Stein, A. Pashov, S. Ospelkaus, and E. Tiemann, "Laser and Fourier transform spectroscopy of ^{7}Li^{88}Sr", *J. Phys. B: At., Mol. Opt. Phys.* 50, 235103 (2017).

[208] M. Borkowski, P. S. Żuchowski, R. Ciuryło, P. S. Julienne, D. Kedziera, Ł. Mentel, P. Tecmer, F. Münchow, C. Bruni, and A. Görlitz, "Scattering lengths in isotopologues of the RbYb system", *Phys. Rev. A* 88, 052708 (2013).

[209] G. Krois, J. V. Pototschnig, F. Lackner, and W. E. Ernst, "Spectroscopy of Cold LiCa Molecules Formed on Helium Nanodroplets", *J. Phys. Chem. A* 117, 13719 (2013).

[210] G. Pichler, A. Lyyra, P. Kleiber, W. Stwalley, R. Hammer, K. Sando, and H. Michels, "Laser-induced chemiluminescence of the LiMg excimer", *Chem. Phys. Lett.* 156, 467 (1989).

[211] M. Borkowski, A. A. Buchachenko, R. Ciuryło, P. S. Julienne, H. Yamada, K. Yuu, K. Takahashi, Y. Takasu, and Y. Takahashi, "Probing Non-Newtonian gravity by photoassociation spectroscopy", *Journal of Physics: Conference Series* 810, 012014 (2017).

[212] J. Gerschmann, E. Schwanke, A. Pashov, H. Knöckel, S. Ospelkaus, and E. Tiemann, "Laser and Fourier-transform spectroscopy of KCa", *Phys. Rev. A* 96, 032505 (2017).

[213] E. Schwanke, H. Knoeckel, A. Stein, A. Pashov, S. Ospelkaus, and E. Tiemann, "Laser and Fourier transform spectroscopy of ^{7}Li^{88}Sr", *J. Phys. B: At. Mol. Opt. Phys.* 50, 235103 (2017).

[214] M. Debatin, T. Takekoshi, R. Rameshan, L. Reichsollner, F. Ferlaino, R. Grimm, R. Vexiau, N. Bouloufa, O. Dulieu, and H.-C. Nagerl, "Molecular spectroscopy for ground-state transfer of ultracold RbCs molecules", *Phys. Chem. Chem. Phys.* 13, 18926 (2011).

[215] M. Guo, R. Vexiau, B. Zhu, B. Lu, N. Bouloufa-Maafa, O. Dulieu, and D. Wang, "High-resolution molecular spectroscopy for producing ultracold absolute-ground-state ^{23}Na^{87}Rb molecules", *Phys. Rev. A* 96, 052505 (2017).

[216] G. Gopakumar, M. Abe, M. Hada, and M. Kajita, "Dipole polarizability of alkali-metal (Na, K, Rb)-alkaline-earth-metal (Ca, Sr) polar molecules: Prospects for alignment", *J. Chem. Phys.* 140, 224303 (2014).

[217] F. Lackner, G. Krois, T. Buchsteiner, J. V. Pototschnig, and W. E. Ernst, "Helium-Droplet-Assisted Preparation of Cold RbSr Molecules", *Phys. Rev. Lett.* 113, 153001 (2014).

[218] G. Krois, F. Lackner, J. V. Pototschnig, T. Buchsteiner, and W. E. Ernst, "Characterization of RbSr molecules: spectral analysis on helium droplets", *Phys. Chem. Chem. Phys.* 16, 22373 (2014).

[219] J. M. Brown and A. Carrington, *Rotational Spectroscopy of Diatomic Molecules*, Cambridge Molecular Science, Cambridge University Press, 2003.

[220] J. V. Pototschnig, G. Krois, F. Lackner, and W. E. Ernst, "Ab initio study of the RbSr electronic structure: Potential energy curves, transition dipole moments, and permanent electric dipole moments", *J. Chem. Phys.* 141, 234309 (2014).

[221] A. Ciamei and et. al, *in preparation*.

[222] V. V. Flambaum, G. F. Gribakin, and C. Harabati, "Analytical calculation of cold-atom scattering", *Phys. Rev. A* 59, 1998 (1999).

[223] J. Szczepkowski, A. Ciamei, and F. Schreck, *in preparation*.

[224] J. Jiang, Y. Cheng, and J. Mitroy, "Long-range interactions between alkali and alkaline-earth atoms", *J. Phys. B: At., Mol. Opt. Phys.* 46, 125004 (2013).

[225] A. Derevianko, S. G. Porsev, and J. F. Babb, "Electric dipole polarizabilities at imaginary frequencies for hydrogen, the alkali-metal, alkaline-earth, and noble gas atoms", *At. Data Nucl. Data Tables* 96, 323 (2010).

[226] J. M. Standard and P. R. Certain, "Bounds to two- and three-body long-range interaction coefficients for S-state atoms", *J. Chem. Phys.* 83, 3002 (1985).

[227] D. A. Brue and J. M. Hutson, "Magnetically Tunable Feshbach Resonances in Ultracold Li-Yb Mixtures", *Phys. Rev. Lett.* 108, 043201 (2012).

[228] A. Mosk, S. Kraft, M. Mudrich, K. Singer, W. Wohlleben, R. Grimm, and M. Weidemüller, "Mixture of ultracold lithium and cesium atoms in an optical dipole trap", *Appl. Phys. B* 73, 791 (2001).

[229] M. Inguscio, S. Stringari, and C. Wieman, "Bose-Einstein Condensation in Atomic Gases", *Proceedings of the International School of Physics "Enrico Fermi"* 140, 321 (1999).

[230] N. S. Dattani and R. J. Le Roy, "A DPF data analysis yields accurate analytic potentials for and that incorporate 3-state mixing near the state asymptote", *J. Mol. Spectrosc.* 268, 199 (2011).

[231] M. Semczuk, X. Li, W. Gunton, M. Haw, N. S. Dattani, J. Witz, A. K. Mills, D. J. Jones, and K. W. Madison, "High-resolution photoassociation spectroscopy of the $^6Li_2$ $1^3\Sigma_g^+$ state", *Phys. Rev. A* 87, 052505 (2013).

[232] J. J. Lutz and J. M. Hutson, "Deviations from Born-Oppenheimer mass scaling in spectroscopy and ultracold molecular physics", *J. Mol. Spectrosc.* 330 Potentiology and Spectroscopy in Honor of Robert Le Roy, 43 (2016).

[233] J. Y. Seto, R. J. Le Roy, J. Vergès, and C. Amiot, "Direct potential fit analysis of the $X^1\Sigma_g^+$ state of Rb2: Nothing else will do!", *J. Chem. Phys.* 113, 3067 (2000).

[234] E. G. M. van Kempen, S. J. J. M. F. Kokkelmans, D. J. Heinzen, and B. J. Verhaar, "Interisotope Determination of Ultracold Rubidium Interactions from Three High-Precision Experiments", *Phys. Rev. Lett.* 88, 093201 (2002).

[235] R. J. Le Roy, C. C. Haugen, J. Tao, and H. Li, "Long-range damping functions improve the short-range behaviour of MLR potential energy functions", *Mol. Phys.* 109, 435 (2011).

[236] C. Douketis, G. Scoles, S. Marchetti, M. Zen, and A. J. Thakkar, "Intermolecular forces via hybrid Hartree-Fock-SCF plus damped dispersion (HFD) energy calculations. An improved spherical model", *J. Chem. Phys.* 76, 3057 (1982).

[237] NIST, *Atomic Spectra Database*, URL: `https://www.nist.gov/pml/atomic-spectra-database`.

[238] A. Pashov, W. Jastrzebski, and P. Kowalczyk, "Construction of potential curves for diatomic molecular states by the IPA method", *Comput. Phys. Commun.* 128, 622 (2000).

[239] C. H. Greene, P. Giannakeas, and J. Pérez-Ríos, "Universal few-body physics and cluster formation", *Rev. Mod. Phys.* 89, 035006 (2017).

[240] J. M. Hutson and P. Soldán, "Molecule formation in ultracold atomic gases", *Int. Rev. Phys. Chem.* 25, 497 (2006).

[241] E. R. Meyer and J. L. Bohn, "Electron electric-dipole-moment searches based on alkali-metal- or alkaline-earth-metal-bearing molecules", *Phys. Rev. A* 80, 042508 (2009).

[242] J. Herbig, T. Kraemer, M. Mark, T. Weber, C. Chin, H. C. Nägerl, and R. Grimm, "Preparation of a pure molecular quantum gas", *Science* 301, 1510 (2003).

[243] J. G. Danzl, M. J. Mark, E. Haller, M. Gustavsson, R. Hart, J. Aldegunde, J. M. Hutson, and H. C. Nägerl, "An ultracold, high-density sample of rovibronic ground-state molecules in an optical lattice", *Nature Phys.* 6, 265 (2010).

[244] A. Guttridge, S. A. Hopkins, S. L. Kemp, M. D. Frye, J. M. Hutson, and S. L. Cornish, "Interspecies thermalization in an ultracold mixture of Cs and Yb in an optical trap", *Phys. Rev. A* 96, 012704 (2017).

[245] *See supplementary information.*

[246] J. Aldegunde and J. M. Hutson, "Hyperfine structure of $^2\Sigma$ molecules containing alkaline-earth-metal atoms", *Phys. Rev. A* 97, 042505 (2018).

[247] W. Dowd, R. J. Roy, R. K. Shrestha, A. Petrov, C. Makrides, S. Kotochigova, and S. Gupta, "Magnetic field dependent interactions in an ultracold Li-Yb($^3P_2$) mixture", *New J. Phys.* 17, 055007 (2015).

[248] S. Kato, S. Sugawa, K. Shibata, R. Yamamoto, and Y. Takahashi, "Control of Resonant Interaction between Electronic Ground and Excited States", *Phys. Rev. Lett.* 110, 173201 (2013).

[249] G. Pagano, M. Mancini, G. Cappellini, L. Livi, C. Sias, J. Catani, M. Inguscio, and L. Fallani, "Strongly Interacting Gas of Two-Electron Fermions at an Orbital Feshbach Resonance", *Phys. Rev. Lett.* 115, 265301 (2015).

[250] M. Höfer, L. Riegger, F. Scazza, C. Hofrichter, D. R. Fernandes, M. M. Parish, J. Levinsen, I. Bloch, and S. Fölling, "Observation of an Orbital Interaction-Induced Feshbach Resonance in ^{173}Yb", *Phys. Rev. Lett.* 115, 265302 (2015).

[251] J. Werner, A. Griesmaier, S. Hensler, J. Stuhler, T. Pfau, A. Simoni, and E. Tiesinga, "Observation of Feshbach Resonances in an Ultracold Gas of ^{52}Cr", *Phys. Rev. Lett.* 94, 183201 (2005).

[252] K. Aikawa, A. Frisch, M. Mark, S. Baier, A. Rietzler, R. Grimm, and F. Ferlaino, "Bose-Einstein Condensation of Erbium", *Phys. Rev. Lett.* 108, 210401 (2012).

[253] K. Baumann, N. Q. Burdick, M. Lu, and B. L. Lev, "Observation of low-field Fano-Feshbach resonances in ultracold gases of dysprosium", *Phys. Rev. A* 89, 020701 (2014).

[254] A. Marte, T. Volz, J. Schuster, S. Dürr, G. Rempe, E. G. M. van Kempen, and B. J. Verhaar, "Feshbach Resonances in Rubidium-87: Precision Measurement and Analysis", *Phys. Rev. Lett.* 89, 283202 (2002).

[255] M. Mark, T. Kraemer, J. Herbig, C. Chin, H. C. Nägerl, and R. Grimm, "Efficient creation of molecules from a cesium Bose-Einstein condensate", *Europhys. Lett.* 69, 706 (2005).

[256] N. Syassen, D. M. Bauer, M. Lettner, D. Dietze, T. Volz, S. Dürr, and G. Rempe, "Atom-Molecule Rabi Oscillations in a Mott Insulator", *Phys. Rev. Lett.* 99, 033201 (2007).

[257] S. L. Kemp, K. L. Butler, R. Freytag, S. A. Hopkins, E. A. Hinds, M. R. Tarbutt, and S. L. Cornish, "Production and characterization of a dual species magneto-optical trap of cesium and ytterbium", *Rev. Sci. Instrum.* 87, 023105 (2016).

[258] A. V. Taichenachev, V. I. Yudin, C. W. Oates, C. W. Hoyt, Z. W. Barber, and L. Hollberg, "Magnetic Field-Induced Spectroscopy of Forbidden Optical Transitions with Application to Lattice-Based Optical Atomic Clocks", *Phys. Rev. Lett.* 96, 083001 (2006).

[259] A. Stein, H. Knöckel, and E. Tiemann, "Fourier-transform spectroscopy of Sr_2 and revised ground-state potential", *Phys. Rev. A* 78, 042508 (2008).

[260] M. Borkowski, A. A. Buchachenko, R. Ciuryło, P. S. Julienne, H. Yamada, Y. Kikuchi, K. Takahashi, Y. Takasu, and Y. Takahashi, "Beyond-Born-Oppenheimer effects in sub-kHz-precision photoassociation spectroscopy of ytterbium atoms", *Phys. Rev. A* 96, 063405 (2017).

[261] Y. Cui, C. Shen, M. Deng, S. Dong, C. Chen, R. Lü, B. Gao, M. K. Tey, and L. You, "Observation of Broad d-Wave Feshbach Resonances with a Triplet Structure", *Phys. Rev. Lett.* 119, 203402 (2017).

[262] X.-C. Yao, R. Qi, X.-P. Liu, X.-Q. Wang, Y.-X. Wang, Y.-P. Wu, H.-Z. Chen, P. Zhang, H. Zhai, Y.-A. Chen, and J.-W. Pan, "Strongly Interacting Bose Gases near a d-wave Shape Resonance", *arXiv:1711.06622* (2017).

[263] J. Pérez-Ríos, M. Lepers, and O. Dulieu, "Theory of Long-Range Ultracold Atom-Molecule Photoassociation", *Phys. Rev. Lett.* 115, 073201 (2015).

[264] V. Bendkowsky, B. Butscher, J. Nipper, J. B. Balewski, J. P. Shaffer, R. Löw, T. Pfau, W. Li, J. Stanojevic, T. Pohl, and J. M. Rost, "Rydberg Trimers and Excited Dimers Bound by Internal Quantum Reflection", *Phys. Rev. Lett.* 105, 163201 (2010).

[265] D. DeMille, Private communication, 2017.

[266] M. S. Safronova, D. Budker, D. DeMille, D. F. J. Kimball, A. Derevianko, and C. W. Clark, "Search for new physics with atoms and molecules", *Rev. Mod. Phys.* 90, 025008 (2018).

Summary

This work started with the rebuilding and optimization of the ultracold Rb-Sr mixture machine after this was moved from Innsbruck (Austria) to Amsterdam (The Netherlands). Our research concerned the investigation of experimental techniques for efficient production of ultracold Sr_2 and RbSr dimers. In the following we summarize our results.

In our works on Sr_2, we have demonstrated molecule production from quantum-degenerate atomic ^{84}Sr samples, both in the MI and BEC phase. In the MI case, we designed and implemented an optimized STIRAP able to cancel the space- and time-dependent light-shifts induced by the PA lasers on the binding energy of the target molecular level, intrinsic to the standard STIRAP scheme. The experiments were interpreted and analyzed by extending the theoretical model for STIRAP to include the effects of deviations from two-photon resonance, which provided analytical insights into the limitations of STIRAP for this application. This optimized STIRAP, together with the use of a far-off-resonance deep optical lattice, allowed to reach an association efficiency in excess of 80%, resulting in a molecular $^{84}Sr_2$ MI with a lifetime longer than a minute. In the BEC case, we have directly observed the products of Bose-enhanced photoassociation for the first time and measured an association efficiency of roughly 10%. The lifetime of the resulting molecular sample trapped alone or together with Sr atoms, gave access to the inelastic dimer-dimer and dimer-atom reactive rate coefficients, which where compared to the theoretical universal rate coefficients for reactive collisions of ultracold molecules.

In the case of RbSr, our optimized STIRAP was attempted without success on doubly occupied sites of a ^{87}Rb-^{84}Sr MI containing exactly one atom of each species. This problem motivated the subsequent research for a deeper understanding of RbSr molecules. On the experimental side this resulted in extensive high-precision one- and two-color optical spectroscopy in ultracold Rb-Sr mixtures of several isotopic combinations. These results, together with the predictions of our theory collaborators [1], led to the first experimental observation of a magnetic Fano-Feshbach resonance in a system composed of a closed-shell and an open-shell atom like RbSr. Fano-Feshbach

[1] Jeremy Hutson and Piotr Żuchowski

resonances induced by both theoretically predicted isotropic and novel anisotropic couplings were subsequently observed in several isotopic combinations. On the theoretical side, this research line resulted in a joint data analysis carried out on our high-precision data and independent thermal fluorescence spectra obtained by our collaborators in the molecular spectroscopy team of Warsaw[2]. The novel data analysis tools developed for this application allowed to benchmark and refine theoretical *ab-initio* Born-Oppenheimer potentials for the ground state and, with less precision, an excited state of the RbSr molecule. The derived ground-state potential interestingly showed predictive power both for weakly-bound optical-magnetic spectra and deeply-bound thermal-fluorescence spectra. Its predictive power was used to accurately infer scattering properties, especially s-wave scattering lengths, and the binding energies of weakly-bound ground-state levels for all isotopologues and quantum numbers (neglecting Sr nuclear moment). The best candidate isotopologue for molecule production, i.e. ^{87}Rb^{84}Sr, and the best candidate Fano-Feshbach resonance for magnetic association, i.e. the s-wave scattering-resonance at $B \simeq 1310\,\mathrm{G}$, was identified based on this fitted potential.

[2] Anna Grochola, Wlodzimierz Jastrzebski, Paweł Kowalczyk and Jacek Szczepkowski

Samenvatting

Dit werk begon met de verbouwing en optimalisatie van een opstelling voor ultrakoude Rb-Sr mengsels, die was verplaatst vanuit Innsbruck naar Amsterdam (Nederland). Ons onderzoek richt zich op de experimentele methodes voor de efficinte productie van ultrakoude Sr_2 en RbSr dimers. We geven onze resultaten hier kort weer.

In ons werk met Sr_2 hebben we molecuulproductie laten zien, beginnende met ontaarde kwantumgassen van ^{84}Sr, zowel in de MI als in de BEC fase. In het MI geval hebben we een geoptimaliseerde STIRAP ontworpen en geïmplementeerd, wat het mogelijk maakt om de ruimte- en tijdsafhankelijke energieverschuiving van het moleculaire doelniveau te verwijderen. Deze energieverschuiving is intrinsiek aan gebruikelijke STIRAP-schema's. Deze experimenten zijn geïnterpreteerd en geanalyseerd door een theoriemodel van STIRAP uit te breiden om de effecten van frequentieverschuiving van de twee-foton-resonantie toe te voegen, een proces dat analytisch inzicht over de grenzen van STIRAP voor deze toepassing leverde. De geoptimaliseerde STIRAP, samen met het gebruik van een sterk niet-resonant diep optisch rooster hebben het mogelijk gemaakt om een verbindingsefficiëntie van meer dan 80% te bereiken, met als resultaat een moleculaire MI van $^{84}Sr_2$ met een levensduur van meer dan een minuut. In het BEC geval hebben we voor de eerste keer direct de producten van Bose-versterkte fotoassociatie waargenomen en een verbindingsefficiëntie gemeten van ongeveer 10%. De levensduur van de moleculaire wolk, gevangen in de val samen met of juist zonder Sr atomen, liet ons de waarden bepalen van inelastische dimer-dimer of dimer-atoom reactiesnelheidsconstanten. Vervolgens hebben we deze vergeleken met de theoretische universele reactiesnelheidsconstanten voor reactieve botsingen van ultrakoude moleculen.

In het geval van RbSr hebben we geprobeerd om de geoptimaliseerde STIRAP te gebruiken op dubbel bezette putjes van een ^{87}Rb-^{84}Sr MI met precies één atoom van elke soort in ieder putje. Dit was helaas zonder succes maar heeft vervolgens wel het onderzoek daarna gestimuleerd om RbSr moleculen beter te begrijpen. In het experiment leidde dit tot uitgebreide en zeer nauwkeurige optische één- en tweekleuren spectroscopie in Rb-Sr mengsels van verschillende isotoopsamenstellingen. Deze resultaten, samen met de voorspellingen van onze collega's van theoretische

fysica[3], leidde tot de eerste waarneming van magnetische Fano-Feshbach resonanties in een systeem dat bestaat uit zowel een atoom met een complete als een incomplete elektronenschil, zoals RbSr. Fano-Feschbach resonanties gefaciliteerd door de theoretisch voorspelde isotrope en nieuwe anisotrope koppelingen werden vervolgens waargenomen in meerdere isotoopsamenstellingen. Op het gebied van theorie leidde dit onderzoek tot een gezamenlijke data analyse van onze zeer nauwkeurige metingen en onafhankelijke metingen van thermische fluorescentiespectra genomen door onze collegas in de moleculaire spectroscopiegroep in Warschau[4]. De vernieuwende data analyse methodes die voor deze toepassing zijn ontwikkeld, hebben een maatstaf en een verfijning geïntroduceerd voor theoretische ab-initio Born-Oppenheimer potentialen voor de grondtoestand en, met minder nauwkeurigheid, ook de geëxciteerde toestand van het RbSr molecuul. Interessant genoeg stelde de resulterende grondtoestand potentiaal ons in staat om zowel zwak gebonden optisch-magnetische spectra als ook sterk gebonden thermische fluorescentiespectra te voorspellen. Het voorspellend vermogen hebben we verder gebruikt om strooingseigenschappen af te leiden voor, in het bijzonder, de s-golf strooilengte en de bindingsenergieën van zwak gebonden grondniveaus voor alle isotopologen en alle kwantumgetallen (afgezien van het magnetisch moment van de kern). De beste isotopologische kandidaat voor molecuulproductie, zijnde ^{87}Rb^{84}Sr, en de beste kandidaat voor een Fano-Feshbach resonantie, zijnde een s-golf strooiingsresonantie op $B = 1310\,\mathrm{G}$, werd gevonden op basis van deze gefitte potentiaal.

[3] Jeremy Hutson and Piotr Żuchowski
[4] Anna Grochola, Wlodzimierz Jastrzebski, Paweł Kowalczyk and Jacek Szczepkowski

List of publications

Published papers:

- Alessio Ciamei, Alex Bayerle, Chun-Chia Chen, Benjamin Pasquiou, and Florian Schreck, "Efficient production of long-lived Sr_2 molecules", Physical Review A 96, 013406 (2017).

  Contributions: Optimization and calibration of optical lattice, implementation of the laser set-up for optimized STIRAP. Experiments, i.e. investigation of light-shifts and of their effects on STIRAP, measurement of the lifetime of the molecular lattice gas. Inclusion of time-dependent two-color detuning into standard 3-level model and derivation of an approximate analytical solution. Interpretation of the experiments and data analysis. Writing of the paper.

- Alessio Ciamei, Alex Bayerle, Benjamin Pasquiou, and Florian Schreck, "Observation of Bose-enhanced photoassociation products", Europhysics Letters 119, 4, 46001 (2017).

  Contributions: Proposal of the experiments. Experiments, i.e. photoassociation in BEC and measurement of reactive scattering cross-sections. Data analysis of both photoassociation and scattering cross-section measurements. Writing of the paper.

- Vincent Barbé*, Alessio Ciamei*, Benjamin Pasquiou, Lukas Reichsöllner, Florian Schreck, Piotr S. Żuchowski, and Jeremy M. Hutson, "Observation of Feshbach resonances between alkali and closed-shell atoms", Nature Physics, Advance Online Publication (2018), doi:10.1038/s41567-018-0169-x. *These authors contributed equally to this work.

  Contributions: Preparation of an ultracold ^{87}Rb-^{87}Sr mixture, photoassociation experiments and calibration of the magnetic field, leading to the first observation of FF resonance at $B = 295\,\mathrm{G}$. Identification of FF resonances originating from anisotropic coupling mechanism III and first experimental observation of their substructure. Prediction of the FF resonance for bosonic ^{87}Rb^{84}Sr at

$B = 366\,\mathrm{G}$. Attribution of quantum numbers to observed FF resonances, extraction of scattering lengths, assessment of prospects of magneto-association, and identification of ^{87}Rb^{84}Sr as best candidate.

Papers submitted for publication:

- Alessio Ciamei*, Jacek Szczepkowski*, Alex Bayerle*, Vincent Barbé, Lukas Reichsöllner, Slava M. Tzanova, Chun-Chia Chen, Benjamin Pasquiou, Anna Grochola, Pawel Kowalczyk, Wlodzimierz Jastrzebski, and Florian Schreck, "The RbSr $^2\Sigma^+$ ground state investigated via spectroscopy of hot & ultracold molecules", preprint: arXiv:1806.08586. *These authors contributed equally to this work.

  Contributions: 2-color photoassociation experiments on ^{87}Rb-^{87,88}Sr mixtures. Design and realization of cross-thermalization measurements on ^{87}Rb-^{84,88}Sr mixtures. Data analysis of our RbSr spectroscopy data and thermal/laser-induced fluorescence data, i.e. derivation of a fitted mass-scaled model potential for the ground state of RbSr and comparison with theoretical predictions. Data analysis of cross-thermalization measurements. Prediction of FF resonances relevant to RbSr isotopologues. Writing of the paper.

Further work:
Further work was executed that we intend to include in future publications.

- "Computer program for combined fit of molecular potential curves on thermal-fluorescence and two-color spectroscopy data" (working title).

  Contributions: Routines for data analysis and predictions concerning alkali – alkaline-earth or alkaline-earth – alkaline-earth dimers. Routines for data analysis of weakly-bound spectrum without input of *ab initio* predictions. Routines for direct potential fit to two-color photoassociation and thermal-fluorescence data with input *ab initio* predictions. Routines for prediction of binding energies. Routines for prediction of locations and strengths of magnetic FF resonances.

- "1-color photoassociation in ultracold Rb-Sr mixtures"(working title, based on chapter 5).

  Contributions: PA beat-locked laser set-up. 1-color photoassociation experiments of all stable isotopologues ^{87}Rb^{x}Sr. Data analysis for extraction of 1-color PA locations, PA rate coefficients and stimulated rates, linewidths and magnetic moments. Writing of the paper draft (chapter 5).

Acknowledgements

Over the past four and a half years I worked hard to become an experimental physicist and contribute to the field of ultracold atoms and molecules. For this I have to thank my supervisor Florian Schreck, who trusted and supported me since my very first visit to his group in Innsbruck, through the move and rebuilding of the ultracold Rb-Sr mixture machine in Amsterdam, and all the way to the very end of my PhD and writing of my thesis. There wasn't a day that I didn't learn something new from him, from the most technical to the most general aspects of experimental physics. I learned from him and experienced firsthand that research seldom goes on a straight line and often in circle, the necessity and importance of perseverance and the crucial role of details and know-how. However, even more than the contents of my research I owe him the shape in which it was presented in this thesis and in the published papers which corresponds to his most careful and critical revision of my writings. I often ask myself: "how would Florian explain this?". Even now.

I am grateful to Alex Bayerle, Chun-Chia Chen and Benjamin Pasquiou, from whom I learned how to work in an atomic physics lab, especially while rebuilding and optimizing the apparatus. We did a great job working together as shown by the RbSr machine, which is an excellent apparatus and is producing many fascinating results. Moreover, from Benjamin I learned how to operate and manage a complex experimental apparatus like the RbSr machine. All that training was essential for me to become a more independent and confident experimental physicist and affected all my subsequent work. I also have to thank Benjamin for his patience and help in paper writing, especially for the effort in bringing paper drafts up to Florian's standards.

I would like to thank Vincent Barbé and Lukas Reichsöllner. We had countless discussions in and out of the lab and obtained many ground-breaking results on RbSr, which I hope will finally end up in the production of RbSr molecules and exciting studies of many-body physics. Without them the understanding of RbSr in the form presented in this thesis would have been impossible. Unfortunately, Severin Charpignon only joined the team at the end of my PhD and I am sure he will be a great addition to the RbSr team and enjoy working within them.

I would like to thank everyone from the Sr BEC group for many discussions and frequent exchange of ideas, especially Shayne Bennetts, Rodrigo Gonzlez Escudero, Oleksiy Onishchenko, Sergey Pyatchenkov, Carla Sanna, Georgios Siviloglou, Alex Urech and our in-house theorist Denis Kurlov. Beyond the Sr BEC group I take this opportunity to thank the whole quantum gases group at UvA for providing a fruitful environment for my research and the regular "journal club" meetings, which helped expanding my horizon beyond ultracold molecules and which I always enjoyed. Among the quantum gases group, my office neighbours Nataly Cisternas, David Davtyan,

Julius de Hond, Graham Lochead, Arthur La Rooij, Maarten Soudijn were always there to help or to listen to my complaints over things not working the way they should in the experiment. I would like to thank the mechanical and electronics workshop for their support and practical help of fundamental importance. I would like to thank the administrative staff of the IoP, especially Joost van Mameren, Rita Vinig, Natalie Wells and Anne-Marieke Crommentuijn, who helped me in many occasions during the years.

I am grateful to theorists Jeremy Hutson and Piotr Żuchowski for their support on the RbSr project and above all for their patience in explaining the theory and answering many questions about weakly bound states of diatomic molecules and their analysis.

A special thank goes to the molecular spectroscopy team of Warsaw, Anna Grochola, Wlodzimierz Jastrzebski, Paweł Kowalczyk and Jacek Szczepkowski, with whom we had a very fruitful collaboration. In particular it has been a privilege to work together with Jacek Szczepkowski on RbSr. His meticulous care and insight as well as his patient explanations during our data analysis were exemplary. He has been always available and never missed a call and we managed to work efficiently despite the distance. Our meeting and discussion during one of his visits here in Amsterdam turned out to be fundamental to my work.

I am grateful to Servaas Kokkelmans, Ben van Linden van den Heuvell, Wybren Jan Buma, Olivier Dulieu, Anne de Visser for taking the time to read my manuscript.

I am grateful to Carla and Oleksiy for their kindness and for accepting to be my paranymphs at the defense.

I would like to thank my friends, especially Andrea e Mattia, for being always there for me since childhood, despite the increasing distance.

I am forever indebted to my family, especially my father Giuseppe, my mother Cinzia, my sister Ambra, as well as my wife Claudia, whose unselfish kindness and patient support gave me strength throughout the years. I owe my scientific research to them, who, albeit ignorant of its contents, are the reason for it.

I dedicate this thesis to B.C.